Novel strategies to design and construct efficient semiconductor-based photocatalyst for enhancing photocatalytic hydrogen evolution and nitrogen fixation under sunlight irradiation

Thèse

Manh Hiep Vu

Doctorat en génie chimique
Philosophiæ doctor (Ph. D.)

Québec, Canada

Novel strategies to design and construct efficient semiconductor-based photocatalyst for enhancing photocatalytic hydrogen evolution and nitrogen fixation under sunlight irradiation

Thèse

Manh-Hiep Vu

Sous la direction de

Trong-On Do, Directeur de recherche

Résumé

L'énergie solaire est la source d'énergie la plus abondante au monde et elle peut être convertie en énergie chimique via des processus photocatalytiques. Au cours des dernières décennies, la photocatalyse sous la lumière du soleil est apparue comme une alternative innovante aux combustibles fossiles afin de résoudre et prévenir des problèmes graves liés à la crise environnementale et énergétique. Actuellement, les matériaux à base de semi-conducteurs (tels que TiO_2, C_3N_4, In_2O_3, WO_3) sont intensivement étudiés pour diverses applications photocatalytiques, y compris la réaction d'évolution d'hydrogène (HER) et la réduction de l'azote en ammoniac (NRR). Cependant, les inconvénients d'une faible absorption de la lumière visible, d'une faible séparation d'électron-trou et d'un manque de sites actifs ont limité les performances photocatalytiques de ces photocatalyseurs à base de semi-conducteurs.

Par conséquent, diverses approches telles que l'ingénierie structurelle, les hétérojonctions nanocomposites ont été étudiées afin de surmonter les problèmes de ces matériaux et ainsi augmenter l'activité catalytique. Dans le cadre de cette thèse, nous avons développé des nouvelles stratégies pour la synthèse des quatre types de photocatalyseurs efficaces pour la production d'hydrogène et la fixation de l'azote sous la lumière du soleil. Nos matériaux présentent une structure unique, qui favorise l'absorption de la lumière visible, la séparation des charges électrons-trous et l'augmentation du nombre de sites actifs.

Pour l'application de la génération d'hydrogène photocatalytique, nous avons d'abord synthétisé les sphères de type éponge $CdIn_2S_4$ monophasées via une méthode solvothermique suivie d'un traitement au gaz contenant H_2S. La formation du complexe Cd/In avec une distribution uniforme de Cd^{2+} et In^{3+} a joué un rôle crucial dans la formation du spinelle monophasé $CdIn_2S_4$. L'énergie de la bande interdite s'est avérée être significativement réduite, ce qui permet une absorption étendue de la lumière visible jusqu'à 700 nm, ceci est principalement attribué à la dispersion d'espèce sulfure sur la bande de valence du $CdIn_2S_4$ monophasé. Avec le dépôt de Ni métallique comme cocatalyseur de réduction, le photocatalyseur hybride Ni-$CdIn_2S_4$ a montré une efficacité améliorée pour la production d'hydrogène sous la lumière solaire, ce qui représente une augmentation de l'activité

d’environ, respectivement, 5,5 et 3,6 fois que celle des échantillons Pt-$CdIn_2S_4$ et Pd-$CdIn_2S_4$.

Le deuxième système photocatalytique développé implique la préparation de nitrure de carbone graphitique dopé au S (Ni-SCN). Ce dernier est chimiquement ancré au nickel par une technique connue sous le nom de processus de photo-dépôt assisté par sulfuration. L'origine de la structure distinctive du Ni-SCN est dû à l'existence de liaisons chimiques Ni-S-C-N dans le système, ce qui favorisait la séparation des charges photogénérées et améliorait la capacité d’absorption lumineuse du photocatalyseur. Par conséquent, l’échantillon Ni-SCN synthétisé présente une excellente activité photocatalytique pour la production d'hydrogène sous la lumière du soleil. En effet, ce système présente une activité beaucoup plus élevée que celle des systèmes g-C_3N_4 dopés au S, Ni supporté g-C_3N_4 et Pt supporté g-C_3N_4 dopés au S.

Pour une application photo (électro) catalytique de fixation de l'azote, nos travaux sont les premiers à rapporter la synthèse de nanoparticules d'Au chargées de nanoparticules $W_{18}O_{49}$ dopées au Fe (notées WOF-Au) par une synthèse solvothermique suivie d'un dépôt in situ des nanoparticules d'Au. L'incorporation de dopants Fe peut non seulement guérir les états de défaut de masse dans les réseaux non stœchiométriques $W_{18}O_{49}$, mais également favoriser la séparation et la migration interfaciale des électrons du photocatalyseur vers les molécules N_2 chimisorbées; tandis que les nanoparticules Au décorées sur la surface dopée au Fe $W_{18}O_{49}$ ont fourni les électrons à haute énergie pour la réduction de N_2 via l'effet de résonance plasmonique de surface localisé (LSPR). Le système WOF-Au plasmonique résultant montre un rendement amélioré pour la production de NH_3, beaucoup plus élevé que celui du $W_{18}O_{49}$ pur ainsi qu'une très grande stabilité. L'amélioration des performances photoélectrocatalytiques est principalement due à l'effet synergique des dopants Fe et des nanoparticules Au dans l'hôte $W_{18}O_{49}$.

Enfin, les cacahuètes creuses de In_2O_3 dopées au Ru (dénotées Ru-In_2O_3 HPN) ont été fabriquées par la nouvelle stratégie d'auto-matrice suivie de la calcination des précurseurs synthétisés. Les nanoparticules uniformes In_2O_3 sont étroitement agglomérées ensemble pour former une structure de cacahuète creuse, ce qui facilite la séparation et le transport des l'électrons-trous photoexcités, améliorant l’absorption de la lumière par multi-réflexion. De

plus, l'introduction des dopants Ru induit de nombreuses lacunes en oxygène à la surface et réduit l'énergie de la bande interdite du système photocatalytique. Ces lacunes d'oxygène agissent comme des centres de piégeage, facilitant la séparation des électrons trous photoexcités. Par conséquent, le taux de production d'ammoniac des Ru-In_2O_3 HPNs est 5,6 fois plus élevé que celui des In_2O_3 HPNs purs et largement supérieur au matériau en vrac d'In_2O_3, lorsqu'il est soumis à l'irradiation solaire.

Abstract

Solar energy is the most abundant energy source in the world, and it can be converted into chemical energy via photocatalytic processes. Over the last decades, sunlight-driven photocatalysis has emerged as an innovative alternative to fossil fuels for solving the severe problems related to environmental diseases and the energy crisis. Currently, semiconductor-based materials (such as TiO_2, C_3N_4, In_2O_3, WO_3, $BiVO_4$) have been intensively studied for diverse photocatalytic applications, including the hydrogen evolution reaction (HER) and the nitrogen reduction reaction (NRR) to produce ammonia. However, the drawbacks of weak visible light absorption, low electron-hole separation with high recombination rate, and lack of surface active-sites have limited the photocatalytic performance of these semiconductor-based photocatalysts. Therefore, various approaches such as structural engineering, nanocomposite heterojunctions have been applied to overcome the limitations of these materials and boosting the catalytic activity. In this thesis, we employed novel strategies to develop four efficient photocatalytic systems for hydrogen production and nitrogen fixation. Our materials possessed a unique structure, which is advantageous to promote the visible-light absorption, facilitate the separation of charge carrier, and increase the number of surface-active sites.

For the photocatalytic hydrogen evolution application, we firstly synthesized the single-phase $CdIn_2S_4$ sponge-like spheres via solvothermal method followed by H_2S gas treatment. The formation of CdIn-complex with uniform distribution of Cd^{2+} and In^{3+} played a crucial role in achieving the spinel structured-single phase $CdIn_2S_4$. The bandgap energy was found to be significantly reduced, resulting in the extended visible light absorption up to 700 nm, which was primarily attributed to the sulfide species-mediated modification of the valence band in $CdIn_2S_4$ single-phase. With the deposition of Ni metal as a reduction cocatalyst, the hybrid Ni-$CdIn_2S_4$ photocatalyst showed enhanced solar light-driven photocatalytic hydrogen evolution efficiency, which is around 5.5 and 3.6 folds higher than that of Pt-$CdIn_2S_4$ and Pd-$CdIn_2S_4$ samples, respectively. The second developed photocatalytic system involved the preparation of chemically bonded nickel anchored S-doped graphitic-carbon nitride (Ni-SCN) through a technique known as sulfidation assisted photo-deposition process. The origin of the distinctive structure of Ni-SCN was due to the existence of Ni-S-

C-N chemical bonds in the system, which fundamentally favored the separation of photogenerated electron-hole and improved the light-harvesting capabilities of the photocatalyst. Consequently, the synthesized Ni-SCN exhibited an excellent sunlight-driven photocatalytic activity toward hydrogen evolution, which was several times higher than S-doped g-C_3N_4, Ni supported g-C_3N_4 and Pt loaded S-doped C_3N_4 systems.

For photo(electro)catalytic nitrogen fixation application, our work is the first to report the synthesis of Au nanoparticles loaded Fe doped $W_{18}O_{49}$ (denoted as WOF-Au) nanorods through a solvothermal synthesis following by in situ deposition of Au nanoparticles. The incorporation of Fe dopants can not only heal the bulk-defect-states in nonstoichiometric $W_{18}O_{49}$ lattices but also promote the separation and interfacial migration of electrons from photocatalyst to chemisorbed N_2 molecules; while Au nanoparticles decorated on the Fe doped $W_{18}O_{49}$ surface provided the high energetic electrons for N_2 reduction via the localized surface plasmon resonance effect (LSPR). The obtained plasmonic WOF-Au system shows an enhanced NH_3 yield, which is much higher than that of the bare $W_{18}O_{49}$, as well as very high stability. The enhancement in photoelectrocatalytic performance is mainly contributed by the synergetic effect of Fe dopants and plasmonic Au nanoparticles on the $W_{18}O_{49}$ host. Lastly, Ru doped In_2O_3 hollow peanuts (demoted as Ru-In_2O_3 HPNs) were fabricated by the novel self-template strategy followed by the calcination of the as-synthesis precursors. The uniform In_2O_3 nanoparticles were closely packed together to form a hollow peanut structure, which facilitated the separation and transportation of photoinduced electron-hole and favored the light-harvesting ability by the internal multi-reflection process. Furthermore, the introduction of Ru dopants induced numerous surface oxygen vacancies and narrow down the bandgap energy of the photocatalytic system. These oxygen vacancies act as trapping centers, facilitating the separation of photoexcited electrons and holes. Consequently, the ammonia production rate of Ru-In_2O_3 HPNs was 5.6 times and much higher as compared to pure In_2O_3 HPNs and bulk material of In_2O_3 under solar light irradiation.

Table of content

List of Figures

List of Tables

List of abbreviations

A	Electron-acceptor
AQY	Apparent Quantum yield
BET	Brunauer-Emmett-Teller
CB	Conduction band
D	Electron-donor
DFT	Discrete Fourier transform
EA	Ethylamine
EDS/EDX	Energy Dispersive X-ray spectroscopy
EM	Electron microscopy
EPR	Electron paramagnetic resonance
FTIR	Fourier transform infrared spectroscopy
GC	Gas chromatography
HER	Hydrogen evolution reaction
HPN	Hollow Peanut
LDH	Layer double hydroxide
LSPR	Linear Surface Plasmon Resonance
MeOH	Methanol
MOF	Metal-organic framework
NHE	Normal hydrogen electrode
NMR	Nuclear magnetic resonance
NP	Nanoparticle
NRR	Nitrogen reduction reaction

OV	Oxygen vacancies
PEC	Photoelectrochemical
PL	Photoluminescence
PS	Photocatalytic system
QE	Quantum efficiency
rGO	Reduced graphene oxide
SAPC	Single-Atom photocatalyst
SEM	Scanning electron microscopy
TEA	Tetrabutylammonium
TEAOH	Tetrabutylammonium hydroxide
TEM	Transmission electron microscopy
TEOA	Triethanolamine
UV-vis	Ultraviolet-visible
VB	Valence band
XPS	X-ray photoelectron spectroscopy
XRD	X-ray diffraction

Acknowledgments

First and foremost, I would like to convey my sincere thanks to Prof. Trong-On Do for giving me this valuable opportunity to pursue an academic research career at Université Laval. His enthusiasm and undoubted expertise motivated me constantly, which greatly made me engaged throughout my research works. Without his guidance and support, the presented work in this thesis would have been impossible.

I would like to express my great appreciation to Dr. Chinh Chien Nguyen and Prof. Sakar Mohan, my colleagues in Prof. Do's group. They are my mentors in research and my close friends in real life. I learned many skills from them since my very first step in my Ph.D. program. Dr. Chinh Chien Nguyen gave me a fundamental knowledge in the field of photocatalysis and Prof. Sakar Mohan taught me to write a scientific paper. Similarly, I would like to extend my gratitude to other members in our group, Dr. Mohammad Reza Gholipour, Dr. Amir Enferadi Kerenkan, Dr. Nhu-NangVu, Duc-Trung Nguyen, Arnaud Gandon, Rokesh Karuppannan, Jorge Becerra Sanchez, Vishnu Nair Gopalakrishnan, Toan-Anh Quach, Pejman Monazzam, and Anis Chouat. I wish them all success in all their future endeavors.

I sincerely appreciate Mr. Alain Adnot for XPS characterizations, Jean Frenette for XRD facility, Richard Janvier for the help with electron microscopes, and other staff members in the Department of Chemical Engineering for their technical and administrative supports and assistance. Also, I would like to convey my special thanks to Mr. Jean-Nicolas Ouellet, Mr. Jérôme Noël, and Mr. Marc Lavoie for their safety advice and guidance in setting up the required experimental facilities for my research in our lab.

I am grateful to the financial support from the Natural Science and Engineering Research Council of Canada (NSERC) through Collaborative Research and Development (CRD), Strategic Project (SP), and Discovery Grants. I would also like to convey my sincere thanks to the Center in Green Chemistry and Catalysis (CGCC) for their international scholarship support to undergo a 6-month internship in the US.

Last but not least, I would like to express my extreme gratitude to my dear parents and my brother for their unconditional love, support, and encouragement in all my studies and

activities. Especially, I would like to thank my fiancée from the bottom of my heart, who is always supporting me whenever I doubted myself the most. Also, I am thankful to all my Vietnamese friends for their love and support during my stay in Quebec.

Without you all, I would have not been able to complete my doctorate.

To my wonderful mother, my respectful father, and my beloved fiancée, Ngoc Oanh

Foreword

This graduation thesis includes eight chapters. Four of them were published in the form of scientific papers during this Ph.D. research and one of them is currently being under the process of submission. The scholar of this Ph.D. thesis is the first author of all these papers.

Chapter 1 Introduction and Chapter 2 Literature review are written by integrating the review paper published by the candidate: Manh-Hiep Vu, Mohan Sakar, Trong-On Do "Insights into the Recent Progress and Advanced Materials for Photocatalytic Nitrogen Fixation for Ammonia (NH_3) Production" Catalysts, 2018, 8 (12), 621.

Chapter 4 has been published as Manh-Hiep Vu, Chinh-Chien Nguyen, Mohan Sakar, Trong-On Do. "Ni supported $CdIn_2S_4$ sponge-like spheres: a noble metal-free high-performance sunlight driven photocatalyst for hydrogen production", Phys. Chem. Chem. Phys., 2017, 19, 29429-29437.

Chapter 5 has been published as Manh-Hiep Vu, Mohan Sakar, Chinh-Chien Nguyen, Trong-On Do. "Chemically Bonded Ni Cocatalyst onto the S Doped g-C_3N_4 Nanosheets and Their Synergistic Enhancement in H_2 Production under Sunlight Irradiation" ACS Sustainable Chemistry & Engineering 6 (3), 4194-4203.

Chapter 6 has been accepted as Manh-Hiep Vu, Chinh-Chien Nguyen, Trong-On Do, "Synergistic Effect of Fe doping, and plasmonic Au nanoparticles on $W_{18}O_{49}$ nanorods for enhancing photoelectrochemical nitrogen reduction", ACS Sustainable Chemistry & Engineering, 2020.

Chapter 7 reports the work entitled "Construction of Ru doped In_2O_3 hollow peanut as an efficient photocatalyst for solar light-driven nitrogen reduction" by Manh-Hiep Vu, Toan Anh Quach, Trong On Do, which is under the process of submission.

In all these works, the candidate performed all the experimental works and collected all the data under the supervision of Prof. Trong-On Do. The candidate wrote the first version of all the manuscripts and the other author helped in revising the manuscripts prior to the submissions.

Introduction

This chapter discusses the potential of sunlight-driven photocatalysts to deal with the global energy crisis and current environmental issues. The fundamental challenges and current development trends in semiconductor-based photocatalyst have been presented. The objectives and organization of this thesis have also been introduced in this chapter.

1.1 Photocatalyst and the biggest challenges facing the world

In this current century, climate change and energy production are some of the most significant and important challenges that are being faced by the people in the world. At present, fossil fuels such as coal, oil, and natural gas play an important role in human life and provide worldwide energy demands. Unfortunately, these fossil fuels are non-renewable resources, and these energy sources will be exhausted within a relatively short time. Moreover, the combustion of these fossil fuels produces large quantities of pollutants, which cause a series of ecological disasters such as environmental pollution and global warming, increasing many risks for human life and organisms. Hence, there is a critical need for the development of green, renewable, and carbon-free energy sources to overcome the challenges of energy and the environment.

Among a variety of available renewable energy sources, being abundant, clean, and free, solar energy is generally an ideal energy source that can be used to address the future energy demand as well as environmental issues. Every single hour, the total solar energy delivered onto the Earth is more than the planet needs to satisfy the global energy needs for an entire year. Currently, the utilization of solar energy is mainly focused on the solar cell, which could transform the power of sunshine into electricity. Although this strategy effectively converts solar energy to usable energy, it requires a large upfront cost and extra elements such as batteries or inverters, which are also very challenging. Alternatively, another approach for the conversion of solar energy into chemical energy via the photocatalytic process can be highly feasible and attractive.

Solar fuel production of hydrogen (H_2) and ammonia (NH_3) from water and nitrogen by photocatalysts have received much attention recently as a possible next-generation energy carrier. Hydrogen and ammonia can be produced by photocatalytic water splitting and nitrogen photo-fixation, respectively. This alternative solution is capable of replacing fossil fuels and providing a sustainable future for our people and the environment. For instance, the combustion of hydrogen releases 143 $kJ.g^{-1,}$ which is 3.5 times higher than that of gasoline (45 $kJ.g^{-1}$). Moreover, hydrogen fuel is zero-carbon-emission fuel since the only product created from burning hydrogen is water. Similar to molecular hydrogen, NH_3 is also a carbon-

free energy-source for the end-users. Ammonia and the associated chemicals could provide an alternative energy resource and use for the synthesis of fertilizers.

Although much research has been devoted to developing an efficient sunlight-driven photocatalyst for durable use, however, the photocatalytic efficiency is still limited, which is always restricted by two fundamental challenges: weak solar light absorption and insufficient charge separation ability. Therefore, an efficient photocatalyst must demonstrate a strong absorption ability of photon energy in the visible light spectrum and perform a high rate of electron-hole separation. However, there is no single component semiconductor that could satisfy all these requirements. Recently, nanocomposites with combined functional components were found to enhance their intrinsic properties to overcome the limitation in the parent materials, thus demonstrating their advanced utility for the different applications.

Apart from these fundamental drawbacks, the photocatalytic nitrogen fixation also suffers from their disadvantage resulting from N_2 molecules and reduction reaction. First, the N_2 molecule with the N-N triple bond is exceptionally stable, and it requires a considerable amount of energy for its activation and dissociation. Second, nitrogen is an inert gas that is difficult to be adsorbed on the surface of catalysts. Another limitation is the competition of the reduction of N_2 to NH_3 with other more kinetically favorable processes such as water splitting, thus, reducing the efficiency. To overcome these challenges, it is necessary to create appropriate active sites that can effectively absorb nitrogen. These active sites can serve as a trapping cage to capture the photogenerated electrons then transfer to the absorbed nitrogen as well as suppress the charge carrier recombination.

1.2 Objectives of the thesis

This thesis aims to design efficient catalysts using advanced strategies of structural engineering and combining multi-component semiconductors for photocatalytic hydrogen evolution and photoelectrocatalytic nitrogen fixation under solar light.

The first objective is to shed light on the recent progress in the development of a variety of routes for the synthesis of advanced materials and emphasize their application for hydrogen evolution and nitrogen photo-fixation. This review also concludes with a concise overview

of the present status, analyzes the potential and future development of photocatalysts with a view towards enhancing the performance of the different photocatalytic materials

The second objective is the main objective of this thesis, where we report the novel catalysts that are developed and studied by us, which is based on $CdIn_2S_4$, g-C_3N_4, WO_3, and In_2O_3 material. Using H_2S gas treatment at high temperature, we have successfully synthesized $CdIn_2S_4$ from its oxide form and doped the sulfur atoms into the crystal structure of g-C_3N_4, which boosted the photocatalytic activity of these materials toward hydrogen evolution. For the nitrogen fixation application, we combine Fe doping and Au loading on $W_{18}O_{49}$ materials. The synergistic effect of Fe dopant and Au nanoparticles significantly promoted the activity of these catalytic systems. In the last material, we construct a hollow structure of In_2O_3 peanuts enriched oxygen vacancies by Ru dopants. Both ruthenium and oxygen vacancy can serve as an active site to promote the photocatalytic performance toward nitrogen fixation of the catalytic system.

The third objective is to provide a suggestion for designing new and effective solar-driven photocatalysts for water splitting and nitrogen fixation

1.3 Organization of the thesis

Introduction

This section typically starts with the general introduction, declares the scope, and gives the outline of the thesis.

Chapter 2: A literature review

Chapter 2 first gives a brief background on heterogeneous photocatalysis followed by the fundamental challenge of photocatalytic hydrogen evolution and nitrogen fixation.

Chapter 3: Characterization techniques

The characterization techniques employed in the present thesis are presented and discussed in this chapter, which included the X-ray diffraction (XRD), Electron microscopy techniques such as scanning electron microscopy (SEM), Transmission electron microscopy (TEM), X-ray photoelectron spectroscopy (XPS), Fourier transform infrared (FT-IR) spectroscopy,

Nitrogen physisorption analysis, Ultraviolet-visible (UV-Vis) spectroscopy, Photoelectrochemical analysis (PEC) and Gas chromatography (GC) spectroscopy.

Chapter 4: Ni Supported $CdIn_2S_4$ Sponge-like Spheres: A Noble Metal Free High-Performance Sunlight Driven Photocatalyst for Hydrogen Production

This chapter reports the synthesis of Ni supported $CdIn_2S_4$ sponge-like spheres for enhancing photocatalytic activity toward hydrogen evolution. The influence of H_2S gas treatment on the structural and optical characteristics of single-phase $CdIn_2S_4$ was studied. The as-obtained Ni loaded $CdIn_2S_4$ exhibited better photocatalytic performance as compared to the noble metal cocatalyst Pt loaded $CdIn_2S_4$

Chapter 5: Chemically bonded Ni co-catalyst onto the S-doped g-C_3N_4 nanosheets and their synergistic enhancement in H_2 production under sunlight irradiation

Chapter 5 reports the preparation of chemically bonded Ni onto the S-doped g-C_3N_4 for sun-light driven photocatalytic hydrogen evolution. The effect of cocatalyst concentration has been investigated. The central feature of this material was the formation of Ni-S-C-N chemical bonds, which greatly facilitated the separation of electron-hole and enhance the absorption of visible-light photons.

Chapter 6: Synergistic Effect of Fe doping and plasmonic Au nanoparticles on $W_{18}O_{49}$ nanorods for enhancing photo-electrochemical nitrogen reduction

In this chapter, the direct synthesis of Fe doped $W_{18}O_{49}$ nanowires has been prepared by a solvothermal method. Then, the Fe-$W_{18}O_{49}$ sample was coupled with Au nanoparticle for improving the utilization of light. The electronic and optical properties of the Au loaded Fe doped $W_{18}O_{49}$ have been also examined. The photoelectrochemical nitrogen fixation of the obtained sample was performed under solar light irradiation.

Chapter 7: Construction of Ru doped In_2O_3 hollow peanut-like structure for enhanced photocatalytic nitrogen reduction under solar light irradiation

Chapter 7 reports the fabrication of Ru doped In_2O_3 hollow peanut structure by self-template assisted method. We have proved that Ru doped In_2O_3 can generate surface oxygen vacancy and promote the surface reduction reaction. The photocatalytic activity of Ru doped In_2O_3

sample was evaluated for the sunlight-driven reduction of nitrogen to ammonia in the liquid phase.

Conclusion and future prospects

In the last chapter, we summarized all works described in the present thesis from Chapter 4 to 6. Further, a compelling strategy of construction of a single atomic active site with advanced structure designs are suggested for the photocatalytic hydrogen evolution and nitrogen reduction reaction

Chapter 2: A literature review

This chapter provides a basic principle along with the critical challenges of the photocatalytic hydrogen evolution (HER) and nitrogen photoreduction (NRR). We present the mechanisms and the recent achievements of photocatalytic HER and NRR. Additionally, the discussions focus on the strategies to promote the photocatalytic performance of semiconductor-based materials, including engineered defects, cocatalyst, and plasmonic effect. These approaches have drawn considerable attention owing to its great potential for solving the problems of weak light absorption, low charge separation, and an insufficient number of active sites.

2.1 The principle of photocatalysis on semiconductors

Semiconductors (SCs) are used as photocatalytic materials, thanks to their suitable amalgamation of electronic properties, structure, light-absorption characteristics, charge transport dynamics, and a favorable lifetime of their excited-state charge carriers. Basically, a semiconductor possesses an energy gap between the top of the filled-valence band (VB) and the bottom of the vacant-conduction band (CB), which is known as the bandgap energy of the SC[1]. Thus, the separation of charge carriers between these bands only occurs with sufficient energy supply. In semiconductors, the photocatalytic process involves three main steps: light absorption, charge separation, and catalytic reaction. Under light illumination, the electron absorbs a photon with energy higher than or equal to the bandgap energy of the semiconductor, excites from VB to CB, and releases holes in the VB (**Figure 2.1**). This light-induced promoting electron-hole separation is a prerequisite step in all semiconductor photocatalysis. Finally, the photogenerated species transfer to the semiconductor surface and initiate redox reaction of absorbed reagents. However, electrons and holes are to recombine and dissipate the energy in the bulk (volume) or on the surface of the semiconductor, because the kinetic-barrier for the electron-hole recombination process is relatively low, resulting in a decrease of reaction efficiency[2]. Therefore, prevention of charge recombination is a significant challenge in the photocatalytic field. In the last decades, there has been a considerable amount of effort to increase the lifetime of photogenerated carriers such as developing photocatalyst with nanostructure, cocatalyst, surface engineering, and junction[3-4].

Moreover, a wide variety of semiconductors, mainly metal oxide and chalcogenides, have been examined with capability for photocatalyst, but only a few of them are considered to be effective photocatalyst because of the appreciable bandgap. In general, wide-bandgap semiconductors prove to be better photocatalytic activity as compared to low-bandgap catalysts. For example, titanium dioxide showed better photocatalysis than cadmium sulfide for hydrogen production, due to the increased free energy of photo-induced charge species of the TiO_2 and the intrinsic low chemical- and photochemical stability of the CdS. However, the narrow-bandgap materials such as metal sulfides are better absorbers of the solar light, proposing the considerable advantage of the potential usage of an available power supply,

the sun. Accordingly, a promising strategy with this concern has been attained with the utilization of several methods aiming to improve the electronic state and optical characteristics of semiconductors, including metal deposition, doping, and dye-sensitization. On the other hand, to obtain effective photocatalytic procedure, the bottom of the CB must be located at a more negative potential than the reduction potential of electron acceptor (A) while the top of CB must beyond the oxidation-potential of electron-donor (D).

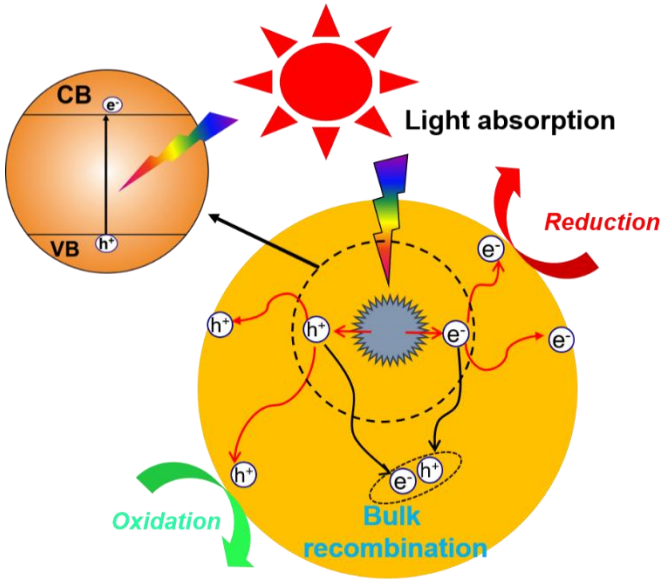

Figure 2.1: Simulation of semiconductor photocatalysis under light irradiation.

2.1.1 Quantum yield (QY)

The efficiency of the photocatalytic process is measured by quantum yield (QY), which has been considered to describe the number of molecules converted relative to the total number of incident-photons on the reactor walls for an unknown reactor-geometry and for polychromatic radiation.

$$QY\ (\Phi) = \frac{\#\ \text{molecule decomposed}}{\#\ \text{photon absorbed}} \qquad \textbf{(2.1)}$$

Additionally, quantum yield could be calculated based on the rate of reaction dividing to the absorbed light intensity (I_a)

$$\Phi = \frac{\text{Rate}}{I_a} \qquad \textbf{(2.2)}$$

Although the measurement of the absorbed light intensity is easy in homogeneous systems, it is difficult for heterogeneous reactions such as thin films or semiconductor suspensions. In this stage, the suspended particle also reflected and scattered incident light instead of total absorption. Thus, it is very exhausted to correct this loss, including 13-76% of the total incident photo flux[5]. Otherwise, light is also absorbed by-products or educts of reaction, suggesting QY should be determined at a very early reaction time. To conquer such problems in heterogeneous photoreaction, it was proposed replacing the absorbed light intensity by the incident intensity (I_0). Therefore, apparent quantum yield (AQY, ς)[6-7] has been termed to measure the efficiency of the photocatalytic process:

$$\varsigma = \frac{\text{Rate}}{I_0} \qquad \textbf{(2.3)}$$

2.1.2 Materials for photocatalysis

Based on the fundamental chemical composition system, all the semiconducting materials can be divided into three main categories, mainly metal oxides, metal sulfides, and metal-free semiconductors.

Usually, metal oxides are the most common materials which can be utilized for photocatalysis in various reactions such as H_2 production, CO_2 reduction, and N_2 fixation. These kinds of materials have wide applications according to their band structure and activities. However, most of them only activate under UV light irradiation due to their large bandgap energy. To overcome this difficulty, the substitutions of cations or anions in the lattice of a wide bandgap semiconductor have been employed to narrow bandgap energy, enhancing the visible light response. This substitution of cations and anions in the crystal lattice may form intermediate energy levels (due to the energy levels of impurities) within the bandgap of photocatalyst that facilitates their absorption in the visible range. For example, titanium dioxide with the properties of stability, non-toxicity, and high photocatalytic activity is a suitable catalyst for water splitting reaction. Nevertheless, it only absorbs UV light due to the wide bandgap energy (Eg = 3.2 eV). To deal with this disadvantage, Khan et al modified n-type TiO_2 chemically by doping C on this material. Carbon replaces some of the lattice oxygen atoms, resulting in a decrease in bandgap energy to 2.32eV[8].

Contrary to metal oxides, the metal sulfides normally possess narrow bandgap. Thus, they can absorb visible light to generate electron-hole. Moreover, the conduction reduction potential of water is less negative than their CB and so they can reduce water into molecular hydrogen. Otherwise, these materials also have several disadvantages such as instability and fast recombination of photoexcited charges. The most common example is cadmium sulfide, one of the best semiconductors with high activity for hydrogen production under visible light illumination. With narrow bandgap materials, the recombination process of electron and hole is very easy. Reducing the particle size of CdS can provide more active sites, decrease the travel path of migration of photoexcited electron to the semiconductor surface, and prevent charge recombination[9]. Also, combining CdS nanoparticles with other semiconductors can enhance their stability and photocatalytic activity[10-13].

Besides these metal-based semiconductors, some nitride-based systems also exhibit photocatalytic activities towards water reduction in the visible range of solar light. Recently, graphitic carbon nitride (g-C_3N_4) has drawn a lot of attention because of its intrinsic properties such as narrow bandgap and non-toxicity. This metal-free polymeric material shows hydrogen evolution under visible light illumination with high chemical stability. Nevertheless, its photo-conversion efficiency is much lower than that of TiO_2 or CdS and therefore it requires further efforts to be made to show the improved photocatalytic activities.

2.1.3 Advanced structural engineering of heterogeneous photocatalysts

2.1.3.1 Heterojunctions

It can be argued that the development of heterojunction photocatalysts is one of the most feasible pathways to improving the efficiency of semiconductor materials. The literature review has been proven that some fundamental properties are required for photocatalytic materials, such as efficient light absorption, and appropriate charge separation. These characteristics can be satisfied by integrating two or more semiconductors. The combined heterojunctions enhance the performance of various instruments, such as solar cells, photoluminescence, and electrochromic devices[14-16]. The key feature of photo(electro)catalytic heterojunctions is the migration of photo-excited electron from a semiconductor to another semiconductor. **Figure 2.2** illustrateswo common types of

heterojunction semiconductors. In the first type of heterojunctions, both photoexcited electrons and holes move from the first semiconductor to the second semiconductor because of their band-edge position. This case seems to be ineffective in improving photocatalytic activity due to the recombination of the charge carrier in one semiconductor. Similarly, the conduction band of semiconductor 1 is more negative than that of semiconductor 2 in type 2. However, the difference between type 1 and 2 is the relative position of the valance band of the two semiconductors. In type 1, the valence band of semiconductor 1 is more positive in comparison with semiconductor 2, while this situation is reversed with group 2 of semiconductor heterojunctions. Because of this distinction, excited electrons can jump from semiconductor 1 to 2 and generated holes can migrate from semiconductor 2 to 1. If both semiconductors have sufficient intimate contacts, an efficient charge separation will occur during light illumination. Consequently, charge recombination is prevented, and the lifetime of photogenerated charges is prolonged, resulting in higher photocatalytic activity.

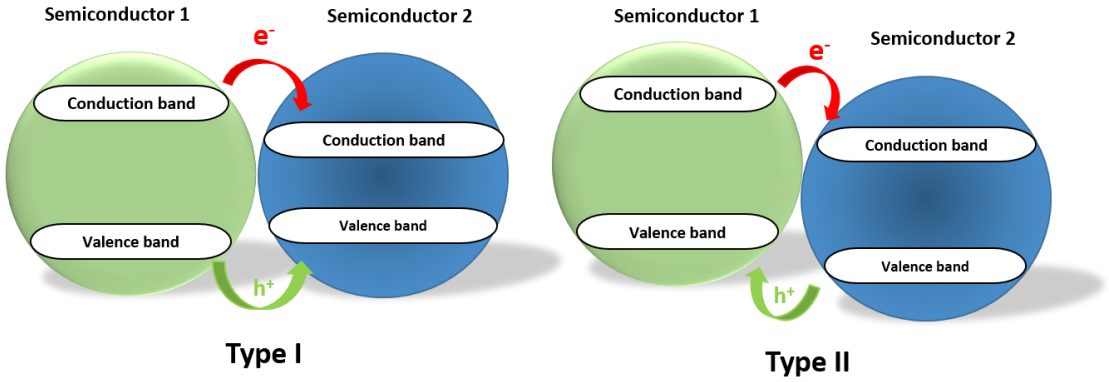

Figure 2.2: Various kinds of photocatalytic heterojunction systems.

2.1.3.2 Z-Schemes nanocomposite

Although the above-mentioned photocatalytic heterojunction systems are efficient for promoting photoinduced charges separation, the reduction and oxidation ability of these heterojunctions is sacrificed because the redox processes occur on the semiconductor with the lower reduction and higher oxidation potentials. To avoid this problem, the Z-scheme photocatalytic conception was invented to overcome the difficulty of the heterojunction systems. The Z-scheme heterojunction is also termed as the electron mediator or a dual photocatalyst system. This photocatalytic system is characterized by the isolation of

photogenerated charges, which reduces the bulk electron-hole recombination. Moreover, the gathering of electrons in the CB of the photocatalytic system I (PS I) make PS I an electron-rich region, which can consume the photo-reduction of PS I. Similarly, the aggregation of photogenerated holes in the VB of photocatalytic system II (PS II) makes it a hole-rich region, appropriating for photo-oxidation reaction (**Figure 2.3**). However, the number of photogenerated electrons and hole in the Z-scheme system is just half of that in the heterojunction under the same condition because the charge carriers will recombine via mediators to bring the electron mediator to their original form. Even then, the Z-scheme photocatalytic systems still attract enormous attention due to the unique electron transfer phenomenon.

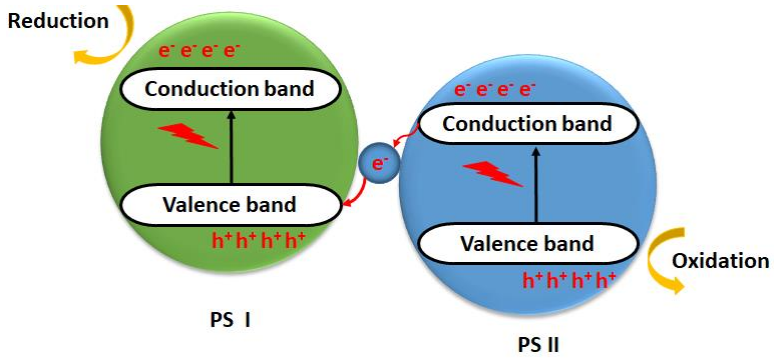

Figure 2.3: Z-scheme photocatalytic system.

2.1.3.3 Defective catalysts

The advanced catalyst syntheses are always accompanied by the introduction of intrinsic defects and impurities phase such as dopants or vacancies. The engineering defects is an effective strategy for tuning and controlling the nature of materials such as their electronic and chemical properties. Generally, engineered defects are classified into four main categories based on defect's dimensions: point, line, planar, and volume defects[17]. Depending on the catalytic purposes, different types of defects have been employed. In this section, the positive and negative impacts of defects are discussed.

Defective materials usually show remarkable activities compared to defect-free materials. A common example is a TiO_2 semiconductor, which is known as one of the most efficient photocatalysts for various applications such as hydrogen evolution[18-19], CO_2 reduction[3, 17, 20],

the volatile organic compound (VOC) degradation[21-23], and nitrogen fixation[24-29]. However, pure TiO_2 demonstrates restricted performance in photocatalytic activity due to large bandgap energy, fast electron-hole recombination rate, and an insufficient number of active sites[29]. On the other hand, major studies revealed that the "*induced*" intrinsic defects in titania help to reduce these limitations and enhance photoactivity. These improvements might be contributed by the following aspects. First, the engineered-defects such as anion vacancies and dopants induced impurity phases can act as trapping centers to capture electrons or holes, inhibiting charge recombination as well as promoting their separation. Additionally, point defects such as oxygen vacancies play a role as active sites which facilitate the adsorption and activation of reactant molecules. Thirdly, creating defects leads to narrow down bandgap energy, resulting in increasing of light absorption ability. It is worth noting that a number of generated electron-hole would be greater if a semiconductor can absorb light in the longer wavelength region. Consequently, photocatalytic activity is improved due to a high number of photo-induced charge carriers.

In addition to the desired effects on the catalytic activity of the semiconductors, intrinsic defects also have negative effects on catalytic materials. Recent studies reported that only the surface defects support the enhanced photoactivity performance, whereas the bulk defects suppress electron-hole separation and inhibit the photogenerated charges migration[30]. For example, Gurylev *et al.* fabricated oxygen vacancies (OVs) supported amorphous titania thin film by atomic layer-by-layer deposition[31]. After depositing the amorphous layer with 100 cycles, the oxygen vacancies in these layers significantly changed their role to bulk defects instead of surface defects in a single layer. These bulk defects trap electrons-holes and leading to the increased recombination rate and reduce photocurrent of the system. Furthermore, as mentioned earlier, the introduction of defects might reduce bandgap energy or create defect bands underneath the conduction band level. Narrowing the bandgap energy could weaken the reduction and oxidation ability of photocatalytic semiconductors since the conduction band and valence band are shifted towards each other[32]. Alternatively, the photoexcited electrons may be relaxed at the defect states formed in bandgap energy. Therefore, only the electrons that can absorb high photon energy and overcome the defect level are valuable to N_2 reduction. So far, to control desired defects formation, various synthesis approaches have been devoted to controlling the surface and bulk defects. Several

recent approaches were developed for controlling the defect formation, such as high-temperature treatment at reducing or inert atmosphere, chemical reduction, vacuum activation, ultraviolet irradiation, phase transformation via fast heating, ball milling, plasma etching, and lithium-induced conversion[33].

2.1.3.4 Cocatalsysts

A cocatalyst is an integrated compound to the semiconducting material to promote their photocatalytic activity. There are three main types of cocatalysts: reduction, oxidation, and plasmonic cocatalysts. The strategy of loading cocatalysts over semiconductor materials has been widely applied in photo(electro)catalytic water splitting and CO_2 reduction[34-35]. Cocatalysts play three main roles for improving the performance of photo(electro)catalysts[36]: (1) lowering the activation energy or overpotential of redox half-reaction; (2) promoting electron-hole separation and inhibiting photogenerated charge recombination; (3) suppressing the photo-corrosion and increasing the stability of photocatalytic materials. In a water decomposition reaction, the cocatalyst can avail enhancing either water reduction or oxidation half-reaction. For water reduction, cocatalysts are usually tiny metal nanoparticles (NCs), which create a Schottky junction with semiconductor and support for charge separation in a photocatalyst of photochemical cell[37-38]. In principle, the contact between the metal and semiconductor induces an electric field that separates excited electrons and holes more easily[39-41]. Additionally, the metal supplies active sites for hydrogen generation due to its relatively low over the potential for water reduction.

The most common cocatalysts for hydrogen production are Pt, Rh, Au, NiO, and RuO_2. Maeda et al report that loading both Rh/Cr_2O_3 and Mn_2O_3 supported GaN:ZnO can effectively promote overall water splitting under visible light although the quantum yield of this system was relatively low[42]. Maeda proved that Rh/Cr_2O_3 acted as electron collectors to host hydrogen evolution while the main function of is the active sites for the water oxidation reaction. However, most cocatalysts are noble metals that are rare and expensive, thus prohibiting their wide-scale application. Therefore, the development of non-noble and low-cost cocatalyst is extremely important.

The physical and chemical characteristics of the cocatalyst such as particle size and valence states, which directly affect their performance, are strongly dependent on the loading method of the cocatalysts. Although depositing more cocatalyst provides more active sites for reactions, it reduces the absorption capability of the photocatalyst. Thus, the concentration of the cocatalyst should be optimized to obtain the maximum activity during water splitting under light illumination.

2.1.3.5 Plasmonic cocatalyst

Although gold metal has never been recognized as a reduction catalyst for nitrogen fixation, the gold nanoparticles (Au NPs) are extensively utilized as cocatalysts due to its localized surface plasmon resonance (LSPR) effect[28, 43-48]. In general, under visible light irradiation, the Au NPs deposited on a semiconductor induce high energy electrons, denoted as hot electrons. These electrons can overcome the Schottky barrier and be irreversibly injected into the conduction band of the semiconductor. As a result, photoexcited electrons and holes are separated in the semiconductor and metal nanoparticles, respectively, preventing charge recombination**. Figure 2.4** illustrates the mechanism of plasmon-induced Au NPs load TiO_2 photocatalyst[49].

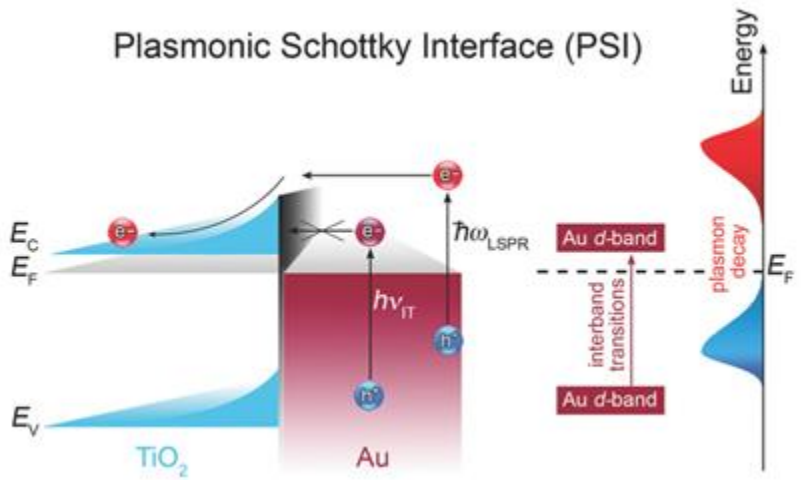

Figure 2.4: (a) Mechanism of plasmon-enhanced Au loaded TiO_2 photocatalyst[49]

2.2 Fundamental principle of photocatalytic hydrogen evolution

2.2.1. Fundamental of photocatalytic hydrogen evolution and water splitting

Photocatalytic hydrogen evolution

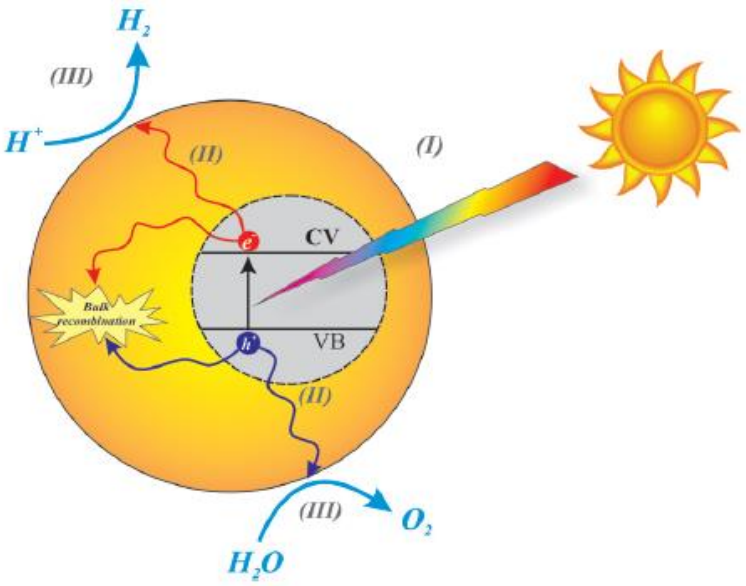

Figure 2.5: Sketch diagram showing the basic overall principle of water splitting on a photocatalyst.

Water this the most plentiful supply that can be utilized for producing hydrogen via photocatalytic water splitting. In recent decades, hydrogen production from water and solar energy has been attracted because it is a green process, using water and photon energy – clean power. On the other hand, this production does not release any dangerous by-product or pollutants. Therefore, water splitting progress is expected to achieve a great contribution to solving energy and environment challenges

In 1972, the discovery of Fujishima and Honda were succeeded in produce hydrogen from water with light irradiation[50]. They found that TiO_2 and Pt can act as anode and cathode electrodes in a photo-electrochemical cell, respectively. Since then, photochemical water splitting on semiconducting material has been investigated extensively. Later, Bard introduced the photocatalysis process for decomposing water into H_2 and O_2 under illumination with light[51]. Generally, photocatalytic water splitting includes three main steps:

(I) a semiconductor absorbs photon energy and electrons-holes are generated inside semiconductor photocatalyst particles by bandgap excitation; (II) the photogenerated charges which do not suffer recombination again inside the bulk materials, migrate towards the surface of semiconductor; (III) on the catalytic surface, electrons can reduce protons to H_2 and hole can oxidize water to O_2. **Figure 2.5** depicts the basic principle of overall water splitting on a semiconductor photocatalyst.

$$H_2O + 2h^+ \rightarrow 1/2O_2 + 2H^+ \qquad \textbf{(2.4)}$$

$$2H^+ + 2e^- \rightarrow H_2 \qquad \textbf{(2.5)}$$

In principle, the water-splitting reaction is possible with both visible and near-infrared light due to the different potentials between H_2/H_2O and H_2O/O_2 half-cell reaction is only 1.23V. Therefore, the bandgap of semiconductors should be at least 1.23eV to split the H_2O molecule. However, by considering related factors such as energy loss during different states in the photocatalysis, a bandgap greater than 2 eV is required for an efficient semiconductor. This energy is equal to the energy of a photon with a wavelength of less than 620nm[52-53]. Other influences than bandgap energy such as charge carrier separation, mobility, and the lifetime of photoexcited electrons and holes also play a critical role in photocatalytic activity. In many cases, recombination is the main process that the charge carrier undergoes. As a general rule, highly crystalline materials with a low density of defects, which act as recombination centers for electrons and holes, are beneficial for the water-splitting reaction. To facilitate the charge separation, photocatalysts are assembled with an appropriate cocatalyst or buffer layer[54-58]. The cocatalysts are typically a noble metal (Pt, Au) or metal oxide (NiO, RuO_2) loaded on the surface of nanoparticles whose principal role is to reduce the electron-hole recombination and to reduce the activation energy for gas evolution.

Overall water splitting

The overall water splitting under sunlight illumination is the ultimate objective of the photocatalytic hydrogen production system. In this progress, a photocatalyst with an appropriate bandgap can absorb photon energy, producing hydrogen and oxygen simultaneously. However, this reaction is an uphill reaction with a positive change in the Gibbs free energy of 237kJ/mol[59].

Several materials can absorb ultraviolet light and split water directly into hydrogen and oxygen, but their energy conversion efficiency is lower than 1%[60-61]. Additionally, they cannot form H_2 and O_2 in a stoichiometric ratio due to the accumulation of one type of photogenerated charges on the surface of the semiconductor[59, 62]. Nevertheless, there was some exception to high quantum efficiency. GaN-ZnO solid solution is one of the unusual examples that can produce hydrogen and oxygen under mono-wavelength irradiation of 420nm with a quantum efficiency of 5.9% [63]. It can be seen that overall water splitting is challenging to achieve, delivering the most significant challenge that needs to overcome.

2.2.2 Advanced Indium-based photocatalyst for hydrogen production

2.2.2.1 Indium oxides based photocatalyst

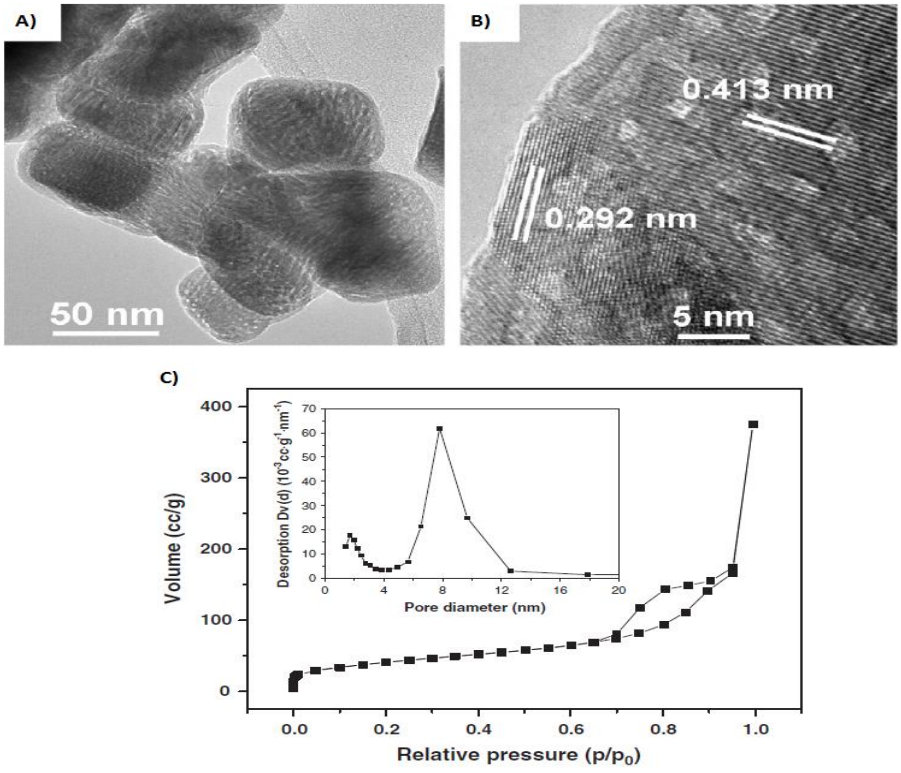

Figure 2.6: TEM (A), HRTEM (B) images and nitrogen adsorption/deposition isotherm with pore size distribution plot (C) of In_2O_3 PNPs[64]

Indium oxides are known as an n-type semiconductor with an indirect bandgap of 2.8 eV. It has been introduced to be an effective sensitizer for extending the light absorption capability from UV to the visible light region[64-65]. Due to its strong visible light absorption ability, many works have been carried out to enhance the photocatalytic efficiency of In_2O_3 by modifying its nano-microstructure. Recently, In_2O_3 semiconducting materials with various geometric morphologies, consisting of nanowires[66], nanotubes[67], nanobelts [68], nanosheet[69], needle-like particle[70], monodisperse spherical nanocrystals[71], nano-microcube[72-73], octahedral structure and hollow microsphere [74] have been synthesized via thermal evaporation, chemical vapor deposition, hydrothermal and solvothermal routes.

In photocatalysis, the construction of nanosized materials is one of the focal points for structure design of photocatalysts because smaller particle size could expose more active sites, provide high specific surface area as well as lower the travel pathway of the charge carriers to the surface. For instance, In_2O_3 porous nanoplates (PNPs) were prepared by calcining porous $In(OH)_3$ at 270 ^oC[64]. The BET result shows that the In_2O_3 PNPs possessed high surface area (156.9 m^2/g) and a large number of mesopores (7.8 nm) and micropores (1.7 nm), resulting in seven times higher quantum yield than that by commercial In_2O_3 (5.27% and 0.76%, respectively). **Figure 2.6** shows TEM, HRTEM image, and nitrogen adsorption/deposition isotherm with pore size distribution plot of In_2O_3 PNPs. Another approach for constructing nanosized materials is a hollow structure designing. Hollow materials are composed of nanoparticles with high porosity, reduced diffusion length, and improved accessibility of active sites by the reactant. Moreover, the multiple reflections within the hollow cavity enhance the efficient utilization of the incident light, enhance the number of photogenerated charge carriers. Zhao et al. reported the synthesis of porous hollow In_2O_3 microcubes with different sizes. In_2O_3 hollow microcubes possess the average edge lengths in the range of 2.0-4.7 nm, which can be obtained by changing the hydrothermal reaction temperature[65]. The experimental results showed that the prepared hollow In_2O_3 microcubes can be obtained via heating the $In(OH)_3$ precursors at 180 ^oC, as shown in **Figure 2.7**, demonstrated the highest photocatalytic activity under visible light illumination at 462 nm. Additionally, the photocatalytic activity exhibited good stability without any obvious decrement after four cycles, indicated the excellent photocatalytic stability of the porous hollow In_2O_3 microcubes.

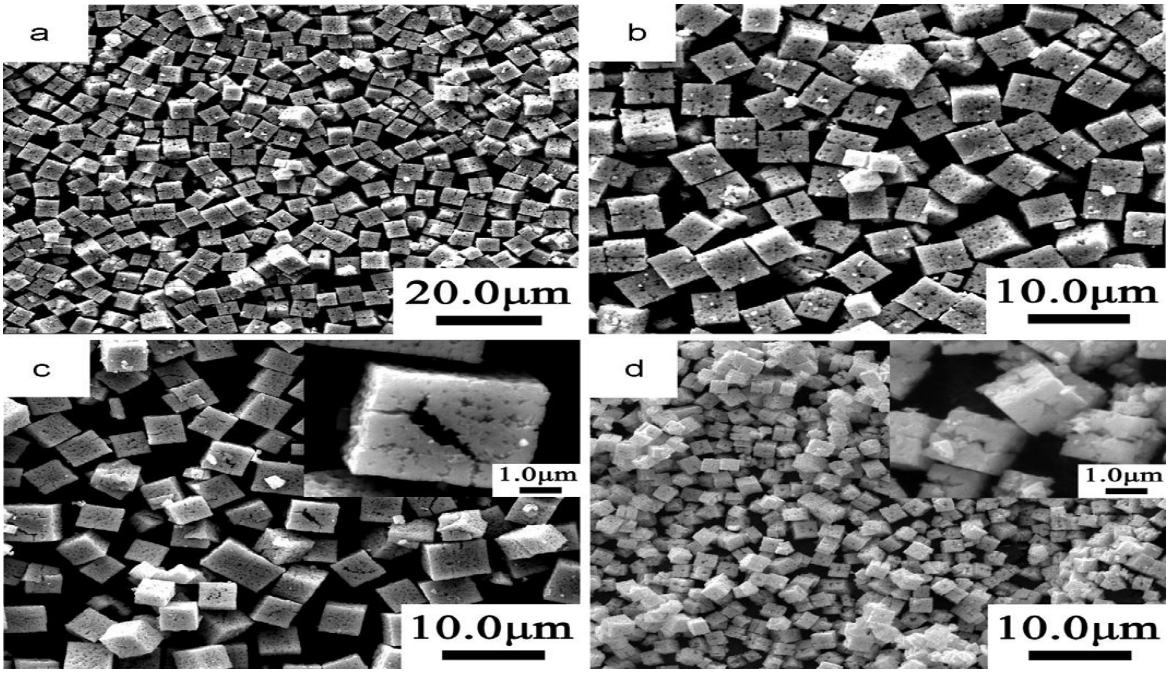

Figure 2.7: SEM images of In_2O_3 microcubes calcined at (a,b)140^oC ,(c) 180 ^oC and (d) 220^oC[65]

The most common way to enhance the photocatalytic activity of In_2O_3 semiconductors is combining with other semiconductors. Various studies have been conducted to investigate the catalytic performance of In_2O_3-based nanocomposites by coupling In_2O_3 with metal oxides such as TiO_2, CuO[75, 76], or metal sulfide such as CdS[77]. Interestingly, some of them achieved higher hydrogen production efficiencies as compared with individual parent materials due to better charge separation and decreasing recombination. For example, Lalitha et al. integrated In_2O_3 with TiO_2 nanoparticles[75] to improve the photocatalytic hydrogen production under visible-light irradiation. The loading of the 2%wt of In_2O_3 on TiO_2-P25 exhibited the photocatalytic activity toward hydrogen production at a rate of 2175 μmol/h. Similarly, 5%-In_2O_3/nano-TiO_2 catalyst produced 4080 μmol of hydrogen per hour, which was 2 times higher than that of In_2O_3/P25. The main reason for this phenomenon was found to be the difference of the surface area between the TiO_2 and P25 materials. As nano-TiO_2 exhibits large surface area, which favors highly dispersed indium oxide species onto TiO_2 nanoparticles, thus increasing activity 2-times as compare to the In_2O_3/P25 system. **Table 2.1** shows some of indium oxide-based nanocomposites and their activity under visible light irradiation.

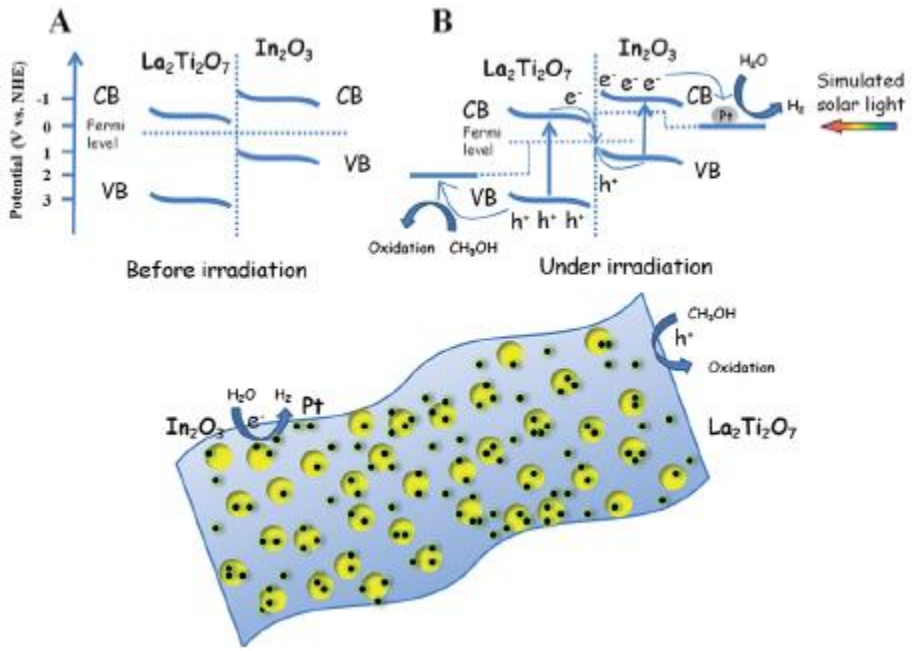

Figure 2.8: The proposed photocatalytic H_2 evolution mechanism over the $In_2O_3/La_2Ti_2O_7$ nanocomposite under simulated solar light irradiation[78]

In addition to binary metal oxides, several approaches have been devoted to develop ternary metal oxide/In_2O_3 nanocomposite systems. In these systems, it is observed that the photo-generated holes can be easily recombined with photoexcited electrons in other semiconductors due to the role of built-in potential and potential barrier. The group of Hu prepared $In_2O_3/La_2Ti_2O_7$ nanocomposite heterojunction via solvothermal method[78]. The recombination of electrons in $La_2Ti_2O_7$ with holes in In_2O_3 releases the holes on the VB of $La_2Ti_2O_7$ and excites the electrons to the CB of In_2O_3. Therefore, the accumulated holes in $La_2Ti_2O_7$ can oxidize the sacrificial reagents, and the holes in In_2O_3 are subsequently transferred to the Pt co-catalyst to produce H_2 (**Figure 2.8**). The optimal molar ratio of $In_2O_3/La_2Ti_2O_7$ was found to be 1.5:1 and the corresponding H_2 production rate was 68.14 μmol h^{-1} g^{-1} with an apparent quantum yield of 0.41%, which is 29.62 times higher than that on pure In_2O_3 and 6.43 times higher than on $La_2Ti_2O_7$. Overall, combining the In_2O_3 with ternary metal oxide is a potential strategy to improve photocatalytic H_2 production. However, it should be noted that the synthesis procedure of these ternary nanocomposites is usually complicated and require careful attention to obtain the desired nanostructure. **Table 2.1**

shows some of the selective In_2O_3-based nanocomposites and their photocatalytic efficiencies.

Table 2.1: Different nanocomposites of In_2O_3 active for hydrogen production

Semi-conductor 1	Semi-conductor 2	Co-catalyst	Sacrificial reagent	Light source	Hydrogen production ($\mu molh^{-1}g^{-1}$)	Quantum yield (%)	Ref.
TiO_2 – NPs TiO_2 – P25	In_2O_3	-	Methanol	400W Hg $\lambda \geq$ 420nm	4080 2175	No data	[75]
Cu_2O-TiO_2 TiO_2	In_2O_3	-	Methanol	500W Halo $\lambda \geq$ 420nm	2149 1829	No data	[76]
In_2O_3	CdS	-	Benzyl alcohol	450W Xe, $\lambda \geq$ 400nm	9382	45.3 at λ = 460nm	[77]
$La_2Ti_2O_7$	In_2O_3	-	Methanol	500W Xe $\lambda \geq$ 420nm	68.14	0.41	[78]
ZnO	In_2O_3	-	Methanol	300W Xe, $\lambda \geq$ 420nm	1784	No data	[79]
$NaNbO_3$ nanorods	In_2O_3	Pt	Methanol	300W Xe, $\lambda \geq$ 420nm	16.4	1.45 at λ = 420nm	[80]
In_2O_3	$Gd_2Ti_2O_7$	-	Methanol	300W Xe,	5789	No data	[81]

				λ ≥ 420nm			
Ta_2O_5	In_2O_3	Pt	Methanol	300W Xe, λ ≥ 420nm	10	No data	[82]

2.2.2.2 Indium sulfides based photocatalyst

Binary indium sulfides

Indium sulfides typically exist in three different crystal phases: α-In_2S_3 (defective cubic structure), β- In_2S_3 (defective spinel structure), and γ- In_2S_3 (layered hexagonal structure)[83]. Among them, β- In_2S_3 was known as a promising material in optical, photoconductive, and optoelectronic fields because of its defective spinel structure[84]. Although In_2S_3 with various morphologies have been studied, however, there are only a few numbers of papers reported the photocatalytic activity towards H_2 production over β-In_2S_3 under visible light illumination. Recently, Wang et al have reported that the cubic In_2S_3 with disordered vacancies exhibited stable photoactivity for the H_2 production, while the tetragonal In_2S_3 with ordered vacancy showed no photoactivity[85]. Chai et al. noted that the single nanoparticles of In_2S_3 and TiO_2 or In_2S_3/TiO_2 were not active for H_2 formation under visible light irradiation. However, the combined In_2S_3/(Pt-TiO_2) nanostructure produced H_2 under visible light at the rate of 135 μmol h^{-1} with a 1% quantum efficiency at $\lambda \geq 420$ nm[86]. The main reason for this improvement was that both Pt/TiO_2 and In_2S_3 nanoparticle were in close contact by the embedding of Pt/TiO_2 nanoparticles in the interstices of the floriated In_2S_3. Meanwhile, the locations of the Pt cocatalyst also had an obvious effect on the photoactivity for H_2 production, nothing but Pt deposition on TiO_2 was found to improve the photocatalytic performance. The optimum ratio of In_2S_3: Pt/TiO_2 was found to be 3:2. Furthermore, Shen et al. synthesized In_2S_3 microspheres, CdS/In_2S_3, ZnS/In_2S_3 and CdS/ZnS/In_2S_3 for hydrogen evolution at 420 nm [87]. However, only the CdS//ZnS/In_2S_3 could produce H_2 from an aqueous solution of sulfides and sulfite ions without using cocatalyst, and it achieved an apparent quantum yield of 40.9% at $\lambda = 420$ nm. The optimum ratio of CdS:ZnS was found to be 3:1, which produced hydrogen at the rate of 8.1 mmol.$h^{-1}g^{-1}$. Despite the fact that indium sulfides-

based nanocomposite showed a very high photocatalytic activity for hydrogen evolution, no further theoretical calculations and experimental data were reported to show the single component In_2S_3 semiconductor with high catalytic activity. **Table 2.2** summarizes the hydrogen produced over different In_2S_3-based nanocomposite under visible light irradiation and their quantum yield.

Table 2.2: Different nanocomposites of In_2S_3 active for hydrogen production

Semi-conductor 1	Semi-conductor 2	Co-catalyst	Sacrificial reagent	Light source	Hydrogen production ($\mu molh^{-1}g^{-1}$)	Quantum yield (%)	Ref.
TiO_2	In_2S_3	Pt	Na_2S-Na_2SO_3	300W Xe, $\lambda \geq$ 420nm	1350	1 at λ = 420nm	[86]
In_2S_3	CdS-ZnS	-	Na_2S-Na_2SO_3	300W Xe, $\lambda \geq$ 400nm	8100	40.9 at λ = 420nm	[87]

Ternary indium sulfides

Because of the inadequate photocatalytic performance of the binary indium sulfide semiconductor, many attempts have been made to integrate In_2S_3 with other metals such as Cu, Na, Zn, Ag[88-96] to form ternary indium sulfides. These materials usually possess small bandgap; thus, they can absorb the wide range of visible wavelengths of the sunlight spectrum. However, the fast recombination rate of electron-hole-pairs in these materials considerably hinders its photocatalytic activity and limits its further commercial application. To overcome this drawback, several approaches have been employed, which include the reduction of particle size, coupling of cocatalyst, and the formation of the nanocomposite. For example, $CuInS_2$ (CIS), with a bandgap of 1.5 eV, is a direct bandgap semiconductor. Ye and co-workers prepared the nanorods of ZnS and CIS [97]. This nanocomposite system was able to split water to produce H_2 in the presence of sacrificial reagents. Also, the loading of Pt cocatalyst to this system exhibited higher activity, which was around 3.5 times higher

than that of the unloaded sample. Moreover, the ratio of ZnS in ZnS/CIS strongly affected its catalytic activity, thus, a large amount of ZnS was found to be necessary to alter the band structure of CIS. The highest H_2 evolution was 1.25 mmol. g^{-1} in 5 h for a ZnS: CIS at the ratio of 10:1.

Hu et al. synthesized nanocomposite of $CuInS_2$ (1,2eV) and $NaInS_2$ (2.44eV) nanosheets by partial ion-exchange reaction[96]. They introduced Cu^+ ions to $NaInS_2$ precursor and obtained 0.5% $CuInS_2$ nanoparticles decorated $NaInS_2$ nanosheets. Due to the built-in electric field at the p-n junction of these semiconductors, it was proposed that the migration of photoexcited electrons from $CuInS_2$ to $NaInS_2$, and the transfer of photogenerated holes from $NaInS_2$ to $CuInS_2$ (**Figure 2.9**) could enhance the charge separation and decrease the charge recombination. It was observed that the 0.5% $CuInS_2/NaInS_2$ showed remarkable photocatalytic activity in comparison with the pure $NaInS_2$. As a result, the highest achieved photocatalytic H_2 evolution rate was 93 µmol. $g^{-1}h^{-1}$, which was about 4.2 times higher than pure $NaInS_2$ nanosheets.

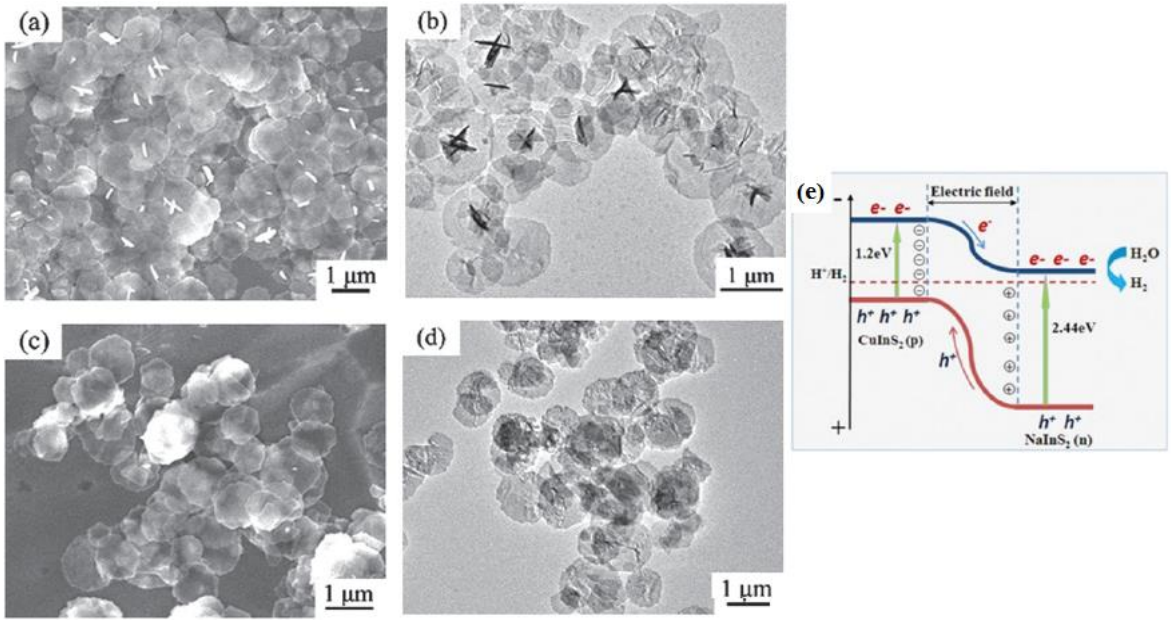

Figure 2.9: a) SEM and (b) TEM images of pure $NaInS_2$ nanosheets. (c) SEM and (d) TEM images of $CuInS_2/NaInS_2$ nanosheets obtained after Cu^+ ion exchange, (e) bandgap structure of integrated heterogeneous $NaInS_2/CuInS_2$ nanosheets[96].

Graphitic carbon nitride (g-C_3N_4) is a metal-free semiconductor that consists of s-triazine or tri-s-triazine units. These units are connected in a two-dimensional graphite-like framework by amino groups in each layer and weak van der Waals forces between layers. As a result, this polymeric semiconductor shows very high thermal and chemical stability. Recently, Shi and co-workers prepared the g-C_3N_4-$ZnIn_2S_4$ via nanocarbon bridges to form the Z-scheme photocatalytic system[98]. Although the bandgaps of $ZnIn_2S_4$ and g-C_3N_4 are determined to be 2.43 and 2.69 eV, respectively, the resultant g-C_3N_4/nanocarbon/$ZnIn_2S_4$ (CN/C/ZIS) nanocomposite exhibited strong absorption over the entire range of visible light because of the excellent visible light absorption of nano-carbons. Eventually, the rate of H_2 production was reached up to 50.32 µmol.h^{-1}, which was around 3.4 times higher than that of ZIS. To explain the significant improvement of the photocatalytic activity of CN/C/ZIS, Shi also proposed the possible electronic transfer mechanisms in the ternary CN/C/ZIS system (**Figure 2.10**). The nanocarbon could not only enhance the light absorption capability of photocatalytic systems but it also acted as the conducting medium to help the electron transfer from ZIS to CN. Therefore, the accumulated electrons in CN were readily available for the reduction of protons.

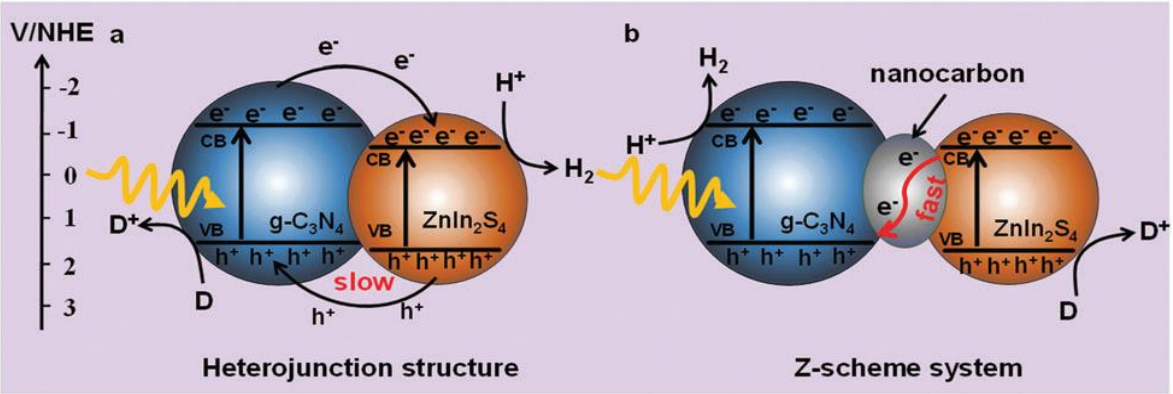

Figure 2.10: Possible electron transfer mechanisms of (a) the CN/ZIS heterojunction nanocomposite and (b) the CN/C/ZIS Z-scheme system[98].

Shen et al. used Pt and CuS as dual cocatalysts to enhance the photocatalytic performance of $ZnIn_2S_4$ [93]. After loading 1%wt CuS combined with 1%wt Pt on ZIS, the activity for H_2 production was boosted to 201.7 µmol/h, which was increased by 1.6 times as compared to the $ZnIn_2S_4$ that only loaded with 1%wt Pt. Interestingly, Shen, et al have also investigated a

series of loaded transition metal sulfide. They found that Ag_2S and CuS could enhance the photocatalytic activity of hydrogen evolution over $ZnIn_2S_4$, while SnS, CoS, and NiS could inhibit the catalytic activity. **Figure 2.11** illustrates the process of photogenerated charge transfer for photocatalytic hydrogen evolution over Pt-CuS/$ZnIn_2S_4$ in an aqueous solution containing Na_2SO_3/Na_2S under visible light. The excited electrons migrated to the Pt sites and participated in the reduction of protons to produce hydrogen. On the other hand, the photogenerated holes are transferred from $ZnIn_2S_4$ to CuS to react with Na_2S/Na_2SO_3 electron donor in the solution.

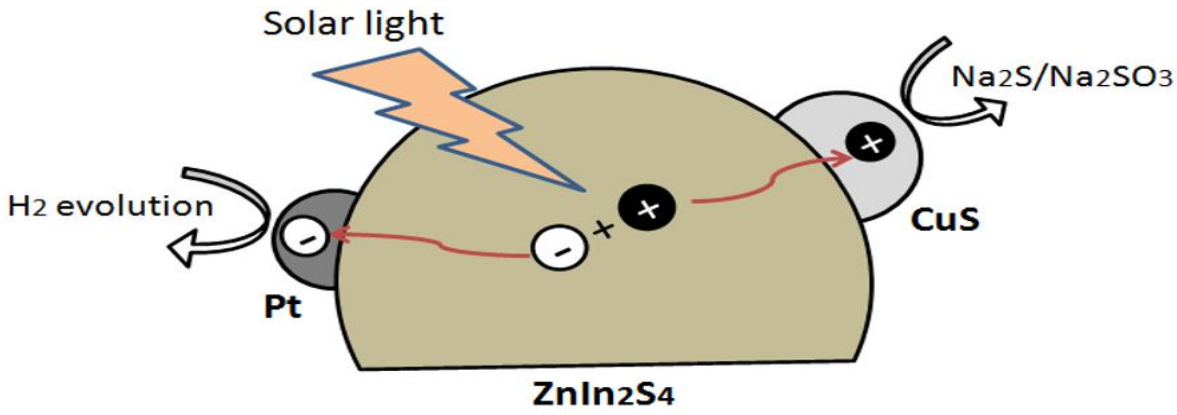

Figure 2.11: Schematic illustration of photo-generated charge-transfer process for photocatalytic hydrogen evolution over Pt-CuS/$ZnIn_2S_4$[93].

As one of the ternary indium chalcogenides compound, the $AgIn_5S_8$ with a general formula of I-III_5-VI_8 has a direct bandgap of 1.7eV and is considered one of the potential candidates for solar light-driven photocatalytic applications. Chen and Ye have developed the Pt loaded $AgIn_5S_8$, which showed high photocatalytic activity for hydrogen generation under visible light illumination ($\lambda \leq 420$ nm). Based on previous studies on $AgIn_5S_8$, Li's group has investigated the photocatalytic activity of a series of Pt loaded $AgIn_5S_8/TiO_2$ nanocomposite towards its H_2 production under visible light irradiation ($\lambda \geq 420$nm)[94]. It was reported that the series of $AgIn_5S_8/TiO_2$ nanocomposites were prepared by one-pot hydrothermal synthesis and they showed higher photoactivity as compared to the pristine $AgIn_5S_8$. The $AgIn_5S_8/TiO_2$ with a molar ratio of 1:10 displayed maximum photoactivity (85 $\mu mol.h^{-1}$), which was found to be 7.7 times higher in comparison with pure $AgIn_5S_8$. Furthermore, a physical mixture of

$AgIn_5S_8$ and TiO_2 showed a very low hydrogen production rate, indicating that the intimate contact between $AgIn_5S_8$ and TiO_2 was the critical factor for improving their photocatalytic activity. **Figure 2.12** shows the proposed mechanism for the enhanced photoactivity over $AgIn_5S_8/TiO_2$ nanocomposite under visible light irradiation. First, the electrons were excited from VB to the CB of $AgIn_5S_8$ and the photogenerated holes reduced the absorbed sacrificial reagents. Therefore, the photoexcited electrons migrated to the CB of TiO_2, then transferred to Pt cocatalyst to produce H_2. To this end, various ternary indium chalcogenide-based nanocomposites are listed in **Table 2.3**

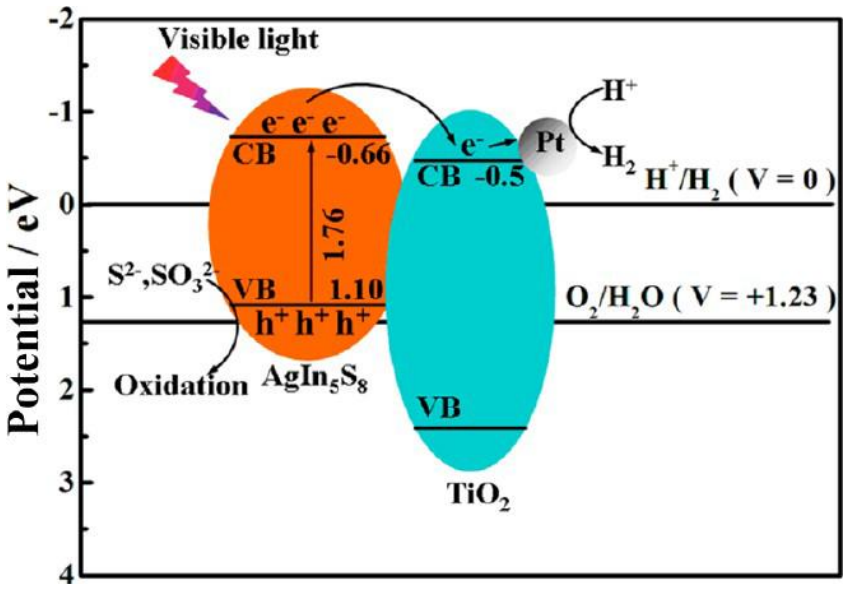

Figure 2.12: The proposed photocatalytic H_2 evolution mechanism over $AgIn_5S_8/TiO_2$ nanocomposite under visible-light irradiation[94]

Table 2.3: Different nanocomposite of ternary indium sulfides

Semi-conductor 1	Semi-conductor 2	Co-catalyst	Sacrificial reagent	Light source	Hydrogen production ($\mu molh^{-1}g^{-1}$)	Quantum yield (%)	Ref.
$ZnIn_2S_4$	-	Pt-CuS	Na_2S-Na_2SO_3	300W Xe $\lambda \geq 420nm$	201.7	No data	[93]
TiO_2	$AgIn_5S_8$	Pt	Na_2S-Na_2SO_3	300W Xe	850	No data	[94]

				λ≥420nm			
$K_2La_2Ti_3O_{10}$	$ZnIn_2S_4$	-	Na_2S-Na_2SO_3	300W Xe λ≥420nm	2096	No data	[95]
$CuInS_2$	$NaInS_2$	-	ascorbic acid	300W Xe λ≥420nm	93	No data	[96]
ZnS	$CuInS_2$	-	Na_2S-Na_2SO_3	300W Xe λ≥400nm	1200	No data	[97]
g-C_3N_4	$ZnIn_2S_4$	-	Na_2S-Na_2SO_3	12W UV LED λ = 420nm	50.32	No data	[98]
$AgIn_5S_8$	-	Pt	Na_2S-Na_2SO_3	300W Xe λ≥420nm	250	5.3 at λ= 411.2 nm	[99]
$ZnIn_2S_4$ couple with graphene	CdS quantum dot	Pt	Na_2S-Na_2SO_3	300W Xe λ≥420nm	27000	56 at λ= 420nm	[100]

Quaternary indium sulfides

The quaternary indium sulfides are emerging as technologically viable materials due to the tunable bandgap over a wide range (1.1-2.4 eV) and high thermal stability. For instance, indium sulfide can be combined with other metal sulfides in various morphologies such as nanorods[101], nanocrystals, nanoporous[102-103], and nanospheres[104] to improve their catalytic performance. Among all metal sulfides, ZnS has attracted much attention due to its strong ability to form a solid solution with In_2S_3, which results in higher charge separation and greater quantum efficiency. A solid solution of $ZnIn_{0.25}Cu_xS_{1.375+x}$ was investigated with various ratios of Cu for H_2 production under visible light and in the presence of Na_2S and Na_2SO_3[104]. This solution contained a large number of nanoparticles with diameters ranging from 5 to 10 nm. The highest photocatalytic activity (apparent quantum yield of 22.6% at 420 nm) was achieved by $ZnIn_{0.25}Cu_{0.02}S_{1.395}$ photocatalyst. In particular, without cocatalysts, this nanostructure reached 3.6 $mmol.h^{-1}$ $0.01g^{-1}$ of the initial rate of hydrogen production.

With the high specific surface area of 147 m^2/g, this material possessed more active sites on the surface and led to the enhanced photocatalytic H_2 production. However, this rate mildly declined to 1.96 $mmol.h^{-1}$ $0.01g^{-1}$ on the next run. The decrease in the rate might be related to the deactivation of photocatalyst because of the consumption of the sacrificial reagents. Another example of the solid solution of ZnS and In_2S_3 was reported by Li and co-workers[103]. Nanoporous ZnS-In_2S_3-Ag_2S solid solutions were synthesized by a facile template-free method that showed relatively high activity for hydrogen evolution under solar light ($\lambda \geq 400$ nm) without the presence of noble metal. A series of $ZnIn_{0.23}Ag_{2x}S_{1.345+x}$ samples were systematically characterized. For x equal to 0.02, the initial rate of photocatalytic hydrogen generation reached 3.3 $mmolh^{-1}.0.015g^{-1}$ in the first run and decreased to 2.6 $mmol.h^{-1}.0.015g^{-1}$ in the fourth run, showing high catalytic stability. An apparent quantum yield of $ZnIn_{0.23}Ag_{0.04}S_{1.365}$ was calculated by 19.8% at 420 nm, and the BET results indicated a high specific area of 150 m^2/g. **Table 2.4** outlines the photocatalytic efficiency and hydrogen production rate of different quaternary indium sulfides

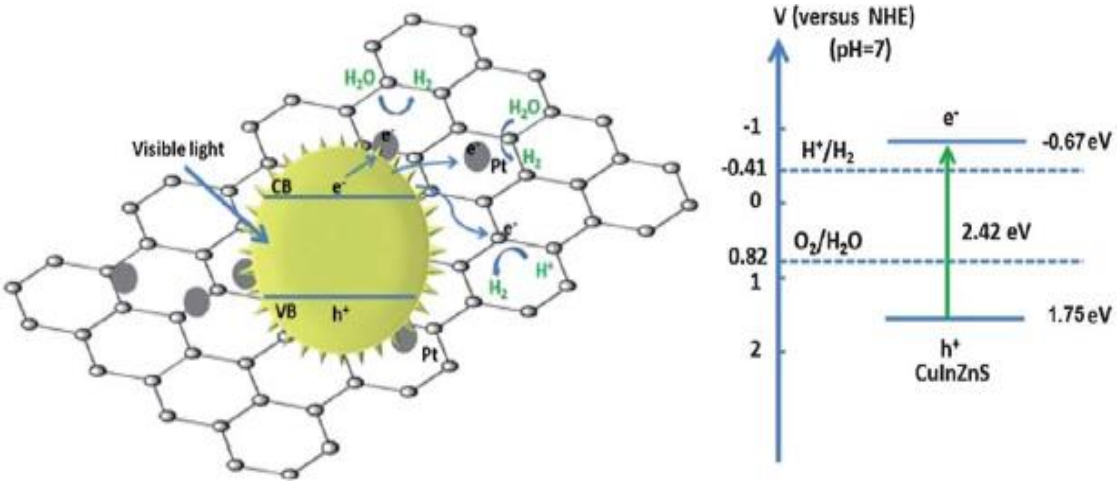

Figure 2.13: Schematic illustration of the charge separation and transfer in the Pt-loaded CIZS–rGO composites under visible light[102].

Recently, Kudo and co-workers reported a new route for the synthesis of quaternary metal sulfides photocatalysts[105-108]. It revealed that the incorporation of Cu or Ag into the photocatalyst led to an increased VB level and a decreased bandgap energy. Takanabe and his group have successfully developed $CuGa_2In_3S_8$ photocatalyst, which can absorb solar light up to 700 nm[109]. This material has been prepared using the solid-state method by heat

treatment at high temperature in an evacuated sealed quartz glass tube. The as-synthesized metal sulfides possess a transition bandgap of 1.8eV and an average particle size of 4 nm. The photocatalytic studies showed that 1% Ru loaded $CuGa_2In_3S_8$ nanocrystal produced 29l mmol.h^{-1}.m^{-2} of hydrogen in an aqueous of Na_2S/Na_2CO_3 over 22 h. The apparent quantum yield was calculated to be 6.9±0.5 % at 560 nm. Although the quaternary metal sulfides often possess narrow bandgap energy and relatively good performance for visible light absorption, the obtained hydrogen production rate from these materials was undesirable. To improve the photocatalytic efficiency, Xue *et al.* composed quaternary metal sulfides with reduced graphene oxide (rGO) nanosheets by the solvothermal method[102]. The new nanocomposite was combined with 2% rGO and $Cu_{0.02}In_{0.3}ZnS_{1.47}$ (CIZS), which generated a high H_2 production rate of 3.8 mmol. $h^{-1}g^{-1}$ under the presence of Na_2S/Na_2SO_3 in solution with visible light irradiation. The BET surface area was found to be 120.30 m^2/g^{-1} for 2% rGO/ $Cu_{0.02}In_{0.3}ZnS_{1.47}$ nanocomposite. This specific surface area improved by increasing the amount of rGO component, resulting in an increased number of active sites. The proposed mechanism of the charge separation and transfer in the CIZS-rGO is demonstrated in **Figure 2.13**. The introduction of graphene in the CIZS-rGO nanocomposites led to the effective improvement in the generation of electron-hole pairs and prolonged lifetime of the charge carriers. Under visible light excitation, the photoexcited electrons were transferred from the CB of to the carbon atom and Pt nanoparticle and reduce H^+ to produce H_2.

Table 2.4: Different quaternary indium sulfides photocatalyst for H_2 production

Semi-conductor 1	Semiconductor 2	Co-catalyst	Sacrificial agent	Light source	Hydrogen production (μmol$h^{-1}g^{-1}$)	Quantum yields (%)	Ref.
Reduce graphene oxide	$Cu_{002}In_{0.3}ZnS_{1.4}$	Pt	Na_2S-Na_2SO_3	300W Xe λ≥420 nm	3800	No data	[102]
-	$ZnIn_{0.23}Ag_{0.04}S_1$	-	Na_2S-Na_2SO_3	300W Xe λ≥420	3300	19.8 at λ=420	[103]

				nm		nm	
-	$ZnIn_{0.25}Cu_{0.02}S_{1.3}$	-	Na_2S-Na_2SO_3	300W Xe λ≥420 nm	3300	22.6% at λ=420 nm	[104]
-	$CuGa_2In_3S_8$ $AgGa_2In_3S_8$	Rh	Na_2S-K_2SO_3	300W Xe λ≥420 nm	No data	15 at 460 and 560nm	[105]
ZnS	$CuInS_2$/$AgInS_2$	Ru	Na_2S-K_2SO_3	300W Xe λ≥420 nm	1080	No data	[106]
ZnS	$CuInS_2$/$AgInS_2$	Ru	Na_2S-K_2SO_3	300W Xe λ≥420 nm	2300	7.4 at 440, 480, and 520 nm	[107]
-	$(AgIn)_{0.22}Zn_{1.56}S$	Pt	Na_2S-K_2SO_3	300W Xe λ≥420 nm	944	20 at λ=420 nm	[108]
-	$CuGa_2In_3S_8$	Ru	Na_2S-Na_2SO_3	300W Xe λ≥420 nm	No data	6.9±0.5 at λ= 560nm	[109]
-	$(CuIn)_{0.09}Zn_{1.82}S_2$	Pt	Na_2S-K_2SO_3	300W Xe	684	12.5 at λ=420	[110]

				λ≥420 nm		nm	

2.2.2.3 Other indium based nanocomposite semiconductor

Despite the above nanocomposites and nanostructures, researchers also have focused on the combination of indium with other metal oxide semiconductors to obtain an efficient photocatalyst for hydrogen generation. The formation of these ternary indium oxide materials can effectively enhance charge separations, prevent charge recombination, and increase the photocatalyst efficiency as summarized in **Table 2.5**.

Table 2.5: Other In-based nanocomposite semiconductors

Semi-conductor 1	Semi-conductor 2	Co-catalyst	Sacrificial reagent	Light source	Hydrogen production ($\mu molh^{-1}g^{-1}$)	Quantum yield (%)	Ref.
In_2TiO_5	-	-	Methanol	450W Hg	44	No data	[111]
$CaIn_2O_4$	Fe-TiO_2	Pt	KI	300W Xe λ≥420nm	280	No data	[112]
CdS	CuIn	Pt	Na_2S-K_2SO_3	300W Xe λ≥420nm	2456	26.5 at λ=420nm	[113]
CdS	CuIn	-	Na_2S-K_2SO_3	300W Xe λ≥420nm	649.9	2.14 at λ=420nm	[113]
$InTaO_4$ $InNbO_4$	-	NiO_x	-	300W Xe λ≥420nm	3.5	No data	[114]
Graphene	$CaIn_2O_4$	-	Methanol	300W Xe λ≥420nm	62.5	No data	[115]

Bharadwaj *et al.* found that In_2TiO_5 nanoparticles synthesized by the solvothermal method, following by calcination at 800 ^oC, were highly active for photocatalytic H_2 evolution in a water/methanol solution, whereas the bulk In_2TiO_5 was incapable to produce H_2[111]. It exhibited a high crystallinity and the BET surface area of 38 m^2/g, which achieved a higher photoactivity for H_2 production (260 µmol H_2 in 6 h) than that of TiO_2 P25 (BET surface area 50 m^2/g, 145 µmol H_2 in 6h). The reason for this unusual phenomenon was that the high crystalline properties which reduced the number of defects in In_2TiO_5 nanoparticles. It is worth noting that these defects act as recombination centers for electrons and holes, thus decreasing the number of defects results in the improvement of photoactivity.

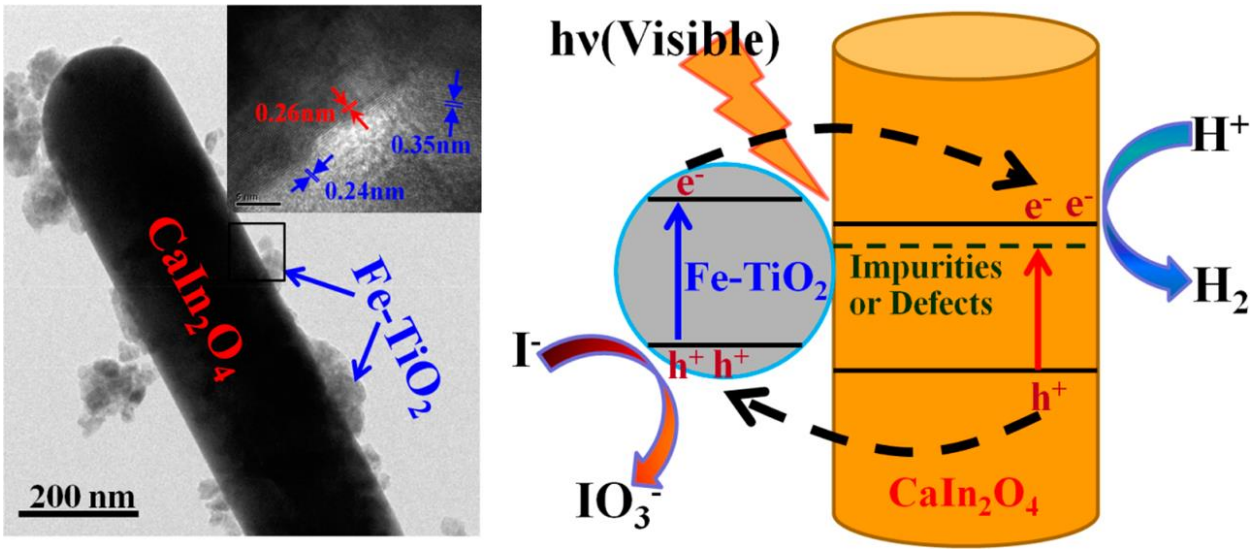

Figure 2.14: TEM image and schematic diagram of the charge separation-transportation of $CaIn_2O_4/Fe\text{-}TiO_2$ under-stimulated visible light.[113]

Gao and co-worker synthesized a Pt-loaded $CaIn_2O_4/Fe\text{-}TiO_2$ composite photocatalyst with tunable $Fe\text{-}TiO_2$ (FTO) content[113]. They aimed to deposit $Fe\text{-}TiO_2$ nanoparticles onto the surface of $CaIn_2O_4$ (CIO) nanorods. The photocatalytic activity of Pt loaded CIO/FTO nanocomposite was evaluated for H_2 evolution at the optimized ratio of CIO and FTO (1:2) under visible light excitation. The highest hydrogen generation rate of 280 $\mu molh^{-1}g^{-1}$ was obtained from this ratio, which was 12.3 and 2.2 times higher than that of pristine $CaIn_2O_4$ and $Fe\text{-}TiO_2$, respectively. The enhanced photocatalytic performance could be attributed to the increased surface area and enhanced visible light absorption. Gao proposed that the

intimate contacts between $CaIn_2O_4$ nanorods and Fe-TiO_2 nanoparticles facilitated efficient charge separation that also led to improved photocatalytic activity. **Figure 2.14** showed the TEM image of CIO/FTO nanorods and illustrated a schematic diagram of the charge separation and transfer over CIO/FTO under solar light illumination. The photocatalyst also demonstrated high stability even after three cycles.

CdS is one of the promising semiconductors for photocatalysis because of its narrow bandgap energy and proper conduction band level position. However, this semiconductor is unstable under light irradiation, and the recombination of the photogenerated charge carrier is also relatively high. To overcome these drawbacks, researchers have modified CdS with other semiconductors for enhancing its photoactivity and stability. Yu *et al.* combined CdS with CuIn to form a solid solution by low-temperature hydrothermal method. It was found that the $(CuIn)_xCd_{2(1-x)}S_2$ is an active photocatalyst for H_2 production under solar light even with or without cocatalyst[113]. The CuIn/CdS and 2% Pt loaded CuIn/CdS produced around 649.9 and 2456 $\mu molh^{-1}g^{-1}$ molecular hydrogen, respectively. The doping of CuIn not only facilitated the photoactivity of CdS but also improved its stability as well in the photocatalytic process.

2.2.3 Advanced carbon nitride-based photocatalyst for hydrogen evolution

Recently, non-metal photocatalysts have attracted great attention because this class of materials possesses many unique features that can address the various limitations in photocatalysis. Among the reported non-metal photocatalysts, graphitic carbon nitride (g-C_3N_4) is found to be a promising candidate for efficient solar light-driven hydrogen production owing to an appropriate band edge potential, a narrow bandgap energy ($Eg \geq 2.7$ eV corresponding to the light absorption at $\lambda \leq 460$ nm), excellent stability and cost-effectiveness. However, the rapid charge carrier recombination rate originated by the weak $\pi-\pi$ conjugation in tri-s-triazine units and hydrogen bonding between –NH groups of the adjacent stacked layers considerably reduce the photocatalytic performance of the conventional bulk g-C_3N_4. To overcome this critical drawback, two main strategies have been proposed for obtaining the high efficient g-C_3N_4-based photocatalyst, including the utilization of a metal cocatalyst as a trapping center that captures the photogenerated electrons, the formation of heterojunction systems by coupling with a second semiconductor could improve the generation and migration of photo-generated electron-hole pairs.

2.2.3.1 Cocatalyst/g-C_3N_4 heterostructure nanocomposite

Noble metal cocatalyst

Over the past five years, assembling reduction/oxidation and plasmonic cocatalysts with g-C_3N_4 is expected to improve the charge carrier separation in g-C_3N_4. Owing to excellent electronic and optical properties, noble metals such as Pt, Ru have been extensively used as reduction cocatalyst to boost up the photocatalytic hydrogen production on g-C_3N_4, which was 4-times higher than that of pristine g-C_3N_4[116]. A Schottky barrier is formed upon the construction of noble metal/semiconductor heterojunction, which affects the migration of photogenerated charge carriers, resulting in an increased number of electrons and holes in the noble metal and semiconductor, respectively. Thus, these noble metals behave as the active electron trapping centers to prevent the recombination of photoinduced charge carriers, promoting the redox function of the catalytic system. For example, Shiraishi and co-workers have successfully synthesized the Pt nanoparticle with a diameter of < 4 nm loaded g-C_3N_4 by H_2 treatment of Pt precursor at 673 K[117]. It is worth noting that the intimate contact between noble metal and host semiconductor at the interface plays a key role in ensuring the smooth transfer of photogenerated electrons to cocatalysts. Then, his group compared the photocatalytic activity of two different synthesis approaches: (i) reduction under H_2 gas at a high temperature and (ii) in-situ photoreduction of Pt precursor. Although both methods produced a similar particle size of platinum, the photocatalytic performance of the photocatalyst prepared by method (i) exhibited 10-times higher than that of the second approach. Moreover, XPS results confirmed that strong interaction between Pt nanoparticles and g-C_3N_4 was obtained via the high temperature treatment.

Noble metal-free cocatalyst

Besides the typical noble metals, the utilization of non-noble metal cocatalysts recently has attracted noticeable attention as effective cocatalysts to drive the electrons from graphitic carbon nitride to non-noble metals such as Ni, Cu, Co, or metal compounds (metal sulfide and metal phosphide). For instance, Vu *et al.* deposited Ni onto the surface of S-doped g-C_3N_4 (Ni-SCN) via in-situ photoreduction method[32]. With the reduction of a Ni^{2+} precursor, the uniform Ni nanoparticles with a size of approximately 20 nm were deposited on g-C_3N_4

nanosheets (**Figure 2.15(a-b)**). The obtained result indicated that the hydrogen production yield was 3628 μmol.g^{-1}.h^{-1}, which was 1.5 times higher than that of Pt loaded S-doped g-C_3N_4 that was synthesized by the same method. XPS analysis showed that the characteristic peak of S^{2-} on Ni-SCN was found to be shifted toward lower binding energy as compared to pristine SCN (**Figure 2.15(c-f)**). It was further suggested that the loaded Ni species were chemically bonded onto the g-C_3N_4 nanosheets via Ni-S-C-N bonding that significantly boosted up the charge separation, leading to the improvement of photocatalytic activity. Furthermore, the photocatalytic recycling test was carried out for four-runs under the same condition, and the result indicated excellent stability over four cycles (8 hours) without any noticeable decrement in the activity, suggested that the Ni loaded S-doped g-C_3N_4 could be a promising photocatalyst for hydrogen evolution[32].

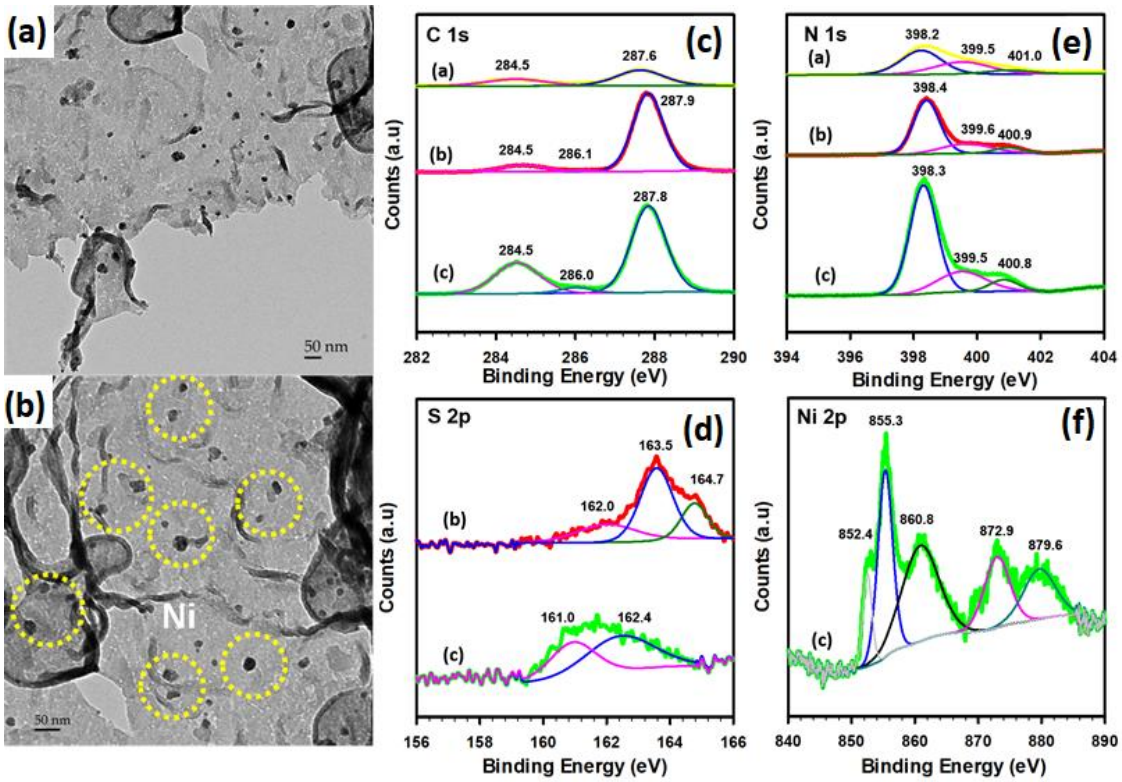

Figure 2.15: (a)-(b) TEM images of Ni-SCN; XPS spectra of (c) C 1s, (d) N 1s, (e) S 2p and (f) Ni 2p. Inset figures, (a) GCN, (b) SCN, (c) Ni-SCN.

2.2.3.2 Semiconductor/g-C_3N_4 heterojunctions

Recently, coupling the graphitic carbon nitride with other semiconductors such as heterostructured photocatalysts reveal a new approach to address the limitation of fast electron-hole recombination in g-C_3N_4. Similar to the cocatalyst/g-C_3N_4 system, a Schottky barrier is established when a semiconductor is hybridized with g-C_3N_4 photocatalyst, producing an internal electric field that provides the driving force for the transfer of the electrons and holes in the opposite direction. In this section, we discuss the most active carbon nitride-based heterojunction nanocomposites, including Type II heterostructures and Z-Scheme.

Type II heterostructure-based g-C_3N_4

Combining the g-C_3N_4 with another semiconductor can build a Type II heterojunction in which g-C_3N_4 could act as an electron donor or acceptor, as depicted in **Figure 2.16**. In this system, the reduction and oxidation reaction takes place separately in g-C_3N_4 and in the second semiconductor, which is because the separation of electron-hole takes place in two different semiconductors[118]. Several semiconductors including metal oxides (TiO_2, Cu_2O, ZnO), metal sulfides (CdS, In_2S_3), metal halides (BiOBr, BiOCl) have been combined with g-C_3N_4 and showed the enhanced photocatalytic activity. For instance, Alcudia-Ramos *et al.* constructed TiO_2/g-C_3N_4 heterostructure nanocomposites for the photocatalytic hydrogen generation[119]. Under visible illumination, the highest hydrogen production yield was achieved by 1041 $\mu mol.g^{-1}.h^{-1}$, which originated from the strong interaction between g-C_3N_4 and TiO_2. As shown in **Figure 2.17**, HRTEM images and XPS analysis confirmed the formation of C-O and O-Ti-N bonds, suggesting an intimate contact at the interface of two semiconductors and resulting in an efficient channel for the migration of photogenerated electron-hole. Consequently, the photocatalytic activity was boosted up effectively as compared to its parental materials. In the same manner, Zhang *et al.* fabricated the CdS/g-C_3N_4 core/shell nanowires with different g-C_3N_4 contents by the combination of solvothermal and chemisorption synthesis[120]. The obtained results suggested that g-C_3N_4 has spontaneously been absorbed on CdS nanowire, forming an intimate contact. The synergistic effect between CdS and g-C_3N_4, with their well-matched overlapping band structure, promoted the charge separation and prevent the photo-corrosion occurred on CdS. These

advanced features, thus, considerably boosted the photocatalytic performance and stability of the catalytic system.

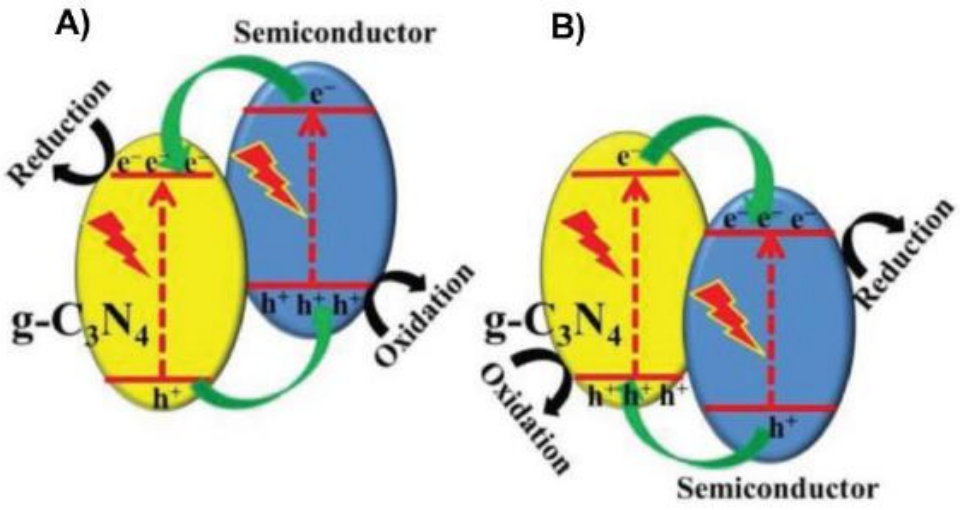

Figure 2.16: Charge transfer in Type II g-C_3N_4- based photocatalysts (A) g-C_3N_4 as electron acceptor; (B) as electron donor[118]

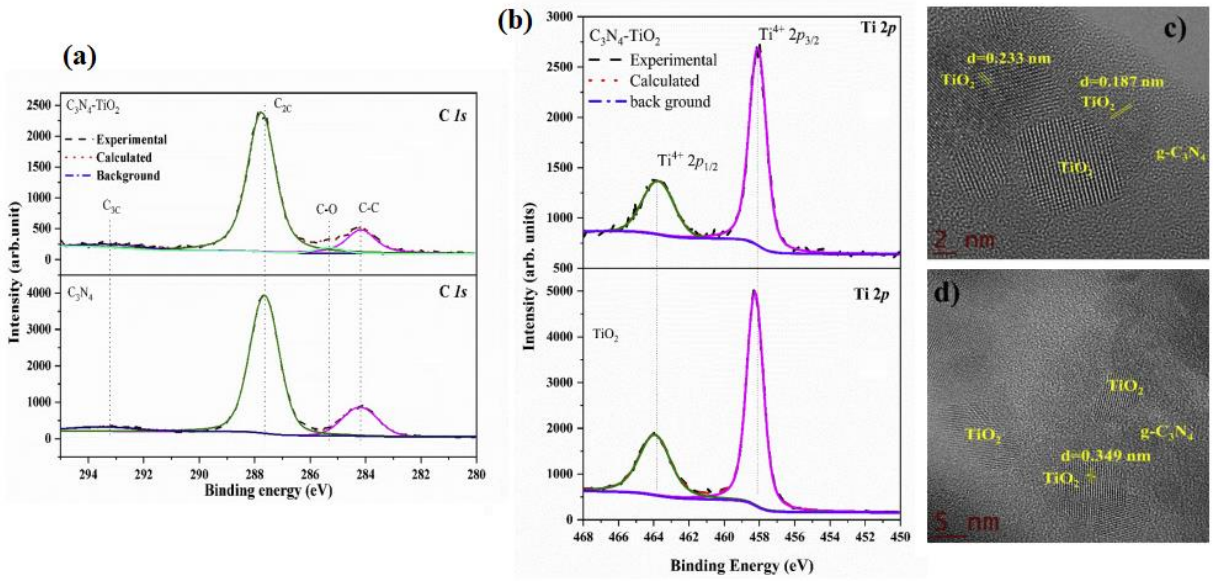

Figure 2.17: High-resolution XPS spectra (a)-(b) comparison of C 1s and Ti 2p; (c)-(d) HRTEM images of C_3N_4-TiO_2 composite material[119]

Z-Scheme-based g-C_3N_4 nanocomposite

In addition to the incorporation of another semiconductor to form Type II heterojunction, the Z-scheme heterojunction nanocomposite is also another fascinating system to enhance the photocatalytic performance. The key feature of the Z-scheme system is the remarkable redox ability, which is minimized in type II heterojunctions due to the transportation of photogenerated charge carriers, as discussed in previous sections. Recently, Ding and his group selected the Au nanoparticle as the electron transfer mediator to design the Z-scheme photocatalytic system, where the CdS and g-C_3N_4 were employed as the two photocatalysts[121]. In comparison with pristine g-C_3N_4, the as-prepared CdS/Au/g-C_3N_4 composite demonstrated enhanced photocatalytic activity toward H_2 production due to the efficient charge separation and transfer process. **Figure 2.18** illustrates the electron transfer pathway of the CdS/Au/g-C_3N_4 photocatalytic system. Under the visible light excitation, both CdS and g-C_3N_4 will generate an electron at the same time. In this process, the photoexcited electrons migrate from the CB of g-C_3N_4 to the Au nanoparticle and then recombine with photogenerated holes in the VB of CdS. Consequently, a large number of electrons on the CB of CdS were available for the reduction of protons to hydrogen, resulting in the improvement of photocatalytic activity for hydrogen generation by 128.5 times higher than that of pure g-C_3N_4. In other work of Zhao's group, the author demonstrated the formation of the all-solid-state Z-scheme system of g-C_3N_4/Au/P25[122]. The photocatalytic hydrogen production rate of the as-synthesis g-C_3N_4/Au/P25 reached 259 $\mu mol.g^{-1}.h^{-1}$, which was 30-folds higher than that of bulk g-C_3N_4. The superior catalytic activity of the catalyst can be attributed to the synergistic effect of Z-scheme nanocomposites, which effectively facilitated the "vectorial" electron transfer process of P25→Au→g-C_3N_4. Moreover, the Z-scheme system exhibited strong absorption in the visible region (460-700 nm) due to the LSPR effect of Au nanoparticles.

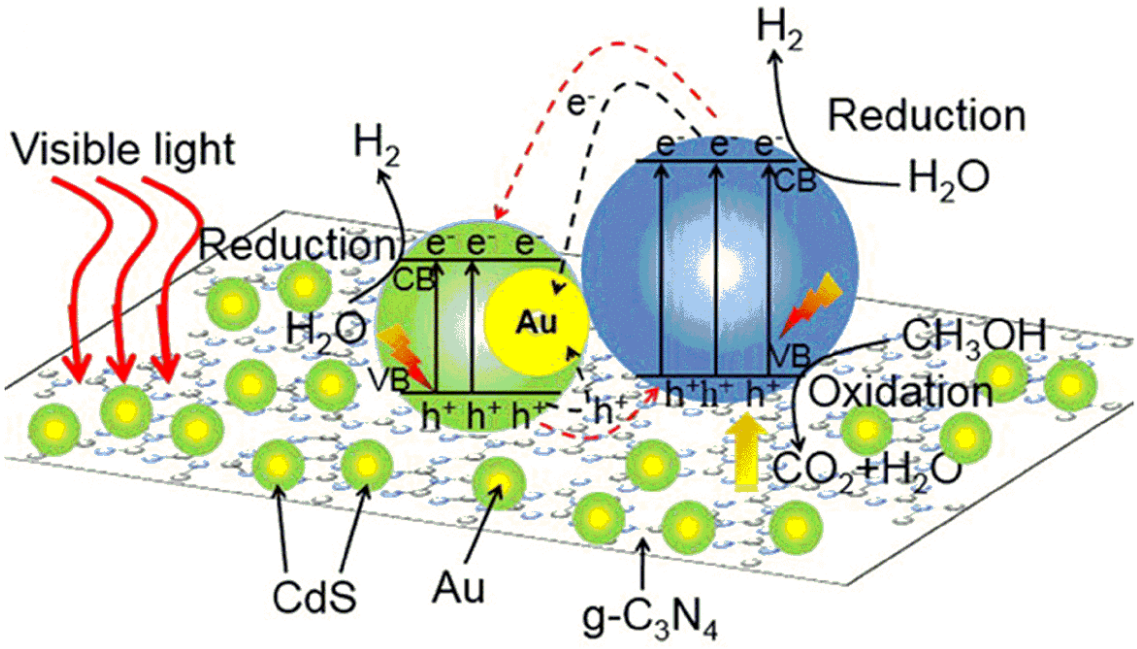

Figure 2.18: Possible photocatalytic mechanism of CdS/Au/g-C_3N_4 composite in H_2 production under visible-light irradiation ($\lambda > 420$ nm)[121].

2.3 Fundamentals of photo(electro)catalytic nitrogen fixation

2.3.1 Basic principles

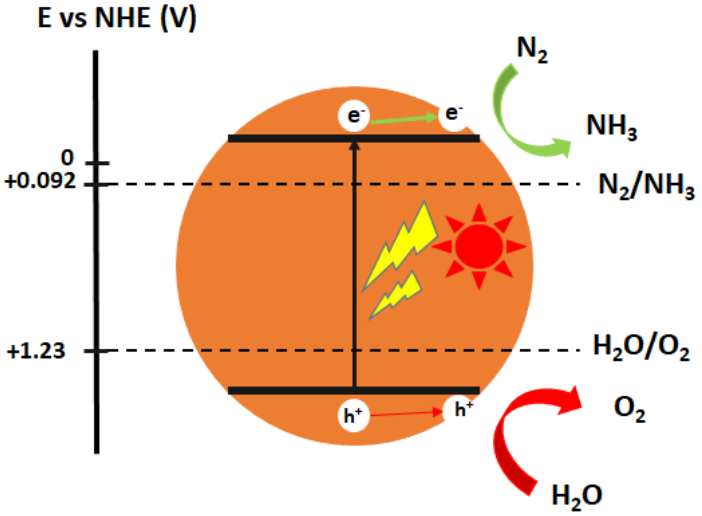

Figure 2.19: Schematic of semiconductor-based photocatalyst used for the N_2 fixation. The redox potentials (V vs NHE) of half reaction water oxidation and dinitrogen protonation are marked on the left.

In the last few decades, a renewed interest has been devoted to photocatalytic NH_3 production, and several papers have illustrated ammonia[123] and nitrate formation[124] using various kinds of semiconducting photocatalysts, plasmon-enhanced systems, and biomimetic systems. Basically, the photocatalytic process of N_2 fixation is divided into several steps as follows. First, under the sunlight irradiation, photo-generated electrons are excited to the CB, leaving holes in the VB. Afterward, some of the electrons and holes recombine together, meanwhile, other photo-formed holes (h^+) oxidize the water into H^+ and O_2, (**Eq 2.6**) and N_2 reduction by hot-electrons lead to the production of NH_3 (**Eq 2.7**). As a result, NH_3 is synthesized from water and N_2 under ambient conditions using the sunlight as an energy source (**Eq. 2.8**). **Figure 2.19** demonstrates the scheme process of photocatalyst materials using for the reduction of nitrogen to ammonia.

$$2H_2O + 4h^+ \rightarrow O_2 + 4H^+ \qquad \textbf{(2.6)}$$

$$N_2 + 6H^+ + 6e^- \rightarrow 2NH_3 \qquad \textbf{(2.7)}$$

$$1/2N_2 + 3/2H_2O \rightarrow NH_3 + 3/4O_2 \qquad \textbf{(2.8)}$$

Although the proposed photocatalytic nitrogen fixing pathway is acceptable, many pending questions regarding the mechanisms, rates, and thermodynamics still remain. The protonation reactions versus standard potential are summarized by Lyndley et al (**Table 2.6**). Thermodynamically, ammonia formation is favored, with an energy difference of 0.43 V between NH_3 and N_2H_4 and a 1.26 V between NH_3 and N_2H_2. In a thermodynamic aspect, the half-reaction generated NH_3 is capable of any photocatalyst semiconductor possessing bandgap energy larger than 1.2 eV with proper conduction and valence band position. However, this half-reaction involves multiple-electron transfer (6 electrons) and thus may be more kinetically challenging. Another limitation is the absorption of N_2 molecules over semiconductor photocatalysts and cleavage of highly stable N-N triple bond in order to activate dinitrogen. To overcome these challenges, it is necessary to create appropriate active sites that can effectively absorb nitrogen. This active site also serves as a trapping cage to capture electrons then transfer to absorbed nitrogen as well as suppress charge carrier recombination.

Table 2.6: Reduction potentials (vs. SHE) of typical hydrogenation reactions relate to the reduction of N_2 to NH_3

Reaction	E^o (V) vs SHE
$N_2 + 2H^+ + 2e^- \rightleftharpoons N_2H_2$	+0.035
$N_2 + 4H^+ + 4e^- \rightleftharpoons N_2H_4$	-0.4
$N_2 + 6H^+ + 6e^- \rightleftharpoons 2NH_3$	-1.22

2.3.2 Fundamental challenges of photo(electro)catalytic nitrogen reduction

The N_2 molecule is composed of two nitrogen atoms linked by a triple bond, which requires 945 $kJmol^{-1}$ for direct cleavage of N_2 molecule[125]. Fortunately, there is a biological example using the MoFe nitrogenase enzyme fixing N_2 to NH_3[126]. Nitrogenase is comprised mainly of two multi-sub proteins, where the Fe protein transfers electrons to the second protein, which leads the bound nitrogen molecule to get reduced into ammonia. This electron transfer mechanism interpreted the nitrogen fixation process under mild condition. Inspired by this phenomenon, various efforts of mimicking nitrogenase have been developed for nitrogen fixation. The key point in this mechanism is the electron donation from σ orbitals and back-donation to π^* orbitals of N_2 molecules. Therefore, N_2 reduces bond strength, enhance bond length, and decreases bond energy. Although the nitrogenase-mimic approach might facilitate the cleavage of the N-N triple bond, there are still a great number of challenges remaining for the design and construction of a high-efficiency N_2 fixation system with enhancing electron-hole separation, improving quantum efficiency, catalytic selectivity, N_2 adsorption, and dissociation.

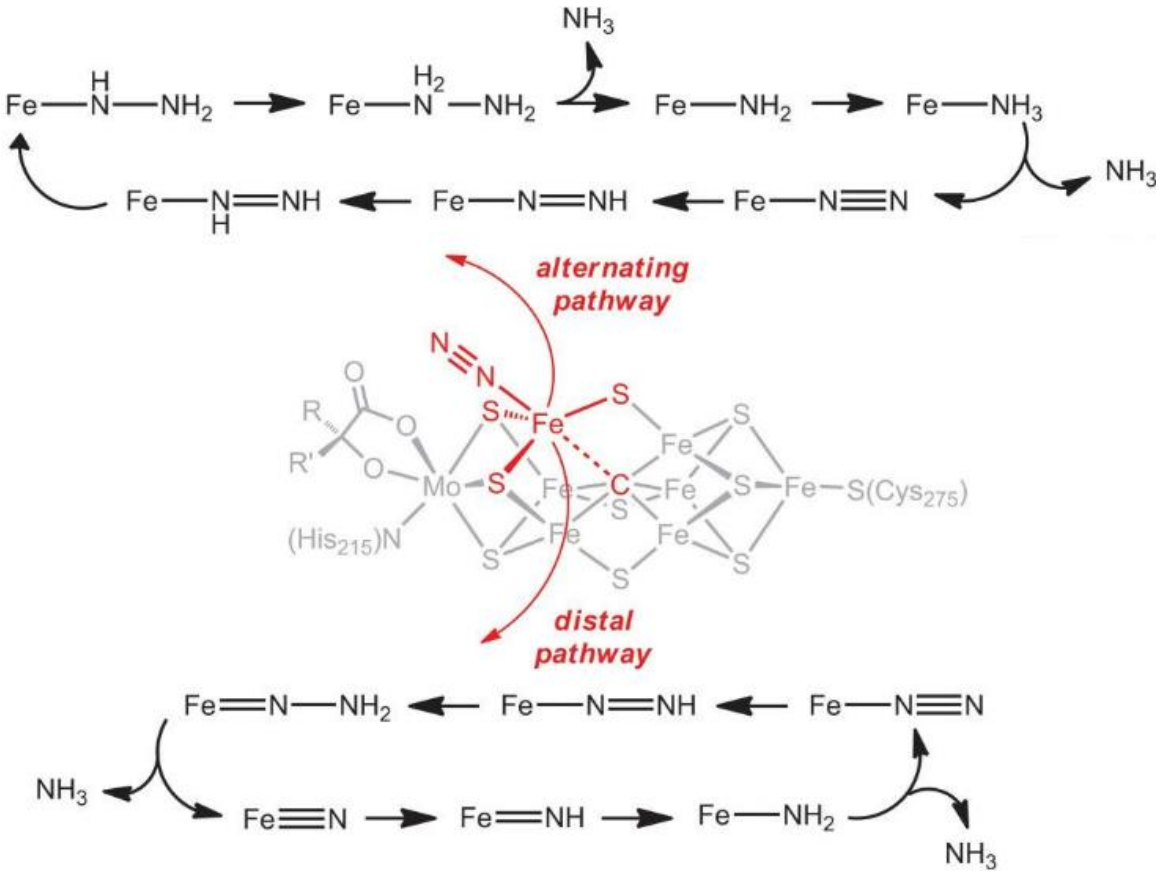

Figure 2.20: Alternating pathway and distal pathway of biological nitrogen fixation by nitrogenase protein[127].

The ultimate mechanism of heterogeneous catalytic nitrogen fixation is an appeal topic that has been devoted to study by the scientific society[128]. Prior studies presented the alternating reaction pathway, which is also called the symmetric pathway. In general, hydrazine is produced as an intermediate form and converts to ammonia at the final step. This alternating pathway is a favorable mechanism for fixing nitrogen of nitrogenase enzyme. Later, another possible scenario, namely the distal or asymmetric pathway, has been explored on iron complexes such as MoFe cofactors (Figure 2.20), where the formation of iron nitride has been observed after releasing ammonia on iron active sites. Recently, much effort in the field of photo(electro)catalytic nitrogen reduction has been focused on engineering single-atom active site catalysts because single atoms aid the activation of dinitrogen and N-N bond cleavage following distal mechanism. Although this mechanism is different in process, the consistency of both mechanisms is the first electron transfer following by the protonation

process. The first electron transfer step is normally considered as the rate-determining step in nitrogen fixation, which always hardly competes with hydrogen evolution. Therefore, it is necessary to design a photocatalyst system that not only follows these reduction pathways but also inhibits the generation of hydrogen.

2.3.2.1 Electron-hole separation, light absorption, and quantum efficiency

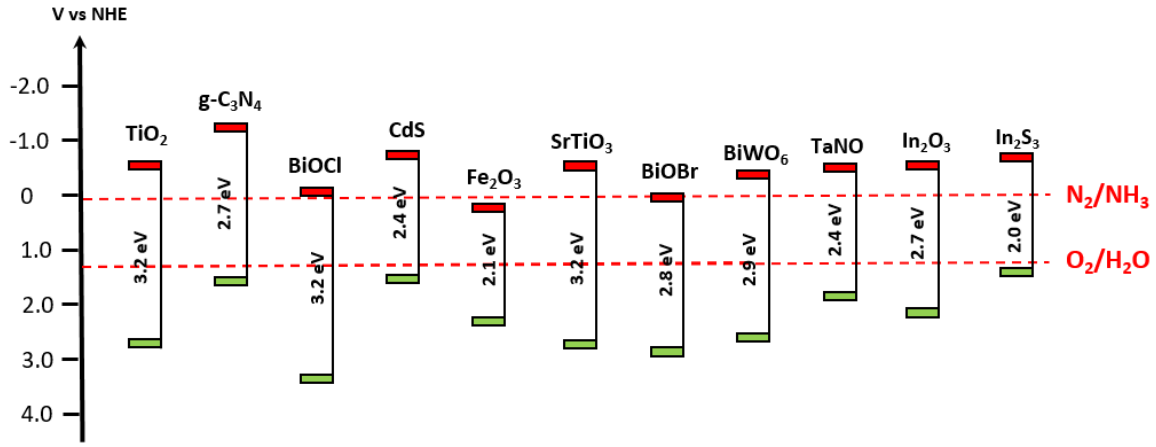

Figure 2.21: Relationship between bandgap energy, VB, and CB positions of several common semiconductors for nitrogen fixation on a potential scale (V) vs. NHE.

Basically, a semiconductor photo(electro)catalyst possesses an energy gap existing between the filled valence band (VB) and the vacant conduction band (CB), which is the bandgap[1]. Thus, the migration of charge carriers (electrons to CB and holes to VB) occurs only with sufficient energy supply. The photo(electro)catalytic nitrogen reduction process involves three main steps: (i) light absorption, (ii) charge separation, and (iii) catalytic reaction. Under light illumination, an electron can only absorb one photon with equal energy or higher than the bandgap energy of the semiconductor and exciting from the VB to the CB and release a hole in VB. This light-induced electron-hole separation is a prerequisite step in all semiconductor photo(electro)catalysts. Finally, these photogenerated species migrate to the semiconductor surface and initiate a reduction reaction with absorbed nitrogen molecules. However, electrons and holes tend to recombine and dissipate energy in the bulk structure or on the surface of the semiconductor, resulting in a decrease of reaction efficiency[2]. Therefore, prevention of charge recombination is a significant challenge in the photocatalytic process.

In the last decades, have been many considerable efforts proposed towards increasing the lifetime of photogenerated carriers such as developing photocatalysts with nanostructures[129-130], cocatalysts loading[131-132], functional groups modification[133-135], surface engineering[136], and heterojunction formations[137].

In addition, it is necessary to maintain suitable bandgap energy of photo(electro)catalysts, which can both prefer working under visible light and satisfying the reduction potential of nitrogen to ammonia. For photo(electro)catalytic nitrogen fixation, the value of the ideal bandgap is approximately 2.0 eV, corresponding to a light wavelength less than 620 nm[53, 138]. Moreover, the CB level must be more negative than the reduction overpotential of N_2 (0.092V vs NHE) and the VB position should be more positive than the oxidation potential of water (1.23V vs NHE). **Figure 2.21** demonstrates band levels of different semiconductor materials. However, most active photocatalysts possess large bandgaps out of the ideal range (TiO_2 E_g = 3.2 eV; g-C_3N_4 E_g=2.7 eV). Accordingly, the bandgap structure engineering such as doping[139] or loading plasmonic cocatalysts[140], defect designing might be applied to enhance the light absorption. Zhang *et al.* investigated the photocatalytic activity of ultrathin layered-double-hydroxide nanosheet photocatalysts ($M^{II}M^{III}$-LDH, M^{II} = Mg, Zn, Ni, Cu; M^{III} = Cr, Al) for nitrogen fixation[141]. Particularly, an as-prepared CuCr-LDH photocatalyst by simple co-precipitation synthesis with tuning oxygen vacancies (OVs) exhibited a significantly superior photoactivity at wavelength up to 500 nm. The introduction of OVs within LDH nanosheets distorted the MO_6 octahedral structure was found to be the main factor contributing to the noticeable enhancement of catalytic activity. Consequently, a photocatalytic NH_3 production rate of 7.1 μmol L^{-1} was achieved, corresponding to the apparent quantum yield of 0.1% at 500 nm. In the later work, Zhang and his coworkers employed hydrothermal method accompanying by a facile Cu doping strategy to control the number of OV active sites in ultrathin titania anatase nanosheets[142]. By having a 6% concentration of Cu dopant, the highest NH_3 generation rate was obtained with 78.9 μmol. $g^{-1}.h^{-1}$ under full solar irradiation. Moreover, owing to abundant OVs, the as-prepared 6% Cu doped TiO_2 demonstrated photocatalytic performance at 700 nm, corresponding to an apparent quantum yield of 0.05%.

Although the electron-hole separation and light absorption capability could be significantly improved by the above-discussed strategies, the challenge of low quantum efficiency still remains. The low quantum efficiency problem could be contributed by the extremely stable triple bond of N_2 molecule with high activation energy, multiple-electron transfer, the competition with photocatalytic hydrogen evolution, and the further oxidation of produced ammonia. For the comparison of quantum efficiency for photocatalytic nitrogen reduction based on photocatalyst, the selected literature report is summarized in **Table 2.7**.

Table 2.7: The quantum efficiency comparison of the most recent photocatalysts for nitrogen fixation

Photocatalyst	**Light source**	**Sacrificial agent**	**NH_3 production rate**	**Quantum yield**	**Ref**
CuCr-LDH	UV-Vis	None	7.1 μmol.h^{-1}	0.1% at 500nm	141
6% Cu/TiO_2	UV-Vis	None	78.9 μmol.g^{-1}.h^{-1}	0.05% at 700nm	142
Reduced TiO_2	UV	PrOH	2.5 μM h^{-1}.g^{-1}	0.02%	143
m-PCN-V	UV-Vis	None	3 μmol.h^{-1}	0.1%	144
BOC-001 BOC-010	Vis	MeOH	1.93 μmol.h^{-1} 4.62 μmol.h^{-1}	1.8% at 254 nm 4,3% at 254 nm	145
BiOBr-(001)	Vis	None	104.2 μmol.g^{-1}.h^{-1}	0.23% at 440 nm	123
Bi_5O_7Br	Vis	None	1.38 mmol.g^{-1}.h^{-1}	2.3% at 420 nm	146

$Ni_2P/Cd_{0.5}Zn_{0.5}S$	Vis	None	101.5 $\mu mol.L^{-1}.h^{-1}$	4.23% at 420	[147]
Au-NPs/Nb-$SrTiO_3$/Zr/ZrOx	Vis	None	0.73 $nmol.h^{-1}.cm^{-2}$	0.9% at 650 nm	[148]
Au-NPs/Nb-$SrTiO_3$/Ru	Vis	None	0.231 $nmol.h^{-1}$	$3.8x10^{-5}$% at 650 nm	[149]

2.3.2.2 N_2 adsorption and activation

In heterogeneous catalysis, the adsorption of reactants onto the catalyst surface is essentially required to prompt catalytic reaction. In other words, active sites on the surface of the catalyst play an important role to initiate the reactions. For photocatalytic reactions, a high specific surface area photocatalyst performs better as compared to a similar photocatalyst with low surface area[150], particularly for H_2 evolution[151-153] and CO_2 conversion[154-156]. However, it seems that the photocatalytic performance of nitrogen fixation has less dependence on this factor[143-144]. Hirakawa and coworkers compared the activities of commercial TiO_2 catalysts with different surface areas[143]. Among these catalysts, the as-prepared titania sample with the highest surface area produced the lowest amount of ammonia, suggesting that this feature is not one of the main impacts that affect the photoactivity. Although the high specific surface area can enhance the physical adsorption of nitrogen molecules, the chemical adsorption is preferably favored in nitrogen fixation since the coordination between dinitrogen and active sites such as anion vacancies[123, 157] or dopant sites[158] could facilitate the dissociation of nitrogen and electron transfer, resulting in increasing ammonia yield. A recent example, oxygen vacancies, with their abundant localized electrons, have been demonstrated to serve as nitrogen trapping centers that can effectively capture and activate inert gas molecules such as O_2, CO_2, particularly for N_2 gas. Li *et al.* investigated the N_2 chemisorption on (001) and (010) BiOCl surfaces[145]. Their previous studies demonstrated that N_2 molecules only absorb on the clean surface of BiOCl by the weak interaction. In the later researches, Li's group revealed that after generating OVs, the (001) BiOCl facet could promote N_2 chemisorption via back dotation of available electrons from OVs to the π^* orbital of N_2, creating a chemical linkage between N_2 and surrounded Bi atoms (**Figure 2.22(a)**). In addition to vacancies, dopant sites such as Fe, Mo ions also have a similar effect on nitrogen adsorption. By doping

Fe on g-C_3N_4 crystalline, adsorbed N_2 prefers coordinating with Fe^{3+} site, creating a coordinative bonding Fe-N[159] (**Figure 2.22(b)**). DFT calculates the chemical adsorption energy is -134.8 kJ.mol^{-1} which is much higher than -14.6 kJ.mol^{-1} of physical adsorption energy when N_2 is adsorbed on pure g-C_3N_4. As a result, chemical bonding between N_2-adsorption sites aids relaxing N-N bond strength and activating the N_2 molecule for further fixation. This chemisorption progress initiates the activation of nitrogen, which is considered as the rate-determining step in photocatalytic nitrogen fixation.

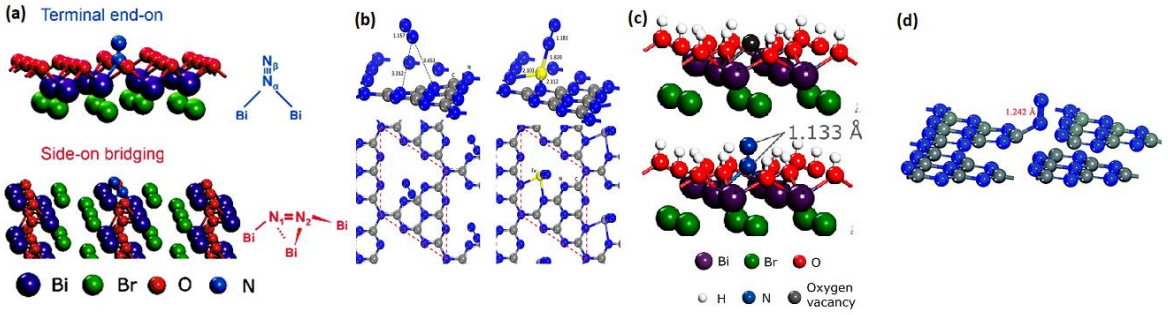

Figure 2.22: (a) Adsorption of N_2 on the different facets of BiOCl[145]; (b) The optimal N_2 adsorption models on pure C_3N_4 and Fe doped C_3N_4[159]; (c) The adsorption geometry of N_2 on the OV of BiOBr (001) surface[123]; (d) The optimal adsorption models on NVs of defective g-C_3N_4[160].

As discussed above, whether molecular N_2 is absorbed on vacancies or dopant sites, it associates with surrounded metallic atoms to form a metal-N_2 complex. This is the basis for the activation of dinitrogen where N_2 molecules donate electron from their occupied σ orbital to empty σ orbital of metal[159, 161-162]. Reversibly, the back-donation of electrons from the metal to unoccupied π* orbital of N_2 molecules occurs, causing the dissociation of dinitrogen. Consequently, the extremely strong N triple bond (N≡N) is weakened and decreased bond energy. Zhang and Li employed theoretical calculation to reveal the N_2 activation availability on OVs of BiOBr (001) facets[123]. Adsorbed N_2 binds with two Bi atoms with an end-on bound geometry. The evidence of electron accumulation and depletion on N_2 orbitals confirms the back transfer of charges to adsorbed N_2, suggesting the possible N-N bond dissociation. Consequently, the N≡N triple bond slightly increases the bond length to 1.133 Å (**Figure 2.22(c)**), which is between the triple bond length (1.078 Å) of free N_2 molecule

and the double bond length (1.201 Å) of diazene. Not only the electron back-donation phenomenon can be found in transition metal-N_2 complexes but also be conceived in coordinate non-metal-N_2 such as carbon[160] or boron[163]. Li et al have fabricated nitrogen vacancies in g-C_3N_4 by infrared ray assisted microwave treatment[160]. His study reported that chemisorbed N-N triple bond on nitrogen vacancies (NVs) is elongated from 1.107 to 1.242 Å due to the formation of σ bond between N_2 molecule and the nearest C atoms (**Figure 2.22(d)**). Accordingly, the construction of chemical adsorption sites establishes a higher possibility to activate and fix adsorbed N_2 efficiently. Therefore, based on the above discussion, it can be concluded that a good catalyst for nitrogen fixation should have the ability of proper chemical bonding to the nitrogen molecules to activate these molecules.

2.3.2.3 The competition between hydrogen evolution and nitrogen reduction

Another challenge in the photo(electro)chemical nitrogen reduction reaction (NRR) is the competition with hydrogen evolution reaction (HER). Although NRR is slightly thermodynamically preferable, HER is much kinetically favorable compared to NRR since HER only involves two electrons transfer process (**I**) while the half-reaction of NRR requires at least the charge transfer of six electrons per one N_2 molecule produced (**II**):

$$2H^+ + 2e^- \Leftrightarrow H_2 \qquad (E^o = 0.00 \text{ V vs NHE}) \quad (\mathbf{I})$$

$$N_2 + 6H^+ + 6e^- \Leftrightarrow 2NH_3 \qquad (E^o = -0.092 \text{ V vs NHE}) \quad (\mathbf{II})$$

The formation of dihydrogen is also one of the primary factors affecting the efficiency of nitrogen fixation in biological ammonia synthesis. Even the catalytic enzymes are highly selective for nitrogen reduction but there is a large amount of hydrogen produced, indicating that selectivity is a difficult issue even in natural system[164]. There is a study of nitrogenase–dependent hydrogen evolution, which has been established by Schubert's group[165]. The results indicated that HER prevents the NRR, since only 40-60% of electrons transfer from nitrogenase to nitrogen, the rest reduces protons to produce hydrogen. Experimentally, most of the artificial fixing nitrogen reactions were carried out in a system, where water acts as the source of protons. Therefore, HER is unavoidable due to the fact that H^+ can be easily adsorbed on the catalytic surface, blocking the availability of N_2 adsorption and dissociation.

It is well known that the introduction of metal cocatalysts such as Pt, Rh, Ni over semiconductor can significantly improve photocatalytic hydrogen evolution and CO_2 reduction[166-168]. However, this strategy seems inapplicable for nitrogen fixation as these metal cocatalysts are more active for HER and suppress NRR efficiency. Ranjit and coworkers reported the impacts of four different cocatalysts (Pt, Rh, Ru, Pd) over TiO_2 for photocatalytic reduction of nitrogen[169]. The yield of ammonia is influenced by the bond strength between H atoms and a metal cocatalyst. Besides acting as an electron sink thus enhancing the photoactivity, the metal such as Ru can also stabilize the adsorbed H atoms on the metal, then, producing more ammonia compared to other cocatalysts. This observation is consistent with electrocatalytic experiments that most noble metals perform low activity or selectivity toward nitrogen reduction. In heterogeneous electrocatalysis, tremendous theoretical and experimental approaches have been studied in order to inhibit HER during NRR. Instead of pure metals, a metal nitride such as VN, CrN, NbN, and ZrN with vacancy defects are expected to be more active toward electrochemical NRR rather than HER[170]. Recent DFT calculation revealed that single-atom active sites supported defective semiconductors can achieve high selectivity for ammonia synthesis due to the significant suppression of H* adsorption[170-172]. Doping earlier transition metals such as Fe, Mo can promote electrocatalytic nitrogen reduction[173]. Also, the utilization of non-aqueous solutions can suppress the proton activity, minimizing the HER. Referred to these progresses in the field of electrocatalytic nitrogen fixation, we propose the strategies for developing advanced photocatalyst for nitrogen reduction. Ideally, engineering the physical and chemical surface structure of semiconductors such as creating anion vacancies, dopant sites composite heterojunctions, or N_2 active cocatalysts can promote both N_2 adsorption and activation and prevent hydrogen generation reaction[174]. Moreover, it is essential to understand the thermodynamic and kinetic mechanisms for the further development of efficient photo(electro)catalyst systems.

2.3.2.4 Side reaction processes

In photocatalysis, it is inevitable for the further oxidation of produced NH_3 to the undesired products of NO_2^-, and NO_3^-[175-176] by photogenerated holes and the participation of O_2 via the following reaction: $2NH_4^+ + 3O_2 + 2h^+ \rightarrow NO_2^- + NO_3^- + + 4H^+ + 2H_2O$, which is leading to

the decrement of NH_3 production. It is worth noting that the photocatalytic decomposition of aqueous NH_3/NH_4^+ is naturally more preferable compared to the oxidation of water into oxygen[177]. Therefore, to prevent the further oxidation to nitrate and nitrite products, the utilization of appropriate sacrificial agents (electron donors) should be employed. The oxidation potential of those sacrificial agents must be more positive than the redox potential of NH_4^+/the oxidation products of NH_4^+. Another strategy is to use a photo-electrochemical cell with a proton-exchange membrane which could inhibit the back-oxidation reactions, where protons are produced on a photoanode and transferred to the cathode to react with nitrogen for the further processes[178].

2.3.3 Advanced materials for photo(electro)catalytic nitrogen fixation

2.3.3.1 Metal active sites

Iron active sites

It should be noted that the iron catalysts are the common catalysts in the Haber-Bosch process due to its good interaction with dinitrogen and weakening N-N bond[179]. Recent studies indicate that ferric photocatalysts are capable of nitrogen reduction to ammonia. However, it is well-known that pure iron oxide had no activity in N_2 photofixation. To overcome this bottleneck, several researchers have employed various methods in the synthesis of defect iron catalysts. Tennakone[180] and his co-worker reported the first system of N_2 reduction using amorphous $Fe_2O_3.nH_2O$ under visible light irradiation. Fe_2O_3 was prepared by gradual addition of KOH to $FeCl_3$ solution and purged with N_2. After irradiated visible light for 40 min, a maximum ammonia concentration of ca. 4 $\mu mol.l^{-1}$ was obtained and continuously decreased due to the decomposition of NH_3 to nitrate in the solution, which poisoned the catalyst. Therefore, NH_3 must be removed immediately from reaction site to maintain catalytic efficiency. Khader *et al.* successfully prepared a mixture of α-Fe_2O_3 and Fe_3O_4, which was effective in the photo-reduction of nitrogen for about 580 h[181]. Interestingly, in the existence of 5 at% iron in the form of Fe^{2+} in the partially reduced Fe_2O_3, NH_3 was detected in an aqueous slurry of the catalyst under UV illumination.

On the other hand, doping Fe into metal oxide such as TiO_2, Al_2O_3, ZnO is a practical strategy for the utilization of iron active site catalysts. Most of the studies have been focused on metallic Fe modified titanium dioxide photocatalysts. In addition, there has been considerable debate over the role of cation Fe on iron titania photocatalyst. The earlier work suggested that the introduction of Fe^{3+} as an impurity in titania can play an indirect role in decreasing the bandgap energy of semiconductors as well as hinders the recombination of photo-generated electron-hole pairs, consequently, enhance the absorption ability and the photoactivity. Zhao *et al.* investigated the photocatalytic activity of Fe-doped TiO_2 with highly exposed (101) facets[25]. The quantum yield of nitrogen photo-reduction using ethanol as scavenger can be reached to $18.27x10^{-2}m^{-2}$. The TEM images confirmed that Fe^{3+} ions are successfully incorporated into the anatase crystal and substituted for Ti^{4+} in the TiO_2 lattice (**Figure 2.23**). Zhao and Soria[182] reported that even doping Fe^{3+} can improve catalytic activity higher than pristine TiO_2, but an excess amount of Fe^{3+} doping can limit the continuous growth of TiO_2 particles and poisoning the catalyst. In a continuous work of previous studies, further investigations of mechanism on iron titanate photocatalyst were conducted by Rusina[183] and Krich[184] The electron transfer system of photo(electro)catalytic N_2 reduction on the $Fe_2Ti_2O_7$ thin film includes a series of processes of nitrogen-diazene-hydrazine-ammonia-nitrate. Also, Lashgari proposed a nitrogen photofixation mechanism based on H-atom production[185]. In addition to Fe doped metal oxide materials, non-metal oxide semiconductors were modified with iron. Hu *et al* adapted graphitic carbon nitride doping with Fe^{3+} for the conversion of nitrogen to ammonia[159]. It was found that the $N\equiv N$ bond is prolonged when N_2 molecules interact with Fe^{3+} sites. The delocalization of electron in $\sigma_g 2p$ orbital (HOMO) of nitrogen when N_2 adsorbed on Fe^{3+} doping sites leads to its orbital energy almost overlaps to that of πg^*2p orbital (LUMO), indicating the direct role of iron in activating the N_2 molecule. The highest NH_4^+ production rate of 5.4 $mg.L^{-1}h^{-1}g^{-1}$ was achieved with 0.05 wt% Fe doping, which is 13.5 folds compared to pristine g-C_3N_4. For the comparison of photocatalytic activities of ammonia production based on iron active site photocatalyst, the selected literature report are summarized in **Table 2.8**.

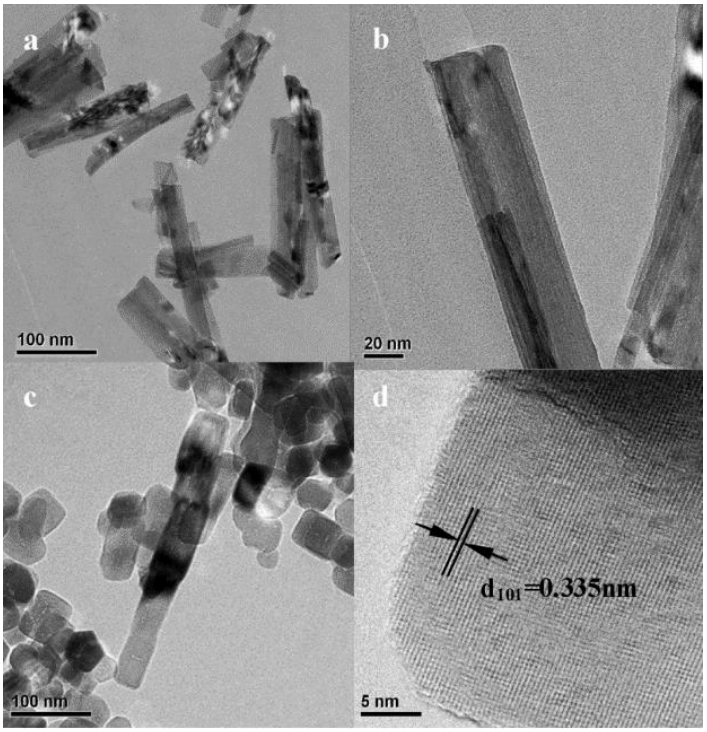

Figure 2.23: (a)-(b) TEM images of titanate nanotubes prepared by hydrothermal reaction. (c) TEM images and (d) HRTEM image of 100 × 10^{-6} Fe^{3+} doped TiO_2. [25]

Table 2.8: Summary of iron active site photocatalysts for the reduction of N_2 to NH_3

Catalyst	**Light source**	**Sacrificial reagent**	**NH_3 rate**	**Ref**
0.2% Fe-doped TiO_2	390-420nm	-	10 μmol$g^{-1}h^{-1}$	[186]
0.5% Fe-doped TiO_2	UV	-	6 μmol$g^{-1}h^{-1}$	[182]
Fe-doped TiO_2	254 nm	Ethanol	400 μM.h^{-1}	[25]
Partially reduce Fe_2O_3	UV-vis	-	10 μmol$g^{-1}h^{-1}$	[181]

Fe_2O_3	UV-vis	Ethanol	1362.5 $\mu M.h^{-1}$	[185]
$Fe_2O_3.nH_2O$	Vis	-	6 $\mu M.h^{-1}$	[180]
Fe(O)OH	Vis	-	9.25 $\mu M.h^{-1}$	[187]
Fe doped C_3N_4	Vis	Ethanol	120 $\mu M.h^{-1}$	[159]
Fe-load 3D Graphene	UV	-	24 $\mu molg^{-1}h^{-1}$	[188]
Hydrous oxide of Fe and Ti	Vis	-	22 $\mu M.h^{-1}$	[189]
Iron loaded bentonite	UV	-	1.33 $\mu M.h^{-1}$	[190]
Iron titanate thin film	> 320nm	Ethanol	0.57 $\mu M.h^{-1}cm^{-2}$	[183]

Titanium active sites

Among all the well-known photocatalysts, TiO_2 is the most prominent material and has applied in a variety of photocatalytic applications, because of its abundance, efficient charge separation, and stability. In earlier publications, the metal-doped titanium dioxide or titanate was used for photocatalytic fixing nitrogen. In later studies, trivalent titanium complexes have been employed to promote the N≡N cleavage[191-192]. **Figure 2.24(a)** illustrates a typical role of Ti^{3+} reacted with N_2 via electron donation. These reduction reactions create Ti^{4+}-amine complexes which finally release NH_3 with regenerated trivalent Ti^{3+} complexed. Inspired by this suggestion, Hirakawa *et al.* have successfully synthesized reduced titania with Ti^{3+} defects, which served as the adsorption sites for N_2 and trapping sites for the photogenerated electron[143]. The proposed mechanism is shown in **Figure 2.24(b**)

with a solar-to-conversion efficiency of 0.02%. However, it is still lower than that of natural- and artificial- photosynthesis, therefore, an improvement of that material in photocatalytic activity is necessary.

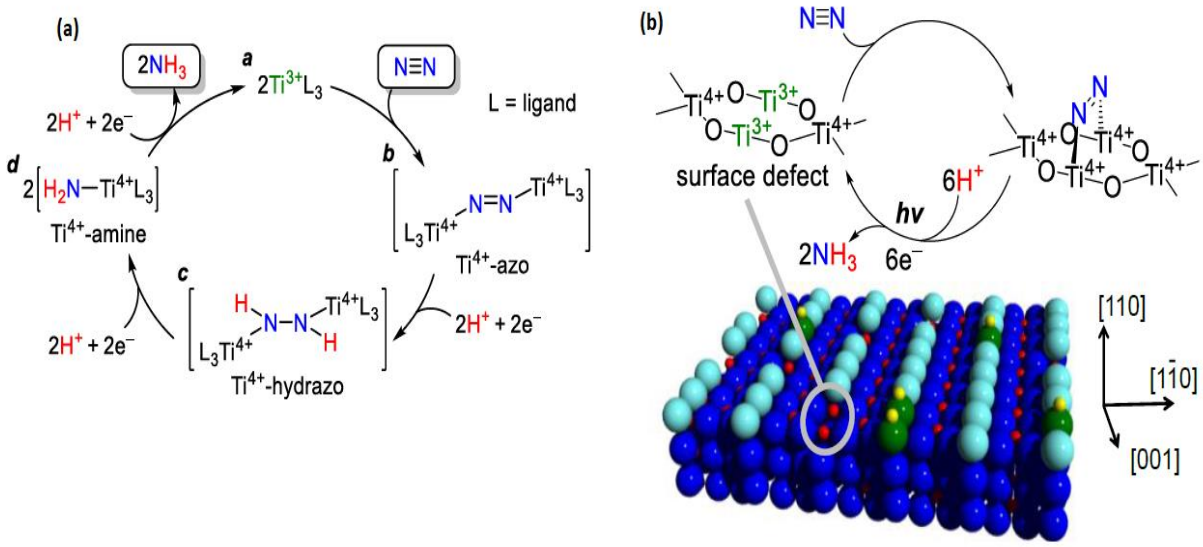

Figure 2.24: Scheme (a). catalytic cycle for N_2 fixation by Ti^{3+}-containing; Scheme (b) proposed photocatalytic cycle for N_2 fixation on the rutile[143].

Molybdenum active sites

Owing to excellent electrical, optical, and photovoltaic properties, ultrathin transition metal dichalcogenides (TMDs) have been considered as promising materials. Among them, MoS_2 semiconductor is known as an efficient photocatalyst for hydrogen evolution and CO_2 conversion reaction. Recently, its application in N_2 reduction has been unveiled since the first report of Sun's group[193]. In this research, the photocatalytic activity of MoS_2 photocatalysts under different preparation conditions was investigated. The results show that the sonicated ultrathin MoS_2 induced charged excitons (trions) when applying visible light (**Figure 2.25(a)**). These trions carried multiple electrons in one bound state, which is located around Mo sites. Naturally, three Mo atoms surround adsorbed dinitrogen on the S vacancy and facilitate the six-electron transfer process. Consequently, the rate of ammonia production of 325µmol.g^{-1}.h^{-1} was achieved, which is much higher than the rate of hydrothermal MoS_2 and bulk MoS_2 samples. Particularly, it can be concluded that a multiple electrons reduction

process was responsible for the enhancement of photocatalytic dinitrogen reduction to ammonia.

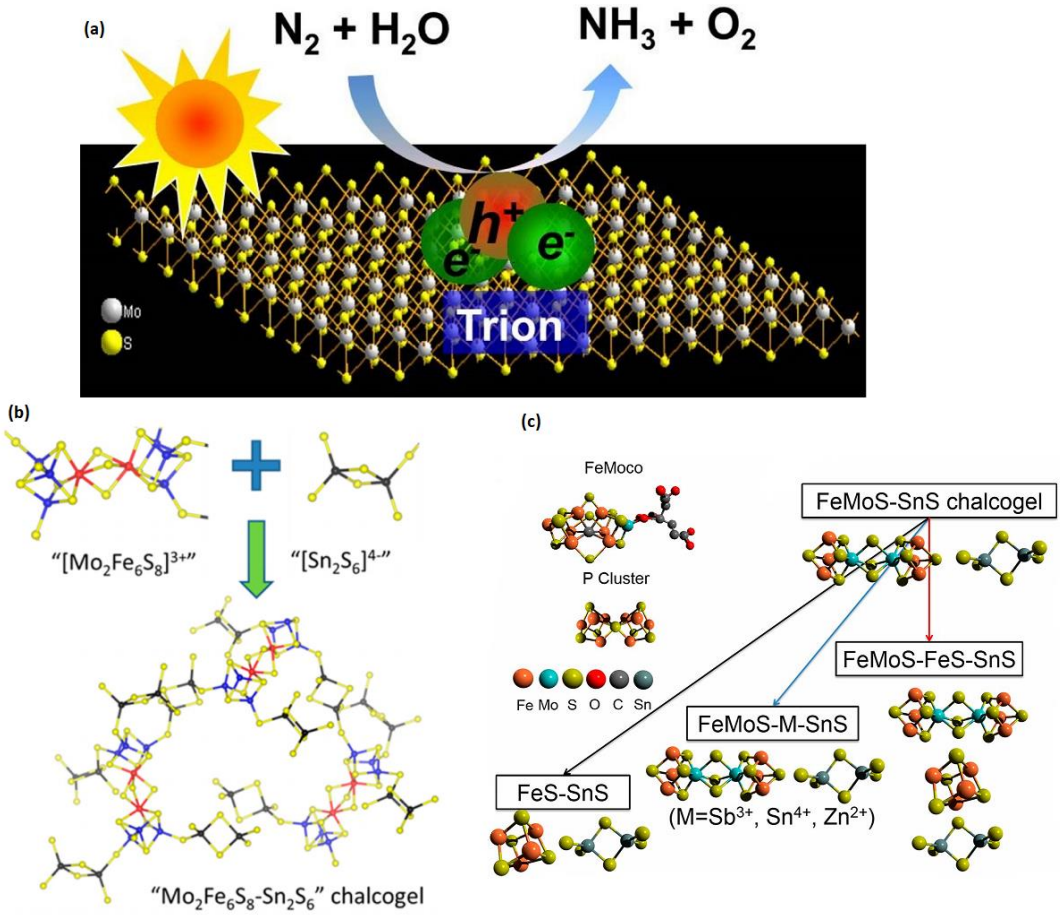

Figure 2.25: (a) Schematic illustration of the trion induced multi-electron N_2 reduction process[193]; (b) Schematic representation of $Mo_2Fe_6S_8$ - Sn_2S_6 biomimetic chalcogel (FeMoS chalcogel), building block scheme (Mo, blue; Fe, red; S, yellow; Sn, black), and a complete chalcogel shown at right[194]; and (c) Nitrogenase-inspired biomimetic chalcogels[195].

In addition, enzyme nitrogenase has also been widely studied for the application of catalytic nitrogen fixation[196]. A nitrogenase is a two-component system comprising a MoFe protein and an associated Fe protein. Based on this inspiration, in 2015, Banergee and Kanatzidis supposed that solid chalcogels consisting of FeMoS inorganic clusters are able to reduce dinitrogen to ammonia by utilizing white light[194]. The double-cubane $Fe_2Mo_6S_8$ units were associated with by Sn_2S_6 ligands (**Figure 2.25(b)**) to form a stable amorphous complex in aqueous solution. The FeMoS cluster of the biomimetic chalcogel system (FeMoS cofactor,

a synthetic cluster bearing Mo−Fe linkages) is a structural and functional analog of the MoFe active site in the enzyme nitrogenase. This work showed that the high density of FeMoS active sites can boost multi-electron transformation as well as mimic the function of biological nitrogenases in N_2 fixation. To gain insights into the performance of the FeMo cofactor in nitrogenases, Brown and coworkers fabricated a biohybird system of nitrogenase coupled with CdS semiconductor. The MoFe protein-coated CdS nanorods produced 315 nmol of NH_3 per min over one mg MoFe-protein, which is estimated for a quantum yield of 3.3%. In MoFe protein, FeMo cofactor plays a role as an active site, receiving photogenerated electrons from CdS nanocrystals. By changing condition reactions, Liu found that the lack of FeMo cofactor did not produce ammonia. Furthermore, the role of Mo and Fe in MoFe protein is revealed in another study. Liu *et al.* discussed the photocatalytic activity of nitrogen reduction by the nitrogenase-inspired biometric chalcogel[195]. In this system, $Mo_2Fe_6S_8(SPh)_3$, Fe_4S_4, and redox-inert ions are assembled with Sn_2S_6 (**Figure 2.25(c)**). However, iron was expected to be more active than molybdenum for the solar reduction of N_2 due to the fact that a weak bonding orbital between nitrogen and iron has emerged via the localized orbital analysis. Moreover, their conclusion that the Fe is a better active site for N_2 binding than Mo has been demonstrated by recent biochemical and spectroscopic data.

Nickel active sites

The study of Schrauzer and Guth examined the effect of various metal dopants over titania for photocatalytic NH_3 formation. In addition to doping Mo and Fe, only Co and Ni dopant performed the contribution to the enhancement of NH_3 production efficiency[186]. The other metal-doped such as Pd, V, Cu showed no improvement in catalytic activity. It can be explained by the influence of Ni, Co accelerates the phase transformation while this phenomenon is unobtainable for other dopants. This explanation is consistent with the conclusion of Ranjit. In his work, Ranjit also compared 12 elements doped TiO_2 photocatalyst and found the order of photoactivity was Fe>Co>Mo>Ni. Ye *et al*. loaded Ni_2P on a binary metal sulfide solid solution for photocatalytic N_2 fixation under visible light[147]. The deposited transition metal phosphide affects both the VB and CB of metal sulfide, resulting in higher photocatalytic reduction ability. Moreover, the transition metal phosphide of Ni_2P supports the photo-induced charge carrier separation process, which is confirmed by

photoluminescence spectra (PL) and electrochemical impedance spectroscopy (EIS). For $Ni_2P/Cd_{0.5}Zn_{0.5}S$, the NH_3 production rate achieved 101.5 μmol L^{-1} h^{-1} (35.7 times than that of unloaded metal phosphine cocatalyst), corresponding to 4.23% of apparent quantum efficiency at 420 nm.

2.3.3.2 Non-metal vacancies

As mentioned in the previous sections, many studies claimed that the vacancy defects such as oxygen vacancies[197-201], nitrogen vacancies[202] and sulfur vacancies[199-201] with their abundant localized electrons can donate their electron for absorbed N_2, forming chemical bonding between N_2 and surrounded atoms and activating N_2 molecule, therefore, enhancing catalytic performance.

Oxygen vacancies

Table 2.9: Summary of oxide catalysts for the photoreduction of N_2 to NH_3

Catalyst	Light source	Sacrificial reagent	NH_3 rate	Ref
BiOBr nanosheets	UV-Vis/Vis	-	104.2 μmol.$g^{-1}h^{-1}$	[123]
Bi_5O_7Br nanotubes	Vis	-	1.38 mmol.$g^{1}h^{-1}$	[203]
$TiO_2/Au/a\text{-}TiO_2$	Vis	-	13.4 nmol $cm^{-2}h^{-1}$	[19]
BiO quantum dots	UV-Vis	-	1226 μmol.$g^{-1}h^{-1}$	[204]

Reduced TiO_2	Infrared light	-	3.33 $\mu molg^{-1}h^{-1}$	[27]
Rutile TiO_2	$\lambda > 280$ nm	2-Propanol	$16.67\mu M.g^{1}h^{-1}$	[143]
BiOCl nanosheets	Solar Light	Ethanol	45 $\mu M.h^{-1}$	[145]
Bi_5O_7I nanosheets	280–800 nm	Ethanol	120 $\mu M.h^{-1}$	[205]
CuCr-LDH	Vis	-	57.1 $\mu mol\ g^{-1}\ h^{-1}$	[141]
Hydrogenated Bi_2MoO_6	Solar light	-	1.3 $mmol.g^{-1}h^{-1}$	[206]

In the earlier studies, the synthesis of ammonia by N_2 photoreduction has been far from acceptable because of the impoverished binding of N_2 to catalytic active sites and the high energy of the intermediates required in the reactions. It has been concerned with a significant challenge of activation and cleavage of the highly stable N≡N triple bond relying only on light-induced electrons from semiconductor materials in solar-driven N_2 fixation. To conquer this challenge, the electron-transfer supportive centers should be introduced as the primary-step active sites to absorb the molecular N_2 and weaken the N≡N bond, which could allow the photo-induced electrons to inject for the subsequent reduction reactions. Oxygen vacancies (OVs), with their rich localized electrons, have been proved to serve as electron trapping centers that can effectively capture and activate the inert gases such as O_2, CO_2, and N_2 in particular. **Table 2.9** summarizes the most recent advanced oxide materials containing OVs for nitrogen photo-fixation.

Oxygen vacancies based on Titanium dioxide

Recently, Zhang *et al.* created solid-state sources of solvated electron based on reduced titanium dioxide for nitrogen photofixation[27] (**Figure 2.26**). Since oxygen vacancies were introduced in TiO_2, electrons are trapped at the vacancy sites and released by IR-light excitation, consequently reducing N_2 to NH_3. The number of trapped electrons can be enriched by tuning the concentration of oxygen defects. However, the amount of generated ammonia nearly ceased after 24 h due to the consumption of releasable trapped electron. For the recharging of electrons, the reacted TiO_2 could be treated with a chemical reduction method.

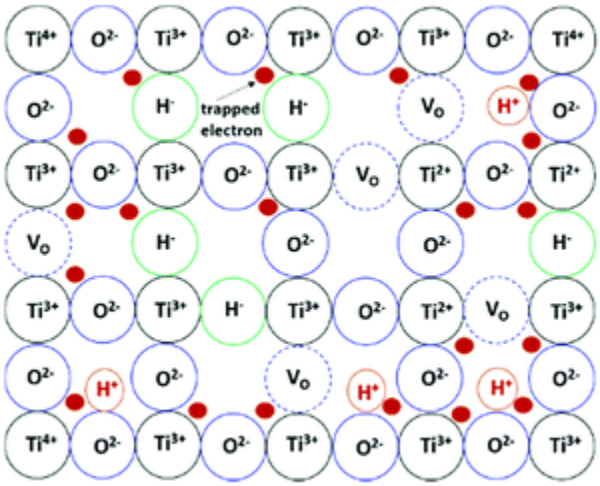

Figure 2.26: Schematic illustration of the main defects existing in reduced TiO_2 upon boron hydride reduction (V_O: oxygen vacancy; H^-: hydride anion in lattice oxygen site; H^+: proton bonding with lattice oxygen). The trapped electrons are also illustrated. [27]

Another group, Li, and his partner conducted the photo-electrochemical reduction of N_2 to NH_3 on the surface oxygen vacancies of plasmon-induced TiO_2[19] (**Figure 2.27**). Li suggested that only superficial oxygen vacancies can act as active sites, the other internal vacancies in crystal structure play a role as undesired defects. By using atomic layer deposition method, oxygen vacancies are successfully introduced onto the surface of TiO_2 without creating bulk defects (introduction of oxygen vacancies to bulk structure to form defects). It is worthy to note that surface oxygen vacancies not only serve as N_2 absorption sites but also promote charge-carrier transportation to the adsorbed nitrogen while bulk-vacancies act as recombination centers to trap the photo-excited electrons and holes. The optimized ammonia

production rate of 13.4 nmol.cm^{-2}.h^{-1} was obtained by the sample of surface oxygen vacancies modified TiO_2/Au/amorphous TiO_2 electrode, which is 2.6-folds higher than pristine TiO_2. Moreover, Hirai and his group have studied systematically the role of oxygen vacancy and Ti^{3+} active site[143]. He concluded that oxygen vacancies can facilitate the dissociation of the N≡N triple bond. This conclusion is consistent with Zhang and Li's group[19].

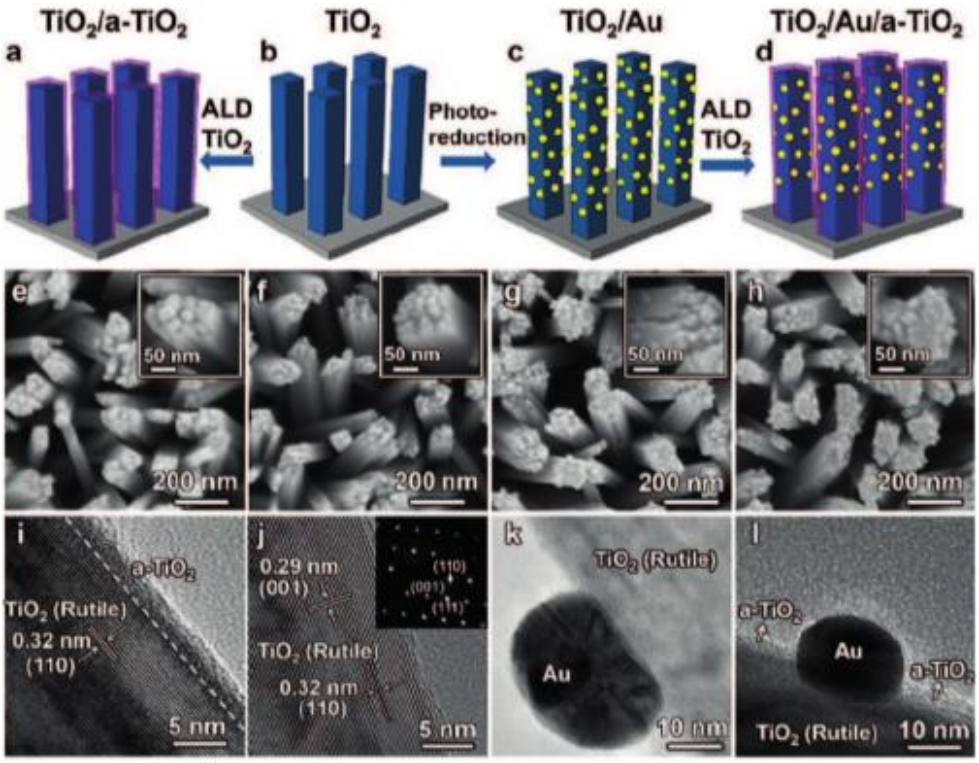

Figure 2.27: a–d) Illustration of the experimental procedures for prepara-tion of bare TiO_2, TiO_2/Au, TiO_2/a-TiO_2, and TiO_2/Au/a-TiO_2 photo-electrodes. e–h) Scanning electron microscopy(SEM) and i–l) HRTEMimages of photoelectrodes. Key: TiO_2/a-TiO_2 (a, e, i),bare TiO_2(b, f, j(inset:selected area electron diffraction (SAED) pattern of the bare TiO_2 NR)), TiO_2/Au (c, g, k), TiO_2/Au/a-TiO_2(d, h, l). [19]

In contrast with the above studies, Medford and Comer employed DFT analysis to discuss the role of oxygen vacancy[24]. The defected surface (110) titania possessing an oxygen vacancy was compared to pristine TiO_2 by examining nitrogen reduction. The DFT calculations rejected the traditional mechanism of nitrogen photofixation that the breaking of

the N-N bond is conducted directly by oxygen vacancy. Otherwise, Medford hypothesizes that a considerable stabilization of the unstable NH_x intermediates by the oxygen vacancy makes NH_x binding close to exo-thermic, indicating that it can enhance nitrogen reduction and ammonia generation after the N–N bond has been dissociated.

Oxygen vacancies based on bismuth oxyhalide

Bismuth oxyhalides, BiOX (X = Cl, Br, and I), have recently gained considerable interest for their intrinsic optical properties; they are also practical for industrial applications, such as the photodecomposition of organic pollutants and CO_2 reduction. The structural layer of BiOX provides sufficient space for the polarization of atoms and the as-formed internal electric field will play an effective role in their efficient charge separation and transfer process.

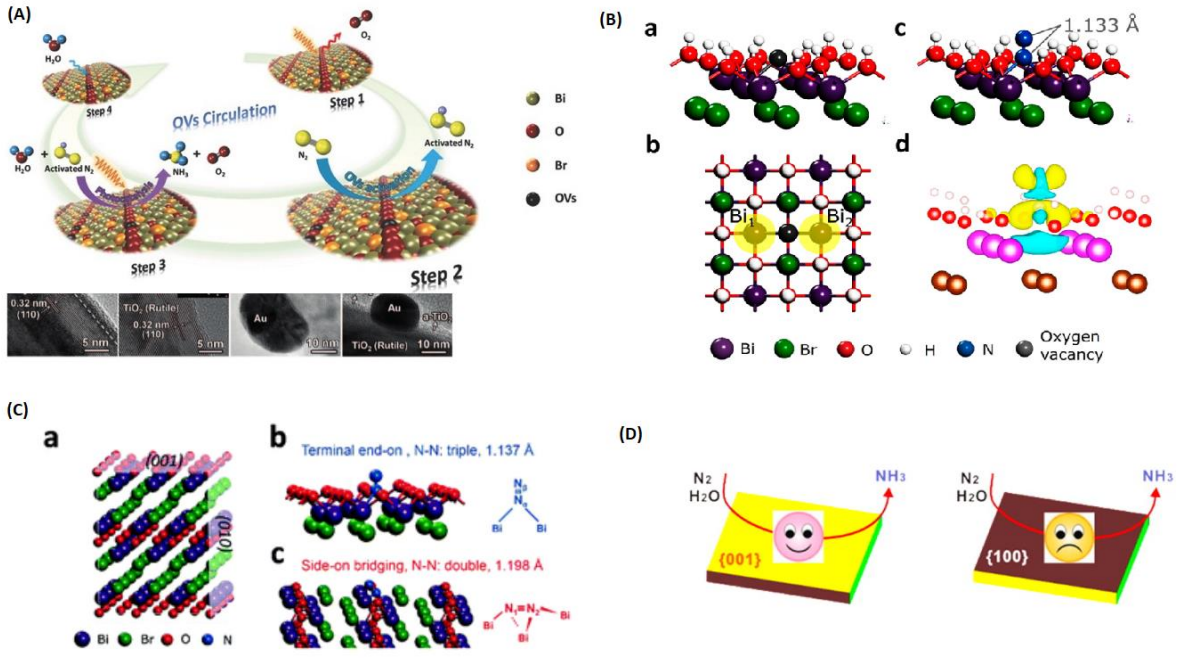

Figure 2.28: (A) Schematic illustration of the photocatalytic N_2 fixation model in which water serves as both the solvent and proton source, as well as the reversible creation of light-induced oxygen vacancies; **(B)** Theoretical prediction of N_2 activation on the OV of BiOBr (001) surface. (a) Side and (b) top view of (001) surface of BiOBr with an OV. (c) The adsorption geometry of N_2 on the OV of BiOBr (001) surface. (d) The charge density difference of the N_2-adsorbed (001) surface; **(C)** Adsorption of N_2 on the (001) and (010)

facets of BiOCl. (a) Crystal structure of BiOCl and the corresponding cleaved (001) and (010) surface. (b) The terminal end-on adsorption structure of N_2 on (001) surface of BiOCl and (c) the side-on bridging adsorption structure of N_2 on (010) surface of BiOCl; **(D)** Schematic illustration of the photocatalytic N_2 fixation over Bi_5O_7I (001) and (100) facers. Figure 10(A), (B), (C), (D) from the references [203], [123], [145], and [205], respectively.

Due to containing interior oxygen vacancy, bismuth oxyhalides have been considered promising catalysts for nitrogen fixation, particularly in photofixation[198, 207]. Most recently, Bi_5O_7Br nanotubes were investigated for the photocatalytic ammonia evolution by Wang *et al.*[203]. Owing to the excessive number of oxygen vacancies as active centers, the highest NH_3 production rate is obtained at 1.38 mmol. $g^{-1}h^{-1}$, corresponding to an apparent quantum yield of 2.3% at 420nm. However, bismuth oxybromide photocatalysts are susceptible to photocorrosion. During the reduction reaction, the oxygen vacancies are filled by O atoms from the water, reducing the number of active sites and lose its activity. Interestingly, the reacted oxygen vacancies can be regenerated by applying visible light illumination, which continuously provides the reversible light-switchable surface oxygen vacancies for N_2 fixation. **Figure 2.28(A)** demonstrates the repeated circulation of oxygen vacancies over TiO_2 for ammonia photo-production.

In 2015, Zhang and Li studied the effect of oxygen vacancies on the exposed (001) facets of BiOBr nanosheets to fix nitrogen under ambient condition[123]. The theoretical analysis calculated the extension of the N-N triple bond increased by 0.055 Å as absorbed N_2 molecules are activated by oxygen vacancies (**Figure 2.28(B)**). Also, the oxygen vacancies as the initial electron acceptor can avoid the electron-hole recombination and considerably promote the interfacial charge transfer. In this paper, the UV-Visible light-driven N_2 fixation rate was measured to be 223.3 $\mu molg^{-1}h^{-1}$ without using a sacrificial agent and a noble-metal cocatalyst. As a succession of the previous study, Zhang's group clarified that two distinct structures of surface oxygen vacancy on different facets of BiOCl nanosheets completely determine the N_2 fixation mechanisms[145]. For instance, the N_2 reduction reaction on the oxygen vacancies of BiOCl (010) facets followed the symmetric alternating pathway which generates N_2H_2-level and N_2H_4-level species. Whereas an asymmetric distal mechanism selectively produces ammonia (001) facets without involving the generation of N_2H_2 or N_2H_4.

By DFT calculation, the accepted adsorption possibility of N_2 on BiOCl surfaces was investigated. On the (001) facets, absorbed N_2 combines with two nearest Bi atoms in the sublayer to form a terminal end-on bridging, consequently, the activation exhibited the increasing N-N bond length to 1.137 Å **(Figure 10(C)-(a)).** Separately, different absorbed N_2 performs a larger extent of N_2 activation and elongates bond length to 1.198 Å (**Figure 2.28 (C)-(b)**) through a side on bridging mode (dinitrogen interacts with two nearest Bi atoms in the outer layer and the one next nearest Bi atom in the sub-layer on the (010) facet). Respectively, the quantum yields under UV irradiation were 1.8% h^{-1} and 4.3% h^{-1} on the (001) and (010) surface of BiOCl**.** Inspired by Zhang's group, Bai et al examined the photocatalytic activity of different Bi_5O_7I facets over solar-driven N_2 fixation reaction[205]. At 356 nm UV-light irradiation, the apparent quantum efficiency of (001) surface Bi_5O_7I was 5.1%, which is 2.2 times higher than that of (100) planes (**Figure 2.28(D)**)**.** After exposure to (001) facets, the charge carrier separation and mobility were dramatically boosted, elucidating the enhancement of photoactivity on (001) Bi_5O_7I facets.

Although most publications highlight noteworthy attention on the exposure of different facets, it is more possible that the combined effects facet-dependent studies and oxygen vacancies-dependent studies will open a new and interesting perspective and provide inspiration for the development of advanced photocatalysts for N_2 photoreduction. In addition, the combination of experimental data and theoretical simulations is highly necessary to fully interpret the N-N triple bond activation and pathway the NH_3 formation mechanism. Thus, further study on the facet controlled and vacancy-mediated bismuth oxyhalides should be dedicated in the future to emphasize the scientific aspects and reveal the appropriate reaction steps for the N_2 photofixation.

Nitrogen vacancies

The introduction of defects in photocatalyst materials is considered an effective method to enhance the photocatalytic nitrogen fixation. Instead of oxygen vacancies, another alternative strategy for using non-metal vacancy to fix nitrogen has been to utilize nitrogen vacancies to absorb and weaken N_2 molecules. Because nitrogen vacancies have the same size and shape as the nitrogen atoms in dinitrogen, nitrogen vacancies (NVs) are favorable in the selective chemisorption and activation of N_2[157]. This explains why the N_2 fixation rate remained

unchanged when N_2 was replaced by air as the N_2 source. Besides, nitrogen vacancies significantly improved the separation of charge carriers by trapping photo-excited electrons and facilitating the interfacial charge transfer to the adsorbed N_2.

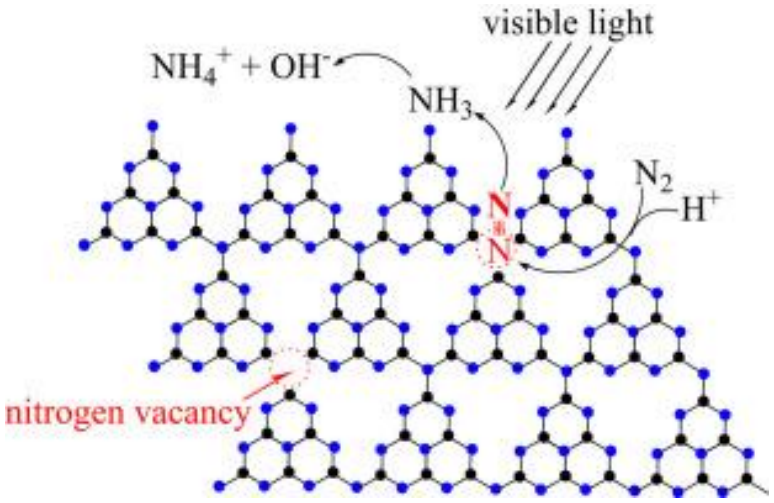

Figure 2.29: The possible nitrogen photofixation process proposed by Ma et al. [208]

From the time when the first report on graphitic carbon nitride (g-C_3N_4) published in 2009, this metal-free polymeric photocatalyst has received tremendous interest due to its specific properties such as excellent stability, cost-effectiveness, and environmental benignity. Recently, graphitic carbon nitride composing of nitrogen vacancies has been employed as a photocatalyst for the reduction of nitrogen to ammonia. In 2015, the first introduction of nitrogen vacancies induced g-C_3N_4 for visible-light-driven NH_3 production was reported by Dong[157]. After 15 h of light illumination, nitrogen vacancies incorporated g-C_3N_4 generated 1.24 mmol. $h^{-1}g^{-1}$ of photofixation rate while bare g-C_3N_4 shows no catalytic activity, suggesting the indispensable role of nitrogen vacancies in promoting photoactivity. However, lacking nitrogen in defects modified carbon nitride structure slightly enlarged bandgap energy than that of pristine samples, resulting in a reduction of visible light absorption ability. In contrast to Dong's research, Li suggests that even the influence of nitrogen vacancies on the band structure decrease the bandgap energy, it is not the main factor that affects the photocatalytic nitrogen reduction. Li *et al* have fabricated nitrogen vacancies assisted g-C_3N_4 by infrared ray assisted microwave[160]. Under microwave treatment, abundant nitrogen vacancies were formed and served as chemical absorption centers. By DFT calculation, it

was found that the chemisorbed N-N triple bond is elongated from 1.107 Å to 1.242 Å due to the formation of σ bond between N_2 molecule and the nearest C atom. Consequently, the NH_4^+ evolution rate obtained by IM-CN(30) sample was 5.1 mg $L^{-1}.h^{-1}.g^1$, which is 5-fold and 2.5-fold higher than those of bulk CN_{520} and M-CN(20). Similarly, Ma and Li have prepared high specific surface area carbon nitride by a dissolve-regrowth method, which is capable of nitrogen photoreduction[208]. Based on experimental results and theoretical simulation, Ma demonstrated the possible nitrogen photofixation over large surface area g-C_3N_4 containing N-vacancies (**Figure 2.29**). First, absorbed N_2 molecule in N-vacancy is activated by four-electron which occupies the anti-bonding orbitals of N atoms, then H^+ reacts with the activated N_2 molecule to produce NH_3 and finally form NH_4^+.

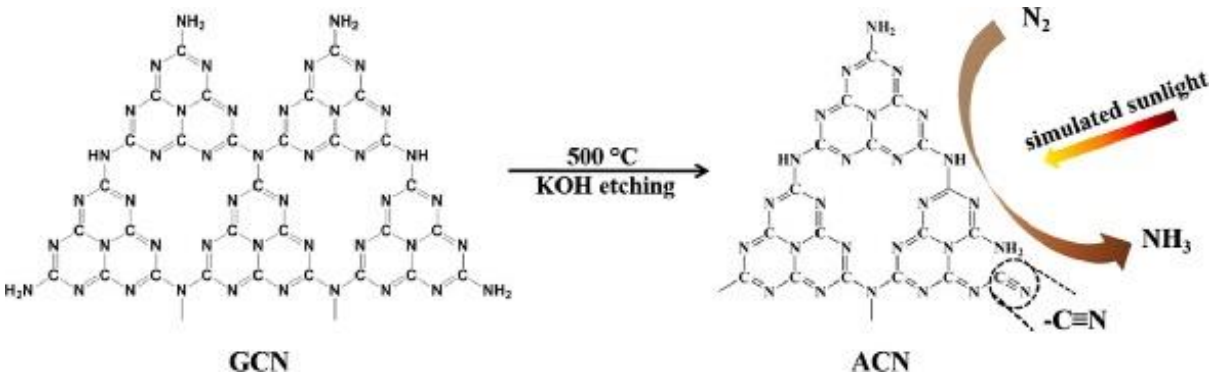

Figure 2.30: The cyano defects were successfully introduced into the g-C_3N_4 framework by KOH etching and could contribute to improving the nitrogen photofixation ability of g-C_3N_4.[209]

Besides using nitrogen-vacancy active sites, nitrogen defects are also applied for producing NH_3 under solar simulation. Li *et al* introduced cyano-deficient onto bulk g-C_3N_4 by cleavage C=N bond via KOH etching treatment[209]. The as-prepared g-C_3N_4 possesses a porous structure with ladder-like thin layers. Li concluded that the presence of cyano groups not only reduces the conduction band of bulk g-C_3N_4 but also acts as an electron acceptor, capturing electrons and inhibiting electron-hole recombination. Moreover, the existence of cyano defects induce more adsorption sites for N_2 activation. Therefore, the formation of cyano groups by etching bulk g-C_3N_4 with KOH is the main reason for the enhanced photocatalytic N_2 fixation activity. After 4 h, the NH_4^+ concentration of ACN-10% increases to 51.65 mg/L,

which is 7.6 times higher than what was observed for bulk samples. **Figure 2.30** shows the formation of cyano deficient g-C_3N_4 and N_2 photofixation mechanism.

Sulfur vacancies

Due to similar chemical properties with oxygen, Hu hypothesized that sulfur vacancies have N_2 absorption ability as oxygen vacancies[200]. In his study, a tri-component metal sulfide of $Zn_{0.1}Sn_{0.1}Cd_{0.8}S$ was prepared by the hydrothermal process. Under visible light irradiation, the photocatalyst performs outstanding activity in nitrogen fixation because of containing a high concentration of sulfur vacancies. This research implied that the photocatalytic nitrogen fixation activity linearly depended on the sulfur vacancy concentration. The NH_4^+ production rates over the various vacancy concentrations were compared and illustrated in **Figure 2.31(a)**, confirming that the concentration of sulfur vacancies plays a significantly pivotal role in the N_2 photofixation ability.

Hu also discussed the role of Zn, Sn metal doping in the creation of sulfur vacancies rather than act as active sites to promote catalytic ability. The elongation of the N-N triple bond from 1.164 Å to 1.213 Å proves that sulfur vacancies can aid the activation of N_2. In this regard, Hu's group continues to investigate the effect of different metal doping on ternary metal sulfide. Mo and Ni-doped CdS can distort the crystal structure, leading to the formation of sulfur vacancies in obtained tri-component metal sulfide[210]. To compare the influence of sulfur vacancies, the as-prepared samples were calcined in O_2 gas to remove sulfur vacancies. In results, the photocatalytic NH_4^+ generation rates of $Mo_{0.1}Ni_{0.1}Cd_{0.8}S$ photocatalyst is 3.2 mg L^{-1} h^{-1} $gcat^{-1}$, which is 10-folds higher in comparison with the oxidized sulfur vacancies sample of $Mo_{0.1}Ni_{0.1}Cd_{0.8}SO$. Hu concluded that the sulfur vacancies not only act as chemical absorption sites but also capture photo-generated electrons, suppress charge recombination, and encourage interfacial charge transfer.

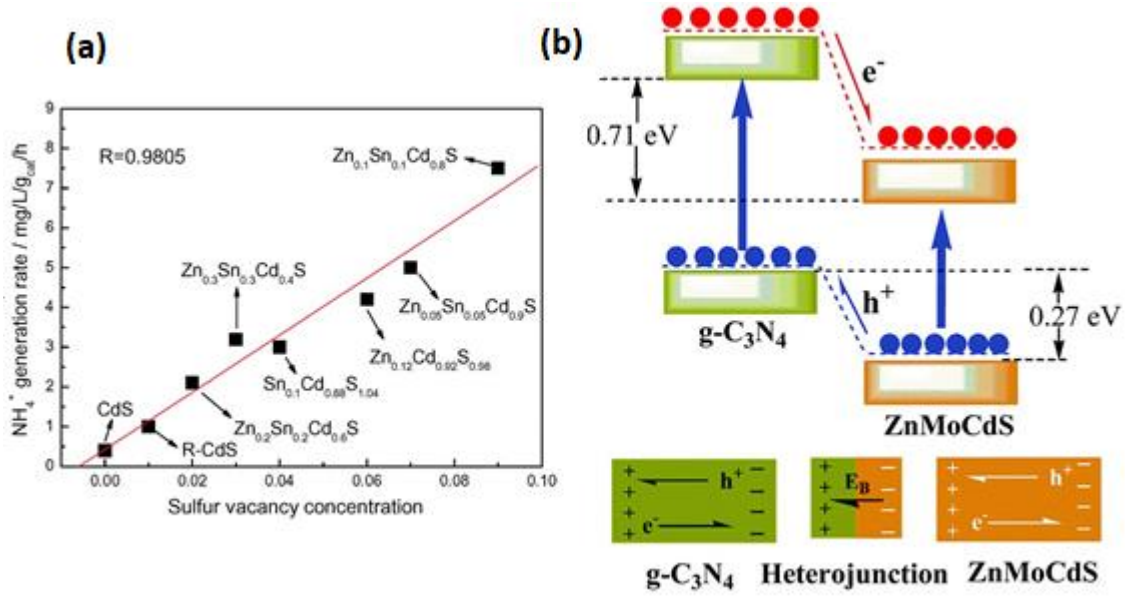

Figure 2.31: (a) Nitrogen photofixation performance of the as-prepared catalysts as a function of the sulfur vacancies concentration[200]; (b) The schematic of electron-hole separation and transport at the g-C_3N_4/ZnMoCdS heterojunction interface. [197]

A strategy of coupling carbon nitride with sulfur vacancies doped metal sulfide was applied for the reduction of N_2 under visible light. At the same time, two similar heterojunction system of g-C_3N_4/ZnSnCdS and g-C_3N_4/ZnMoCdS were assembled by Cao *et al*[199, 201]. In general, the photo-induced electrons will be excited and migrated from g-C_3N_4 to the quaternary metal sulfide whereas the photo-generated holes are transferred in the reversed direction and consumed by hole scavenger. Additionally, the sulfur vacancies could trap immigrated electrons form g-C_3N_4 and intrinsic electrons in metal sulfide then transport immediately to activated N_2. The schematic of electron-hole separation and transportation is depicted in **Figure 2.31(b)**. As the photoinduced electrons and holes are spatially separated, the charge recombination will be drastically inhibited, which is of highly beneficial for enhancing the photocatalytic activity. Under visible light irradiation, the highest NH_4^+ evolution rates of g-C_3N_4/ZnSnCdS and g-C_3N_4/ZnMoCdS are 7.5 and 3.5 $mg.L^{-1}.h^{-1}.g^{-1}$, respectively, which is 33.3 and 13.5 times higher compared to those of individual g-C_3N_4.

Carbon vacancies

Apart from these typical vacancies, carbon vacancies (CVs) have been attracted certain interests. Recently, carbon vacancies and sulfur dopants have been introduced into graphic carbon nitride[211]. In this screening, the generated CVs not only induced more chemical adsorption sites but also trapped and transferred charge carriers to adsorbed nitrogen, hence, promoting photofixation efficiency (**Figure 2.32(a)**). Furthermore, DFT calculation predicts that the introduction of CVs onto MoC can prevent the accumulation of adsorbed H-atom, mitigating hydrogen evolution[212]. The diagram (**Figure 2.32(b)**) depicted that (110) MoC facet is highly active for HER since it is located at the top of the volcano curve. Oppositely, introducing carbon vacancies on (111) and (001) facets shifted its positions to the left or right bottom of the triangle. On the right side of the volcano curve, low stability of adsorbed H atom inhibits proton transfer and then limits the formation of hydrogen. On the left side, the HER yield is decreased due to the lack of the available H^+/H recombination sites when the adsorption energy of hydrogen increase. Despite engineered vacancies, manufactured defects in semiconductor materials by introducing heteroatoms as a dopant is also a reliable approach for photo(electro)catalytic ammonia synthesis. Since both dopant sites and vacancies have similar advantages in adsorption and activation of nitrogen as well as suppression of electron-hole recombination. It is possible to anticipate that synergistic effect by the combination of vacancy defects and dopant sites is beneficial for developing efficient nitrogen photofixation catalysts.

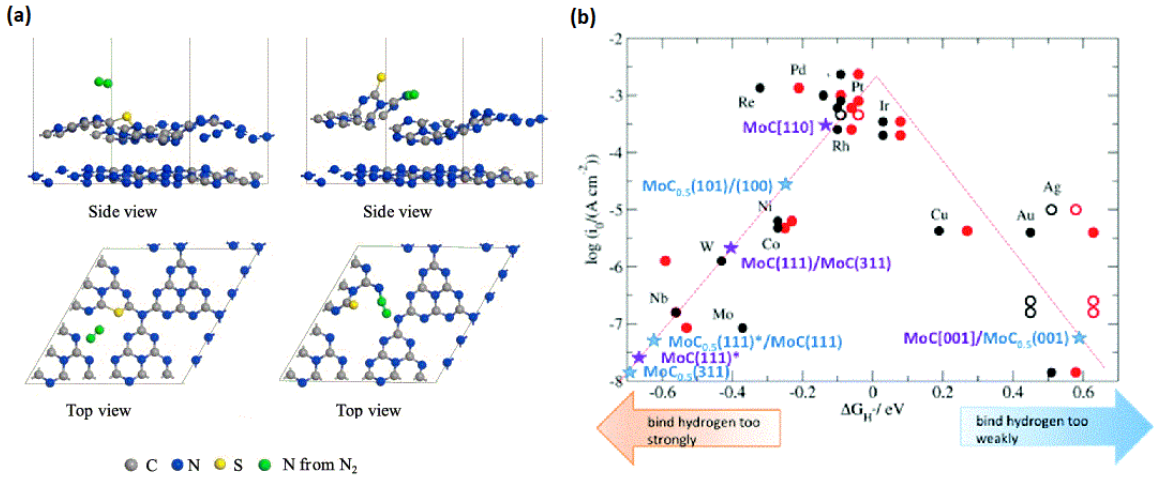

Figure 2.32: (a) Side views and top views of the optimized geometry of the optimal N_2 adsorption models on bulk S doped C_3N_4 (left) and CVs assisted S doped C_3N_4 (right)[160, 211];

(b) Experimentally measured exchange current, log(i_0) for hydrogen evolution over different metal surfaces plotted as a function of the DFT calculated hydrogen adsorption free energies for 0.25 mL coverage (red) and 1 mL coverage (black)[212]. Open circles correspond to single-crystal data.

2.3.3.3 Metal cocatalyst and plasmon enhancement

Metal cocatalyst

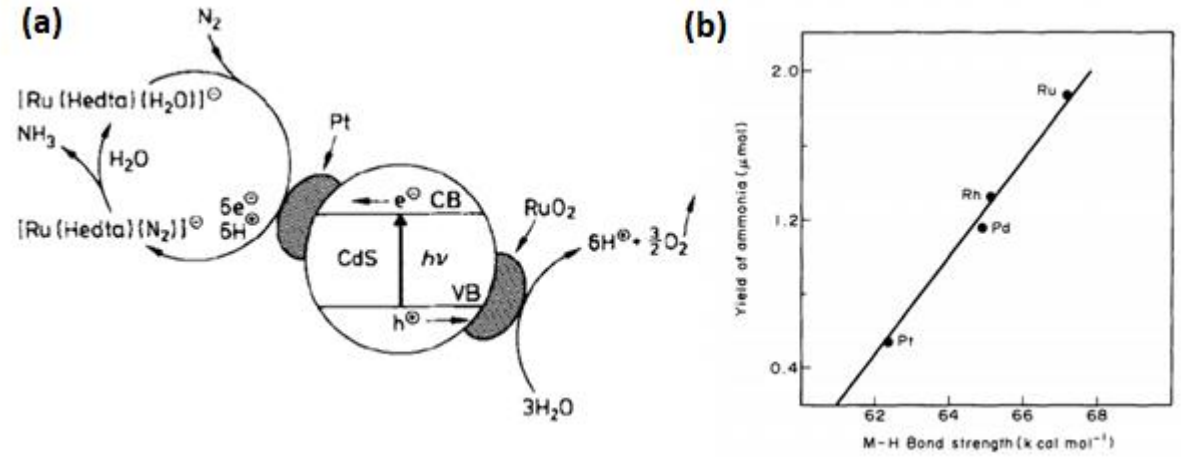

Figure 2.33: (a) The mechanism of photocatalytic N_2 fixation over CdS/Pt/RuO_2; [213] (b) M-H bond strength vs yield ammonia[169]

In addition to the introduction of interior active sites, transition metals can be employed as exterior active sites by loading on the semiconductor photocatalysts, namely cocatalyst. Cocatalysts play a critical role in photocatalysis. As electron acceptors, cocatalysts promote electron-hole separation and impede photogenerated charge carrier recombination. Among a variety of cocatalysts, platinum and ruthenium have been considered as the most effective cocatalysts, particularly in hydrogen evolution and CO_2 conversion. Inspired by prior research, Miyama engaged Pt loading TiO_2 and CdS for the improvement of N_2 photoreduction[214]. For both TiO_2 and CdS, the yield of ammonia was increased approximately 1.5 times after introducing noble metal cocatalyst. Several years later, Mirza's group applied both Pt and RuO_2 as a reduction and oxidation cocatalyst in CdS[213]. The Pt

particles in this system act as electron trapping centers which capture photoexcited electrons and perform reduction reaction. Whereas, the RuO_2 serves as a hole scavenger to consume generated hole, balancing electric charge. **Figure 2.33(a)** demonstrates the mechanism of photocatalytic ammonia evolution based on CdS/Pt/RuO_2 photocatalyst.

In 1996, Ranjit *et al* systematically investigated the impact on photocatalytic NH_3 evolution by the nature and amount of four noble metals decorated TiO_2[169]. It is worth noting that ammonia was not produced by using pure TiO_2 photocatalyst. However, the metallization of titania increases the ammonia generation rate. It was found that the production rate is depended on several factors. First, the noble metals form the ohmic contact with the semiconductor and serve as electron sinks where can easily accommodate the flow of electron transfer, suppressing electron-hole recombination. Secondly, the report supposed that the key role of the installed metal is to stabilize H_{ads} formed on the metal, thus enhancing the ammonia yield. **Figure 2.33(b)** illustrates the linear dependence between the Metal-H_{ads} bond strength and the yield of ammonia. This proposal is consistent with another work investigating Ru, Fe, and Os cocatalysts[215], where it was found that metal cocatalysts for NH_3 production needed to have a high over-potential for H_2 evolution; where the metals with high over-potentials for the hydrogen evolution reaction (Ru and Fe) having higher NH_3 activity than the metals with low hydrogen evolution reaction over-potential. Based on experimental data, Ranjit deduced that the catalytic activity of the nanocomposite photocatalyst is observed in the trend Ru > Rh > Pd > Pt. It is clearly seen that the trend is reversed in the hydrogen evolution reaction. Medford suggested that the role of the metal site is to minimize hydrogen evolution rather than being a cocatalyst for NH_3 synthesis[216].

Non-metal cocatalyst

Despite metal cocatalysts, non-metal materials should be concerned as a promising material for photofixation of nitrogen. An example of non-metal cocatalyst for photocatalytic NRR, black phosphorous (BP) decorated g-C_3N_4 nanosheets showed superior photoactivity under visible light irradiation[217]. Due to the formation of C-P chemical surface coordinating, electrons preferred locating on neighboring P of C-P bonds, hence, P atoms can serve as electron donors that donate photoexcited electrons to adsorbed N_2 on the surface of BP

(**Figure 2.34**). Additionally, BP supported graphitic carbon nitride exposed high stability without any significant degradation in photoactivity after five cycles.

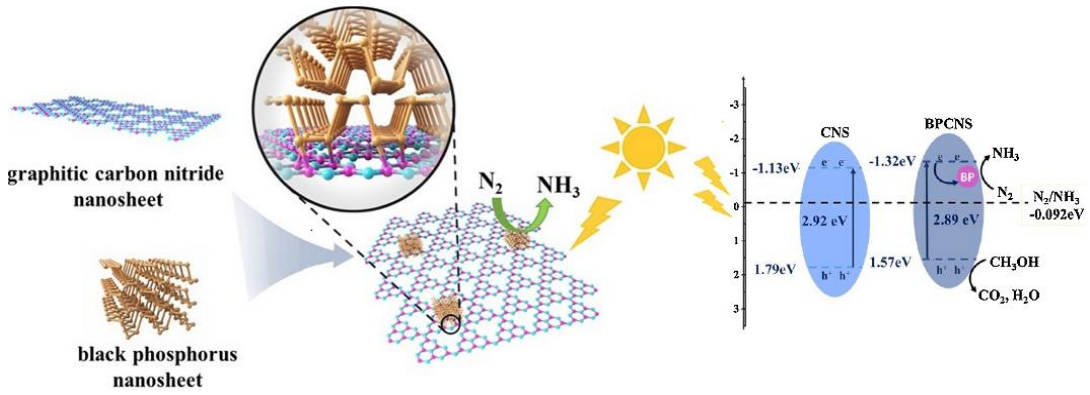

Figure 2.34: The possible photocatalytic nitrogen fixation mechanism over black phosphorus/carbon nitride nanosheets. [217]

Another suggestion, carbon quantum dots (CQDs) are known as excellent electron donors and acceptors for diverse applications[218]. The hybrid system of CQDs decorated with biological nitrogenase Azotobacter for nitrogen fixation has been investigated by Kang et al[219]. The result illustrated that the CQDs could exceptionally enhance the fixing activity of nitrogenase by 1.5-folds in comparison with free enzyme due to the acceleration of electron transfer among CDQs and nitrogenase (**Figure 2.35(a)**). However, to date, there is no publication has been conducted for the photocatalytic nitrogen fixation using CDQs. In addition, Li *et al* apparently proved the critical roles of carbon in weakening the N≡N triple bond[220]. The universality of surface carbon modification over different materials was examined. The results indicated that photoactivity of NH_3 production of P25, TiO_2, BiOBr, and $WO_3.H_2O$ catalysts are considerably enhanced. The surface carbon greatly promoted charge-separation and transportation in semiconductors, which is confirmed by small semi-circles in the Nyquist plots and the much higher photocurrent density. Inspired by the research of Kang's group, therefore, CDQs should be considered as a potential cocatalyst, combining with different photo(electro)catalyst for ammonia synthesis. Another type of carbonaceous materials, Mxene, consisting of transition metals such as Mo, W, Ti, and C have been explored their possibility for the application of nitrogen fixation by DFT calculation[221]. Among them, Mo_2C and W_2C showed the best catalytic activity due to the

large electron transfer during the step of hydrogenation, suggesting that the beneficial design of Mxene cocatalysts has a significant meaning for synthesizing the novel catalysts for nitrogen reduction. Over again, Benjamin and his group recently combined theoretical DFT calculation and preliminary experimental results to support their hypothesis which surface-bound carbon radicals (C*) and other carbon-based sites selectively assist the reduction of nitrogen at ambient conditions (**Figure 2.35(b)**)[222]. Overall, there is no doubt that the cooperation of cocatalyst enables the promotion of photo(electro)catalytic nitrogen fixation. In addition, it is possible to believe that the construction of reduction cocatalysts containing carbon-based active sites revealed a new strategy for efficient photo(electro)catalysts which not only provide adsorption and activation sites but also promote electron-hole separation, avoiding the limitation of defects on semiconductors.

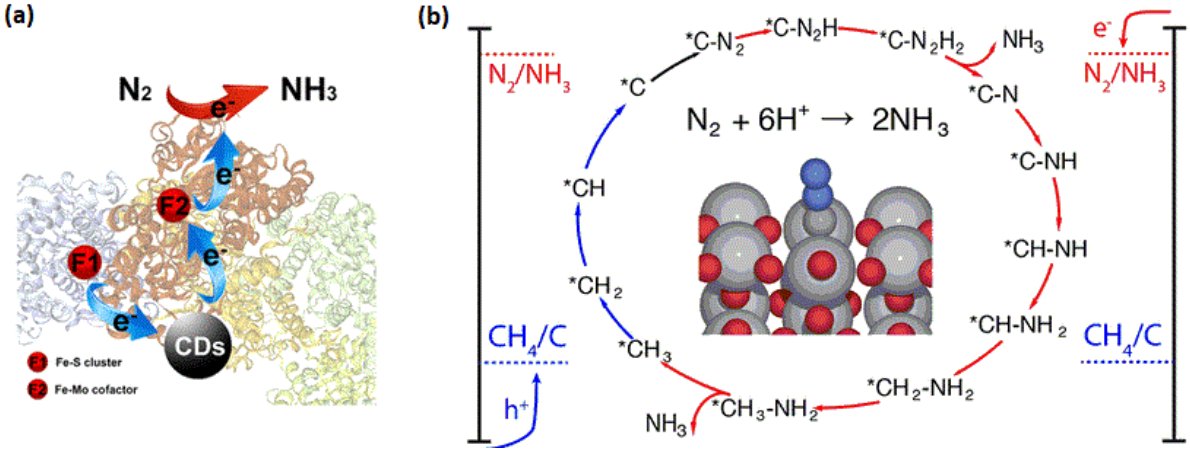

Figure 2.35: (a) Schematic diagram of electron transfer pathways for nitrogenase-CD hybrids[219]; (b) Thermodynamic cycle of N_2 reduction on a carbon substitution at bridging oxygen. [222]

Plasmon enhancement

A fundamentally different approach for loading transition metal supported fixing nitrogen has been demonstrated to enhance light absorption through the surface plasmonic enhancement[43, 47, 148-149, 223]. To increase the NH_3 production rate by harnessing the localized surface plasmon resonance, most recent studies have focused on using gold nanoparticles as a plasmonic structure. Owing to high light-harvesting properties, gold in a nanoparticle can

absorb visible light and induce surface plasmon effect, which can inject hot electrons into the semiconductor conduction band. Oshikiri and his partner assembled a photoelectrode, with Au nanoparticles and a Ru cocatalyst co-loaded on Nb-$SrTiO_3$[149]. The hypothesized mechanism was proposed that the photoexcited hot electron is transferred to $SrTiO_3$ semiconductor and continuously injected into Ru cocatalyst. At the Ru surface, nitrogen and proton are reduced to ammonia. In contrast, the generated holes localized near the Au/Nb-$SrTiO_3$/water interface and immediately oxidize hydroxyl ions and ethanol (**Figure 2.36(a)**). The ammonia production was observed at long wavelengths up to 800 nm, implying plasmon-induced charge separation promoted nitrogen reduction in the cathode and oxidation in the anodic side. However, Ru cocatalyst not only accelerates N_2 reduction but also for H_2 evolution because of stable absorption of H_2 onto a Ru surface. Later, a replacement of Ru cocatalyst with Zr/ZrO_x cocatalyst was reported by the same group in 2016[148]. In the Au/Nb-$SrTiO_3$/Zr/ZrO_x system, the NH_3 generation rate is prominently higher than that of the Ru-$SrTiO_3$ system due to Zr prefers binding N* adatoms rather than H* adatoms. DFT calculation proved that the Zr is effective at limiting the hydrogen evolution reaction. An energy diagram of this system is provided in **Figure 2.36**(b).

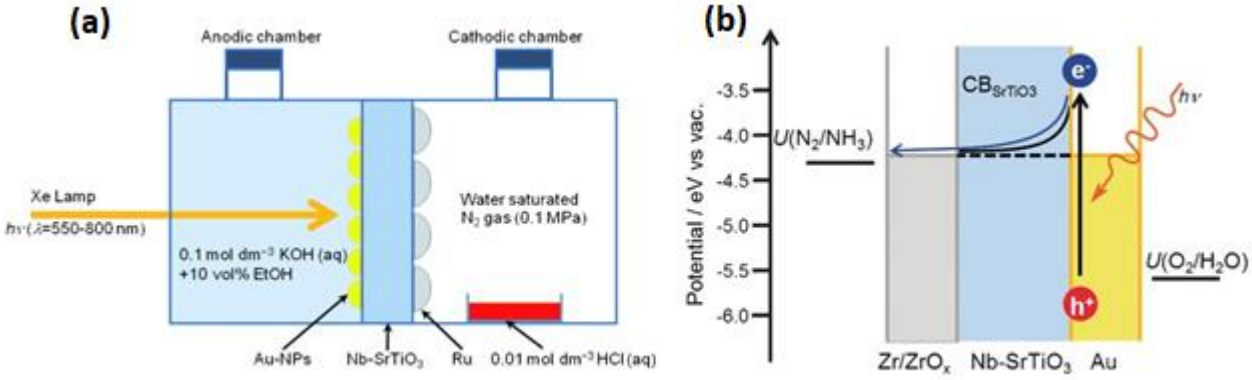

Figure 2.36: (a) A schematic illustration of the NH_3 synthesis device using an Nb-$SrTiO_3$ photoelectrode loaded with Au nanoparticles;[149] (b) Energy level diagram of the plasmon-induced NH_3 synthesis device. [148]

Furthermore, Zheng, Terazono, and Tanuma attempted to synthesize ammonia at room temperature using an Os-Au nanocomposite catalyst which was prepared by directly sputtered Os onto Au layer[43]. The generation of ammonia was observed under visible light irradiation between 550 and 650 nm, corresponding to the conversion rate of 0.003% at 550 nm. Originally, neither pure Au nor Os nanoparticle showed photoactivity in ammonia synthesis. Although pure Au nanoparticles exhibit the LSPR effect of photon energy absorption to generate electron but are unable to encourage the N_2 reduction reaction. Whereas, Os nanoparticle is active for N_2 fixation but inactive in the visible light region. Therefore, the assembly of Au-Os nanocomposite motivates the photon energy resonance transfer from Au nanoparticles to the Os layer (**Figure 2.37(a)**), enhancing NH_3 yield. By contrast, for the first time, Ali and his colleagues hypothesized that gold nanoparticles can serve as reduction cocatalyst[47]. In his work, solar-driven nanostructured plasmon-enhanced black silicon photoelectrode produces an ammonia yield of 320 mg m^{-2} in a day. The variety of controlled experiment confirms the roles of individual layers, which is described in **Figure 2.37(b)**. Gold nanoparticles loaded black silicon (bSi) provide reduction active sites, receiving transferred electron form photon absorber bSi. While Cr layer acts as a sacrificial hole sink where scavenge photogenerated holes by the oxidation of sulfite ions. In results, the NH_3 production of the GNP/bSi/Cr cell increases to around two-folds that of the GNP/bSi and eight-folds that of pure bSi.

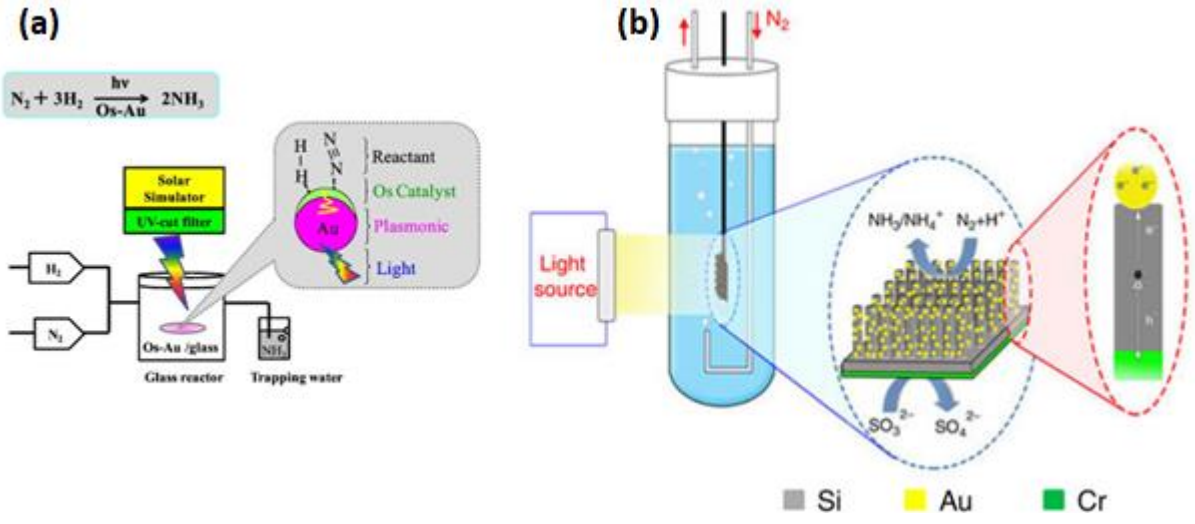

Figure 2.37: (a) A schematic illustration of the mechanism of Au-Os nanocomposite for NH_3 photofixation;[43] (b) Schematic diagram of photochemical nitrogen reduction of Au/bSi/Cr. [47]

Besides Au NPs, the LSPR effect can be also performed by other metal-based materials as Ag, Cu, TiN, and Ru. For example, Zhang and his coworkers developed a photo-thermocatalytic system using multiple functional Ru nanoparticles as a plasmonic cocatalyst and actives site for adsorbed N_2 molecules[224]. Even the reaction was carried out at room temperature, the localized temperature of the catalyst reached around 360 ^oC by its plasmonic behavior, initiating the Haber-Bosch reaction. The OVs on $TiO_{2-x}H_x$ enriched the electron density around the Ru nanoparticles. Moreover, $TiO_{2-x}H_x$ surface accepted the implanted H atoms from the Ru catalyst and donated back to Ru for the protonation of adsorbed N_2. This mechanism prevents the poisoning of Ru surface by H_2 gas during thermal synthesis, enables efficient fixing nitrogen to ammonia.

2.3.3.4 Semiconductor heterojunction structures

Heterojunction systems

Most recent heterojunction photo(electro)catalysts toward nitrogen reduction focused on the type II system. For example, Shaozheng et al have demonstrated that the construction of g-C_3N_4 with ternary metal sulfide can significantly improve the nitrogen photofixation efficiency compared to bare g-C_3N_4 or ternary metal sulfide. With the optimal mass percentage of 80% ZnMoCdS[199, 201], the heterojunction system performed the highest nitrogen fixation ability. The great enhancement in photocatalytic activity is contributed by a huge number of sulfur vacancies which not only act as an active center but also promote interfacial charge transfer to dinitrogen. Also, the evidence by UV-Vis, XPS, and EIS results indicated that there is an existence of strong electronic coupling, promoting the photogenerated electron-hole separation among the two semiconductors. The main driving force for this efficient separation and transfer causes by the potential difference between two semiconductors. The theoretical explanation proposed the charge transfer mechanism following type II heterojunction. Under light irradiation, the photoexcited electrons jump from the CB of g-C_3N_4 to ZnMoCdS while the photogenerated holes transfer from VB of ternary metal sulfide to g-C_3N_4. It is worth noting that interfacial contact is one of the most

important factors determining the photoactivity of the heterojunction system. Insufficient interfacial contact between semiconductors leads to ineffective performance. Therefore, a strategy of electrostatic self-assembly has been applied for engineering reduced graphene oxide (rGO) and graphitic carbon nitride to form heterojunction[225]. By the protonation process, the negative surface of g-C_3N_4 has changed to a positive charged surface, which is capable to stack with the oxygen-containing group on the surface of rGO, forming π-π stacking interaction effectively. Consequently, the protonated g-C_3N_4/rGO showed the highest photofixation ability among pure g-C_3N_4, protonated g-C_3N_4, and physical mixture of g-C_3N_4/rGO which is 42.4, 8.3, and 3.7 times higher, respectively. It can be interpreted that the strong interaction caused by the electrostatic attractive forces exists between protonated g-C_3N_4 and rGO, leading to better charge separation and suppress charge recombination. Another example, thermal delivered TiO_2 form Mxene coupled with carbon nitride nanosheets, which is systematically studied by Liu and coworkers[26]. This heterojunction exhibits a structural feature of abundant surface defects, excellent electron transportation ability, and strong nitrogen activation performance. It is also demonstrated that the *in situ* growth strengthens the intimate interfacial contact between TiO_2@C and g-C_3N_4, thus exhibits superior performance for fixing nitrogen to ammonia with the production rate of 250.6 $\mu mol.g^{-1}.h^{-1}$.

Z-Scheme system

A typical example of Z-scheme heterojunction in the photoreduction of nitrogen is Ga_2O_3/graphitic carbon nitride with the functional group of 3,4-dihydroxybenzaldehyde (Ga_2O_3-DBD/g-C_3N_4), acting as electron mediators[226] (**Figure 2.38**). The key role of the aromatic ring is the bridge enhancing the interaction between NH_2- group in g-C_3N_4 and Ga_2O_3 particle and led to the formation of a well-developed combined interface, which greatly promoted the transfer of charge carriers. As a result, the photocatalytic ammonia production rate was 3.37 times faster than that of pure g-C_3N_4. The author proposed a possible mechanism that electrons of Ga_2O_3 recombine with holes of g-C_3N_4 via aromatic functional groups, whereas a hole on the VB of Ga_2O_3 directly oxidizes OH^- to OH radical. Similarly, electrons in the CB of carbon nitride reduce O_2 to H_2O_2, which continuously produces OH radical. These OH radicals immediately reduce methanol to CO_2^- radicals, which facilitates

N_2 reduction to NH_3. Although there are still several minor difficulties to achieve perfect heterojunction photocatalyst systems, it is clearly proved that coupling heterojunction semiconductors can significantly improve photocatalytic performance, particularly in nitrogen fixation reactions.

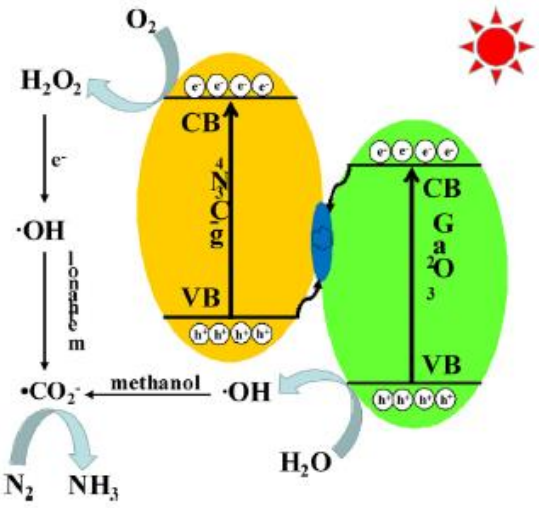

Figure 2.38: Photocatalytic nitrogen fixation mechanism over Z-scheme Ga_2O_3-DBD/g-C_3N_4. All panels reproduced with permission. [226]

2.4 Summary and outlook

Utilization of solar light for energy production and environmental protection is one of the most critical challenges in the near future for researchers and scientists. Photocatalysts based on semiconductors are an effective route to employ the plentiful energy from the sun. Unfortunately, the industrial application of this strategy is still limited by ineffective light absorption and fast electron-hole recombination processes of photocatalyst semiconductors. Thus, the development of active photocatalysts is required. A variety of methods have been introduced to improve the photocatalytic efficiency such as combining multicomponent semiconductors, metal or non-metal doping, usage of cocatalysts, and plasmon-enhancement. These methods are to enhance the ability of absorbing visible light, to narrow the bandgap energy of semiconductor, to increase the charge separation, to decrease charge-

recombination, and to supply more active sites on the surface of the nanocomposite semiconductors.

Graphitic carbon nitride and indium-based materials have been considered as the most promising photocatalysts toward hydrogen generation due to its small bandgap energy. Combining these nano-sized semiconductors with other appropriate semiconductors produce nanocomposite semiconductor heterojunctions that inherit superior properties than pristine semiconducting materials, resulting in an enhanced photocatalytic activity for H_2 production under visible light illumination. Although integrated multicomponent semiconductors have shown improved photoactivity, the overall water splitting reaction efficiency is still very low. There are many related factors such as the interface between semiconductors, morphology, semiconductor component, which directly affect the catalytic activity of photocatalysts. All of these factors need to be investigated carefully.

For photo(electro)catalytic nitrogen fixation, the unavoidable challenges of N_2 adsorption and activation along with NRR selectivity must be addressed. The key solution for these issues is creating chemical bond channels between nitrogen molecules and the surface of the catalysts. The introduction of metal dopant sites and vacancies not only provide more adsorption centers for absorbed nitrogen but also weaken and N-N triple bond by electron back-donation to antibonding orbitals of nitrogen. Besides, vacancies and dopant sites also promote photoexcited charge separation and inhibit their recombination. On the other hand, engineered defects are highly unstable. Therefore, more efforts should be devoted to designing sustainable and substantial surface defects. Another approach for long-term stable catalysts is the utilization of cocatalysts. However, due to the competition between the 2-electron transfer of HER and 6-electron transfer of NRR, the best cocatalysts for nitrogen fixation are expected to use early transition metal and non-metal elements rather than noble metals since the latter ones strongly bind with adsorbed protons compared to dinitrogen molecules, which facilitates hydrogen production. It is also worth noting that the construction of defective nanostructured cocatalysts and the cooperation of engineered heterojunctions could help to enhance the ammonia yield. Otherwise, photocatalysis based on semiconductors for nitrogen fixation is still restricted by ineffective light absorption. Noble metals such as Au, Ag nanoparticles induce localized surface plasmon resonance (LSPR

effect), which promotes visible light absorption. A combination of plasmon-enhancement and surface engineered defects is a promising strategy for photocatalytic nitrogen fixation.

The next chapters (4-7) will provide new approaches to synthesize efficient photo(electro)catalyst which could have excellent photocatalytic activity toward HER and NNR, owing to a strong absorption ability, high electron-hole separation, and abundant surface active sites.

Chapter 3 Characterization techniques

This chapter aims to discuss the basic principles of various advanced characterization techniques employed to study the physical and chemical characteristics of the various as-synthesized materials reported in the thesis.

3.1 Electron microscopy

Electron microscopy (EM) is an extremely powerful technique to capture the morphology of micro-nanoscale materials at a superior resolution and magnification as compared to optical microscopy. This technique not only provides the size and shape of materials but also their chemical composition through the energy-dispersive X-ray spectroscopy (EDS) technique. Basically, in electron microscopy, a high-intensity electron beam will be applied to examine the solid specimens of a few hundred nanometers scale, as shown in **Figure 3.1**. The information about the samples (such as size, shape, surface morphology, composition analysis) is derived by electron scattering when the high energetic beam interacts with the sample. There are two main types of scattering modes: elastic and inelastic. In the case of elastic scattering, the collisions between the incident electrons and target have total conservation of kinetic energy, whereas the kinetic energy is converted into other forms such as heat, waves, and sound in inelastic mode. Depending on the type of scattering process and state of the samples, the diffraction pattern, spot pattern, Kikuchi pattern, and ring pattern can be produced. The EM characterization could provide three main categories of analysis: (1) transmission electron microscope (TEM), (2) scanning electron microscope, and (3) energy-dispersive X-ray spectroscopy (EDS). The operation principles of these techniques are presented in the following sessions.

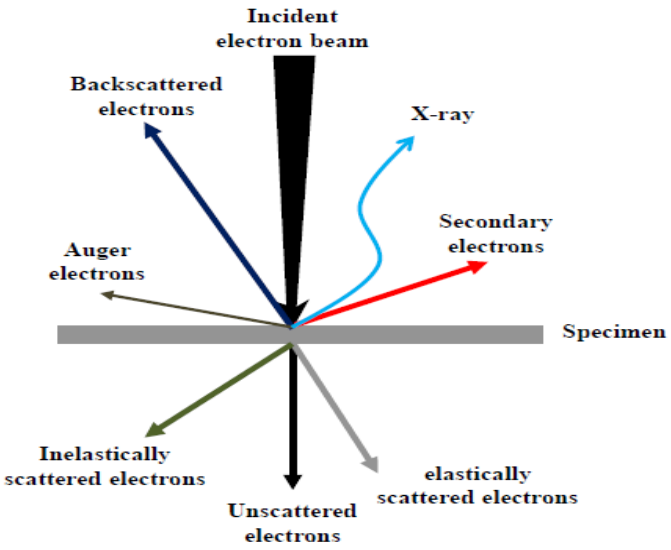

Figure 3.1: Scheme of the interaction between an electron beam and a solid matter (specimen).

3.1.1 Transmission electron microscope

Transmission electron microscopy (TEM) is a unique technique providing high-resolution images of an object when an electron beam interacts and passes through the specimen. The electrons emitted by a source are focused and magnified by a system of magnetic lenses. **Figure 3.2** illustrates the configuration of a TEM instrument. First, the high voltage gun produces a primary electron beam of high intensity. Then the electron beam passes through a series of condenser lenses before hitting the sample. It is worth noting that the main function of the condenser lenses is to control the diameter and the convergence angle of the beam. After traveling through the solid matter, the transmitted electrons create a 2D black-white image of the sample.

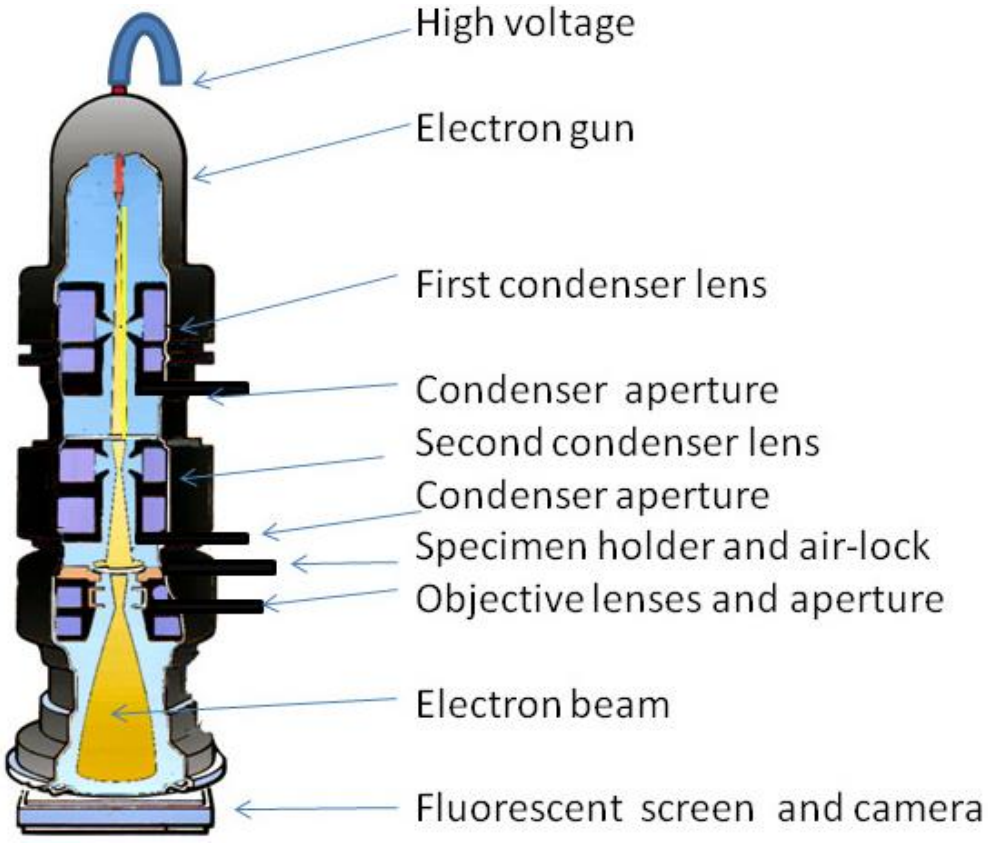

Figure 3.2: Structure of a transmission electron microscope and the optical path.

TEMs are capable of imaging at a significantly higher resolution than light microscopes, owing to the small de Broglie wavelength of electrons. This enables the user of the instrument to examine fine details as small as a single column of atoms, which is a thousand times smaller than the smallest resolvable object in optical microscopy. TEM has become a major analysis method in a range of scientific fields, in both physical and biological sciences. In addition, TEMs also find applications in cancer research, virology, materials science as well as pollution, nanotechnology, and semiconductor research.

At smaller magnifications, contrast TEM images can be formed due to the absorption of electrons in the sample, which is due to the thickness and composition of the sample. At higher magnifications, the complex wave interactions modulate the intensity of the image, requiring expert analysis of observed images. The use of alternate modes allows the TEM to observe the modulations in chemical identity, crystal orientation, electronic structure, and sample-induced electron phase shift as well as the regular absorption-based imaging.

3.1.2 Scanning electron microscope

The Scanning electron microscope (SEM)is a technique that examines the microstructure of the solid matter through scanning its surface with high resolution and great depth. The SEM allows us to observe the morphology of the specimens at nano- and microscale. It should be noted that the ability to capture the 3D structure of the sample is the key feature of the SEM method, which cannot be obtained by TEM or other characterizations. Additionally, SEM could be used for confirming the chemical components of a sample by an X-ray energy dispersive spectrometer (EDS). A basic SEM system is composed of two main parts: an electron gun and a series of electromagnetic optics. Similar to TEM operation, the electron gun generates an electron beam while the other lenses and apertures condense the beam to a fine probe for surface scanning. A detector collected the emitted electrons that come from the sample, which are subsequently converted into images. Hence, the quality of produced SEM images is depended on the acquisition signal generated by the interaction of the electron beam and the sample.

3.1.3 Energy-dispersive X-ray spectroscopy

The energy-dispersive X-ray spectroscopy (EDS, EDX, or XEDS) is an analytical technique used for the elemental analysis or chemical composition characterization of a sample. It relies on the interaction of an X-ray and a sample. Its characterization capabilities are due to the fundamental principle that each element has a unique atomic structure allowing a unique set of peaks on its X-ray spectrum. To stimulate the emission of characteristic X-rays from a specimen, a high-energy beam of charged particles such as electrons or protons, or a beam of X-rays, is focused on the sample being studied. At rest, an atom within the sample contains ground state (or unexcited) electrons in discrete energy levels or electron shells bound to the nucleus. The incident beam may excite an electron in an inner shell, ejecting it from the shell while creating an electron-hole where the electron existed. An electron from an outer, higher-energy shell then fills the hole, and the difference in energy between the higher-energy shell and the lower energy shell may be released in the form of an X-ray. The number and energy of the X-rays emitted from a specimen can be measured by an energy-dispersive spectrometer. As the energy of the X-rays is characteristic of the difference in energy between the two shells, and of the atomic structure of the element from which they were emitted, this allows the elemental composition of the specimen to be measured. **Figure 3.3** demonstrates the principle of EDS.

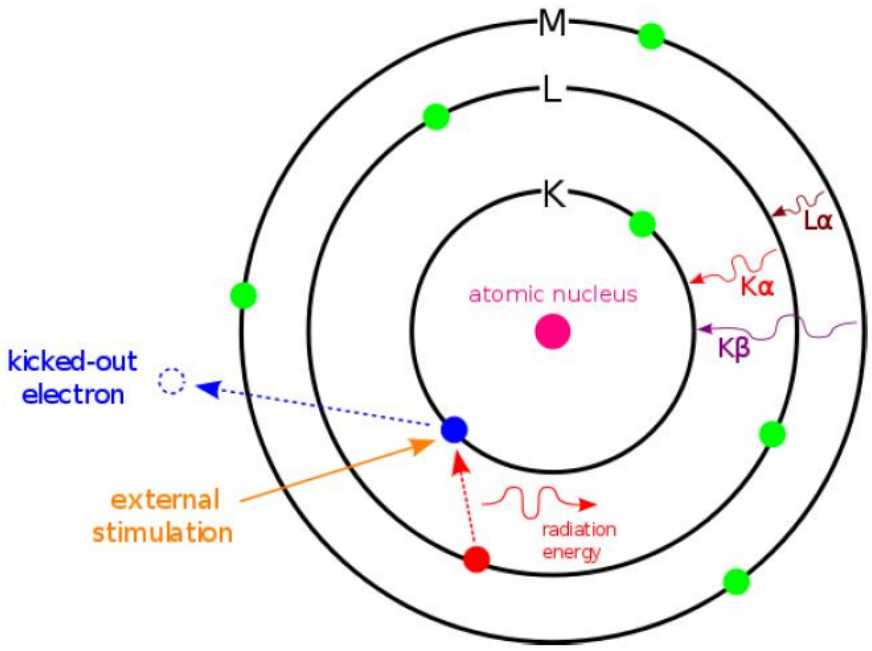

Figure 3.3: Principle of energy-dispersive X-ray spectroscopy with stimulation.

3.2 X-ray diffraction

X-ray diffraction (XRD) is one of the most widely used techniques to characterize the crystalline nature and structural composition of matter using mathematical models. XRD utilizes targeted X-ray beams to hit the matter and generate a diffraction pattern[227]. Data collected using this method undergoes a systematic analytical process that employs mathematical models and computer algorithms to obtain the final 3D atom model of a matter. XRD analysis is applied to identify the composition and chemical bonds between atoms of crystal, liquid, powder, or amorphous samples.

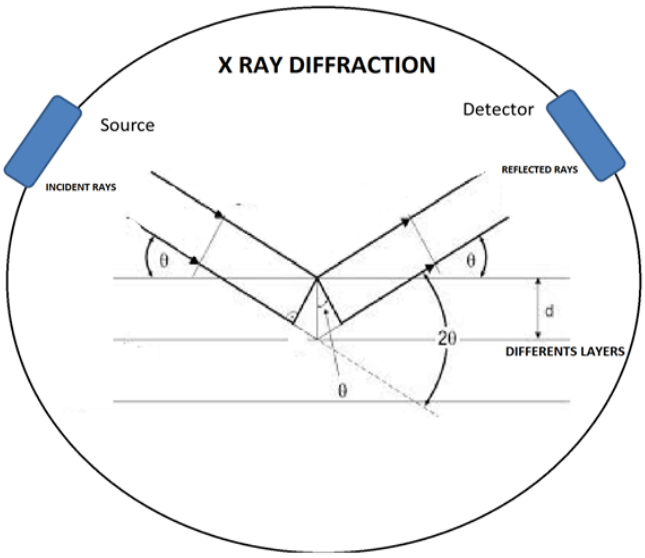

Figure 3.4: Schematic diagram of the technique of X-ray diffraction[227]

As depicted in **Figure 3.4**, the fundamental principle of X-ray diffraction is based on constructive interference of monochromatic X-rays and a crystalline sample. The X-rays are generated by a cathode ray tube, filtered to produce monochromatic radiation, and irradiated directly towards the sample. The interaction of the incident rays with the sample produces constructive interference (and a diffracted ray), which results in the diffraction patterns in the XRD spectrum when the distance between the lattice planes satisfy Bragg's Law (**Equation 3.1**)

$$n\lambda = 2d \sin\theta \qquad (\mathbf{3.1})$$

Where, n is the order of reflection and equal to the number of wavelengths in the path difference between diffracted X-rays from adjacent crystal planes, λ is the wavelength of X-ray, d is lattice plane distance, and θ is the angle of incidence relative to the crystal lattice plane.

Besides the crystalline phases, the crystalline size can also be calculated from the Debye-Scherrer's equation as given in **Equation 3.2**

$$D = \frac{K\lambda}{\beta cos\theta} \qquad \textbf{(3.2)}$$

Where D is the measured size of the dimension of the particle, λ is the wavelength of X-ray, K is Scherrer's constant, β is the full width of a diffraction peak at half maximum in radians and θ is the angle of incidence.

3.3 X-ray photoelectron spectroscopy

X-ray photoelectron spectroscopy (XPS), also known as electron spectroscopy, is a highly sensitive analytical technique for measuring the composition, chemical state, and binding state of the elements existed on the surface of materials. It is worth reminding that XPS can detect all of the elements except hydrogen and helium. In a typical XPS experiment, an X-ray of high energy photons is irradiated to a sample, which results in the emission of electrons. These electrons are identified as photoelectron, which is broken away from the nuclear attraction force at the core level, escaping from the surface into the surrounding vacuum. An electron analyzer collected and measure the kinetic energy of these photo-ejected electrons. Then, the signals of the photoelectron versus binding energy are displayed in the XPS spectrum. Each characteristic peak corresponds to a specific element. **Figure 3.5** demonstrates the scheme of the photoemission process in XPS. In addition to identifying elements in the solid matter, the intensity of the peaks can also tell the composition of each compound is in the sample.

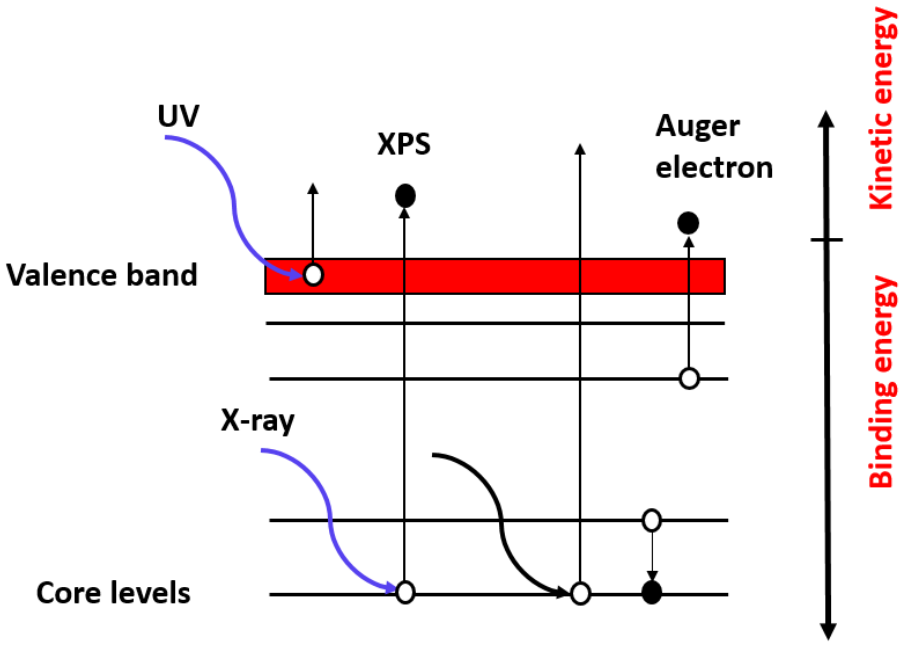

Figure 39.5: Schematic illustration of the photoemission process.

The binding energy of the photo-ejected electron could be calculated via the following equation:

$$E_B = h\nu - E_K - \phi - \delta E \qquad (3.3)$$

In which E_B is the binding energy of the photoelectron with respect to the Fermi level of the sample, h is Planck's constant, ν is the frequency of the exciting radiation, E_K is the kinetic energy of the photoelectron, ϕ is the work function of XPS spectrometer and δE is the electrostatic charging of the specimens

In **Equation 3.3**, the binding energy of photoelectrons can be easily calculated because the other terms (hν, E_K, ϕ) are known. The presence of term δE in the equation is due to the electrostatic charge of the samples, which slightly reduces the binding energy of the photoelectrons (0-3 eV), resulting in peak shifts on a binding energy scale. In general, the decrease in the oxidation state causes the binding energy to decrease. Hence, a standard peak at a fixed position should be chosen as a reference peak for the calibration of the whole spectrum. In the next chapters (4-7), the carbon peak C_{1s} (binding energy 284.5-285 eV) is employed to correct other peaks.

3.4 Fourier Transform Infrared Spectroscopy

Fourier Transform Infrared Spectroscopy (FT-IR) is a useful method to identify the organic functional groups present in materials. The fundamental principle of FT-IR is based on the absorption of infrared radiation by the sample that excites a molecule into a higher vibrational movement. It is worth noting that the absorbed wavelength by a particular molecule corresponds to the energy difference between the rest and the excited vibration state. Thus, each molecular structure exhibits the vibrations at certain wavenumber, which can be defined as the characteristic vibrations. The appearance of a specific vibration mode in an FT-IR spectrum can be used to determine the presence of the corresponding chemical structure on the investigated sample. Generally, an FT-IR spectrum is recorded between 400 and 4000 cm^{-1}.

There are two primary categories of vibration, including stretching (symmetric and asymmetric) and bending (scissoring, rocking, wagging, and twisting), which are classified based on the changes of bond length or bond angle. The strong vibrations usually appear at a higher wavenumber of the infrared radiation as compared to the bending mode. Each vibration mode has its natural frequency of motion. The characteristic frequencies of these vibrations are strongly affected by several factors such as the mass of the constituent atoms, the shape of the molecule, the stiffness of the bonds, and the periods of the associated vibration coupling.

3.5 Ultraviolet-Visible spectroscopy

The Ultraviolet-Visible (UV-Vis) spectroscopy is one of the most popular techniques used to examine the optical properties of a solid or compounds in a solution. It measures the absorbance of light energy or electromagnetic radiation of the material. The Beer-Lambert Law is the principle behind the absorbance spectroscopy, as given in Equation 3.4.

$$A = \varepsilon bc = \text{Log}\,(I_o/I) \qquad \textbf{(3.4)}$$

Where A is the absorbance, ε is the molar absorptivity of the compound, b is the path length of the cuvette or sample holder, c is the concentration of the solution I_0 is the intensity of the monochromatic light entering the sample, I is the intensity of the light transmitted through the sample.

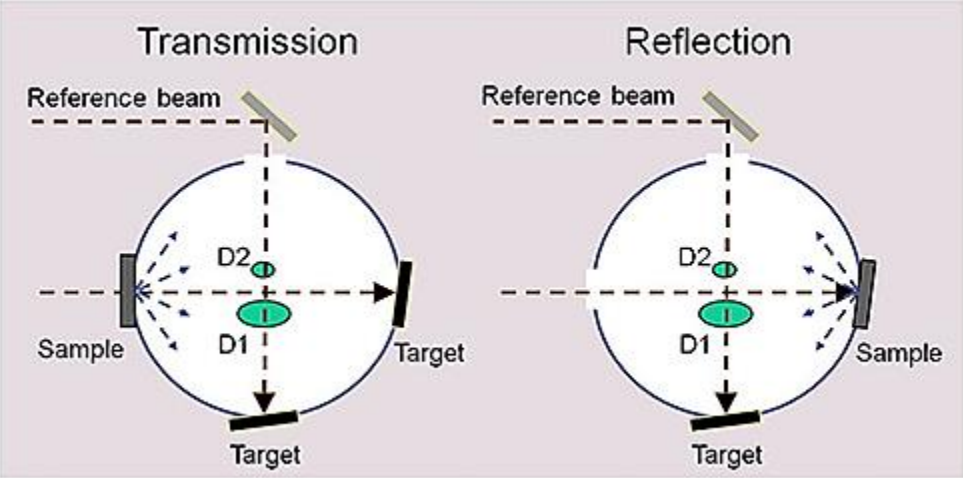

Figure 3.5: (Left) a schematic of a transmission UV-vis measurement, (Right) a schematic of a diffuse reflectance UV-vis measurement.

The UV-vis absorbance can be categorized into two groups: transmission and diffuse reflectance spectroscopies. Transmission UV-vis spectroscopy can be used for a sample with sufficient transparency that permits a significant amount of photons to pass through the sample. Typically, the irradiated light transmits through the sample and is being collected by a detector, as shown in **Figure 3.6** (left)**.** The difference between the transmitted light from a reference and an examined sample is recorded in the spectrum. It allows us to evaluate the absorption properties and measure the concentration of solid and liquid samples, respectively. Thus, this instrumental technique is appropriate for analyzing organic dyes, metal, or semiconductor nanoparticles highly dispersed in a solution.

The UV-Vis diffuse reflectance spectroscopy (DRS) is usually applied for opaque objects. As a consequence, the illumination of light beams on the sample results in light reflection in all directions. An integrating sphere has a responsibility to collect this reflected light for further analysis with a detector (**Figure 3.6**(right)). In this thesis, the diffuse reflectance UV-vis absorbance spectroscopy was employed to study the light absorption ability of semiconductor-based photocatalyst. Moreover, the transmission UV-vis spectroscopy was also used for the detection of ammonia via the indophenol blue method.

3.6 Nitrogen physisorption method

The nitrogen physisorption is a unique technique used to measure the surface area, pore size, pore size distribution, and porosity of materials. In this method, N_2 adsorption and desorption on the surface of materials are measured at liquid nitrogen temperature (77 K) and the different partial pressure of nitrogen. The obtained physisorption isotherm is known as a plot representing the relationship of the volume adsorbed/desorbed nitrogen and relative pressure at a constant temperature. The porosity of materials determines the shape of the isotherm.

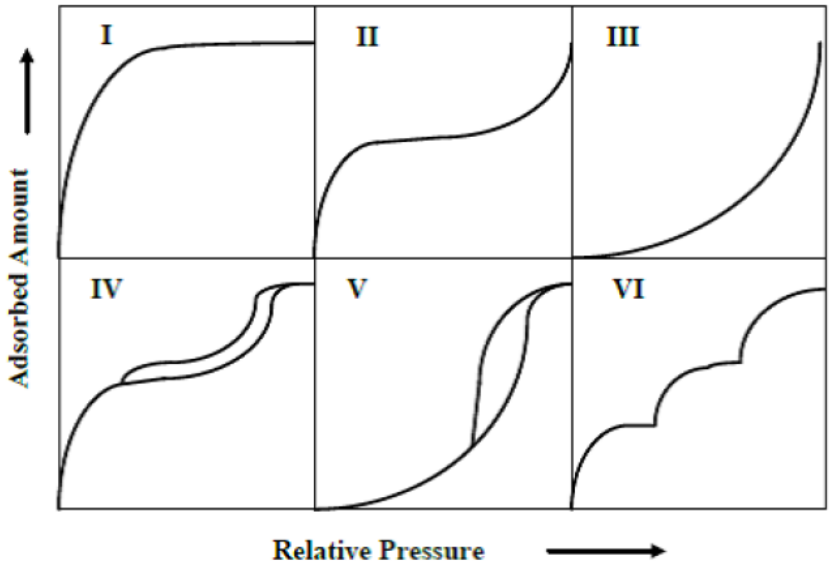

Figure 3.6: Six types of physisorption isotherms

According to the International Union of Pure and Applied Chemistry (IUPAC), the sorption isotherm can be classified into six types (labeled I through VI), as depicted in **Figure 3.6**. Type I isotherms are characteristic of microporous materials that have a relatively small external surface. In this type, the amount of absorbed nitrogen rapidly rises and reaches a limiting value at low pressure (P/P_o) due to monolayer adsorption proceed. The reversible Type II and III can be ascribed to nonporous or macroporous solid materials. These types are the characteristics of the multilayer adsorption. Type IV and V represent the mesoporous materials with multilayer adsorption consisting of capillary condensation. In the case of type VII isotherm, stepwise multilayer adsorption indicates a uniform nonporous surface.

By now, the Brunauer-Emmett-Teller (BET) theory is the most common method to calculate the specific surface area of the porous materials. The BET equation is always given in the form:

$$\frac{P/P_o}{n(1-\frac{P}{P_0})} = \frac{1}{n_m c} + \frac{c-1}{n_m c} \times \frac{P}{P_o} \qquad (3.5)$$

Where n is the amount of adsorbed nitrogen at relative pressure P/P_o, n_m is monolayer capacity, c is the constant related exponentially to the heat of adsorption in the first adsorbed layer.

Equation 3.5 shows a linear relationship between $\frac{P/P_o}{n(1-\frac{P}{P_0})}$ and P/P_o. The intercept $\frac{1}{n_m c}$ and slope $\frac{c-1}{n_m c}$ can be used for the calculation of c and n_m. Thus, the specific surface area can be determined by Equation 3.6 from the monolayer capacity on the assumption of close packing

$$A = n_m \alpha_m L \qquad (3.6)$$

Where α_m is the molecular cross-sectional area and L is the Avogadro constant. Nitrogen is the most appropriate gas for surface area determination. If it is assumed that the BET monolayer is close-packed, α_m will be 0.162 nm^2 at 77 K.

3.7 Photoelectrochemical characterization

Photoelectrochemical (PEC) characterization is a crucial technique in both photocatalytic and photoelectrocatalytic processes. In this method, the electronic properties and the photogenerated charge carrier separation efficiency of semiconductor-based materials could be evaluated by transient photocurrent and electrochemical impedance. Moreover, this technique can be used to determine the CB of photocatalyst via Mott-Schottky records. Typically, a PEC system is constructed of three-electrode configuration, including a working electrode (WE), which is made of Carbon paper or Fluorine-doped Tin Oxide (FTO) glass coated with a photocatalyst, a counter electrode (CE), and a reference electrode (RE). **Figure 3.7** shows the basic setup of the photoelectrochemical system. Under light irradiation and appropriate applied voltage, photogenerated electrons migrate to the counter electrode, producing a transition photocurrent. The obtained current density reflects the behavior of charge carrier separation and transportation.

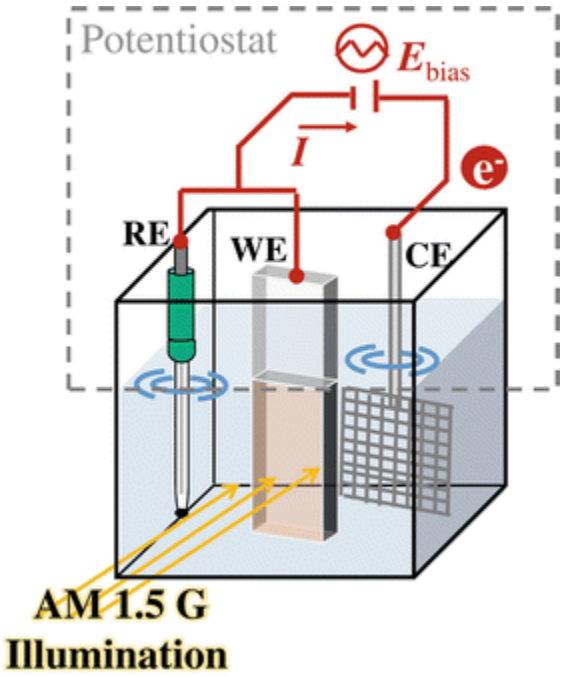

Figure 3.7: Basic setup for a photoelectrochemical (PEC) process[227]

Electrochemical impedance provides the information of charge resistance of semiconducting materials, which can be obtained by measuring the current response when an AC voltage is applied. By Ohm's Law, the calculation of impedance is given as the following equation:

$$Z_\omega = \frac{E_v}{i_\omega} \qquad (3.7)$$

Where Z_ω is the impedance, ω is the AC frequency, E_v is applied potential (V) and i_ω is the current (A)

In polar coordinates, Z_ω is given by **Equation 3.8:**

$$Z = |Z|\, e^{\omega\phi} \qquad (3.8)$$

Where: |Z| is the magnitude of the impedance and ϕ is the phase shift

In Cartesian coordinates, the impedance is given by **Equation 3.9**:

$$Z = Z' - j.Z'' \qquad (3.9)$$

Where: Z′ is the real part of the impedance, and Z" is the imaginary part of the impedance.

The plot describes the relation between Z′ and Z”, which is identified as a Nyquist plot, and the diameter of the Nyquist plot semi-circle signifies the charge transportation ability. A smaller radius of semi-circle indicates lower charge resistance.

3.8 Photoluminescence spectroscopy

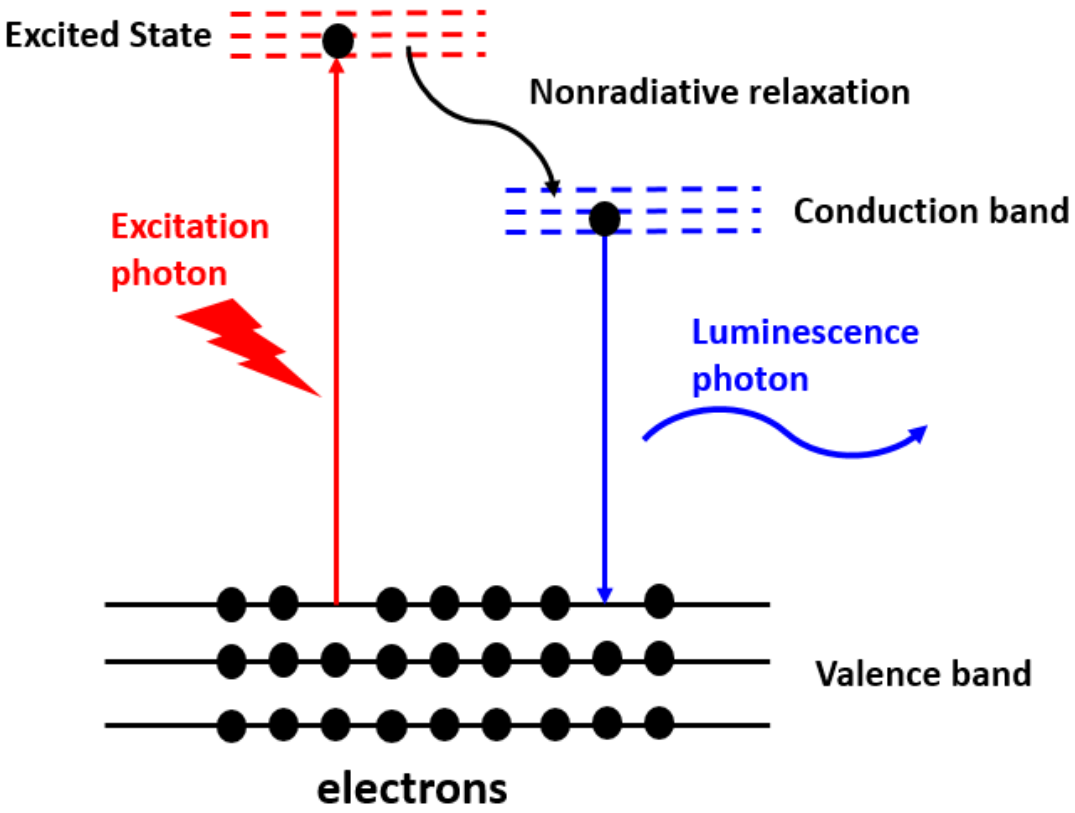

Figure 3.8: Principle of photoluminescence spectroscopy

Similar to photoelectrochemical analysis, photoluminescence (PL) spectroscopy is a useful technique to characterize the photochemical properties of semiconductors such as the lifetime of a photoexcited electron, the charge separation, and transportation ability. Besides, PL can also be utilized to study crystal defects, such as atomic vacancies and substitutions mediated optical properties. There are three main forms of PL, including resonant radiation, fluorescence, and phosphorescence. The fundamental principle of photoluminescence is described in **Figure 3.8**. Upon light irradiation, a photocatalyst absorbs a photon with higher energy than its bandgap energy and generates electron-hole pairs. The excited electrons at a

higher electronic state, then, release energy, return to the VB and recombine with the hole. This recombination process results in luminescence emission, which is known as the PL of the semiconductor. In detail, the excited electrons firstly expose a non-radiative transition and transfer to the bottom energy level of the CB. Then, the band-band PL process occurs in which electrons emit luminescence photons and come back to the top VB. In this case, the emitted photon energy is equal to the bandgap energy. Therefore, the stronger band-band PL signal indicates the higher recombination rate of photogenerated electron-hole.

3.9 Gas chromatography

Gas Chromatography (GC) is an analytical method that allows the separation of a mixture of different compounds. This technique is employed to identify and measure the concentration of the vaporized compound. In general, the basic principle of gas chromatography is based on the interaction of components on a stationary phase. The different affinity with the stationary phase is the key factor leading to the separation of each component from the mixture. A compound having a stronger affinity creates a stronger interaction with the stationary phase, then, retains longer in a column as compared to the substance with weak affinity. When a flowing mobile phase passes through the column, the component is eluted with a carrier gas and analyzed by an appropriate detector.

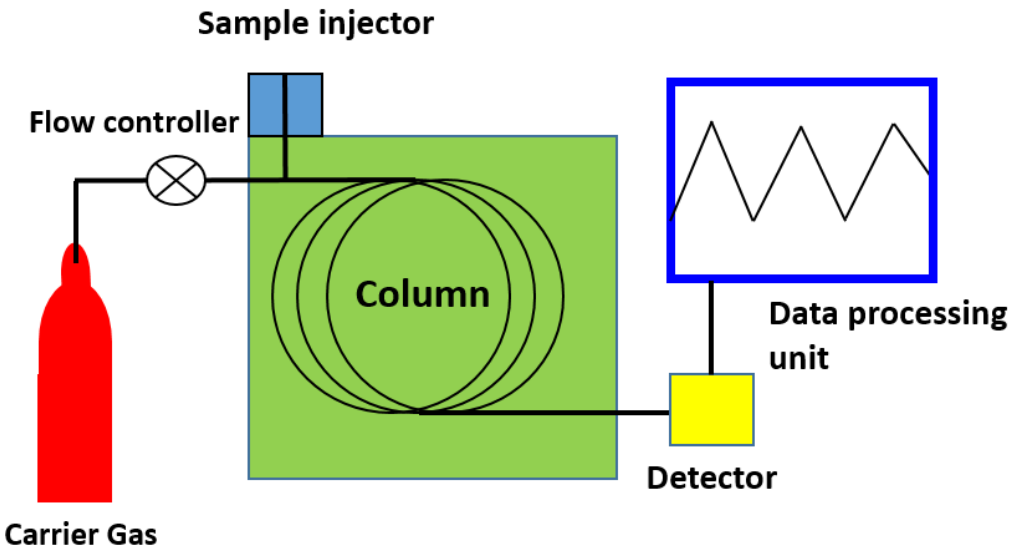

Figure 3.9: Basic component of an atypical gas chromatography system

Figure 3.9 describes a typical gas chromatography system. Generally, a gas carrier such as helium, nitrogen or argon is utilized to flow continuously through a GC column and a detector. It is worth noting that the type of carrier gas should be carefully chosen, and its flow rate is also optimized to improve the efficiency of the column as well as minimize the drift and noise of the detector. In the present work, the GC is used to analyze the produced H_2 gas using a TCD detector. The TCD measures the thermal conductivity of the mixture of flow gas and compares it with the reference flow. The compounds are identified based on their different thermal conductivities.

Chapter 4: Ni Supported $CdIn_2S_4$ Sponge-like Spheres: A Noble Metal Free High-Performance Sunlight Driven Photocatalyst for Hydrogen Production

Manh-Hiep Vu, Chinh-Chien Nguyen, M. Sakar and Trong-On Do*

Department of Chemical Engineering, Laval University, Québec, G1V 0A6, Canada

1065, avenue de la Médecine, Québec (Québec), G1V 0A6, CANADA

*E-mail: trong-on.do@gch.ulaval.ca

Phys. Chem. Chem. Phys., **2017**,19, 29429-29437

We have reported a strategy to develop high-performance photocatalysts based on noble metal-free Ni supported $CdIn_2S_4$ sponge-like spheres for hydrogen evolution under solar light.

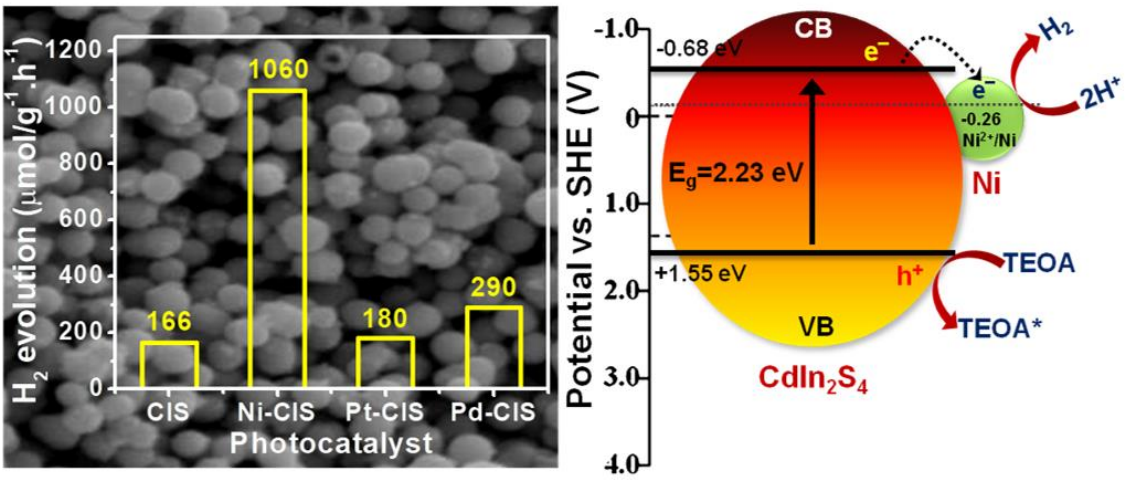

Résumé

Des sphères spongieuses de type $CdIn_2S_4$ (Ni-CIS) supportées par nickel ont été développées en utilisant un mécanisme d'alcoolyse, suivie d'un processus de sulfuration par exposition à une atmosphère contenant du sulfure de dihydrogène (H_2S). La formation du $CdIn_2S_4$ nanocristallin monophasé a été confirmée par une analyse DRX (diffraction des rayons X). Des images de microscopie électronique ont montré que les sphères de type spongieux sont composées de nanoparticules de $CdIn_2S_4$ avec des tailles moyennes d'environ 25 nm. Les spectres photoélectroniques des rayons X ont indiqué la présence des éléments dans leurs états d'oxydation stables respectifs qui ont conduit à la formation de $CdIn_2S_4$ monophasé avec une excellente intégrité structurelle et composition chimique. Les spectres d'absorption ont montré l'activité du matériau sous la lumière visible et indiqué une valeur de la bande interdite de 2,23 eV. La performance photocatalytique du Ni-CIS synthétisé pour produire de l'hydrogène sous irradiation solaire est estimée à 1060 $\mu mol.g^{-1}.h^{-1}$, soit environ 5,5 et 3,6 fois plus élevée que celle du Pt-CIS (180 $\mu mol.\ g^{-1}.h^{-1}$) et du Pd-CIS (290 $\mu mol.g^{-1}.h^{-1}$), respectivement obtenus dans cette étude. En conséquence, un mécanisme de l'efficacité observée des nanoparticules Ni-CIS a également été proposé. Le test de recyclabilité a indiqué une efficacité constante pour la génération d'hydrogène sur 3 cycles (9 h), ce qui révèle essentiellement l'excellente stabilité de l'efficacité photocatalytique et les propriétés chimiques du photocatalyseur. La stratégie consistant à utiliser des métaux non-nobles tels que le Ni, plutôt que des métaux nobles, comme cocatalyseur, ouvre de nouvelles possibilités pour le développement de photocatalyseurs de haute performance sous la lumière solaire et à faible coût, comme cela a été réalisé dans cette étude.

Abstract

Nickel supported $CdIn_2S_4$ (Ni-CIS) sponge-like spheres have been developed using alcoholysis followed by the sulfidation process. The formation of nanocrystalline-single phase $CdIn_2S_4$ was confirmed using X-ray diffraction studies. Electron microscopy images showed that the sponge-like spheres are composed of $CdIn_2S_4$ nanoparticles with average sizes around 25 nm. X-ray photoelectron spectra indicated the presence of elements with their respective stable oxidation states that led to the formation of single-phase $CdIn_2S_4$ with enhanced structural integrity and chemical composition. The absorption spectra indicated the visible light activity of the material and the bandgap energy is deduced to be 2.23 eV. The photocatalytic efficiency of the synthesized Ni-CIS on its ability to produce hydrogen under solar light irradiation is estimated to be 1060 μmol g^{-1} h^{-1}, which is around 5.5 and 3.6 folds higher than that of Pt-CIS (180 μmol.g^{-1}.h^{-1}) and Pd-CIS (290 μmol.g^{-1}.h^{-1}), respectively as obtained in this study. Accordingly, the mechanism of the observed efficiency of Ni-CIS nanoparticles is also proposed. The recyclability test showed consistent hydrogen evolution efficiency over 3 cycles (9 h), which essentially revealed the excellent photo- and chemical-stability of the photocatalyst. Strategy to utilize non-noble metals such as Ni, rather than noble-metals, as co-catalyst opens up a new possibility to develop low cost and high-performance sunlight-driven photocatalysts as achieved in this study.

4.1 Introduction

Photocatalytic hydrogen production using semiconductor-based photocatalysts has grabbed significant attention as it greatly helps in solving the issues in energy and environmental demands. Recently, metal sulfides have been considered as promising photocatalysts due to their suitable bandgap energy and excellent photocatalytic activity and stability.[228-230] As compared to the metal oxides based photocatalyst, sulfides are more promising as their bandgap energy and band edge position can be easily tunable. It is known that in oxides, the valence band (VB) that is composed of oxygen species is often suffering due to defects and other limitations such as poor band dispersion and restrained band potentials. Alternatively, the VB potential that constructed band using sulfides species offers the dispersed potentials that manifest the tunable bandgap energy and band edge positions in semiconductors.[1,231]Among the various types of metal sulfide photocatalysts, $CdIn_2S_4$ is reported as a potential material for applications in photocatalysis and solar cells.[232-233] It is reported that the combined functional characteristics of indium and cadmium can enhance their optical and chemical properties into many folds as compared to their individual counterparts. Owing to the enhanced chemical stability and narrow bandgap energy (2.2~2.4eV), $CdIn_2S_4$ could overcome the limitation of its parent materials such as In_2S_3 and CdS.[3] However, $CdIn_2S_4$ mainly lacks due to the fast recombination of generated electron-hole pairs that eventually reduces its photocatalytic activity. It should be noted that the fast recombination of the charge carriers could be regulated via controlling the chemical composition (e.g. anion/cation defects free) of a photocatalyst and this could be effectively achieved through the synthesis processes.[197, 234]Accordingly, here we have meticulously developed $CdIn_2S_4$ single-phase in two-step alcoholysis and sulfidation process at high temperature. In addition to this, it is also realized that the coupling of $CdIn_2S_4$ with a co-catalyst can significantly improve the separation of photo-induced charge carriers and greatly reduce the recombination possibilities in $CdIn_2S_4$. Recently, nickel (Ni) has been demonstrated as an effective co-catalyst, especially for the metal sulfide photocatalyst such as CdS.[235-236] Hence, the utilization of nickel-based compounds as co-catalysts to build sulfide-based photocatalytic systems could lead to achieving an enhanced photocatalytic activity under visible light irradiations.

Considering the materials development aspects, the construction of photocatalysts based on hollow/spongy like spherical nanostructures has been believed as an effective strategy to improve their photocatalytic activities.[136] A hollow/spongy like spherical structure is constructed using solid nanoparticles can improve the photo-induced charge separation and promote the charge carriers to the surrounding molecules by lowering their travel path to the surface of the particles.[237] Also, such structures inherently possess porous-like structures that greatly enhance the accessibility of active sites by the reactant molecules. Besides, multiple scattering of light within their interiors allow the absorption of light more efficiently.[238-239] It should be noted that compared to the number of studies carried out on the development of metal oxide-based nanostructures,[240] there are only limited studies that have been carried out on the metal sulfide-based nanostructures. This is essentially due to the complexities involved in synthesizing the metal sulfide materials at the nanoscale. For instance, Lou *et al.*[241] have successfully fabricated multi-shelled $NiCo_2S_4$ by using an anion exchange method and they found that the $NiCo_2S_4$ hollow spheres exhibit uniform morphology with much higher conductivity in comparison with their metal oxides.

In this context, this study is the first to report the synthesis of highly uniform sponge-like spheres of the $CdIn_2S_4$ through alcoholysis mediated sulfidation process. This fabrication process is essentially a one-pot synthesis of CdIn@glycerate solid spheres followed by calcination and sulfidation to achieve sponge-like spheres of $CdIn_2S_4$ single-phase. Further, Ni as a co-catalyst was deposited onto $CdIn_2S_4$ and the materials were investigated for their photocatalytic hydrogen production efficiency under solar light irradiation, where it was also compared with noble metals such as Pt and Pd deposited $CdIn_2S_4$ sponge-like spheres.

4.2 Experimental Section

4.2.1 Materials

Glycerol, Indium (III) nitrate hexahydrate, Cadmium (II) nitrate hexahydrate, Ammonium Nickel (II) sulfate hexahydrate, Isopropanol, and Ethanol were purchased from a commercial source Alfa Aesar. All reagents were directly used without further purification.

4.2.2 Material syntheses

The synthesis of mixed cadmium-indium metal sulfides (denoted as CIS-*x*; where x represents In/Cd molar ratio; (where *x* is 3.0, 2.0, 1.0 and 0.5) consisted of three steps: *(i) Synthesis of CdIn@glycerate templates:* In a typical synthesis, different ratio of In/Cd precursors and 8 mL of glycerol were dissolved completely in 40 mL of isopropanol to form a colorless solution. Then, the solution was transferred into a Teflon-lined stainless steel autoclave and kept at 180 °C for 6 h. After cooling to room temperature naturally, the brown white precipitate was separated by centrifugation, washed several times with anhydrous ethanol, and dried in an oven at 80 °C to obtain CdIn@glycerate templates. *(ii) Synthesis of $CdIn_2O_4$ sponge-like spheres:* To obtain the $CdIn_2O_4$ sponge-like spheres (denoted as CIO-*x*)., the as-synthesized CdIn@glycerate solid spheres were then calcined at 500 °C in air for 3 h with a slow heating rate of 1 °C per min. *(iii) Preparation of $CdIn_2S_4$ sponge-like spheres:* 100 mg of the obtained $CdIn_2O_4$ were treated under H_2S atmosphere at 450 ^oC for 3 h.

4.2.3 Characterizations

The transmission electron microscopy (TEM) images of the samples were obtained using a JOEL JEM 1230 operated at 120 kV, and high-resolution TEM (HRTEM) images were obtained using a Philips G2 F30 Tecnai instrument operated at 300 kV. The scanning electron microscopy (SEM) images were obtained using a JEOL 6360 operated at 15 kV. Powder X-ray diffraction (XRD) patterns of the samples were obtained using a Bruker SMART APEXII X-ray diffractometer equipped with a Cu Kα radiation source (λ = 1.5418Å). X-ray photoelectron spectroscopy (XPS) measurements were carried out in the ion-pumped chamber (evacuated to 10^{-9} Torr) of a photoelectron spectrometer (Kratos Axis-Ultra) equipped with a focused X-ray source (Al Kα, hν = 1486.6eV). UV-Vis spectra were recorded on a Cary 300 Bio UV-visible spectrophotometer. N_2 adsorption-desorption isotherms of the samples were obtained at 77K using a Quantachrome Autosorb-1 MP analyzer. Prior to the respective measurements, the samples were out-gassed under vacuum for 6 h at 150 °C.

4.2.4 Photocatalytic activity test

All the photocatalytic reactions were conducted in a home-built top-irradiated reactor at ambient temperature and atmospheric pressure. Initially, 100 mg of the photocatalyst was dispersed for the photo-deposition of Ni, Pt and Pd separately (at an optimum amount of 3

wt%) before the photocatalytic tests. In a typical photocatalytic experiment, an optimized amount of 5 mg of the co-catalyst loaded photocatalyst was dispersed in a solution containing 9 mL water and 1mL of the sacrificial agent (Triethanolamine/TEOA) and taken in the reactor cell. After that, the mixture was purged with nitrogen for 10 min. Then, the reactor cell was illuminated using a solar simulator 100 W for 3 h. For the recyclability test, the reactor cell was purged again with nitrogen for 30 min, before to start each cycle. The recycling studies were conducted for 9 h into 3 cycles and each cycle was carried out for 3 h. The amount of H_2 gas generated was determined using a gas chromatograph equipped with a thermal conductivity detector (TCD), and using N_2 as the carrier gas.

4.3. Result and discussions

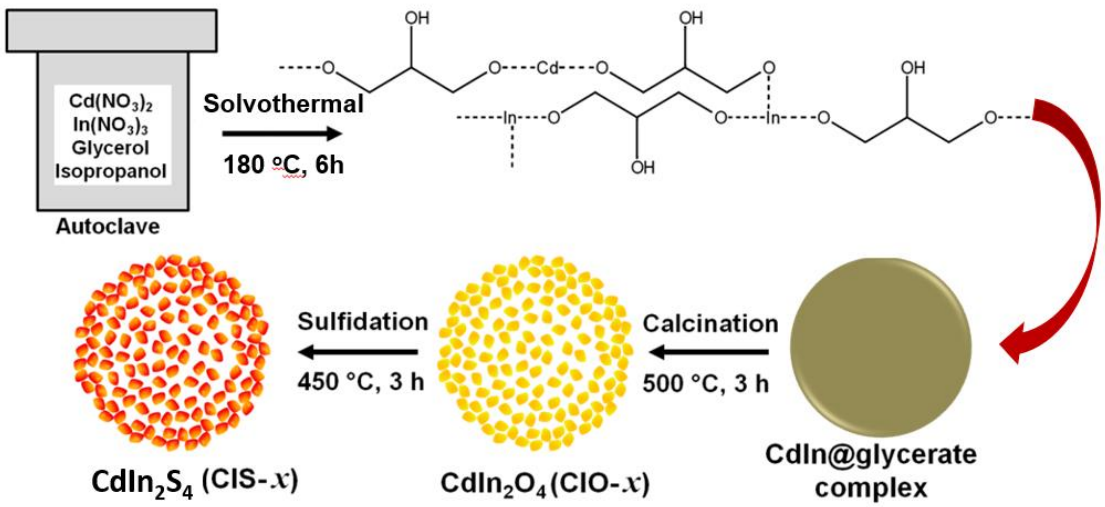

Figure 4.1: Formation mechanism of the CIO-*x* and CIS-*x* sponge-like spheres.

The formation mechanism of the $CdIn_2S_4$ (CIS) sponge-like spheres is schematically illustrated in **Figure 4.1**. As described above, firstly the CdIn@glycerate templates were prepared based on the general alcoholysis mechanism.[242] Then, the Cd^{2+} and In^{3+} precursors were diluted with glycerol ligand to form a bimetallic CdIn-Glycerol complex. At high temperature and pressure, the glycerol was polymerized into esters along with the elimination of water, where the water initiated the hydrolysis process of CdIn-Glycerol complexes and led to the production of CdIn@glycerate templates. Then, the process of calcination under air removed the glycerate core, leading to the formation of $CdIn_2O_4$ (CIO-*x*) spheres. In the

next step, CIO-*x* was transformed to CIS-*x* by a sulfidation process under H_2S treatment as shown in **Figure 4.1**. After the H_2S treatment, the color of the prepared sample changed from pale-yellow to bright-yellow. The formation of CIS-*x* can be attributed to the anion exchange reaction in the CIO-*x*. The inward diffusion of H_2S gas in CIO-*x* spheres leads to the inclusion of S in the lattices of CIO-*x*, which replaces the oxygen with sulfur species at higher temperatures and leading to the formation of CIS-*x* compositions. Then, Ni was further deposited on these synthesized CIS-*x* compositions with at an optimized concentration of 2 wt%. The photo-deposition of Ni onto the CIS-2.0 sample was confirmed through the observed color change from bright-yellow to grayish-yellow as shown in **Figure S4.1** (Supporting information (SI)).

The influence of off-stoichiometric In/Cd ratios on the structural and optical absorption characteristics of $CdIn_2S_4$ phase was studied using X-ray diffraction and UV-visible absorption spectroscopy and the obtained results are shown in **Figure 4.2(A)-(B)**, respectively. The XRD patterns reveal the spinel structure with enhanced crystalline properties of the CIS-x samples as shown in **Figure 4.2(A)**. The peaks at $2\theta = 27^o$ and 43.5^o corresponding to (311) and (440) are the two characteristic diffraction planes of single-phase $CdIn_2S_4$ (JCPDS card #027-0060). The observed small peaks corresponding to the (002) plane for the samples CIS-1.0 and CIS-0.5 (line c and d in **Figure 4.2(A)**) indicate the presence of hexagonal CdS phase. The formation of CdS phase could be possible because of the precipitation of excess Cd^{2+} ions owing to their poor solubility product constant.This essentially shows the evolution process of $CdIn_2S_4$ phase with respect to the tunable In/Cd ratios.

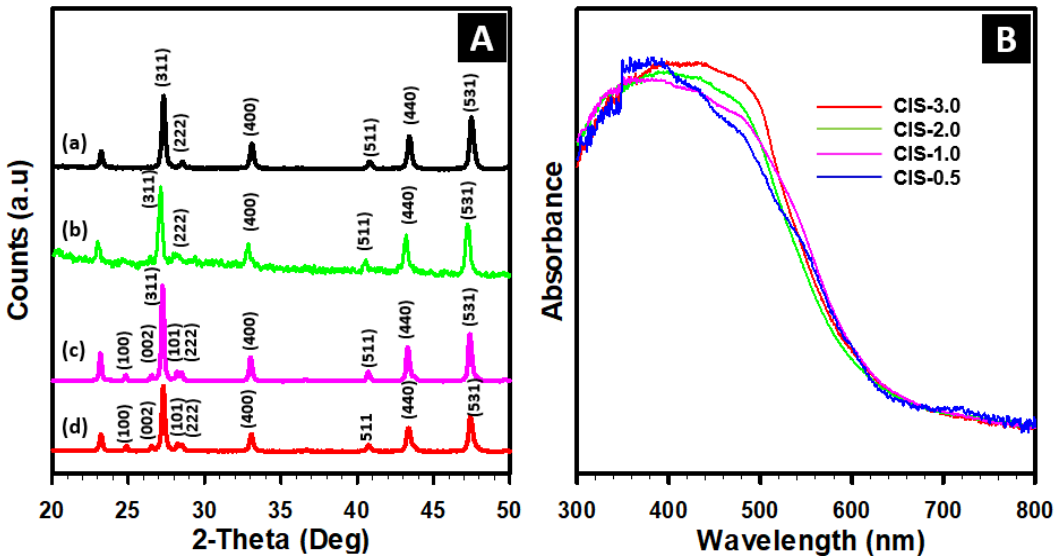

Figure 4.2 (A) XRD pattern and (B) UV-Vis spectra of $CdIn_2S_4$ different precursor ratios, where (a) 3.0, (b) 2.0, (c) 1.0 and (d) 0.5.

The UV-Vis absorption spectra of the synthesized CIS-*x* samples are given in **Figure 4.2(B)**. It can be seen that the CIS-*x* samples show noticeable visible light absorption band edges. This indicates that these materials can exhibit strong optical activities under visible light. It is noteworthy that the decreasing In/Cd ratio tends to influence the visible light activity of the materials as the slight changes can be observed in the region from 350 nm-500 nm.

Figure 4.3 shows the amount of hydrogen generated over Ni-CIS-*x* compositions with different In/Cd ratios. Among the samples, the Ni-CIS-2.0 showed the highest photocatalytic hydrogen evolution of 1060 µmol.g^{-1}.h^{-1}. It is observed that increasing the concentration of In^{3+} or Cd^{2+} leads to a significant decrement in the H_2 evolution. As shown in **Figure 4.3**, the average amount of hydrogen produced was calculated to be 227, 318, and 48 µmol.g^{-1}.h^{-1} for Ni-CIS-0.5, Ni-CIS-1.0, and Ni-CIS-3.0, respectively. It is expected that when the In/Cd ratio is lower than 2.0, it leads to the off-stoichiometry in the $CdIn_2S_4$ phase and results in the formation of In_2S_3 and CdS phases due to the existence of excess Cd^{2+} or In^{3+} ions in CIS-*x* compositions. Thereby, the presence of In_2S_3 or CdS, as impurities phases, considerably limits the photocatalytic activity as these impurities affect the charge separation and band edge position of the host $CdIn_2S_4$ phase.[5]

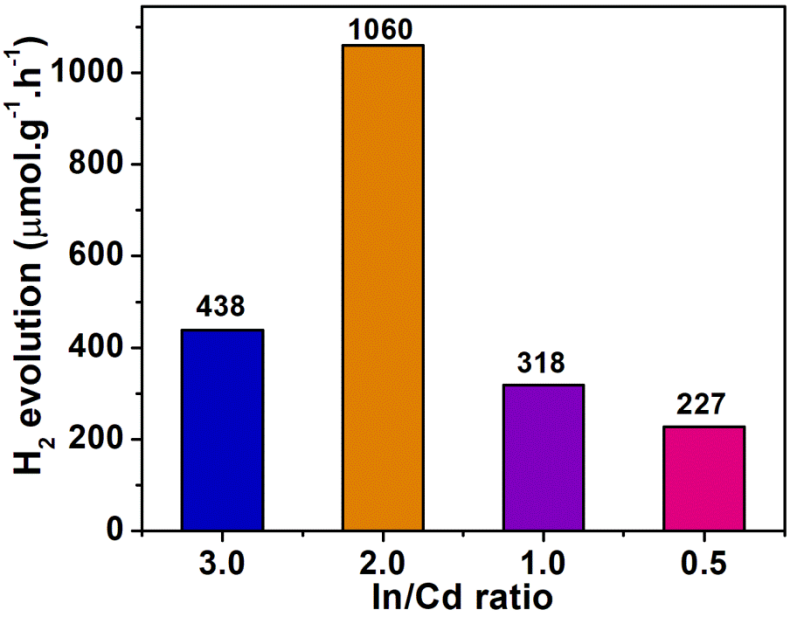

Figure 4.3: Photocatalytic hydrogen evolution over Ni deposited CIS-*x* photocatalysts (where *x* = 3.0, 2.0, 1.0 and 0.5)

Among the Ni-CIS-*x* samples, the Ni-CIS-2.0 showed the enhanced photocatalytic hydrogen evolution and therefore this sample was taken for further extensive analysis to understand their photocatalytic mechanism. In addition, the photocatalytic performance of the herein prepared Pt and Pd deposited CIS-2.0 samples were also studied for their photocatalytic hydrogen evolution efficiencies under sunlight in comparison with Ni deposited CIS-2.0 sample.

Figure 4.4 (A)-(C) shows the SEM image of the CdIn@glycerate templates, CIO-2.0 ($CdIn_2O_4$), and CIS-2.0 ($CdIn_2S_4$) sponge-like spheres, respectively. The size of CdIn@glycerate template spheres is quite uniform with a diameter in the range of 600-700 nm, which is found to be decreased to 400-500 nm after the calcination at 500 ^oC and transformed to the sponge-like structure due to the complete combustion of the glycerate core. The existence of sponge-like morphology can be seen in **Figure 4.4(B)-(C)**, where the broken spheres show clearly the hollowness inside the spheres as shown in the insert image of **Figure 4.4(B)-(C)**.

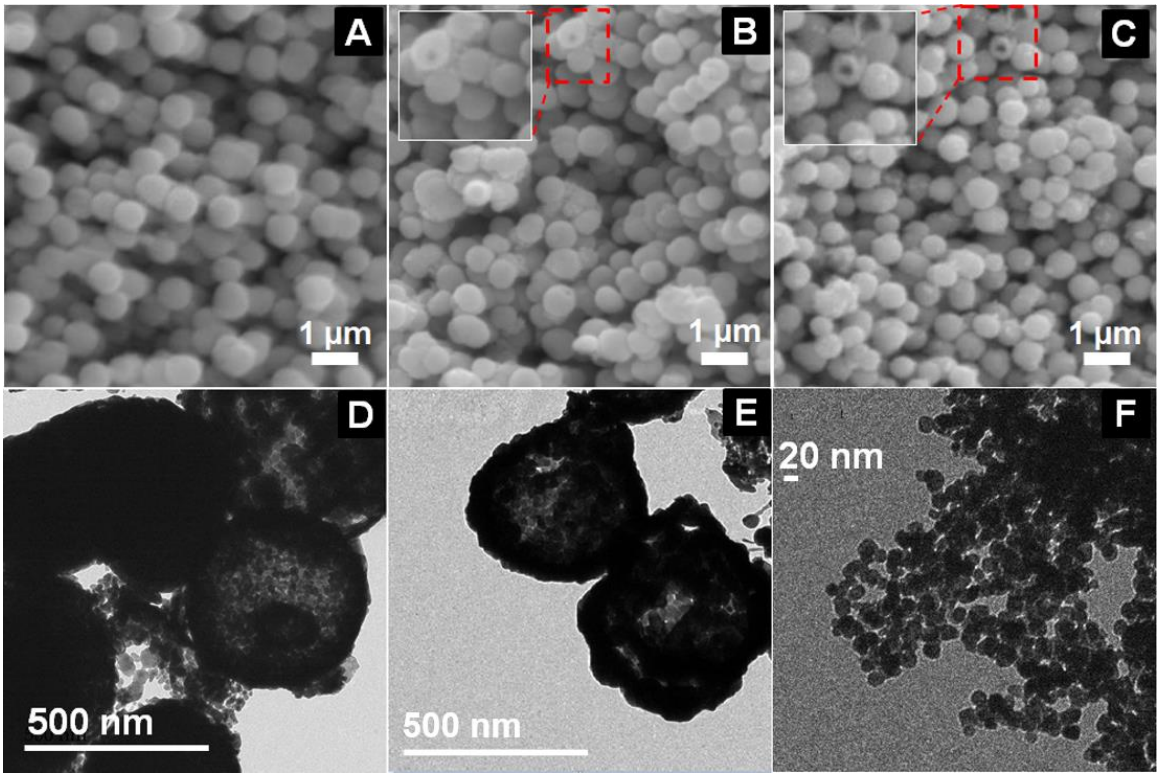

Figure 4.4: (A)-(C) shows the SEM images of CdIn@glycerate template spheres, CIO-2.0, and CIS-2.0 sponge-like spheres, respectively and (D)-(E) shows the respective TEM image of the sponge-like spheres and (F) broken CIS-2.0 spheres into smaller nanoparticles. (Insert image shows the closer view of the respective morphology)

It was observed that after the sulfidation process at 450 ^{o}C for 3 h, the color of the sample was changed from pale-yellow to bright-yellow, suggesting the formation of the sulfide phase of the material. Further, the observed sponge-like morphology of materials was also confirmed from the obtained TEM images as shown in **Figure 4(D)-(E)**, respectively. It is noteworthy that the surface of sponge-like spheres has become rough after the sulfidation process. Interestingly, **Figure 4.4(F)** shows the TEM image of the broken CIS-2.0 spheres that essentially reveals that these sponge-like spheres are composed of numerous closely packed nanoparticles of the average size of 25 nm, which is obtained through alcoholysis followed by sulfidation process. The average crystallite size of CIS-2.0 was also calculated using Scherrer's formula ($d = 0.9\lambda/\beta\cos\theta$, where d-crystallite size, 0.9-shape factor, λ-wavelength of the incident X-rays, β-full width at half maximum and $\cos\theta$-diffraction angle) corresponding to the (311) and (440) plane and it was found be 22 nm, and this observation

was also found to be consistent with the respective TEM image of the sample (**Figure 4.4(F)**). The energy-dispersive X-ray spectroscopy (EDS) analysis of the CIO-2.0 sample confirmed the presence of the elements Cd, In, and O (given in SI, **Figure S4.2**). Similarly, the EDS spectrum of CIS-2.0 samples, as shown in SI-**Figure S4.3**, confirmed the existence of Cd, In, and S in the material. It should be noted that the oxygen is not observed in the CIS-2.0 sample, suggesting the complete sulfidation of the material. Further, the peak corresponding to Au appeared in the spectra because of the sputtering of Au onto the samples during their electron microscopy imaging analysis.

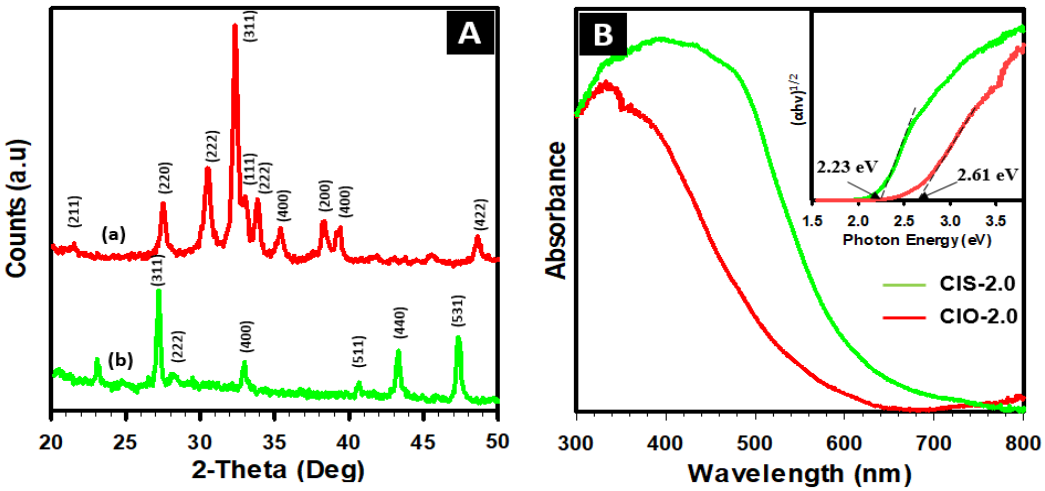

Figure 4.5: (A) XRD spectra of (a) CIO-2.0 and (b) CIS-2.0; (B) UV-Vis spectra of CIO-2.0 and CIS-2.0; Inset image: Estimation of bandgap energy of CIS-2.0 and CIO-2.0.

For comparison, **Figure 4.5(A)** shows the XRD pattern of the CIO-2.0 sample. The diffraction peaks at 2θ = 27°, 32°, and 34° indexed to (220), (311), and (222) are the characteristic planes of spinel structured $CdIn_2O_4$ phase. These peaks with high intensity indicate the enhanced crystalline properties of the sample. However, the diffraction peaks at 30.5°, 35° corresponding to (222) and (400) planes and 33° and 39° corresponding to (111) and (200) planes are indicating the existence of In_2O_3 and CdO phases, respectively in the sample. The co-existence of In_2O_3 and CdO impurity phases could be originated from the presence of point defects such as oxygen vacancies or the interchange of Cd^{2+} and In^{3+} ions that could be due to the insufficient reaction conditions.[243] On the other hand, the XRD pattern of the sulfide-sample ($CdIn_2S_4$) indicates the formation of a single phase of the

material, where it essentially suggests that the H_2S treatment induces the complete replacement of O ions as well as oxygen vacancies by S ions.

The UV-Vis absorption spectra of the CIO-2.0 and CIS-2.0 samples are shown in **Figure 4.5(B).** The observed prominent red shift in the absorption edge of CIS-2.0 could be originated due to the transformation from oxide phase into sulfide phase. The observed hump-like peak in the UV region (around 320 nm) may be due to the presence of impurity phases in the CIO-2.0 sample, while the smooth absorption edge indicates the single-phase nature of the CIS-2.0 sample, which is in good agreement with the obtained XRD result. It should be noted that the absorption range of the CIO-2.0 sample was observed up to 640 nm, while it was extended up to 780 nm for the CIS-2.0 sample. This observed enhancement is much higher than that of those reported in literature.[244-249] The inset image in **Figure 4.5(B)** shows the $(\alpha h\nu)^{1/2}$ versus photon energy curve that was plotted using the Kubelka-Munk function for the estimation of the bandgap energy of the samples. Accordingly, the estimated bandgap of CIS-2.0 and CIO-2.0 was found to be 2.23 and 2.61 eV, respectively. It is known that the band edge potential of the conduction band (E_{CB}) and valence band (E_{VB}) is an important parameter to validate the suitability of materials for photocatalytic applications. For an efficient water splitting reaction, the band edge position of the conduction band should be located above the hydrogen evolution potential, while the valence band edge potential should be below the O_2/H_2O potential.[1] Accordingly, the E_{VB} and E_{CB} potential of the CIS-2.0 sample was calculated using the empirical formula,[244, 247] $E_{CB} = X - E^e - 0.5E_g$ and $E_{VB} = E_{CB} + E_g$, (Detailed calculations can be found in SI) where X is the absolute electronegativity of the semiconductor ($CdIn_2S_4$), E^e is the difference between the normal hydrogen electrode (NHE) and the vacuum that has a value of ~4.5eV. Based on the equations, the bottom of the conduction band and the top of the valence band of CIS-2.0 is determined to be -0.73 eV and +1.50 eV, respectively. From the obtained values, the conduction band edge potential is found to be more negative than the H^+/H_2 (E = 0 eV) potential and the valence band edge is more positive than the O_2/H_2O potential (E = +1.23eV), indicating that $CdIn_2S_4$ could be an efficient visible-light-driven photocatalyst for water splitting, particularly for hydrogen generation.

The specific surface area of the sample was measured by N_2 adsorption-desorption isotherms analysis and the obtained curves are shown in **Figure S4.4** (Supporting Information). It is found that the CIO-2.0 possesses a specific surface area of 26 m^2g^{-1}, which is found to be decreased to 19 m^2g^{-1} for CIS-2.0. This could be attributed to the replacement of oxygen ions by sulfur ions in the material that increased the molecular weight of the CIS-2.0 composition and decreased the surface area.

The surface chemical state of CIO-2.0, CIS-2.0, and Ni-CIS-2.0 was examined using the XPS technique. The survey XPS spectra as shown in **Figure 4.6(A)** indicate the existence of Cd, In, O, S, and Ni in their respective samples. The corresponding high-resolution XPS spectra of O 1s, In 3d, Cd 3d, S 2p, and Ni 2p of all the three samples are given in **Figure 4.6(B)-(F).** As seen in the O 1s spectrum of CIO-2.0 (**Figure 4.6(B)**), the de-convoluted peak centered at 529.6 eV can be assigned to the metal-oxide bond and the peak appeared at 531.5 eV may be originated from the surface adsorbed H_2O and CO_2 under the high-temperature air pyrolysis. On the other hand, the only peak appeared around 532.2 eV for CIS-2.0 and Ni-CIS-2.0 samples could be attributed to the adsorbed oxygen on their surface. The disappearance of the peak at lower binding energies corresponding to the lattice oxygen suggested a complete sulfidation of CIO-2.0 into CIS-2.0. The XPS spectra of In 3d can be fitted to two separated peaks as shown in **Figure 4.6(C)**. For the CIO-2.0, the two peaks at 444.0 and 451.5 eV can be attributed to In $3d_{5/2}$ and In $3d_{3/2}$, respectively.[250] After sulfidation (CIS-2.0), these peaks have been found to be shifted by ~1.0 eV towards higher binding energy and centered at 445.0 and 452.6 eV. This could be attributed to the transformation of indium-oxide bond into indium-sulfide form. Moreover, the replacement of larger electronegativity elements (oxygen) with smaller electronegativity elements (sulfur) might have increased the electron density of In^{3+} cation and thereby these peaks are slightly shifted towards higher binding energy for CIS-2.0 over CIO-2.0.

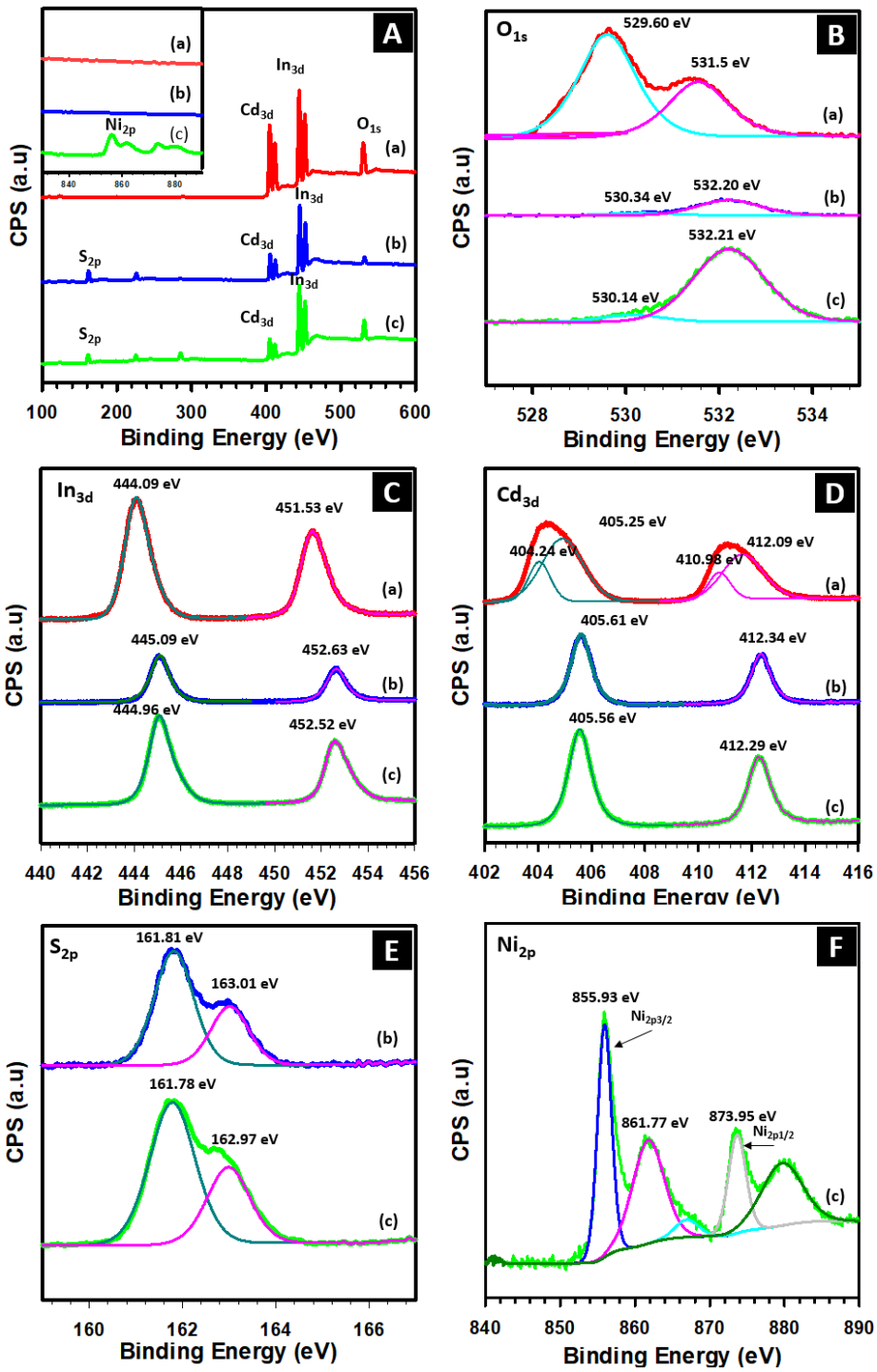

Figure 4.6: XPS (A) survey spectra, (B) O 1s, (C) In 3d, (D) Cd 3d, (E) S 2p, and (F) Ni 2p; Inside the figures, (a) CIO-2.0, (b) CIS-2.0 and (c) Ni-CIS-2.0.

Figure 4.6(D) shows the high-resolution Cd 3d XPS spectrum of CIO-2.0(line a) and CIS-2.0 (line b) and Ni/CIS-2.0 (line c). The strong peaks of CIO-2.0 centered at 405.2 and 412.0

eV revealed the peaks corresponding to Cd $3d_{5/2}$ and Cd $3d_{3/2}$ respectively, which indicated that the existence of Cd ions with +2 oxidation state as observed in spinel structures.[251] Similarly, the other two weak peaks with a binding energy of 404.24 and 410.9 eV were also deconvoluted in the Cd 3d XPS spectrum of CIO-2.0. These peaks can be ascribed to the Cd $3d_{5/2}$ and Cd $3d_{3/2}$ lines corresponding to +2 oxidation state of Cd ions as in cadmium oxides. These results are in good agreement with their corresponding XRD results that confirmed the presence of cadmium oxide impurity phase in $CdIn_2O_4$ spinel structure. Interestingly, only two peaks at 405.6 and 412.3 eV were observed in Cd 3d XPS signals for CIS-2.0 and Ni-CIS-2.0 samples, which can be assigned to Cd $3d_{5/2}$ and Cd $3d_{3/2}$ lines indicating the Cd^{2+}oxidation state in the spinel phase. The disappearance of two peaks at 404.24 and 410.9 eV can be interpreted by the completed sulfidation of mixed oxides (CdO, In_2O_3, and $CdIn_2O_4$) to form a single phase of spinel structure ($CdIn_2S_4$) under H_2S gas treatment at high temperature. The S 2p spectra of CIS-2.0 and Ni/CIS-2.0 are shown in **Figure 4.6(E)**. These signals can be divided into two separate peaks at 161.11 and 162.31 eV, corresponding to the binding energy of S $2p_{3/2}$ and S $2p_{1/2}$ lines indicating the -2 oxidation of S in $CdIn_2S_4$.[252] From the obtained XPS results, it was found that all the elements presented in the CIO-2.0, CIS-2.0, and Ni-CIS-2.0 possess their respective native-stable oxidation states that eventually indicate the appropriate chemical composition and structural integrity of the obtained materials.

As described above, metallic Ni as co-catalyst was deposited on the surface of CIS-2.0 sponge-like spheres through chemical photo-reduction of nickel precursor and its mechanism can be described as follows. Under the light irradiation, electrons will be excited form the VB (+1.50 eV vs NHE) to the CB (-0.73 eV vs NHE) and these excited electrons reduced Ni^{2+} species into metallic Ni particles because the Ni^{2+}/Ni potential (-0.257 eV vs NHE) is much lower than the CB level of $CdIn_2S_4$ and it led to the deposition of Ni onto the surface of CIS. However, the XPS spectra of Ni $2p_{3/2}$ and Ni $2p_{1/2}$of the Ni-CIS-2.0 sample showed two peaks at a binding energy of 855.93 and 873.95 eV, which are the characteristic peaks of NiO[253] and also the peak corresponding to Ni $2p_{3/2}$ at 861.77 eV indicates the Ni^{2+} turns into Ni(0) species.[254] The absence of a firm peak corresponding to metallic Ni could be due to the existence of adsorbed oxygen species on the surface of $CdIn_2S_4$ sample, which could be due to the exposure of the sample in the air.[255]

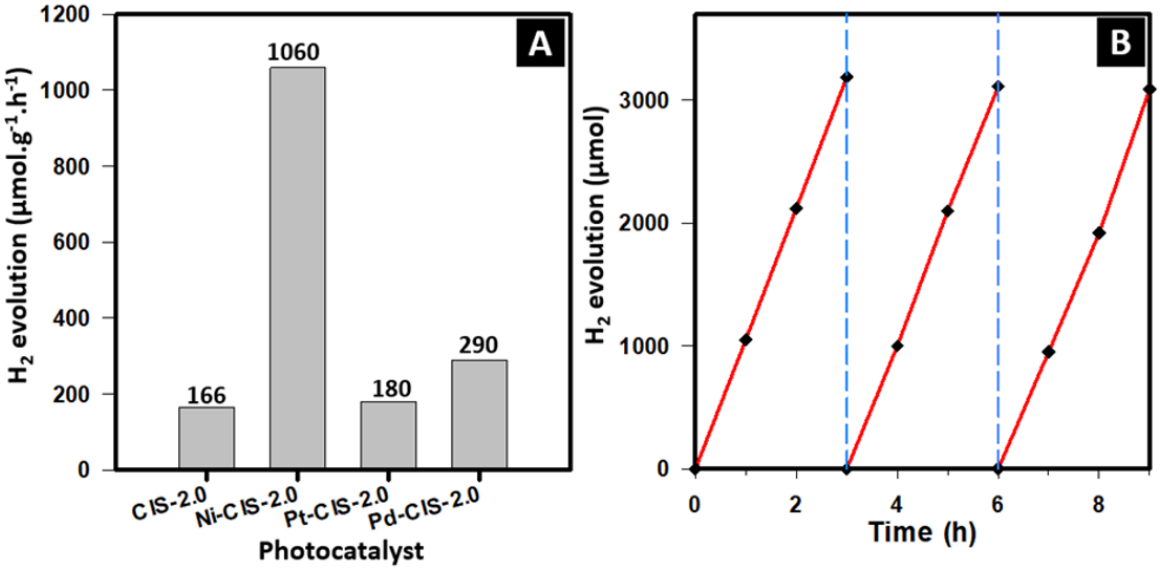

Figure 4.7: (A) Sunlight driven photocatalytic hydrogen production efficiency of CIS-2.0 sponge-like spheres with different co-catalysts loading and (B) Recyclable efficiency of Ni-CIS-2.0.

The photocatalytic hydrogen evolution efficiency of the CIS-2.0 sample with different co-catalysts loadings such as Ni, Pt, and Pd is displayed in **Figure 4.7(A)**. The photocatalytic hydrogen generation of Ni-CIS-2.0 was found to be much higher than that of Pt-CIS-2.0 and Pd-CIS-2.0 samples. From the obtained results, the amount of H_2 production was estimated to be 1060 µmol.g^{-1}.h^{-1}, which is much higher than the H_2 produced by Pt-CIS-2.0 (180 µmol.g^{-1}.h^{-1}) and Pd-CIS-2.0 (290 µmol.g^{-1}.h^{-1}) samples. In addition to this, the recyclability of Ni-CIS-2.0 photocatalyst was also evaluated and it showed enhanced stability over 3 cycles (for 9 h) without any significant decrement in its activity (**Figure 4.7(B)**). It suggests that Ni-CIS-2.0 could be a promising photocatalyst for hydrogen evolution and water splitting applications.

Based on the above experimental results, a possible mechanism for the hydrogen generation efficiency of Ni-CIS-2.0 sponge-like spheres is proposed and depicted in **Figure 4.8**. Under light irradiation, the electrons are excited from the valence band (VB) to the conduction band (CB) of CIS and the excited electrons are further transferred to the deposited nickel on the surface of the photocatalyst. Consequently, water molecules are reduced into hydrogen by

the photo-induced electrons on the metallic nickel. Meanwhile, the holes in the VB of $CdIn_2S_4$ are consumed by the sacrificial agent TEOA.

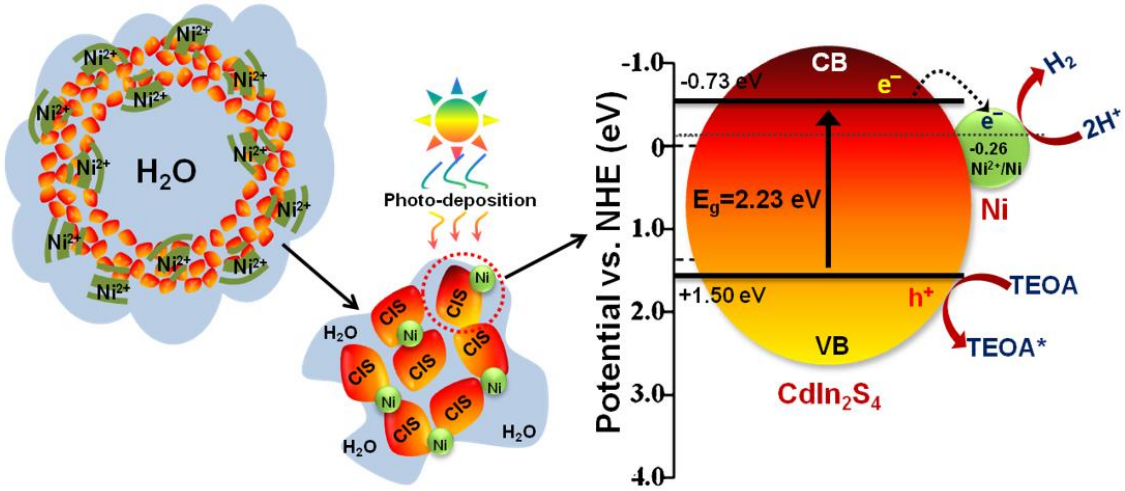

Figure 4.8: Illustration of the formation and photocatalytic hydrogen evolution mechanism of Ni-CIS-2.0 photocatalyst under solar light.

As mentioned, at the given amount of metal (Ni, Pt, Pd) loading, Ni-CIS showed the highest photocatalytic activity, followed by Pd and Pt, respectively. To validate these observations, the physical and electrochemical properties of all three metals should be considered[26] and the relevant properties are given in **Table 4.1.**

Table 4.1: Electro-chemical properties of co-catalyst employed.[256]

Element	Electronegativity (Pauling scale)	Electron affinity (eV)	Work function (eV)
Ni	**1.91**	**1.16**	**5.04-5.35**
Pt	**2.28**	**0.56**	**5.22-5.60**
Pd	**2.20**	**2.13**	**5.12-5.93**

Firstly, the electronegativity of all the three metal co-catalysts (Ni, Pt, Pd) as compared to that of the host (Cd, In): As given in **Table 4.1**, the electronegativity of Ni is in the range of Cd (1.69 eV) and In (1.78 eV), while the Pt and Pd are relatively very high. The equivalence in the electronegativity of these elements constitutes the favorable reaction sites for the

effective transportation of electrons from the CB of $CdIn_2S_4$ to the Ni. It should be noted that the CB of $CdIn_2S_4$ is composed of Cd and In species, and VB is composed of S species.[257] Accordingly, the increased electronegativity of the noble metal co-catalysts Pt and Pd causes a mismatch of electron transfer potential between the host and co-catalysts that significantly affects the photocatalytic activities of Pt and Pd supported $CdIn_2S_4$ photocatalysts.[258] Secondly, the electron affinity of the metal co-catalysts: Fundamentally, the electron affinity of the supported co-catalyst should be adequately enough to sustain the stability of photo-induced electrons until the proton reduction reaction occurs on the photocatalyst surface. Accordingly, any metalPt-SCN that synthesized in the with high or low electron affinity may unfavorably limit the release of trapped electrons to the water molecules. This probably leads to the lower photocatalytic effect in the Pt and Pd supported $CdIn_2S_4$ as compared to Ni supported $CdIn_2S_4$ photocatalyst.[259] Thirdly, the work function of the co-catalysts: As given in **Table 4.1**, the work function of Ni is relatively lower as compared to Pt and Pd with respect to the CB potential of host photocatalyst $CdIn_2S_4$. Thereby, the Ni co-catalyst possibly enhances the hydrogen production by effective transfer of electrons to the surrounding water molecules more efficiently than that of the Pt and Pd co-catalyst. Therefore, the Ni-$CdIn_2S_4$ photocatalyst showed enhanced photocatalytic hydrogen production properties as compared to the Pt and Pd supported $CdIn_2S_4$.

4.4 Conclusion

In summary, nickel supported $CdIn_2S_4$ (Ni-CIS) sponge-like spheres were successfully prepared through a novel one-pot solvothermal alcoholysis mediated sulfidation process. The obtained hydrogen production efficiency of Ni-CIS was found to be around 6.3, 5.5 and 3.6 folds higher than that of the bare, Pt and Pd supported $CdIn_2S_4$, respectively. The observed enhanced photocatalytic activity of Ni-CIS was attributed to strong visible light absorption and the synergistic interaction between the host CIS photocatalyst and nickel co-catalyst. From the obtained results, Ni supported $CdIn_2S_4$ as co-catalyst could be realized as a more promising photocatalytic system, over noble-metal supported photocatalysts, towards hydrogen production under sunlight irradiations.

Acknowledgments

This work was supported by the Natural Science and Engineering Research Council of Canada (NSERC) through the Collaborative Research and Development (CRD), Strategic Project (SP), and Discovery Grants. The author would like to thank EXP Inc. and SiliCycle Inc. for their support.

4.5 Supporting Information

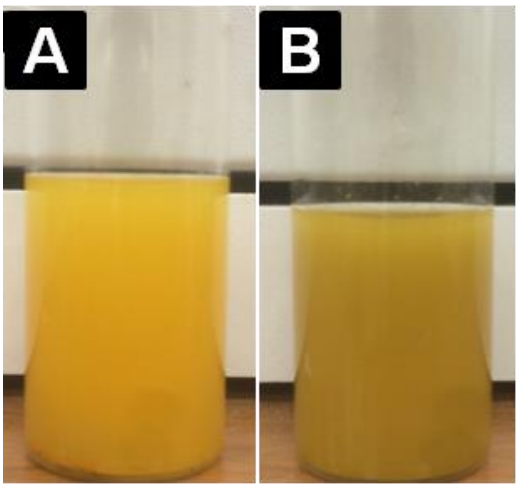

Figure S4.1: Color of the $CdIn_2S_4$ solution **(A)** before and **(B)** after photo-deposition of Ni.

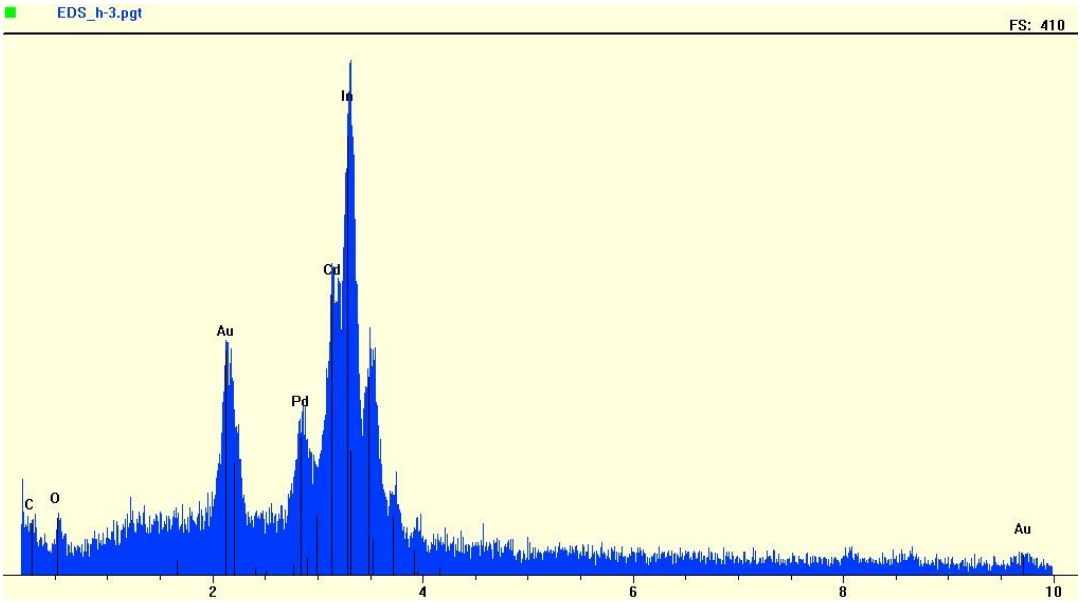

Figure S4.2: EDX spectrum of $CdIn_2O_4$ sponge-like spheres.

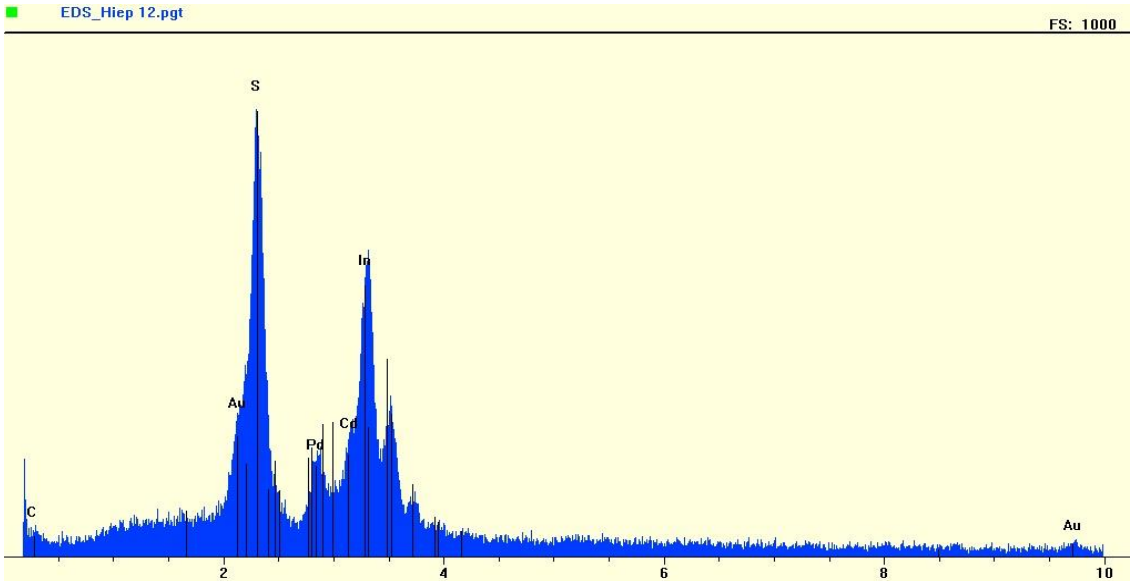

Figure S4.3: EDX spectrum of $CdIn_2S_4$ sponge-like spheres.

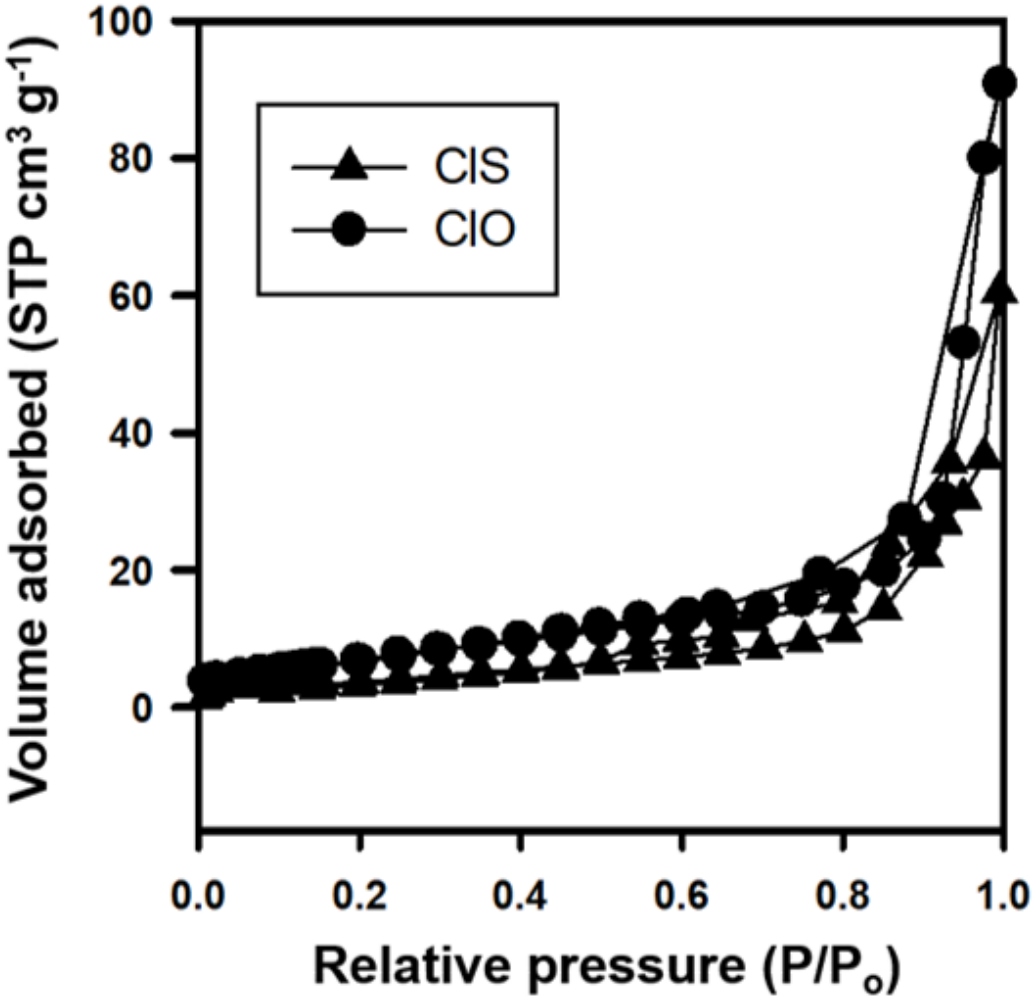

Figure S4.4: N_2 adsorption-desorption isotherm curves of $CdIn_2O_4$ and $CdIn_2S_4$ sponge-like spheres.

S4.1 Band edge potential calculations

The band edge position of the material was calculated using the well known and standard empirical equations that were widely reported in the literature.[244, 247-248, 260]

$$E_{CB} = X - E^e - 0.5E_g \quad (1)$$

$$E_{VB} = E_{CB} + E_g \quad (2)$$

Where, the X is the electronegativity of the semiconductor which is $CdIn_2S_4$ and it was calculated using the following formula,

$$X = [x(A)^a x(B)^b x(C)^c]^{1/(a+b+c)} \quad (3)$$

Where A, B and C are the constituted elements, i.e. Cd, In and S respectively; and a, b, c are the respective number of atoms in the composition, which is 1, 2 and 4, respectively (as in $CdIn_2S_4$).

x(A) can be calculated as follows,

x(A) = [Ionization energy of the element + electron affinity of the element]/2

x(Cd) = [8.9938 + 0.725]/2 = 4.8594

x(In) = [5.78636 + 0.3]/2 = 3.0432

x(S) = [10.36001 + 2.07]/2 = 6.215

Substitute above values in Eqn. (3) as follows,

$X(CdIn_2S_4) = [4.\ 8594 \text{ x } (3.0432)^2 \text{ x } (6.215)^4]^{1/7}$

$X(CdIn_2S_4) = [67144.15]^{1/7} = 4.89$

$E_{CB} = 4.89 - 4.5 - (0.5 \text{ x } 2.23) = -0.73$ eV

$E_{VB} = -0.725 + 2.23 = +1.50$ eV

S4.2. Apparent quantum efficiency of H_2 evolution

The apparent quantum efficiency (AQE) of the photocatalyst depends on various parameters that include the measurement methods, reaction conditions, amount of photocatalyst taken, wavelength taken for the estimations, etc.[5-7]

The details of AQE calculation as follows;

The evolved H_2 molecules at the end of 3 h, for 15 mg of photocatalyst at the irradiation wavelength of 420 nm was found to be 0.383 µmol and accordingly, AQE was estimated using the following formula and it was found to be 3.35%.

AQE (%) = [Number of reacted electrons or holes]/[number of incident photons] x 100 = [2 x number of H_2 molecules evolved]/[number of incident photons] x 100

Chapter 5: Chemically bonded Ni co-catalyst onto the S-doped g-C_3N_4 nanosheets and their synergistic enhancement in H_2 production under sunlight irradiation

Manh-Hiep Vu,[1] M. Sakar,[1] Chinh-Chien Nguyen,[1] Trong-On Do[1,*]

Department of Chemical Engineering, Laval University, Québec, G1V 0A6, Canada

1065, avenue de la Médecine, Québec (Québec), G1V 0A6, CANADA

*E-mail: trong-on.do@gch.ulaval.ca

ACS Sustainable Chem. Eng. 2018, 6, 3, 4194–4203

We have demonstrated the chemically bonded Ni co-catalyst-induced sunlight driven photocatalytic hydrogen generation efficiency of sulfur-doped g-C_3N_4 nanosheets.

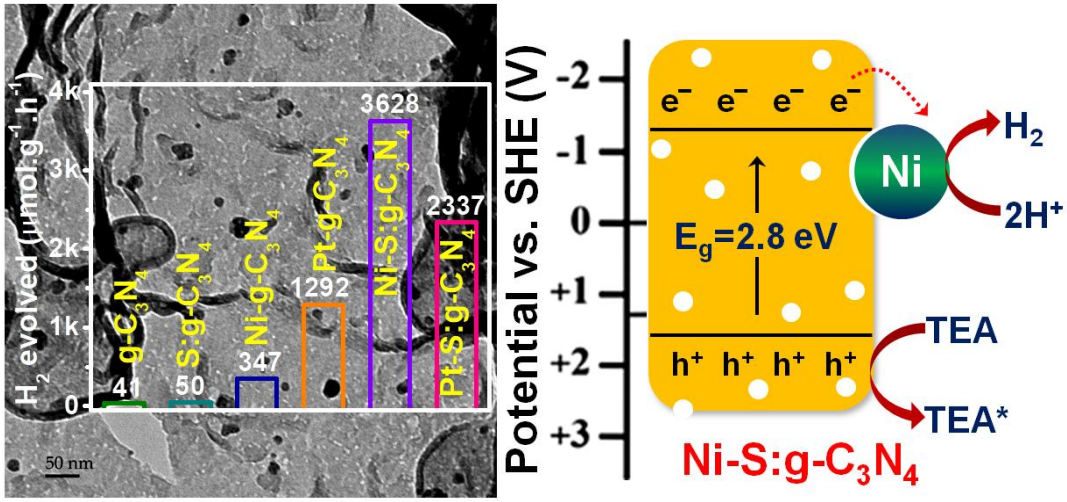

Résumé

Des nanoparticules de nickel déposés sur des nanofeuilles de nitrure de carbone graphitique dopé au soufre avec des nanoparticules de nickel déposées à la surface (Ni-S: g-C_3N_4/Ni-SCN) ont été synthétisées en utilisant une calcination, suivie d'une étape de sulfuration. Les spectres photoélectroniques aux rayons X (XPS) ont révélé que les atomes dopant de soufre sont introduits avec succès dans le réseau cristallin de l'hôte g-C_3N_4. Les spectres XPS ont indiqué que les espèces de Ni déposées sont liées chimiquement aux nanofeuilles de hôtes SCN via des liaisons nickel-soufre. L'efficacité de la production photocatalytique d'hydrogène des nanofeuilles Ni-SCN synthétisées apparait être de 3628 µmol. $g^{-1}.h^{-1}$ sous irradiation de la lumière visible, ce qui est environ 1,5 fois plus élevé que celui du Pt-SCN synthétisé dans la présente étude. L'efficacité observée est attribuée à la liaison chimique entre le Ni et le S qui favorise largement le processus photocatalytique en terme de séparation des charges ainsi que de réactions autocatalytiques. Son efficacité quantique à 420 nm est estimée de 17,2%, ce qui est l'une des valeurs les plus élevées rapportées dans la littérature pour les matériaux de nitrure de carbone. Les résultats de recyclabilité ont montré une efficacité constante de dégagement d'hydrogène sur 4 cycles (8 h) qui a démontré l'excellente stabilité du photocatalyseur. Ce travail a prouvé que la liaison chimique du cocatalyseur sur le photocatalyseur hôte est une stratégie relativement efficace par rapport à la méthode conventionnelle pour la préparation de cocatalyseur au moyen de forces électrostatiques ou de Van der Waals.

Abstract

Nickel deposited S-doped carbon nitride (Ni-S:g-C_3N_4/Ni-SCN) nanosheets have been synthesized using calcination followed by the sulfidation process. X-ray photoelectron spectra revealed that the doped S atoms are successfully introduced into the 301 lattices of the host g-C_3N_4. XPS spectra indicated that the deposited Ni species are chemically bonded onto the host SCN nanosheets through sulfur bonds. The sunlight-driven photocatalytic hydrogen production efficiency of the synthesized Ni-SCN nanosheets is found to be 3628 $\mu mol.g^{-1}.h^{-1}$, which is around 1.5 folds higher than that of Pt-SCN that is synthesized in the present study. The observed efficiency is attributed to the chemical bonding of Ni through S that largely favored the photocatalytic process in terms of charge-separation as well as self-catalytic reactions. The apparent quantum efficiency of the photocatalyst at 420 nm is estimated to be 17.2%, which is relatively one of the higher values reported in the literature. The photocatalytic recyclability results showed consistent hydrogen evolution efficiency over 4 cycles (8 h) that revealed the excellent stability of the photocatalyst. This work has demonstrated that the chemical bonding of co-catalyst onto the host photocatalyst is a relatively effective strategy as compared to the conventional deposition of co-catalyst by means of electrostatic or Van der Waals forces.

5.1 Introduction

The increasing depletion of the fossil fuels and the crisis for energy resources and the associated environmental issues have urged alternative routes towards the development of renewable energy sources through the techniques such as photocatalysis, electrocatalysts, solar cells, and rechargeable metal-air batteries, etc. to be found [261-263] Of various techniques, photocatalysis is one of the most promising approaches for sustainable energy production as it effectively converts the solar energy into chemical energy. Especially, since the last several decades, the photocatalytic H_2 evolution reaction (HER) through water splitting under solar energy has received tremendous attention because of its potential in concurrently dealing with the energy crisis and environmental problems.[264] In this direction, the noble metals sensitized photocatalysts have been found to be efficient for such effective water splitting applications. [265] However, the practical implementation of such photocatalytic system is limited due to the cost of the noble metals. Therefore, the explorations of noble metal-free photocatalytic systems have gained significant interest. Among the various photocatalysts, the metal-free graphitic carbon nitride (g-C_3N_4/GCN), a nitrogen-rich carbon, is considered as a promising candidate for photocatalytic applications,[266 267]thanks to its promising features that include excellent stability, the narrow bandgap energy (E_g ~ 2.7 eV),[268] straightforward preparation and cost-effectiveness. However, the conventional bulk g-C_3N_4 exhibits limited photocatalytic activities due to the faster carrier recombination rate, originated by the weak π-π conjugated stacked structure and low specific surface area. It has been reported that the recent strategies in the design of effective GCN-based photocatalysts comprise mainly the preparation of nanoscale GCN,[269-271] bandgap tailoring through doping,[20, 272-276] molecular-modification, and the combination of GCN-based semiconductor composites.[246, 264, 277] Accordingly, the current and future developments in the field of g-C_3N_4 involve increasing their efficiency in terms of quantum efficiency (QY) and solar-to-hydrogen (STH) conversion.[278] To achieve the former, g-C_3N_4 has been modified for their size and morphological designs and integrating with various types of materials to produce g-C_3N_4 hybrids and nanocomposites as to essentially increase their surface area and reduce the electron-hole recombination process. Similarly, to achieve the latter, g-C_3N_4 has been modified for their optical properties through making their hybrids with visible-light-driven

semiconductors (~600 nm), plasmonic nanomaterials and doping with metals and non-metals to suitably engineer their bandgap to absorb full-sunlight energy (UV-Vis-NIR).[278]

In particular, enormous attention has been devoted to the fabrication of nanosheets of GCN because of their thin-layered structure and large specific surface area, which could mainly overcome the existing limitations such as low surface area and poor stacking of the polymeric layers of GCN. Therefore, it is necessary to find appropriate methods for separating those bundles of layers into thin layers. Niu *et al.*[279] employed a conventional thermal-exfoliation of dicyandiamide-delivered bulk GCN to obtain the GCN-nanosheets with a high surface area of 306 m^2/g. However, the bandgap of nanosheets was increased to 2.97 eV due to a decreased size, and as it is known that the extended bandgap energy may decline visible light absorption ability. On the other hand, the tunable bandgap in GCN can be achieved by doping with foreign elements.[280-282] Especially, the bandgap of the bulk GCN could be reduced by anion doping via three main strategies: (i) formation of localized states in the bandgap structure, (ii) elevation of the valence band, and (iii) lowering of the conduction band.[283-284] It is known that the valence band (VB) of g-C_3N_4 is composed of N 2p state, while the conduction band (CB) is composed of the hybridized N 2p and C 2p states. Therefore, the site-dependent substitution of elements helps to tune the VB and CB edge positions. Especially, the doping of non-metals such as S increases the visible light absorption efficiency of g-C_3N_4, due to the generation of localized energy levels in the band structure of the system.[283] Besides, it is reported that doping of non-metals with low electro-negativity relatively elevates the VB maximum.[285-286] The Density Functional Theory (DFT) calculations also revealed that the bandgap energy of g-C_3N_4 can be reduced by doping it with non-metals such as S and P.[286] It is also concluded from the results that the non-metal doping facilitates the photocatalytic activity of g-C_3N_4 by (i) increasing the visible light absorption, (ii) modifying their carrier mobility and (iii) efficiently separating the electron-hole pairs in the system.[286] In this context, our strategy is to achieve tunable bandgap energy through S doping and to increase the surface area through the separation of the layers.

On the other hand, in the photocatalytic perspective, the integration of a co-catalyst onto the host photocatalysts can effectively enhance their photocatalytic activities by means of charge-separation, transportation, and self-catalytic properties. Conventionally, the

cocatalysts are often found to be noble metals such as Pt, Pd, etc.[281-282]. However, the rarity and cost of these noble metals limit their practical applications in the scale-up production of such noble-metals deposited photocatalysts. Therefore, the development of non-noble metal-based co-catalysts with enhanced properties is a great challenge. Among the known non-noble metal co-catalysts, Ni has been realized to be one of the stable, active, and cost-effective cocatalysts towards HER and CO_2 reduction.[287-288] In particular, Ni has been reported as an ideal co-catalyst for sulfur-based photocatalysts such as CdS, $Cd_{1-x}Zn_xS$, and $ZnIn_2S_4$.[236, 289-291] It is reported that the deposition of Ni^{2+} onto the g-C_3N_4 facilitates an efficient photochemical proton reduction and thereby enhances the H_2 production.[292] This is essentially due to the trapping of electrons in Ni species that effortlessly reduces H^+ ions into H_2 as given in **Equation (5.1)**.[293]

$$Ni/2H^+ + 2e^- \rightarrow Ni + H_2 \qquad (\mathbf{5.1})$$

However, the key issue in the above process is the conversion of Ni^{2+} ions to Ni^0, which considerably reduces the long-term proton reduction. Motivated by this issue, herein we have attempted a strategy to deposit Ni onto the g-C_3N_4 through S bonding and studied for their sunlight-driven photocatalytic properties towards H_2 production. This strategy of integrating the Ni co-catalyst by means of chemical bonding onto the host g-C_3N_4 nanosheets essentially facilitates a synergistic enhancement in the photocatalyst system as compared to the conventional co-catalyst integrated photocatalysts through electrostatic or Van der Waals forces.

5.2 Experimental Section

5.2.1 Materials

Dicyandiamide, Nickel ammonium sulfate, Chloroplatinic acid hexahydrate, H_2S gas (5% H_2S; 95% N_2), Ethanol, and distilled water were purchased from the commercial sources and used without further purification.

5.2.2 Synthesis of S-doped g-C_3N_4:

Graphitic carbon nitride was prepared to the method reported in other literature studies previously with some modification[294]. Briefly, 30 g of dicyandiamide precursor was calcined in a muffle furnace at 600 ^oC for 4 h with a heating rate of 2 ^oC/min. After cooling down to

ambient temperature, the as-prepared g-C_3N_4 sample (denoted as GCN) was washed with distilled water and ethanol several times and dried at 60 ^oC overnight. In the next step, the dried sample was further treated under H_2S gas flow of 4 L/h at 450 ^oC for 2 h (H_2S treatment of g-C_3N_4, denoted as SCN). For comparison, different gases have been employed such as argon, air. Also, the photodeposition of Pt on SCN was examined and compared to that of Ni-based cocatalyst.

5.2.3 Photodeposition of Ni onto SCN

Typically, 50 mg of the photocatalyst was dispersed in 100 mL of an aqueous solution of 10% triethanolamine, which acts as a sacrificial reagent. Then, the mixture was purged with nitrogen for 30 min to remove dissolved oxygen. After that, an optimized amount of 2 wt% of Ni precursor was added to the above dispersion and stirred well for 30 min, and then solution-dispersion was irradiated with the simulated solar light. The change of solution-color from white to grayish indicated the Ni disposition onto the samples as shown in **Figure S5.1**, given in the supporting information. Finally, the Ni-supported SCN was washed with distilled water and ethanol before testing photocatalytic activity and further characterizations. This process was repeated with Pt-precursor as to prepare the Pt-deposited samples.

5.2.4 Characterizations

Transmission electron microscopy (TEM) images of the samples were obtained on a JEOL JEM 1230 operated at 120 kV. Powder X-ray diffraction (XRD) patterns of the samples were obtained on a Bruker SMART APEXII X-ray diffractometer equipped with a Cu Kα radiation source (λ = 1.5418 Å). X-ray photoelectron spectroscopy (XPS) measurements carried out in an ion-pumped chamber (evacuated to 10^{-9} Torr) of a photoelectron spectrometer (Kratos Axis-Ultra) equipped with a focused X-ray source (Al Kα, hν = 1486.6 eV). The UV-Vis absorption spectra were recorded on a Cary 300 Bio UV-Vis spectrophotometer. Fourier transform infrared (FTIR) spectra were measured with an FTS 45 infrared spectrophotometer with the KBr pellet technique. The photocurrent measurements were carried out in a conventional three electrodes station (Autolab PGSTAT204).

5.2.5 Photocatalytic studies

In a typical photocatalytic experiment, firstly, an optimized amount of 50 mg of the photocatalyst was dispersed in a solution containing 90 mL of water and 10 mL of a sacrificial agent of triethanolamine (TEA), which was taken in a reactor cell. Then, the reactor cell was illuminated using a solar simulator 150 W Xe lamp for 2 h and measured the evolved hydrogen using GC. This procedure was repeated for 4 cycles, where the residual hydrogen was removed by purging the nitrogen gas for 30 min before starting every new cycle. The amount of H_2 gas generated was determined using a gas chromatograph (GC) equipped with a thermal conductivity detector (TCD), and N_2 as the carrier gas.

The apparent quantum efficiency (AQE) of the prepared sample was calculated according to the following equation;

AQE (%) = (Number of reacted electrons or holes)/(number of incident photons)x 100 = (2 x number of H_2 molecules evolved)/(number of incident photons) x 100

5.2.6 Photoelectrochemical Measurements

The working electrodes were prepared as follows: 5 mg of photocatalysts was dispersed in 2.5 mL ethanol and 2.5 mL isopropanol to make the slurry of the materials. Then, the slurry was coated onto 1 cm x 1 cm F-doped SnO_2-coated (FTO) glass electrode by spin coating technique. Next, the as-prepared electrodes were dried overnight and calcined at 350 ^oC in a nitrogen gas flow. Transient photocurrent response was performed on an electrochemical workstation (Autolab PGSTAT204) based on a standard three-electrode system using the as-prepared electrodes as the working electrodes. A Pt wire and Ag/AgCl was used as the counter electrode and reference electrode, respectively. The photocurrent was measured under solar light irradiation (150 W xenon lamp) with 10s light on-off cycles. For the electrochemical impedance (Nyquist plots) measurements, the perturbation-signal was set to be 10 mV and the frequency range was from 0.1 MHz to 0.1 Hz.

5.3 Results and discussion

Figure 5.1(A) shows the simulated-sunlight driven photocatalytic hydrogen production of the Ni and Pt deposited GCN and SCN samples. The obtained results showed that the Ni-SCN exhibited the highest hydrogen production efficiency as compared to Pt-SCN at the same concentration. In contrast, the Ni-GCN showed decreased photocatalytic efficiency as

compared to Pt-GCN. This observation clearly indicates that the S doping in g-C_3N_4 readily facilitates the integration of Ni than that of Pt and the favors enhanced photocatalytic reactions. This enhancement could be attributed to the integration mechanics of Ni onto the SCN. In addition to this, the quantum efficiency (QE) of the Ni-SCN was calculated and found to be 17.2% at 420 nm (**Figure 5.1(B)**), which is relatively one of the higher values in the literature as listed in **Table S5.1**-given as the supporting information. The calculated AQE values of Ni-SCN nanosheets at different wavelengths with respect to their absorption spectrum are shown in **Figure 5.1(B)**.

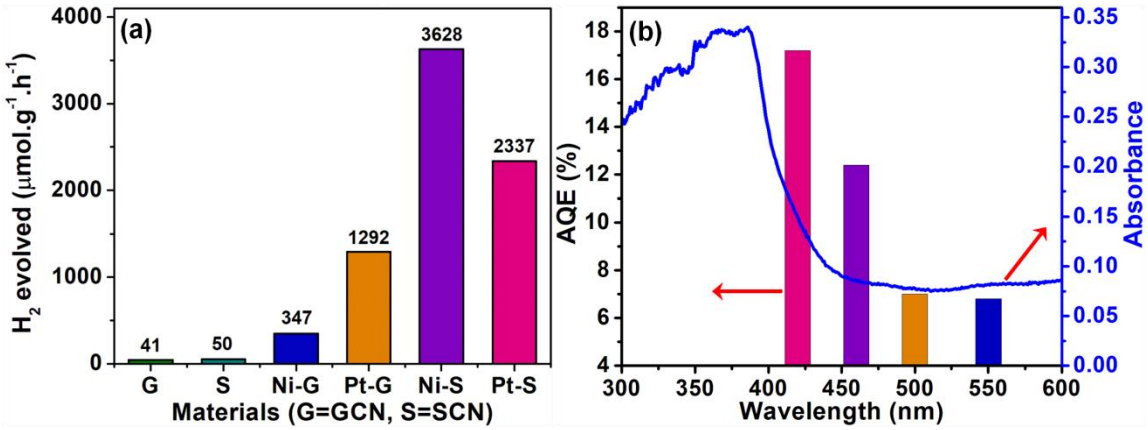

Figure 5.1: (A) Photocatalytic hydrogen evolution over various samples under solar light; **(B)** AQE values of H_2 production over the Ni-SCN sample under various monochromatic light irradiations given with respect to its absorption spectrum.

To gain insights into the observed photocatalytic efficiency, the samples were further analyzed in detail. Accordingly, the high-resolution XPS spectra of C, N, S, and Ni in the respective pristine g-C_3N_4, SCN, and Ni-SCN samples are obtained and displayed in **Figure 5.2(A)-(D)**, respectively. As shown in the C 1s spectrum of GCN (**Figure 5.2(A)**), the deconvoluted peaks centered at 284.5 and 287.6 eV could be attributed to sp^3-bonded carbon in C-C and N-C=N, correspondingly. However, the XPS peak of N-C=N is found to be at positive shift to higher binding energies at 287.9 and 287.8 eV in SCN and Ni-SCN samples. This may be due to the factor that during H_2S treatment at high temperature, some of the C atoms in tri-s-triazine units leached and led to carbon vacancies in the SCN, which is also further confirmed by elemental analysis as provided in **Table S5.2** in the supporting information. Moreover, the observed increase in the intensities of the C 1s spectra of both

SCN and Ni-SCN demonstrated that C atoms neighboring carbon vacancies have reduced electron density than those ones on the normal sites,[295] leading to a shifted peak to the higher binding energy. The existence of a hump-like peak at 286.1 and 286.0 eV in the XPS spectrum of SCN and Ni-SCN, respectively can be assigned to C-O bonding,[296] which may be originated from the absorbed oxygen on the surface.

The XPS spectra of N in pristine g-C_3N_4, SCN, and Ni-SCN are shown in **Figure 5.2(B)**. The N 1s spectrum is found to be similar for all the samples, except the variation in the profile of the peaks. The de-convoluted peaks located at ~398.2 eV can be ascribed to the sp^2-bonded nitrogen in C-N=C groups while the peaks at ~399.5 eV correspond to the nitrogen in the tertiary group (N-$(C)_3$). In addition, the amino-functional groups with a hydrogen atom C-NH can be attributed to the weak peaks at ~401.0 eV. The observed peak of S 2p for SCN at 164.5 eV is due to the lattice S in the host g-C_3N_4 (**Figure 5.2(C)**). Similarly, the peaks located at 162.0 and 163.5 eV are corresponding to C-S bonds in SCN. Importantly, these observed binding energies indicate the -2 oxidation state of S atoms in SCN. On the other hand, these characteristic peaks are found to be shifted towards lower binding energy by around 1.0 eV in the case of Ni-SCN. This essentially indicates that the interaction of Ni with SCN is not through physisorption, but it could be due to chemisorption, where it reveals that Ni is chemically bonded onto the SCN rather than the through electrostatic or Van der Waals interactions. Further, the peak corresponding to the lattice S (164.7 eV) is completely suppressed as it is largely dominated by Ni through their chemical bonding with S in the SCN. Moreover, it should be noted that the S atoms replace the N atoms and make bonds with C atoms in the SCN system, while in Ni-SCN, the S atoms also make bonding with Ni atoms. Therefore, the chemical environment of the S species is different in the SCN as compared to their chemical environment in Ni-SCN. These changes in the chemical environment of S atoms lead to significant modifications in both the binding energy and profile of XPS peaks of S species. It is also noteworthy that the physisorption such as electrostatic interaction will lead to only a slight shift in the binding energy of the species as the interaction occurs through the electrical charges, while the chemisorptions make significant changes in the binding energy as the species are chemically bonded. Accordingly, during the photo-deposition process, the adsorbed Ni^{2+} ions on the SCN sample readily bind

with S^{2-} species in the host SCN, thereby it establishes a strong chemical bonding between the deposited Ni and the host SCN, through the Ni-S-C-N bond formation in the system.

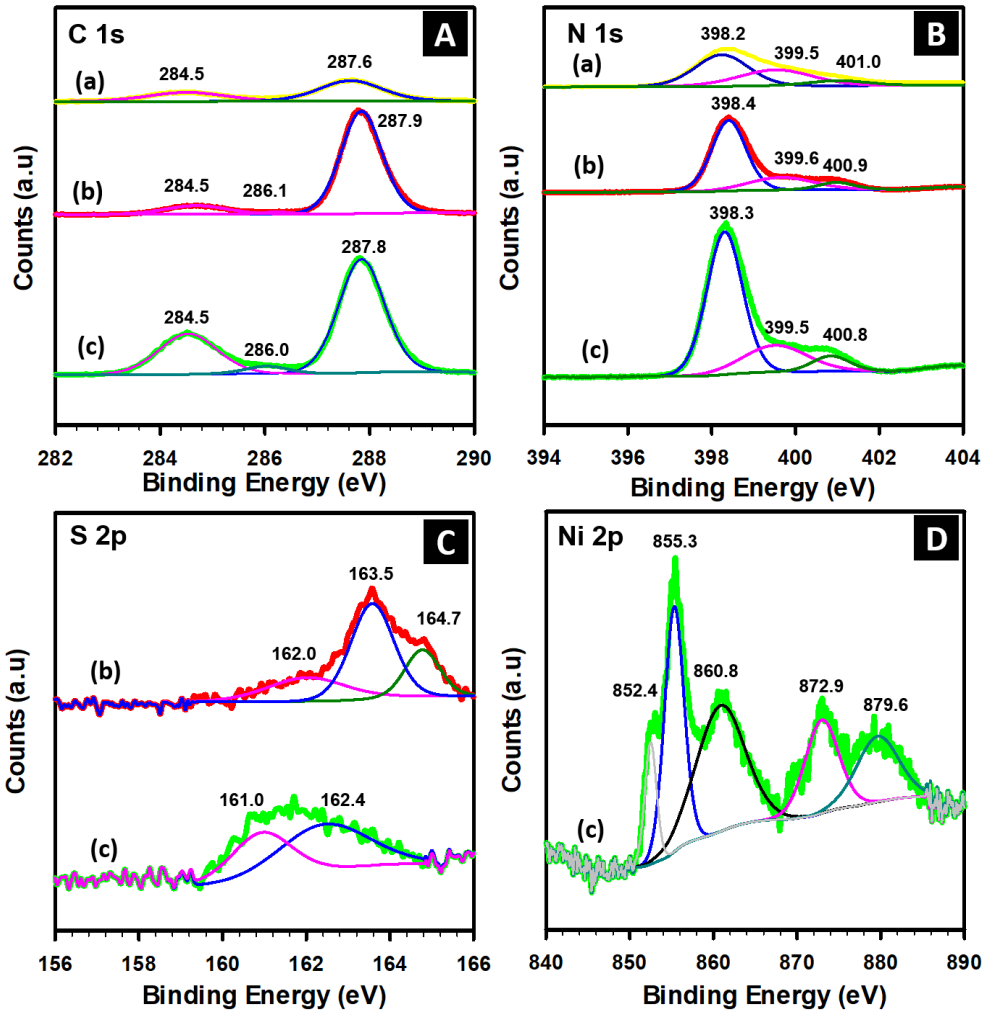

Figure 5.2: XPS spectra of **(A)** C 1s, **(B)** N 1s, **(C)** S 2p and **(D)** Ni 2p. Inset figures, **(a)** GCN, **(b)** SCN, **(c)** Ni-SCN.

The XPS spectrum of Ni 2p is displayed in **Figure 5.2(D)**, where the deconvoluted peak at 852.4 eV indicates the zero oxidation state (metallic Ni) of Ni, while the other two peaks at 855.3 and 860.8 eV can be assigned to Ni^{2+} that due to the formation of Ni-S bonds. Sergey *et al.*[297] reported that the sulfur tends to donate its electron to π-π conjugation system to form p_x and p_y-orbitals, while in some cases a partial back-donation of electrons to the S p_z-orbital also takes place. It is therefore the metallic nickel with an electron pair occupied in s-orbital that becomes electron donor which can easily donate electrons to S p_z-orbital to form Ni-S

bonds. Such chemical bonding will essentially lead to an increase in the electron density in S atoms along with increasing electron density in C atoms, which leads to a significant shift towards the lower binding energy in the XPS spectra of Ni-SCN. These results suggest that the Ni is chemically bonded onto the S doped g-C_3N_4, which effectively drives the charge carriers and enhances the photocatalytic reactions.

Figure5.3 shows the XRD pattern of the synthesized pristine g-C_3N_4, SCN, and Ni-SCN samples. The obtained XRD patterns indicate the crystalline phase of g-C_3N_4 without any secondary or impurity phase (JCPDS #87-1526). The two respective peaks centered at 13.1^o (100) and ~27.8^o (002) are attributed to the in-plane structural packing of tri-s-triazine motifs and repeated inter-planar stacking of conjugated aromatic systems corresponding to the stacking distance of 0.682 and 0.326 nm, respectively.[298] The observed slight shift in the XRD pattern of bare g-C_3N_4 with respect to the standard peaks may be due to the reduced size (layer thickness) of g-C_3N_4 layers, while the standard patterns conventionally represent the bulk materials. Similarly, it should be noted that the profile of the peak corresponding to (100) plane is found to be significantly modified for SCN and Ni-SCN as compared to GCN, which could be attributed to the reduced length of the interlayer periodicity and the larger distance between carbon nitride nanosheets, which occurred possibly due to the lattice-occupation of S atoms in the host g-C_3N_4. Similarly, a visible shift can be observed for SCN and Ni-SCN with respect to GCN, which could be attributed to the doping-induced modification in the lattices and structure of the g-C_3N_4 layers.

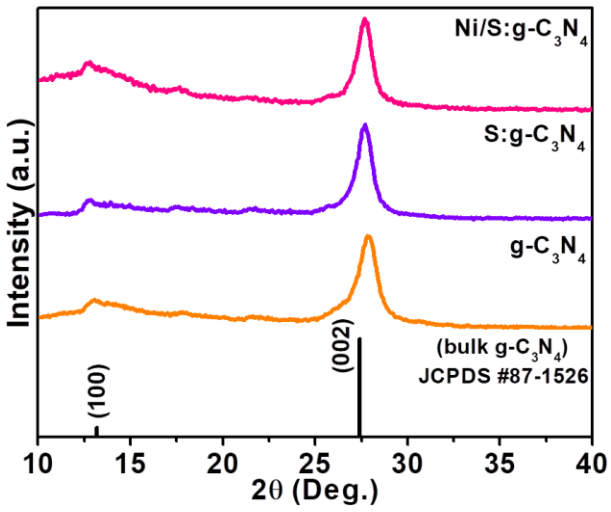

Figure 5.3: X-ray diffraction patterns of the synthesized samples.

The transmission electron microscopy (TEM) images of SCN and Ni-SCN, as given in **Figure 5.4(A)-(D)**, show their typical 2D nanosheet-like structures with a corrugated thickness of around 30 nm. It can be seen that the surface of SCN is likely found to be porous with nano-sized holes that may be formed due to the high-temperature formation of SCN at 600 °C. It should be noted that these nanoholes and distorted atomic arrangement essentially serve as rich-active sites and may lead to a significant enhancement in the charge transfer characteristics of the nanosheets and improvement in their photocatalytic activities. **Figure 5.4(C)-(D)** displays the TEM images of Ni-SCN, where the average size of the integrated Ni nanoparticles is measured to be 10 nm, and they found to be highly dispersed on the surface of SCN, which might have possibly functioned as abundant reduction and self-catalytic sites over SCN surface.

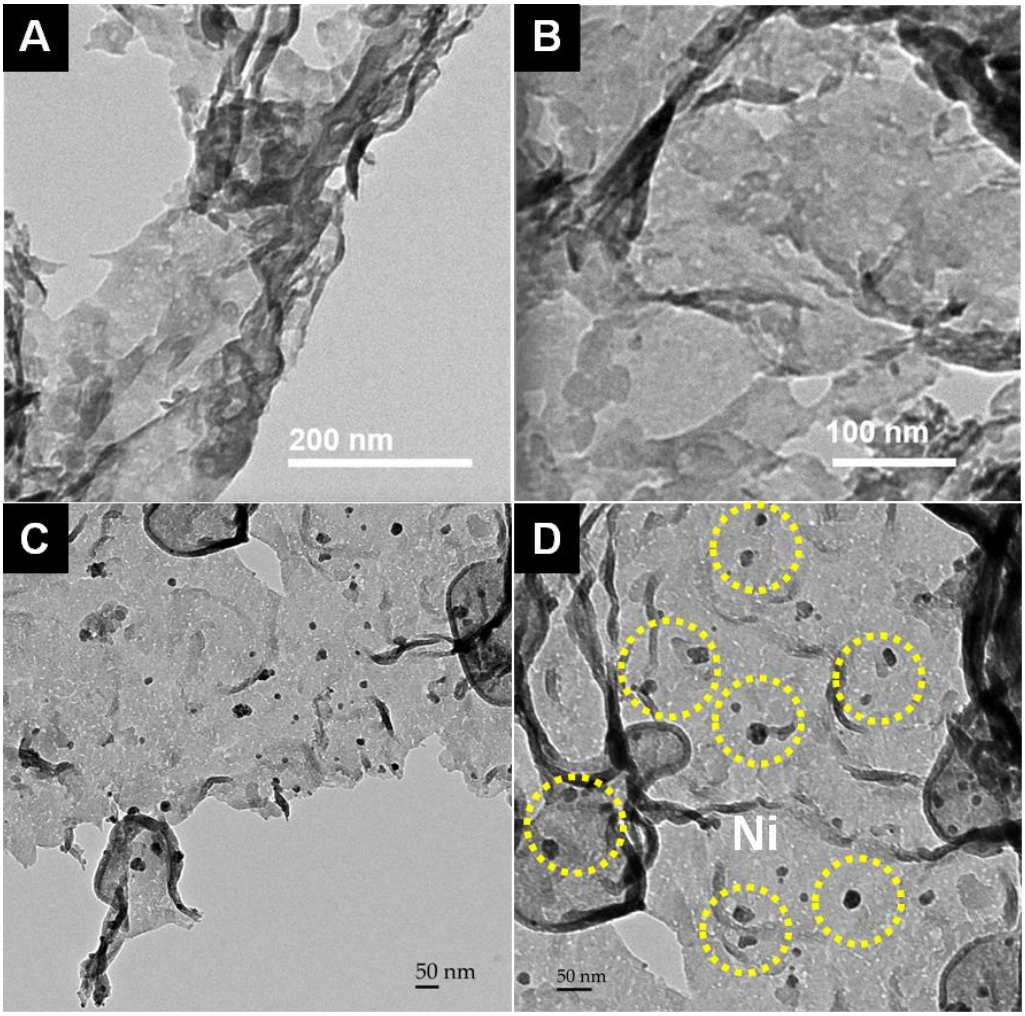

Figure 5.4: (A)-(B) TEM images of SCN and **(C)-(D)** TEM images of Ni-SCN.

The CNSH elemental analysis of the SCN sample is given in **Table S5.2** (in SI). The respective stoichiometric ratio of C/N and sulfur content is determined to be 0.56 and 0.6 at%, suggesting that sulfur is successfully introduced into the host g-C_3N_4. Also, the off-stoichiometric C/N ratio suggested a number of carbon vacancies presented in the sample of SCN. The N_2 adsorption/desorption isotherm and pore-size distribution curves of the GCN and SCN are shown in **Figure 5.5(a)-(b)**, respectively. From the results, the specific surface area of GCN is calculated to be 26 m^2g^{-1}, which is increased to 85 m^2.g for SCN. This could be attributed to (i) the thermal exfoliation of GCN during H_2S treatment, which reduced the thickness of GCN layers by separating the stacked layers along with the S doping, and (ii) the porous surface of SCN. These changes in the size and morphological parameters eventually resulted in the increased specific surface area of SCN.

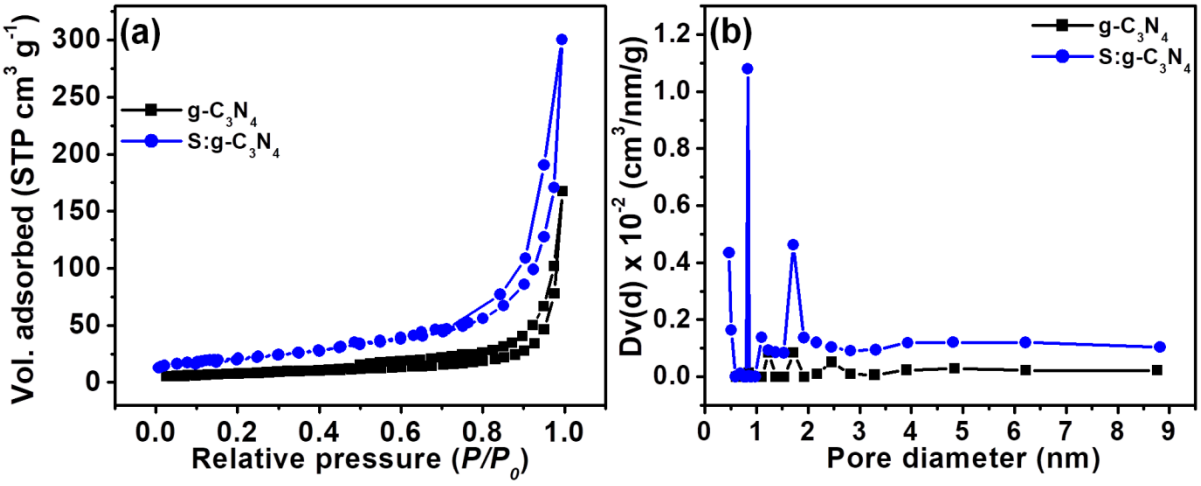

Figure 5.5: (a) Nitrogen adsorption-desorption isotherms at 77 K and (b) Pore-size distribution.

The UV-Vis absorption spectra of the GCN, SCN, and Ni-SCN are presented in **Figure 5.6(A)** and the bandgap energy of the obtained materials was calculated using Tauc plot[299-300] and found to be 2.84, 2.81, and 2.79 eV for GCN, SCN, and Ni-SCN, respectively (**Figure 5.6(B))**. Both GCN and SCN showed a similar absorption profile with a strong absorption edge around 400 nm along with a slight absorption enhancement for SCN. By contrast, the absorption curve of Ni-SCN extended up to 800 nm as compared to GCN and SCN. It should be noted that the S-doping on GCN is not leading to any "shift" in the absorption profile essentially because of the hardly altered bandgap structure of SCN. This may be due to the

amalgamated role of S doping and the carbon vacancy defects along with the reduced size of SCN layers. In general, while the S doping and defects tend to reduce the bandgap energy of SCN, the reduced size of SCN layers tends to increase it. Therefore, the competition between the S doping induced defects and reduced size of SCN layers resulted in the relatively unmodified optical properties in SCN. Similarly, the absorption profile of Ni-SCN is also not largely altered except for an extended absorption band edge in the range from 450-800 nm, which could be attributed to the chemical bonding of Ni onto the host SCN. It is discussed that the VB and CB of g-C_3N_4 is composed of N 2p states and hybridized N 2p-C 2p states, respectively. Accordingly, it is found that the doping of S atoms into the N site slightly modified their optical properties. Under such circumstances, the Ni, which is chemically bonded through the S atoms, creates localized electron trapping centers that influenced the optical properties of the material and led to an extended absorption up to 800 nm as akin to the plasmon-sensitized systems.

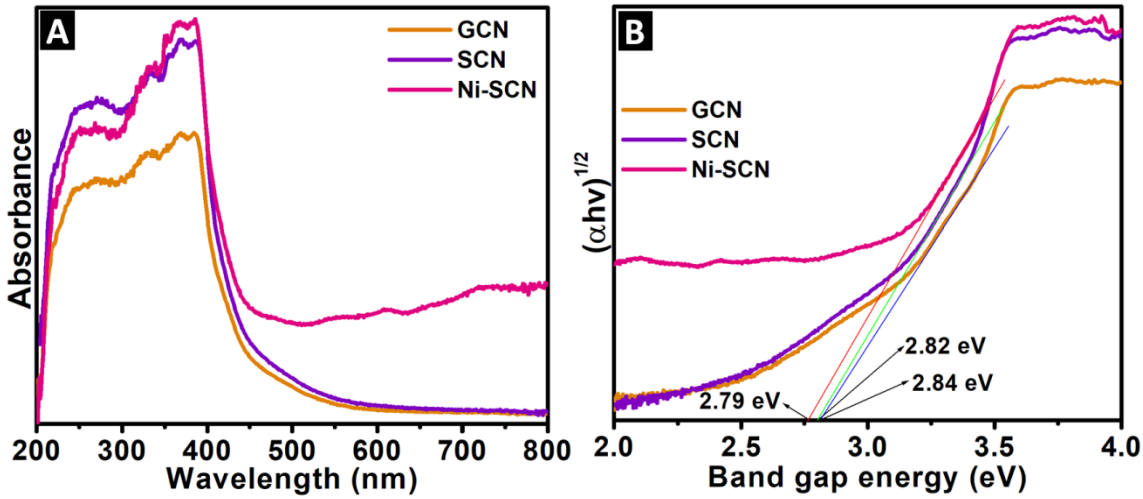

Figure 5.6: (A) UV-Visible absorption spectra of GCN, SCN, and Ni-SCN; **(B)** Estimation of bandgap energy of GCN, SCN, and Ni-SCN.

The FTIR analysis was performed in order to investigate the chemical bonding in GCN, SCN, and Ni-SCN nanostructures, and obtained spectra are shown in **Figure 5.7.** The FTIR skeletal structure of g-C_3N_4 is found to be unaltered due to S doping and Ni integration. However, the intensity of the peaks is decreased, which essentially represents the influence of S and Ni over the stretching of C-N bonds. Accordingly, the observed signals in the range from 1200-1650 cm^{-1} could be assigned to the stretching vibrations of heptazine heterocyclic ring (C_6N_7)

units.[301-302] The peak appeared at 810 cm^{-1} represents the characteristic breathing vibration of triazine units, which is due to the condensed-CN heterocycles.[303] The peak at 885 cm^{-1} could be ascribed to the deformation of N-H bonds.[304] A band at 2380 cm^{-1} can be assigned to the adsorbed CO_2 on the surface of the samples. The bands in the range from around 2900 cm^{-1} to 3500 cm^{-1} regions can be ascribed to the adsorbed H_2O molecules and N-H vibration of the uncondensed amine groups[305] in the compositions. Interestingly, these bands are almost disappeared for Ni-SCN, which could be due to the S doping as it established a surface chemical bonding through the Ni-S-C-N formation. Overall, the absorbed decreased intensity in the FTIR spectrum of Ni-SCN with respect to GCN and SCN could be attributed to the S doping, Ni integration, and sized reduction induced changes in the chemical bonding in the functional groups of the g-C_3N_4 structure.

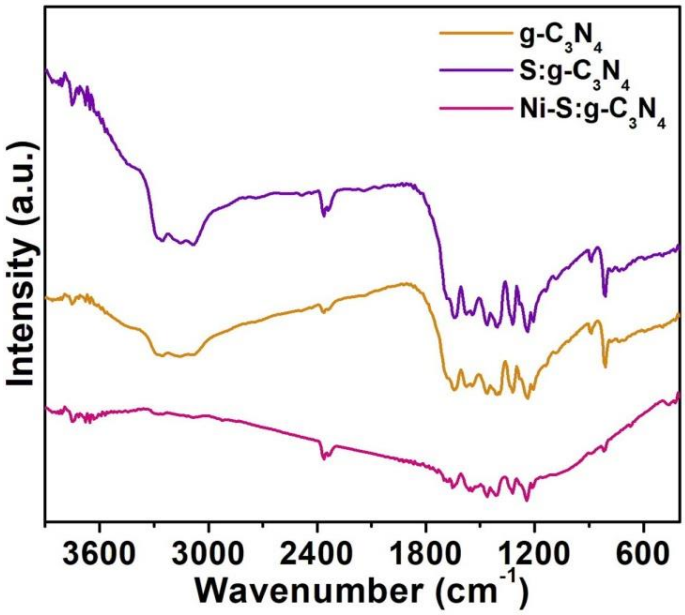

Figure 5.7 FTIR spectra of the synthesized materials.

Figure 5.8(A) shows the amount of hydrogen generated over the Ni-SCN system with different Ni concentrations. It should be noted that the loading of Ni cocatalyst on SCN significantly enhances the photocatalytic activity towards H_2 evolution. Without cocatalyst, only around 50 $\mu mol.g^{-1}.h^{-1}$ of hydrogen was evolved. Interestingly, at 1 wt% Ni-SCN, the production rate can be drastically increased to 3107 $\mu mol.g^{-1}.h^{-1}$. It was further observed that the increasing amount of Ni to 2 wt% led to the production of the highest yield of 3628 $\mu mol.g^{-1}.h^{-1}$ H_2 molecules. However, at the higher loading of Ni at 3 wt%, the H_2 production efficiency was relatively decreased to 2528

$\mu mol.g^{-1}.h^{-1}$. It may be due to the poor bonding of Ni onto the SCN and screening behavior of excess Ni on the surface of SCN, which eventually inhibited the ability of light absorption and subsequent charge separation and transportations. Also, the photocatalytic activities of S doped g-C_3N_4 and Pt integrated SCN with increasing concentrations were also obtained and the results are shown in **Figure S5.2(a)-(b)**, respectively in the supporting information. From the results, it was observed that the H_2 production is found to be 1437, 2337, and 1828 $\mu mol.g^{-1}.h^{-1}$ for 1 wt%, 2 wt%, and 3 wt% Pt-SCN, respectively. These results demonstrated that the Ni integration is exceptionally better than Pt-SCN, which is mainly because of the factor that S doping sufficiently modifies g-C_3N_4 as to facilitate the chemical bonding of Ni co-catalyst. Further, the recyclability of Ni-SCN photocatalyst was also evaluated and it exhibited enhanced stability over 4 cycles (for 8 h) without any significant decrement in its activity (**Figure 5.8(B)**). Further, as mentioned in the introduction, Ni^{2+} could trap electrons for H_2 production, and the conversion from Ni^{2+} to Ni^0 would result in its decreased performance. Accordingly, the stability of Ni through the inhibition of Ni^{2+} to Ni^0 conversion due to Ni-S bonding is further verified using the XPS technique by recording the Ni spectrum of recycled Ni-SCN along with its TEM image as shown in **Figure S5.3(a)-(b)** given in SI. It suggests that chemically bonded Ni-SCN could be a promising photocatalyst for hydrogen evolution through water splitting process.

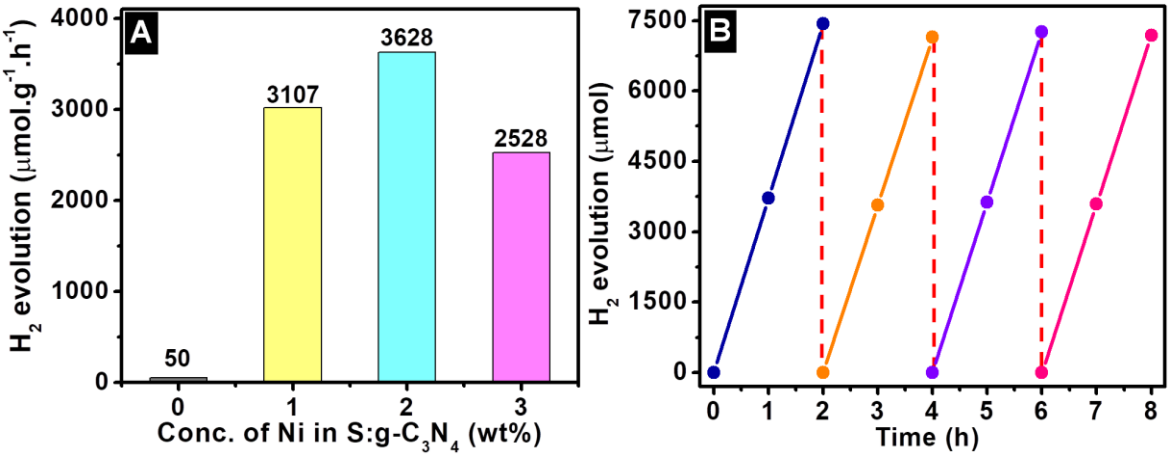

Figure 5.8: (A) Photocatalytic hydrogen evolution over Ni-SCN photocatalysts; **(B)** Recyclable efficiency of Ni-SCN.

As to further validate the observed results, the photocurrent efficiencies and electrochemical impedance behavior of SCN and Ni-SCN are studied and the obtained results are displayed

in **Figure 5.9(A)-(B)**, respectively. The photocurrent response of the samples was obtained via eight on-off cycles. It is clearly seen the photocurrent density of Ni-SCN is increased nearly 5 times as compared to SCN, which demonstrates a significant improvement in the separation of photo-generated charge carriers. [292] Similarly, it can be observed from the Nyquist plots (**Figure 5.9(B)**) that the impedance of SCN is much higher than Ni-SCN, which suggests that the enhanced charge transferring ability of Ni-SCN than that of SCN.[292] This further confirms the better charge transfer and decreased recombination possibilities in Ni-SCN, which is consistent with the photocurrent response of the sample. These observed enhancements could be attributed to the chemically bonded Ni-cocatalyst onto SCN that largely facilitates the photocurrent and improves the rapid migration of generated charge carriers to the surface.

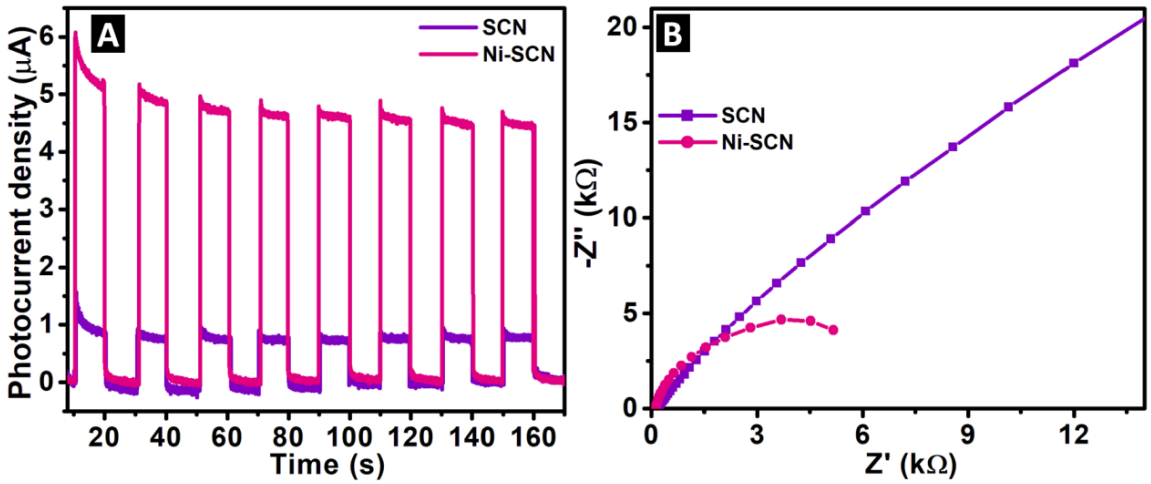

Figure 5.9: (A) Photocurrent response and **(B)** Nyquist plots for the electrochemical impedance of SCN and Ni-SCN photocatalyst.

Based on the above results, the photocatalytic efficiency of Ni-SCN can be explained as follows and the schematic illustration of the mechanism is given in **Figure 5.10(A)-(B)**. The mechanism of the observed efficacy could be attributed to two stages of the process; (i) enhanced charge separation and transportation and (ii) the self-catalytic behavior of chemically bonded Ni co-catalyst. Accordingly, the former could be attributed to the chemically bonded Ni-S induced modification in the band structure of g-C_3N_4,[283] where it forms new energy levels underneath the conduction of band (CB) as the energy states of S hybridized with C-N states, where it facilitates extended visible light absorption and rapid

charge separation and transportations as shown in **Figure 5.10(A)**, which is evidenced from the XPS results, transient photocurrent response and impedance results. Similarly, the latter mechanism, which is the self-catalytic behavior of the chemically bonded Ni, offers excellent proton reduction process as shown in **Figure 5.10(B).** Upon the irradiation, the excited electrons are trapped (as shown **in Equation (5.2)-(5.3)**), and they first lead to the formation of an intermediate HNi-S by absorption-reduction of H^+ and then generate H_2 by the subsequent reduction of H^+ as shown in **Equation (5.4)-(5.5)**.[306-308] The possibility of the formation of such type of HNi-S intermediate has been demonstrated through computational and experimental studies of hydro-treating processes.[309]

$$S{:}g\text{-}C_3N_4 + h\nu \rightarrow e^- (CB, S{:}g\text{-}C_3N_4) + h^+ (VB, S{:}g\text{-}C_3N_4) \quad (5.2)$$

$$Ni + e^- (CB, S{:}g\text{-}C_3N_4) \rightarrow e^- (Ni) + S{:}g\text{-}C_3N_4 \quad (5.3)$$

$$Ni\text{-}S + e^- + H^+ \leftrightarrow HNi\text{-}S \quad (5.4)$$

$$HNi\text{-}S + e^- + H^+ \leftrightarrow H_2 + Ni\text{-}S \quad (5.5)$$

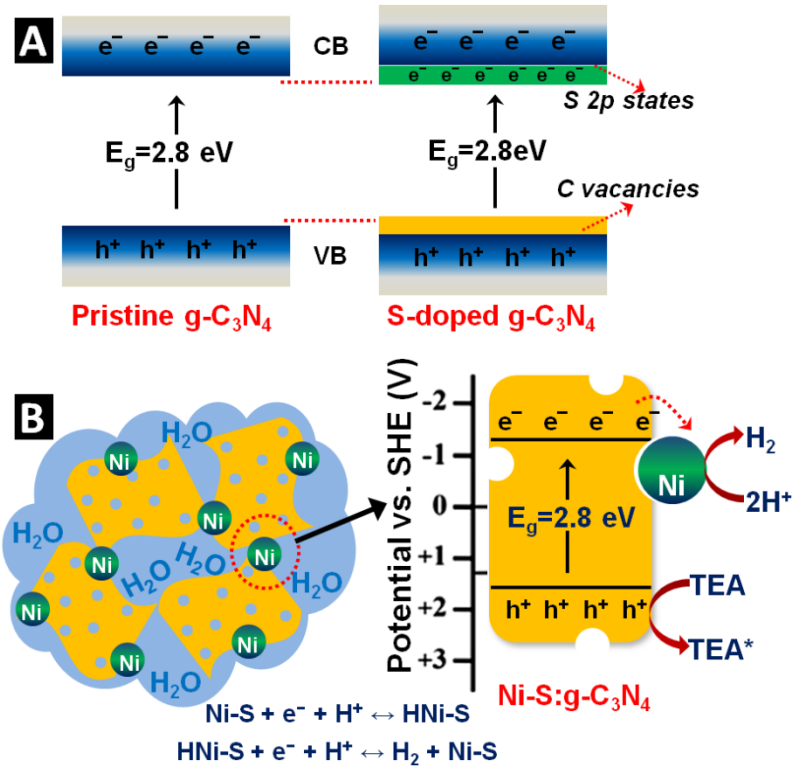

Figure 5.10: Illustration of **(A)** bandgap formation and **(B)** photocatalytic hydrogen evolution mechanism of Ni-SCN photocatalyst under solar light.

Apart from these chemical-structures induced contributions, the observed features in the physical structures such as the reduced size and nanoholes (pores) on the surface of Ni-SCN also facilitated a stronger interaction between the catalyst and surrounding molecules, which could also be attributed to the observed enhanced photocatalytic H_2 generation efficiency of the chemically bonded Ni-SCN system.

5.4 Conclusion

In summary, nickel supported S-doped g-C_3N_4 (Ni-SCN) nanosheets were successfully prepared through the calcination of dicyanamide followed by the sulfidation process. The obtained hydrogen production efficiency of Ni-SCN was found to be around 72.5, 10.5, and 1.5 folds higher than that of the bare SCN, Ni-GCN, and Pt-SCN, respectively. The apparent quantum yield was found to be 17.2% at 420 nm. The observed enhanced photocatalytic activity of Ni-SCN was attributed to the extended visible light absorption, high surface area, and the synergistic effect between the host SCN photocatalyst and the chemically bonded nickel co-catalyst through Ni-S-C-N chemical bonds, which enhanced the rapid charge separation and transportation and self-catalytic behavior of the Ni co-catalyst. From the obtained results, the chemical bonding of co-catalyst onto the photocatalyst can be realized as a promising strategy as compared to the other conventional deposition strategies, which eventually has the potential to replace the deposition of noble-metals as co-catalyst towards enhancing the visible-light-driven photocatalytic hydrogen production.

Acknowledgments

This work was supported by the Natural Science and Engineering Research Council of Canada (NSERC) through the Collaborative Research and Development (CRD), Strategic Project (SP), and Discovery Grants. The author would like to thank EXP Inc. and SiliCycle Inc. for their support.

5.5 Supporting Information

Literature comparison of the obtained efficiency of the material (**Table S5.1**), results of elemental analysis (**Table S5.2** and **Table S5.3**), photographic images of the samples (**Figure S5.1(a)-(b)**), photocatalytic hydrogen production of the samples (**Figure S5.2(a)-(b)**), TEM image and XPS spectrum of the recycled sample (**Figure S5.3(a)-(b)).**

Table S5.1 Comparison diagram of H_2 evolution activity and QE values reported in the literature and this work.

Photocatalyst	**Cocatalyst**	**AQE**	**Reference**
S-doped C_3N_4	Ni	17.2 (420 nm)	This work
C_3N_4	$Ni(OH)_2$	1.1 (420 nm)	[303]
C_3N_4	Ni	2.01 (400 nm)	[310]
C_3N_4	Ni	2.19 (365 nm)	[311]
C_3N_4	NiS	1.9 (440 nm)	[312]

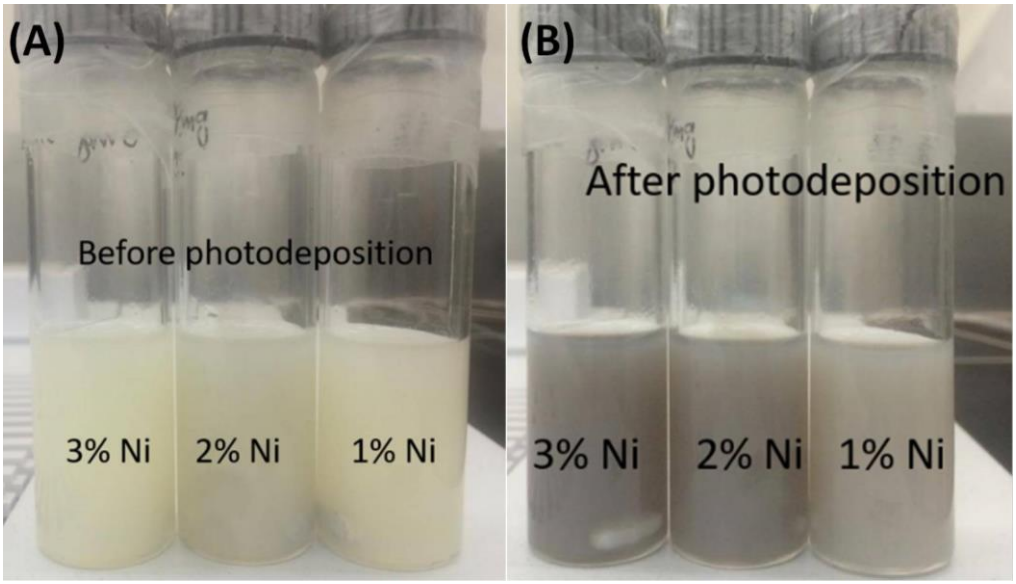

Figure S5.1 Color of the SCN solution (A) before and (B) after photo-deposition of Ni.

Table S5.2 CHNS elemental analysis of SCN (4 L/h H_2S).

Expt. No	Nitrogen	Carbon	Hydrogen	Sulfur
1	60.38	33.95	2.18	0.68
2	60.46	34.05	2.10	0.52
Average	60.42	34.00	2.14	0.60

Synthesis of S doped g-C_3N_4 with tunable concentration

To synthesize the S doped g-C_3N_4 with different concentrations, the flow rate of H_2S gas was varied such as 3, 4, 5, and 6 L/h at 450 °C for 2 h. These S doped g-C_3N_4 samples were denoted as 3SCN, 4SCN, 5SCN, and 6SCN, respectively. The samples were analyzed for their elemental analysis and the concentration of S was estimated and given in Table S3. The amount of H_2 produced on these S doped g-C_3N_4 samples is shown in **Figure S2(b)**. It can be observed from the obtained data that the ability of H_2 production is found to be decreased for 5SCN and 6SCN, which could be due to the off-stoichiometric presence of C/N and S content as given in the Table S3. It is realized that the stoichiometric ratio of the doped S atoms and C/N ratio could be an essential parameter for the efficient doping of S into the lattices of g-C_3N_4. Similar to the metal oxide systems, which have the limitations in doping, the stoichiometric ratio of C/N in g-C_3N_4 likely determines the successful doping S atoms in the system.

Table S5.3 CHNS elemental analysis of S doping in g-C_3N_4 at different concentrations.

System	Nitrogen	Carbon	Hydrogen	Sulfur
3SCN	62.83	38.12	2.11	0.51
4SCN	60.42	34.00	2.14	0.60
5SCN	59.01	32.47	2.02	0.67
6SCN	58.36	31.72	1.98	0.78

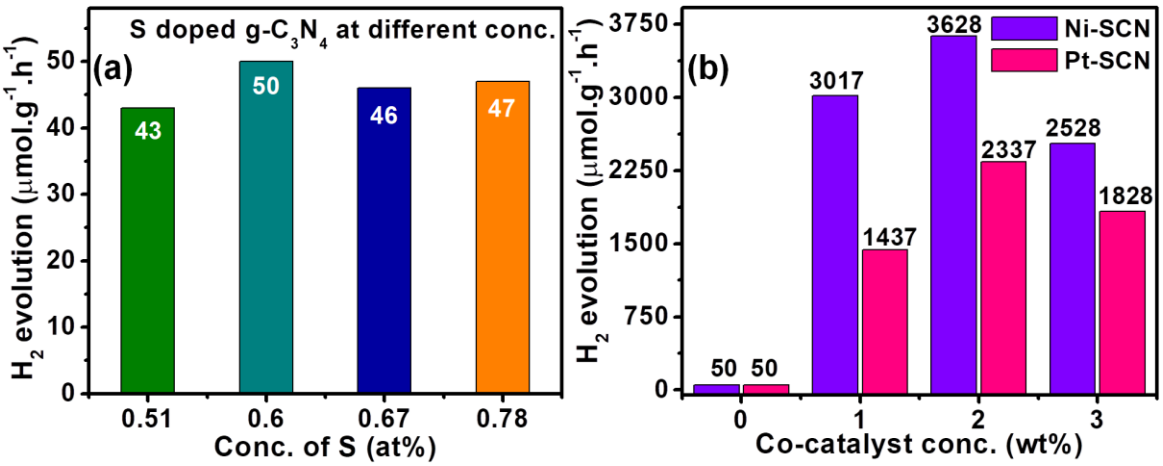

Figure S5.2 Photocatalytic H_2 evolution of (a) S doping in g-C_3N_4 (b) Pt and Ni supported S-doped g-C_3N_4 at increasing concentrations.

Morphological and structural analysis of the recycled photocatalyst

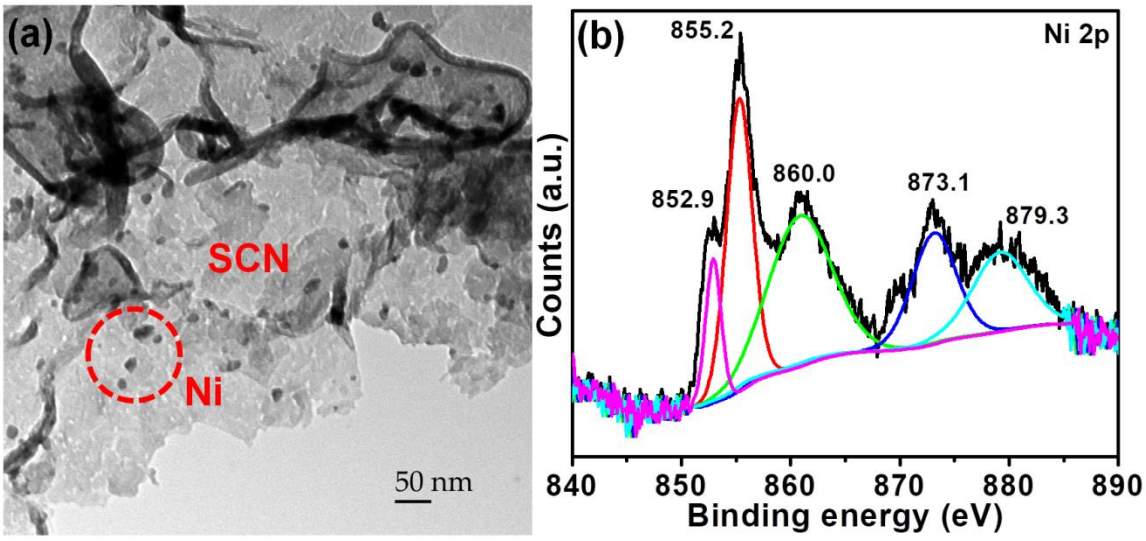

Figure S5.3 (a) TEM image of the recycled Ni-SCN and (b) XPS spectrum of the Ni 2p-in the recycled Ni-SCN sample showing unaltered oxidation state of Ni that confirms the stability of Ni due to Ni-S bond.

Chapter 6: Synergistic Effect of Fe doping and plasmonic Au nanoparticles on $W_{18}O_{49}$ nanorods for enhancing photo-electrochemical nitrogen reduction

Manh-Hiep Vu, M. Sakar, Chinh-Chien Nguyen, Trong-On Do*

Department of Chemical Engineering, Laval University, Québec, G1V 0A6, Canada

1065, avenue de la Médecine, Québec (Québec), G1V 0A6, CANADA

*E-mail: trong-on.do@gch.ulaval.ca

Submitted to ACS Sustainable Chem. Eng. 2020

Our work is the first to report the synthesis of Au loaded Fe doped $W_{18}O_{49}$ (WOF-Au) nanorods through a solvothermal process following by in situ deposition of Au nanoparticles for enhancing photoelectrochemical nitrogen reduction

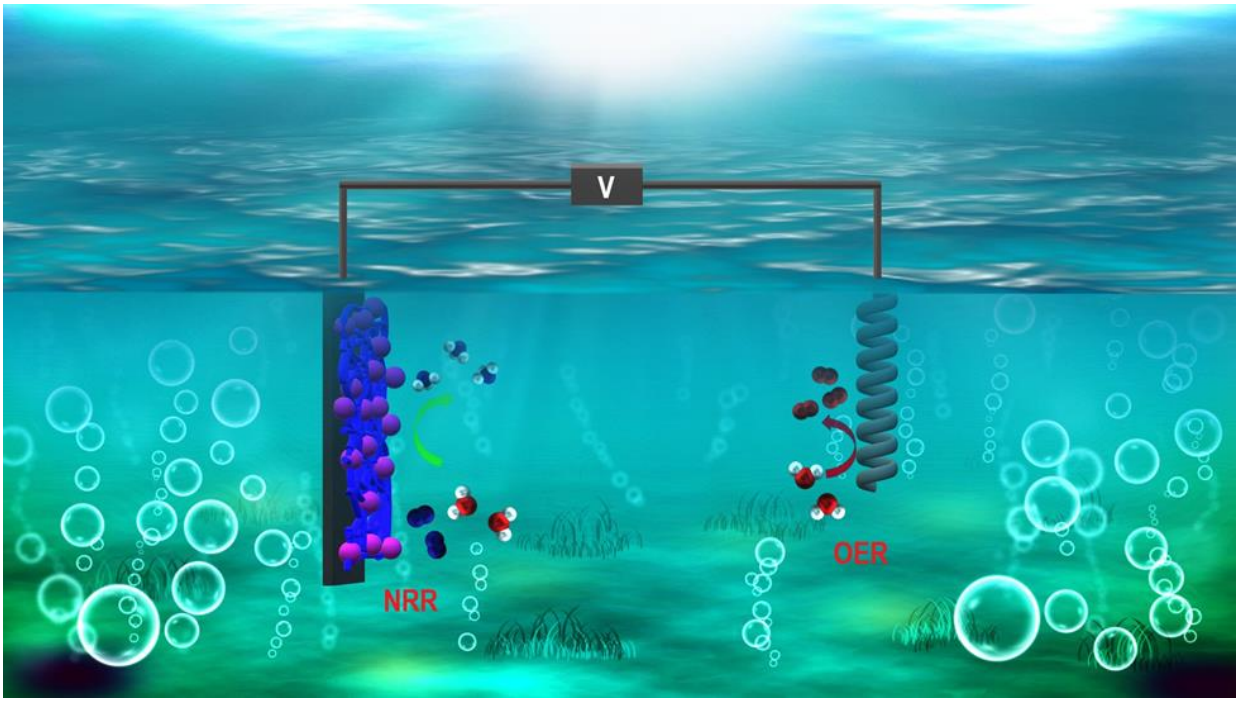

Résumé

La fixation photoélectrochimique (PEC) de l'azote a ouvert de nouvelles possibilités pour la production d'ammoniac à partir de l'eau et de l'air dans des conditions douces, mais ce processus est confronté aux défis inhérents associés aux travaux théoriques et expérimentaux. Cependant, des difficultés limitent l'efficacité de la réaction de réduction de l'azote (NRR). Ici, nous rapportons pour la première fois un système photoélectrocatalytique innovant et efficace, qui a été préparé en assemblant des nanoparticules plasmoniques d'or avec des nanotiges d'oxyde de tungstène ($W_{18}O_{49}$) dopées au fer (désignées WOF-Au). (i) L'introduction d'élément exotiques de Fe dans le $W_{18}O_{49}$ non-stœchiométrique peut éliminer les défauts de volume de l'hôte $W_{18}O_{49}$, ce qui a entraîné un rétrécissement de l'énergie de la bande interdite et une facilitation de la séparation et du transport de paire électron-trou. (ii) Ainsi, la combinaison des nanoparticules Au et du semiconducteur induisent de la résonance plasmonique de surface localisée (LSPR) et génèrent des électrons énergétiques (chauds), ce qui augmente la densité électronique sur les nanotiges de $W_{18}O_{49}$. Par conséquent, ce système plasmonique WOF-Au présente un rendement de production de NH_3 de 9,82 µg. $h^{-1}.cm^{-2}$ à -0,65 V par rapport à une électrode de référence Ag / AgCl, ce qui est environ 2,5 fois plus élevé que celui du WOF (sans nanoparticules d'Au) ainsi qu'une stabilité très élevée. Aucune formation de NH_3 n'a été trouvée pour le $W_{18}O_{49}$ pur (WO). Cette activité élevée peut être associée aux effets synergiques entre le dopant Fe et les nanoparticules plasmoniques Au sur le semi-conducteur hôte $W_{18}O_{49}$. Ce travail peut apporter quelques éclairages sur la conception ciblée des systèmes hybrides plasmoniques efficaces pour la fixation de N_2 et la photocatalyse artificielle.

Abstract

Photoelectrochemical (PEC) nitrogen fixation has opened up new possibilities for the production of ammonia from water and air under mild conditions, but this process is confronted by the inherent challenges associated with theoretical and experimental works, limiting the efficiency of the nitrogen reduction reaction (NRR). Herein, we report for the first time a novel and efficient photoelectrocatalytic system, which has been prepared by assembling plasmonic Au nanoparticles with Fe doped $W_{18}O_{49}$ nanorods (denoted as WOF-Au). (i) The introduction of exotic Fe atoms into nonstoichiometric $W_{18}O_{49}$ can eliminate bulk defects of the $W_{18}O_{49}$ host, which resulted in narrowing bandgap energy and facilitating electron-hole separation and transportation. (ii) Meanwhile, Au nanoparticles combined with a semiconductor induce the localized surface plasmon resonance (LSPR) and generate energetic (hot) electrons, increasing electron density on $W_{18}O_{49}$ nanorods. Consequently, this plasmonic WOF-Au system shows an NH_3 production yield of 9.82 $\mu g.h^{-1}.cm^{-2}$ at -0.65 V vs. Ag/AgCl, which is ~2.5-folds higher than that of the WOF (without Au loading) as well as very high stability, and no NH_3 formation was found for the bare $W_{18}O_{49}$ (WO). This high activity can be associated with the synergistic effects between the Fe dopant and plasmonic Au NPs on the host semiconductor $W_{18}O_{49}$. This work can bring some insights into the target-directed design of efficient plasmonic hybrid systems for N_2 fixation and artificial photocatalysis.

6.1 Introduction

Natural ammonia (NH_3) synthesis has been considered to be one of the essential processes for the growth and development of living organisms because it plays a crucial role in metabolic pathways[313]. Additionally, it is well known that ammonia can be used as a useful source in manufacturing industries such as a chemical intermediate to produce fertilizers, in hydrogen energy storage, and in food manufacturing among others[314-315]. Currently, the ammonia is industrially produced mainly from the traditional Haber-Bosch (HB) process under extreme reaction conditions of 400-450 ^oC and 200-250 bar[316-317]. For this HB process, ammonia is produced from nitrogen and hydrogen obtained from steam-methane reforming, which annually contributes to 3-5% global consumption of natural gas. Furthermore, fossil fuel energy is also used to drive ammonia synthesis making this process a major contributor to carbon emission[318].

Furthermore, for this HB process, high temperature and high pressure are required. Therefore, the development of green and sustainable alternatives for the fixation of N_2 into NH_3 under ambient conditions has fascinated many researchers in this field. Inspired by the fact that biological nitrogenase can reduce nitrogen through the electron transfer mechanism[196], photoelectrochemical (PEC) nitrogen fixation recently has attracted numerous research activities because it takes the advantage of solar energy and electricity to generate electrons, offering an auspicious tactic for the synthesis of ammonia at room temperature and pressure[319-321]. Although the PEC nitrogen reduction reaction (NRR) has been studied on various semiconducting materials, so far, the high yield of N_2 to NH_3 is still challenging owing to (i) the incredibly stable N≡N bond with a dissociation energy of 945 $kJmol^{-1}$ and (ii) the competition between hydrogen evolution reaction (HER) and NRR[216]. Although both NRR and HER have the same reduction potential, HER only requires two electrons for the catalytic reaction while NRR needs six electrons, making HER more favorable. Various approaches have been introduced to overcome these obstacles, promoting the performance of PEC systems such as loading noble metal cocatalysts and defect engineering (e.g., doping semiconductors with impurity elements or tuning surface lattice vacancies)[322-326].

Recently, Zhang et al. demonstrated that Mo doped $W_{18}O_{49}$ nanowire could achieve a solar-to ammonia production rate of 0.195 μmol.h^{-1} under simulated AM 1.5G illumination[327]. On the other hand, Sun *et al.* indicated that the WO_{3-x} catalysts with tailored surface oxygen vacancies could enhance the yield of NH_3[328]. Although the catalytic activity towards nitrogen reduction of these materials was improved, it is still limited. Tungsten-based oxide (WO_{3-x}) materials have been considered as promising catalysts for photocatalytic and electrocatalytic NRR; however, these types of materials have never been reported for PEC nitrogen fixation thus far. Even though sub-stoichiometric WO_{3-x} has emerged as a potential candidate for NRR application owing to its high stability, low toxicity, and high redox potential[329-330], its larger bandgap (2.9 eV) and monoclinic structure containing a limited number of intrinsic oxygen deficiencies[331-332] are the primary bottle-neck restricting the usage of WO_{3-x} for photoelectrochemical NRR. Fe doping can reduce the bandgap energy and improve the visible light absorption ability of semiconductors. Recently, it has been reported that Fe doping can promote the photocatalytic activity of TiO_2 and C_3N_4-based semiconductors for ammonia formation[25, 159, 333-334].

On the other hand, assembling plasmonic nanoparticles such as gold, silver, aluminum, and copper with a semiconductor can induce localized surface plasmon resonance (LSPR)[335]. Recently, Zhang *et al.* have successfully prepared a Z-scheme TiO_2/ZnTe/Au nanocorncob[336]. Zhang reported that the LSPR effect of Au nanoparticles can synergistically make effective utilization of broad-range solar light irradiation and enhance the separation efficiency of photogenerated charge carriers. Consequently, the as-prepared sample exhibited high photocatalytic activity towards hydrogen evolution, corresponding to approximately 1%. The intimate contact between noble metal NPs and semiconductors leads to the formation of a Schottky barrier, which inhibits the recombination of photogenerated charge carriers; thus, more active charge carriers are available for the photocatalytic process. The LSPR phenomenon allows the plasmonic metal NPs to concentrate the surrounding light energy and absorb the photons toward the visible light and near IR region to generate energetic (hot) electron[337]. The hot electrons with high kinetic energy can overcome the Schottky barrier and activate the reactant molecules, consequently enhancing the photocatalytic performance under visible light irradiation.

Inspired by these reasons, in this work, we report a novel photoelectrocatalytic (PEC) system, which is assembled using plasmonic Au nanoparticles with Fe doped $W_{18}O_{49}$ nanorods (denoted as WOF-Au) for efficient photoelectrocatalytic ammonia production. In this work, (i) Fe doping was used as a medical technique to heal the bulk-defect-states in the nonstoichiometric $W_{18}O_{49}$ lattice as well as enhances visible light absorption and promotes the interfacial migration of electrons from the photocatalyst to chemisorbed N_2 molecules. (ii) The decoration of Au nanoparticles on Fe doped $W_{18}O_{49}$ is to induce the LSPR. This resulting plasmonic WOF-Au system exhibits very high NH_3 production which is approximately 2.5-folds higher than that of the sample WOF (without Au loading) and high stability. Therefore, this novel photocatalytic system could be a promising technology as a sustainable and alternative method for nitrogen fixation to produce ammonia by photocatalysis.

6.2 Experimental

6.2.1 Materials

Gold (III) chloride trihydrate ($HAuCl_4$), iron (III) chloride anhydrous ($FeCl_3$), tungsten hexachloride (WCl_6), and sodium borohydride ($NaBH_4$) were purchased from Sigma Andric, Ethylenediamine and Nafion solution were obtained from Alfa Aesar. Ethanol and distilled water were purchased from commercial sources. All chemical products used in this work were purchased in analytical grade and used without any purification.

6.2.2 Synthesis of Fe-doped $W_{18}O_{49}$ nanorods

Fe-doped $W_{18}O_{49}$ nanorods were prepared by the solvothermal method without using any surfactant or capping agent. Briefly, 300 mg of tungsten hexachloride was dissolved into 100 mL of ethanol to obtain a yellow-transparent solution. Afterward, 10 mg of iron (III) chloride was added into the as-prepared solution, which was further vigorously stirred for 30 min. In the next step, the mixture was sealed in a 150 mL Teflon-lined autoclave and heated at 200 ^oC for 18 h. After cooling down to room temperature, the precipitated product was collected by centrifugation at 9000 rpm for 10 min and washed with anhydrous ethanol three times. Finally, the Fe-doped $W_{18}O_{49}$ sample (WOF) was dried at 70 ^oC in a vacuum oven overnight

for further utilization and characterization. The bare $W_{18}O_{49}$ (WO) nanorods were prepared using the same procedure without adding iron (III) chloride at the initial stage.

6.2.3 Synthesis of Fe-doped $W_{18}O_{49}$ nanorods with Au decoration

100 mg of the WOF sample was dispersed into 45 mL ethanol and stirred for 1 h for preparing a dark-green solution (solution A). A certain amount of gold (III) chloride trihydrate was dissolved into 1 mL distilled water followed by adding 4 mL of ethylenediamine. Then the as-prepared gold solution was mixed with solution A and stirred for 2h. Afterward, 1.97 mg sodium borohydride was added into the mixture, which changed the color of the suspension from dark-green to dark-purple immediately. After 1h, the suspended product was removed from the mixture and washed with anhydrous ethanol three times. Hence, the obtained product was dried under vacuum overnight to receive Fe-doped $W_{18}O_{49}$ with Au decoration (WOF-Au) powder.

6.2.4 Photocatalyst characterization

Transmission electron microscopy (TEM) images of the samples were obtained on a JEOL JEM 1230 operated at 120 kV. Powder X-ray diffraction (XRD) patterns of the samples were collected on a Bruker SMART APEXII X-ray diffractometer equipped with a Cu Kα radiation source (λ = 1.5418 Å). X-ray photoelectron spectroscopy (XPS) measurements were carried out in an ion-pumped chamber (evacuated to 10^{-9} Torr) of a photoelectron spectrometer (Kratos Axis-Ultra) equipped with a focused X-ray source (Al Kα, hν = 1486.6 eV). The UV-Vis absorption spectra were recorded on a Cary 300 Bio UV-Vis spectrophotometer. Fourier transform infrared (FTIR) spectra were measured with an FTS 45 infrared spectrophotometer with the KBr pellet technique. The photocurrent measurements were carried out in a conventional three electrodes station (Autolab PGSTAT204).

6.2.5 Photoelectrochemical Measurements

Commercial F-doped SnO_2-coated (FTO) glass was employed as a substrate for loading catalysts. In general, the working electrodes were prepared as follows: 5 mg of the photocatalysts was dispersed in 2 mL anhydrous ethanol to form a slurry of the materials. Then, the slurry was coated onto an FTO glass electrode (1 cm x 1 cm) by the drop-casting

method. Next, the as-prepared electrodes were dried naturally overnight under vacuum. Transient photocurrent response was performed using an electrochemical workstation (Autolab PGSTAT204) based on a standard three-electrode system using the as-prepared WOF-Au/FTO cell as the working electrode. A Pt wire and Ag/AgCl cell were used as counter and reference electrodes, respectively. The photocurrent was measured under solar light irradiation (1 sun with AM 1.5G filter) with 10 seconds light-on-off cycles) with an applied potential of -0.65 V vs. Ag/AgCl. For the electrochemical impedance (Nyquist plots) measurements, the perturbation-signal was set to be 10 mV, and the frequency range was between 0.1 MHz and 0.1 Hz. The experiment was carried out under solar light illumination. Linear sweep voltammetry (LSV) curves were scanned at a rate of 100mV/s.

6.2.6 Photoelectrocatalytic ammonia production

The as-synthesized catalysts were coated onto carbon papers (WOF-Au/C) as working electrodes. In general, 5 mg of the catalyst was dispersed in 2 mL anhydrous ethanol followed by the addition of 20 µL Nafion solution. Then, the mixture was sonicated for 30 mins to form a suspended solution. Afterward, the suspended solution was cast by dropping on carbon paper (1.5 cm x 3.5cm) and dried under vacuum at 25^{o}C.

The NRR test was carryout n the self-assembled photoelectrochemical reactor (**Figure S6.1**) with an applied potential of -0.65 V vs. Ag/AgCl under simulated solar light illumination (1 sun with AM 1.5G filter) for 2h. During the test, N_2 gas was continuously bubbled into the electrolyte of 0.5M Na_2SO_4 (the electrolyte was purged with N_2 for 30 mins prior to the test). This procedure was repeated for five cycles, where the electrolyte solution was changed before starting every new cycle. The amount of NH_3 production was determined using the indophenol blue method.

6.3 Result and discussion

Figure 1(a) illustrates the synthesis of Fe doped $W_{18}O_{49}$ with Au decoration via a simple solvothermal method, where ethanol can function as both the morphology-controlling agent and solvent, which provides an appropriate medium for the gradual hydrolysis of WCl_6 [338]. Consequently, the slow hydrolysis and shape-controlling agent encourages the growth of rod-like nanostructures. Fe dopants are incorporated into the WOF-Au semiconductor using

$FeCl_3$ as the precursor. The presence of the Fe element was proved by energy dispersed X-ray spectroscopy (EDS), as shown in **Figure S6.2.** The morphology of the WOF-Au nanorods was confirmed by TEM, featuring two specific dimensions that correspond to the width approximately 10 nm and the length exceeding several hundred nanometers. In the following step, ionic gold chloride adsorbed on the surface of WOF nanorods was reduced to metallic gold nanoparticles in the presence of a sodium borohydride reducing agent. The TEM and HRTEM images of WOF-Au nanorods are displayed in **Figure 6.1(b)-(c)**, where deposited gold nanoparticles are found in a spherical shape with an estimated diameter of 5-10 nm. It can be clearly seen that the Au nanoparticles are highly dispersed on the surface of the nanorods, which have possibly functioned as plasmonic nanoparticles.

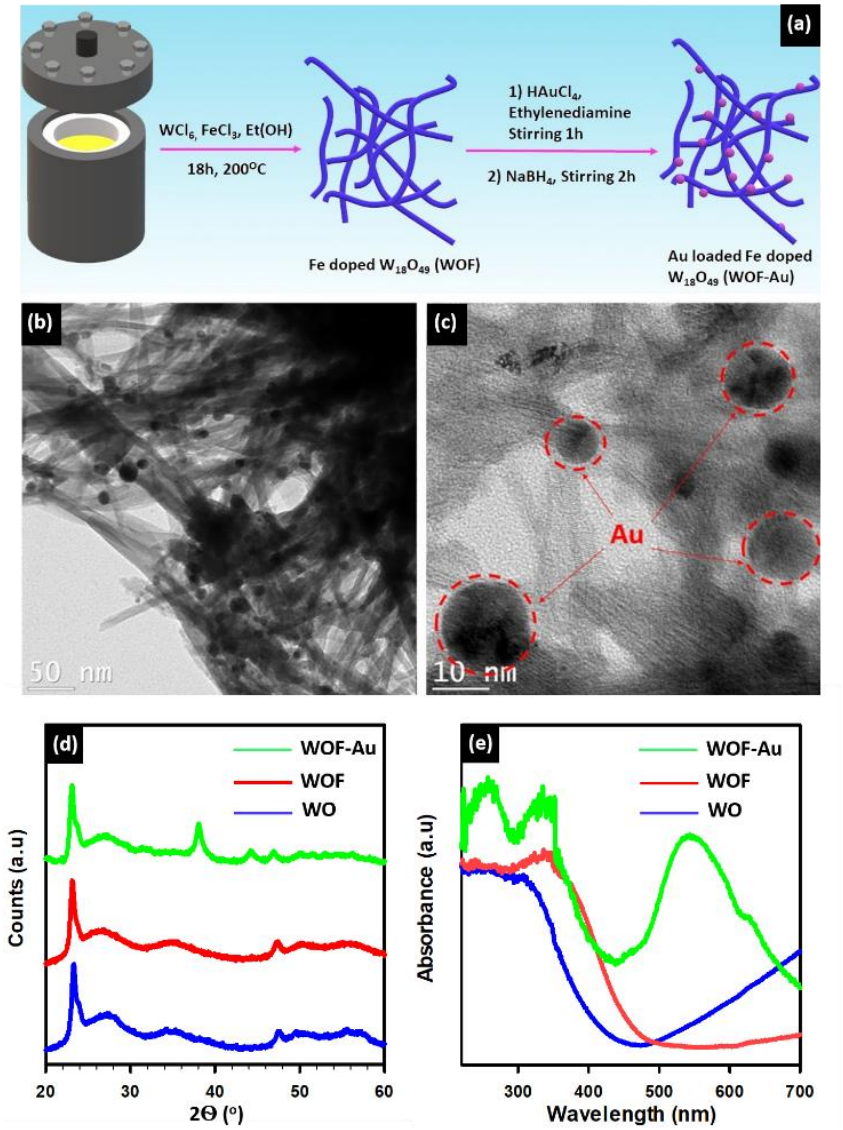

Figure 6.1: (a) Schematic demonstration of solvothermal synthesis of WOF and WOF-Au nanorods; (b) The TEM and HRTEM images of WOF-Au nanorods; (d) X-ray diffraction spectra of WO, WOF, and WOF-Au samples; (e) UV-Vis diffuse reflectance spectra of WOF-Au, WOF, and WO samples.

Figure 6.1(d) shows the XRD patterns of pure (WO) and modified tungsten oxide (WOF and WOF-Au) nanorods, which can be matched well with monoclinic $W_{18}O_{49}$ (JCPDS file 71-2450 as shown in **Figure S6.9**). The intense peak locates at 23.3^o corresponded to the (010) facet, while other diffraction peaks are broadened with low intensities, suggesting that the growth orientation of $W_{18}O_{49}$ nanorods is dominant along the (010) plane [339]. It can be anticipated that the monoclinic skeletal patterns of pure $W_{18}O_{49}$ still remained after doping with the Fe element, without generating a new diffraction peak, which indicates that the incorporation of Fe into $W_{18}O_{49}$ nanorods has successfully formed a homogeneous structure. Otherwise, the XRD patterns of the WOF and WOF-Au samples are observed with slight shifts (≈ 0.2^o) towards the smaller angle compared to the WO sample, suggesting that there was a change in the main crystalline structure during the Fe-doping process. According to Feng and Zhong[340], this observation is due to the replacement of W by exotic atoms in the lattice structure, leading to the decrement in the number of oxygen defects of $W_{18}O_{49}$ nanorods[341] which might suggest the reformation of the $W_{18}O_{49}$ lattice from defect states. After decorating with Au nanoparticles, two distinct peaks appeared at 2Θ values of 38.1^o and 44.3^o. These peaks can be ascribed to (111) and (200) reflection planes of the gold cubic phase, respectively, which is in good agreement with the previous report for the standard metallic gold[342]. The highest diffraction intensity at 38.1^o implies that the preferential growth orientation of metallic gold was fixed in the (111) direction.

Figure 6.1(e) demonstrates the UV-Vis absorption spectra of the as-obtained samples at the wavelength ranging between 200 and 700 nm. The WO sample exhibits intense absorption in the UV and near-visible region (<400 nm), which is ascribed to the intrinsic absorption of the $W_{18}O_{49}$ material. Meanwhile, the extended absorption tail of the WO sample could be observed from 500 nm, suggesting incontrovertible evidence for the abundance of surface and bulk phase oxygen defects. Liu *et al.* and Cong *et al.* claimed that this extended absorption tail to visible and near-infrared regions apparently implies the high number of

oxygen defects and vice versa[331, 343]. Although surface oxygen vacancies are particularly beneficial for the separation of charge carriers as well as facilitating the adsorption and dissociation of nitrogen molecules[344-345], bulk oxygen defects of tungsten suboxide generally act as trapping centers to recombine electrons and holes[35]. According to previous studies, the bulk oxygen defects are unfavorable for the photocatalytic performance of $W_{18}O_{49}$[346-347], particularly for N_2 fixation. By doping with Fe, the intrinsic absorption edge of the WOF sample is extended up to 500 nm. Moreover, the smooth absorption curve without any observable hump indicates the homogeneous incorporation of Fe into the $W_{18}O_{49}$ lattice structure, which is in accordance with the XRD results. Interestingly, the absorbed intensity of WOF is reduced in the visible region (500-700 nm) as compared to WO, indicating the removal of oxygen defects which suggests that the structural defects of $W_{18}O_{49}$ were cured by the substitution of W by Fe atoms[327]. After loading Au nanoparticles, the intrinsic absorption profile of the WOF-Au sample was still maintained, except for a new peak appearing at around 550 nm. This phenomenon was originated from the LSPR effect on the surface of Au nanoparticles. By using the Kubelka-Munk function, Tauc plots of three samples were plotted using UV-Vis diffuse reflectance spectral data to estimate the optical bandgap energy of the fabricated catalysts (**Figure S6.3**). The estimated bandgap of WO is found to be 2.98 eV, while the optical bandgap of WOF and WOF-Au is determined to be a value of 2.65 eV. It can be interpreted that the doping of Fe atoms in the W site creates localized electron trapping centers, which slightly modified the optical properties of $W_{18}O_{49}$, leading to extended light absorption in the visible region.

Electron paramagnetic resonance (EPR) spectra of WO and WOF-Au were further examined to confirm the presence of oxygen vacancies in the samples. As shown in **Figure 6.2** the bulk WO sample exhibited two distinct symmetrical EPR signals at g~2.002, which are because of the lone pair electrons on W^{5+} trapped by oxygen vacancies. Whereas, the WOF-Au showed only a weak signal peak. The stronger signal of WO indicates a higher concentration of oxygen vacancies on bulk $W_{18}O_{49}$ in comparison with WOF-Au. This observation suggests that the number of bulk oxygen vacancies was reduced after doping with Fe, which is consistent with the UV-Vis results. It can be explained that dopants such as Fe^{3+} can act as electron acceptor centers[348]. When doped with Fe^{3+} impurities, this acceptor-type element

can prevent the reduction of W^{6+} to W^{5+}as well as neutralize the donor action of oxygen vacancies, hence, inhibiting the formation of oxygen vacancies

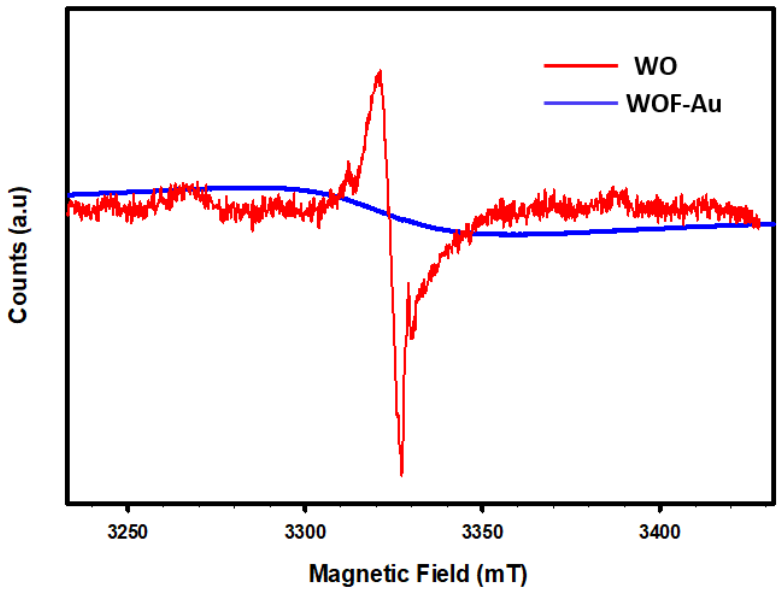

Figure 6.2: EPR spectra of WO and WOF-Au sample at room temperature

To ascertain the chemical states of the Fe dopant as well as confirming the status of metallic Au, the WOF-Au sample was further analyzed by XPS. As shown in **Figure S6.5**, the survey XPS spectrum of WOF-Au indicates the surface of the WOF-Au nanorods is composed of W, Fe, Au, O, and carbon contamination. The high-resolution XPS spectra of W 4f, Fe 2p, Au 4f, and O 1s are obtained and depicted in **Figure 6.3(a)-(d)**, respectively. As seen in the W 4f spectrum (**Figure 6.3(a)**), the deconvoluted peaks located 35.9 and 38.0 eV could be assigned to W $4f_{7/2}$ and W $4f_{5/2}$ spin-orbit doublets of the W^{6+} oxidation state[349]. In addition to these main peaks, the lower intensity peaks at 34.3 and 36.5 eV can be ascribed to the +5 oxidation state of W atoms[350]. The weak peaks of W^{5+} species suggest a small number of oxygen vacancies occupying on the surface of WOF-Au nanorods. Similarly, the XPS spectrum of Fe 2p can be fitted into two pairs of peaks, as depicted in **Figure 6.3(b)**. The sharp peaks centered at 709.9 and 723.4 eV correspond to Fe $2p_{3/2}$ and Fe $2p_{1/2}$, respectively. This doublet peak, with a binding energy difference of 13.5 eV, could be the firm evidence for the occurrence of the Fe^{3+} state in metal-oxide bond[351], which is in good accordance with the EDS results. Moreover, the satellite peak with a binding energy of 728.5 eV can also be

attributed to Fe^{3+} species. Interestingly, another satellite peak is found at 714.5 eV which is attributed to the binding energy of Fe^{2+} species. The formation of Fe^{2+} species was probably because of the partial reduction of Fe^{3+} along with the presence of neighboring surface oxygen vacancies. These observations are in good agreement with the XPS analysis of W 4f that confirmed the existence of surface oxygen vacancies. The XPS core level spectrum of Au 4f is shown in **Figure 6.3(c)**, where the signals can be separated into two peaks at 83.8 and 87.5 eV. These peaks match with the binding energy of Au $4f_{7/2}$ and Au $4f_{5/2}$, indicating the metallic state[352] of Au nanoparticles on the surface of WOF nanorods, which is consistent with the XRD results. The peak observed at 530.6 eV in the O 1s XPS spectrum is completely associated with the O^{2-} state in the crystal lattice of $W_{18}O_{49}$[353] while the shoulder peak appearing at 531.3 eV could be originated from the surface chemisorbed H_2O and OH radicals or other species[354] (**Figure 6.3(d)**).

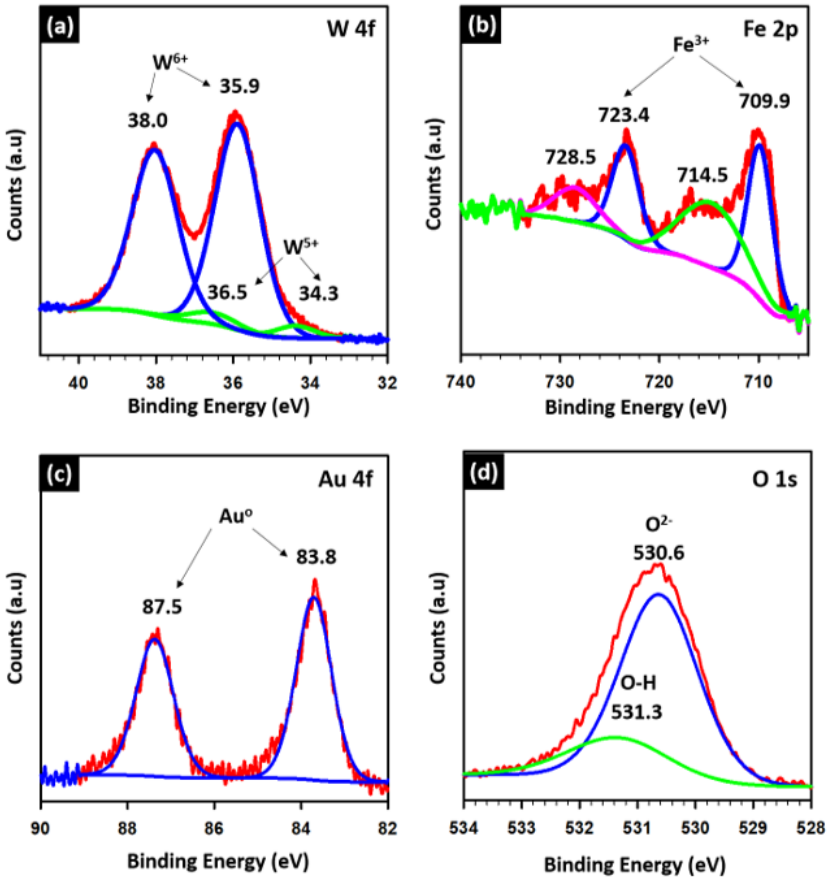

Figure 6.3: XPS spectra obtained from WOF-Au nanorods: (a) W 4f, (b) Fe 2p, (c) Au 4f, and (d) O 1s spectrum.

Figure 6.4(a) shows the PL spectra of WO and WOF-Au under an excitation wavelength of 350 nm at room temperature. It is clearly seen that the strong recombination of photogenerated charges in the bulk $W_{18}O_{49}$ sample produced a broad and intense peak located at ~ 500nm, which has been reported in many previous works[355-356]. Meanwhile, the steady-state PL spectrum of WOF-Au exhibited a significant PL quenching. Furthermore, WOF-Au also exhibited a longer lifetime of charge carriers than that of WO, as depicted in **Figure 6.4(b).** The drastically decreased PL intensity and lifetime increase indicate the improvement of charge separation and transportation of the WOF-Au sample, which is originated from the synergistic effect of Fe doping and LSPR of the Au nanoparticles.

In order to gain insight into the charge transfer efficiency for the fixation of nitrogen, photocurrent measurement of WO, WOF, and WOF-Au were established with the repetition of eight-on-off cycles under solar light irradiation. The obtained results are illustrated in **Figure 6.5(a)**. The modifications by Fe doping and Au loading show a significant enhancement in current intensity compared to pure $W_{18}O_{49}$, suggesting a noticeable improvement in charge separation and transportation of photogenerated electron-hole. For the initial illumination, the instantaneous photocurrent of WOF-Au can reach 60 $\mu A.cm^{-2}$. Although the photocurrent decays rapidly and remains stable at a constant current around 45 $\mu A.cm^{-2}$ in the last four cycles, WOF-Au still exhibits a higher current density than that of WOF and WO samples which are approximately 28 and 18 $\mu A.cm^{-2}$, respectively. It is worth noting that the enhancement in photocurrent of WOF-Au is attributed to the incorporation of Fe, which can reduce the number of oxygen vacancies in the bulk structure, minimizing the charge recombination. Moreover, with the LSPR effect, gold nanoparticles can concentrate and absorb higher photon energies, thus, more electrons are generated and transferred to $W_{18}O_{49}$ that significantly promotes the photocurrent density[357-358]

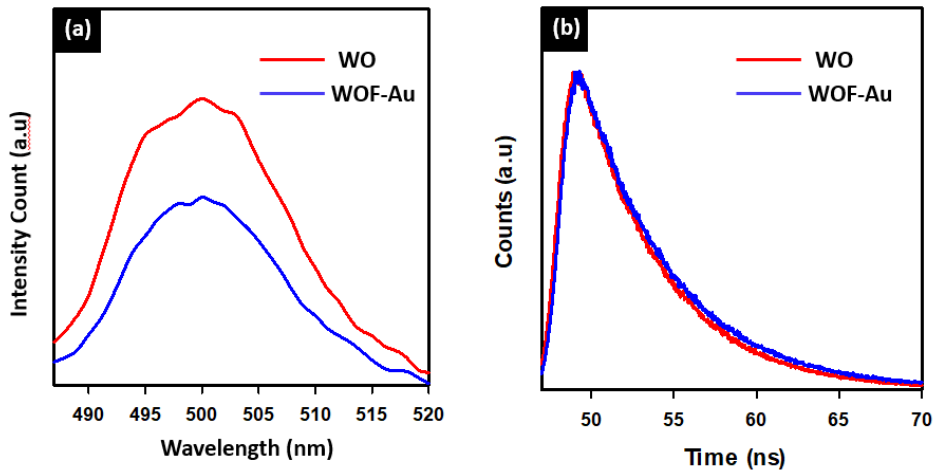

Figure 6.4: (a) Photoluminescence of the WO and WOF-Au samples; (b) Time-resolved photoluminescence of the WO and WOF-Au samples.

Furthermore, electrochemical impedance spectroscopy (EIS) was also engaged to evaluate the charge-transfer resistance (R_{ct}) at the interface of catalyst/electrolyte under light illumination. Theoretically, a small diameter of the Nyquist plot indicates high electronic conductivity as well as low R_{ct}[359]. The Nyquist plot of the WOF electrode exhibits a smaller radius than that of bare $W_{18}O_{49}$, demonstrating a significant improvement of photo-induced charge transportation. The electron transfer resistance can be further reduced by gold deposition, which is affirmed by the smallest semicircle illustrated in **Figure 6.5b**. Hence, the radius following the order of WOF-Au<WOF<WO is consistent with the transient photocurrent of three samples. Otherwise, the Nyquist plot of the WOF-Au electrode in the dark was also recorded and depicted in **Figure S6.6**, which exhibits a the larger diameter in comparison with the Nyquist semicircle of the WOF-Au electrode under the light irradiation, suggesting a better performance in the exchange current density at the semiconductor/electrolyte interface. This observation can be ascribed to the effect of surface plasmon resonance of metallic gold nanoparticles[360].

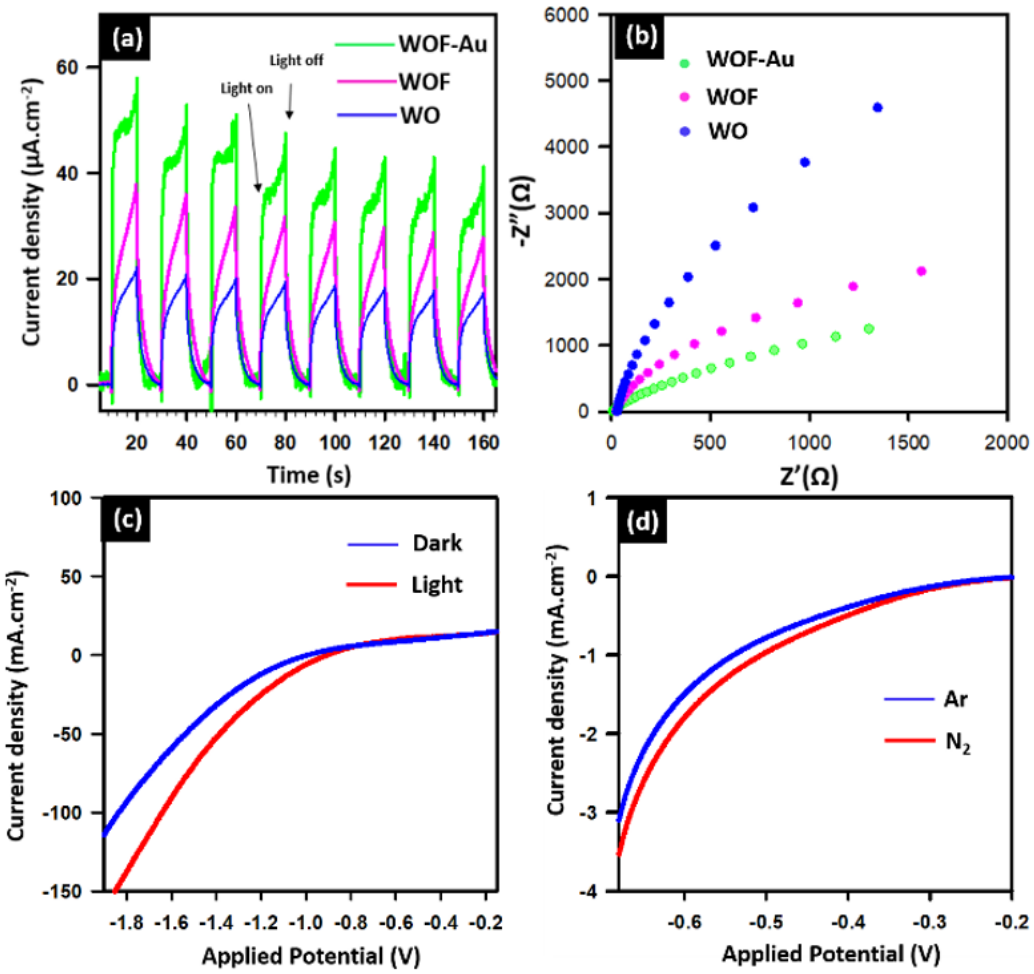

Figure 6.5: (a) Photocurrent responses of WO, WOF, and WOF-Au at an applied potential of -0.65V vs. Ag/AgCl in 0.5M Na_2SO_4 under saturated N_2 and (b) Nyquist plots of the samples at an applied potential of -0.65V vs. Ag/AgCl in the 0.5M Na_2SO_4 electrolyte under saturated N_2 under light irradiation; LSV of the as-prepared WOF-Au sample (c) in the N_2-saturated 0.5M Na_2SO_4 electrolyte and (d) in N_2- and Ar-saturated 0.5M Na_2SO_4 electrolytes.

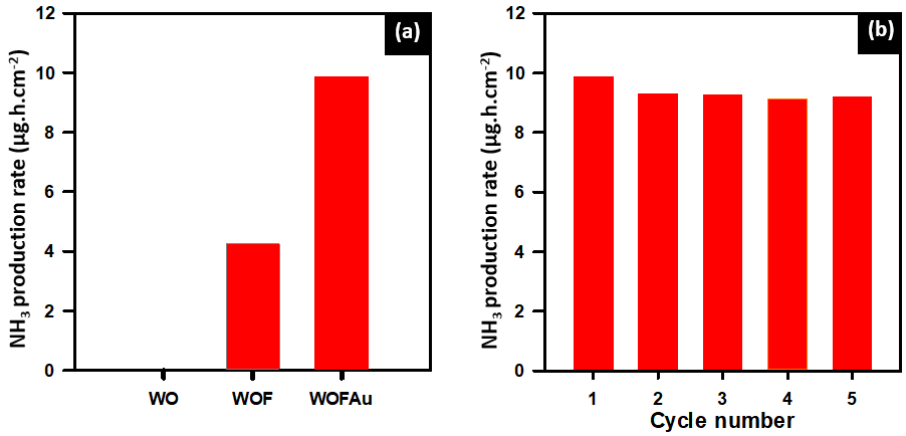

Figure 6.6: (a) PEC NH_3 production rate of WO, WOF, and WOF-Au samples and (b) recycling test of WOF-Au in N_2-saturated 0.5M Na_2SO_4 at an applied potential of -0.65 V vs. Ag/AgCl.

To further understand the performance of the photoelectrocatalytic system, linear sweep voltammetry of the WOF-Au/FTO electrode was recorded with and without light irradiation. As expected, a higher current density was observed under the illumination of the solar simulator (**Figure 6.5(c)**). The onset potential of the LSV curve is shifted by 0.15 V vs. Ag/AgCl to the more positive potential, suggesting a better catalytic activity for nitrogen fixation than that in the dark. Because the formation of dihydrogen is also one of the primary factors affecting the efficiency of ammonia synthesis[317], LSV scans of the WOF-Au/C electrode in N_2 and Ar-bubbled environments were also conducted to comprehend the selectivity between hydrogen evolution reaction (HER) and nitrogen reduction reaction (NRR) (**Figure 6.5(d)**). In N_2-saturated 0.5M Na_2SO_4, a moderate enhancement of current intensity is achieved when the applied voltage sweeps negatively from -0.3 V vs. Ag/AgCl, indicating that more photogenerated electrons have been transferred from WOF-Au/C photoelectrochemical cell to absorbed N_2 for producing NH_3. As shown in **Figure 6.5(d)**, the most substantial difference between the two LSV plots is observed at the potential between -0.3 V and -0.7 V vs. Ag/AgCl. It is presumed that the highest ammonia yield can be obtained at an applied voltage in this potential range. Hence we have performed the photoelectrocatalytic test of the WOF-Au/C photocathode for nitrogen fixation at the applied potential of -0.65V vs. Ag/AgCl.

The photoelectrochemical N_2 fixation of the as-prepared samples was assessed by their chronoamperometry performance in N_2-saturated 0.5M Na_2SO_4 over 2-hour-period at room temperature, as shown in **Figure 6.6(a)**. The concentration of ammonia in the electrolyte was determined by the indophenol blue method (see experimental session and **Figure S6.7**). Under solar light irradiation, WOF and WOF-Au as photocathodes are capable of producing ammonia from nitrogen and water, whereas the WO electrode is inactive for nitrogen reduction. It is worth noting that the significant difference in catalytic performance between bare and doped samples could be attributed to the homogeneous incorporation of Fe dopants. Doping Fe not only removes bulk structural defects, narrowing the optical bandgap of the semiconductor as well as enabling visible light absorption but also acts as active sites, which capture and accumulate electrons for adsorbed N_2 molecules to dissociate N-N bonding[159]. Under the same condition, WOF exhibited a production rate of 4.25 $\mu g.h^{-1}.cm^{-2}$, which was significantly enhanced to 9.82 $\mu g.h^{-1}.cm^{-2}$ after loading with Au nanoparticles. The solar conversion efficiency is calculated to be 0.067%, which is higher than that of previously reported photocatalytic N_2 fixation systems[143-144]. Otherwise, the samples of Au loaded $W_{18}O_{49}$ (WO-Au) have been prepared and tested. The results showed that $W_{18}O_{49}$-Au exhibited no catalytic activity toward nitrogen reduction, which is similar to the sample of pure $W_{18}O_{49}$. It can be explained that gold nanoparticles only play a role as LSPR and the lack of active sites on WO-Au lead to the inactivity for the conversion of nitrogen to ammonia. Hence, the combination of the Fe dopant for introducing active sites and gold nanoparticles for the LSPR can induce a synergistic effect, which significantly enhances the photoelectrocatalytic performance of the WOF-Au sample. The control experiments were conducted to confirm the source of N_2 for ammonia synthesis. As seen in **Figure S6.8**, a trace of ammonia was detected in the Ar-saturated environment. Otherwise, no generation of NH_3 was found when using bare carbon paper as a working electrode or at open-circuit voltage. These observations indicated that NH_3 was primarily evolved from N_2 gas rather than from the other contamination sources. It can also be explained that the detectable amount of ammonia in control experiments was caused by the leakage of atmospheric N_2 absorbed onto the surface of the electrode[361]. Notably, the recyclability of the WOF-Au catalyst was further investigated over five consecutive cycles, as depicted in **Figure 6.6(b)**, which exhibited excellent stability without any noticeable decrement in catalytic activity, suggesting that Fe

doped $W_{18}O_{49}$ with Au decoration could be a promising catalyst for photoelectrochemical nitrogen fixation.

Based on the above experimental results, we proposed a plasmon-induced mechanism for photoelectrocatalytic nitrogen reduction by decorating the Fe-doped $W_{18}O_{49}$ photocathode with Au nanoparticles, as shown in **Figure 6.7**. Upon solar light irradiation, electrons are excited to the conduction band (CB) of $W_{18}O_{49}$, leaving highly oxidized holes on the valence band (VB). Because of abundant structural defects, the photogenerated charge carriers can be rapidly recombined in bulk oxygen vacancies, resulting in poor photoactivity towards the nitrogen reduction of bare WO. However, with the incorporation of Fe impurities, the crystal lattice of $W_{18}O_{49}$ was restored from the bulk-defect-rich state as well as the bandgap energy of WOF was narrowed, which facilitate visible light absorption and promote the separation of photogenerated electron-hole. More importantly, Au nanoparticles on the surface of nanorods take advantage of the LSPR effect to generate hot electrons. These energetic electrons facilely traverse the Schottky barrier and inject directly to the CB of the semiconductor. The intrinsic electrons of $W_{18}O_{49}$ and hot electrons then diffuse to the Fe dopants, and further transfer to the absorbed N_2 molecules, facilitating the reduction reaction. Meanwhile, under the driving force of the electric current, generated holes migrate towards the Pt wire electrode for the water oxidation to maintain the charge balance in the photoelectrochemical system.

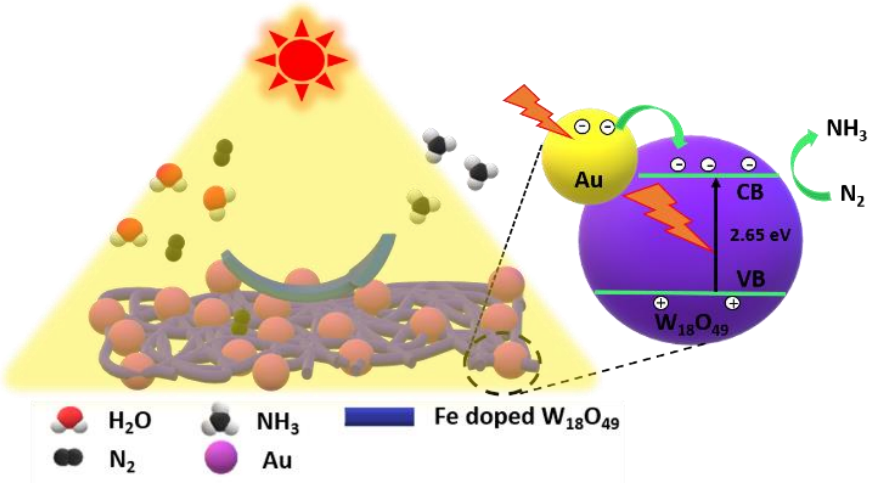

Figure 6.7: Schematic demonstration of the proposed mechanism for photoelectrochemical nitrogen fixation of the WOF-Au catalyst.

Apart from the contribution by the above-discussed features, the physical characteristics in the engineered structure such as the small size of Au nanoparticle assembled on the surface of Fe doped $W_{18}O_{49}$ nanorods enhance the intimate interaction between the cocatalyst and the semiconductor, which could also be considered as the critical factor to determine the efficient photoelectrocatalytic nitrogen reduction of Fe doped $W_{18}O_{49}$ with Au decoration.

6.4 Conclusion

We demonstrated a new strategy for the synthesis of an efficient plasmonic WOF-Au system which was obtained through the synthesis of Fe doped $W_{18}O_{19}$ nanorods followed by in situ deposition of Au nanoparticles. The homogeneous distribution of Fe in $W_{18}O_{49}$ enhances visible light absorption and improves electron-hole separation; while Au nanoparticles decorated in Fe in $W_{18}O_{49}$ induce the LSPR. The resulting plasmonic WOF-Au system has been shown to be very effective for photoelectrochemical nitrogen to ammonia. The high NH_3 production rate (9.82 $\mu g.h^{-1}.cm^{-1}$) was obtained under solar light irradiation at -0.65 V vs. Ag/AgCl and under ambient conditions and is ~2.5-folds higher than that of the Fe doped $W_{18}O_{19}$ (without Au loading) and much higher than that of bare $W_{18}O_{19}$ with high stability. The high photoelectrocatalytic efficiency of this system could be due to the synergetic effect between Fe dopants and Au nanoparticles in $W_{18}O_{49}$ nanorods.

From the obtained results, it can be concluded that structural engineering and plasmon enhancement could be realized as a promising strategy to develop efficient plasmonic hybrid systems for the photoelectrochemical NRR under solar light. We anticipate that this strategy will be widely adopted as a means of improving photocatalytic performance in a diverse range of photocatalytic reactions

Acknowledgment

This work was supported by the Natural Science and Engineering Research Council of Canada (NSERC) through the Collaborative Research and Development (CRD), Strategic Project (SP), and Discovery Grants.

6.5 Supporting information

Determination of ammonia

The ammonia concentration was spectrophotometrically measured by the indophenol blue method[362]. Briefly, 1 mL of the electrolyte solution was removed from the photoelectrochemical reactor. Next, 2 mL of 1M NaOH containing 5 wt% salicylic acid and 5 wt% sodium citrate, 1 mL of 0.05 M NaClO, and 0.2 mL of 1 wt% $C_5FeN_6Na_2O$ (sodium nitroferricyanide) were sequentially added to the solution. After 2h at ambient temperature, 2 mL of as-prepared solution was drawn out for UV-Vis measurement at a wavelength of 655 nm to determine the formation on indophenol blue. For the calibration of the concentration-absorbance curve, standard ammonia chloride solution with the concentration of 0, 0.5, 1, 1.5, 2 μg/mL were used (**Figure S6.6**), which contained the same concentration of Na_2SO_4 as the electrolyte solution.

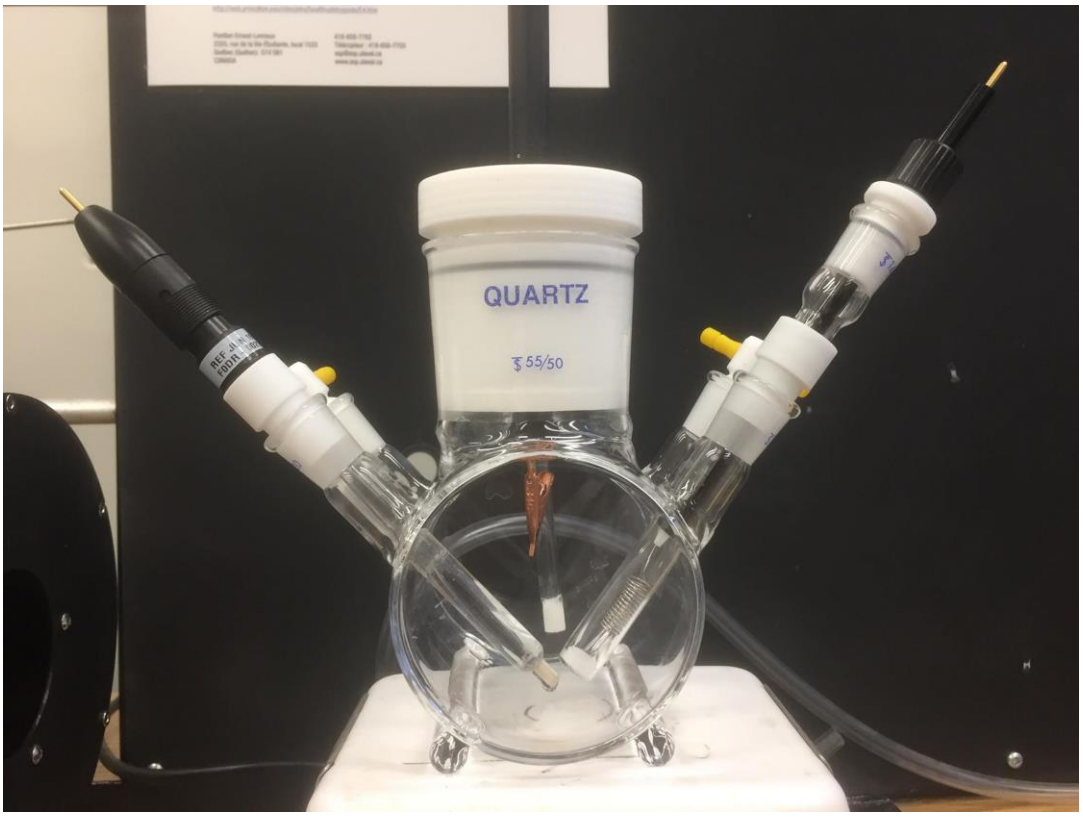

Figure S6.1: The picture of photoelectrochemical reactor

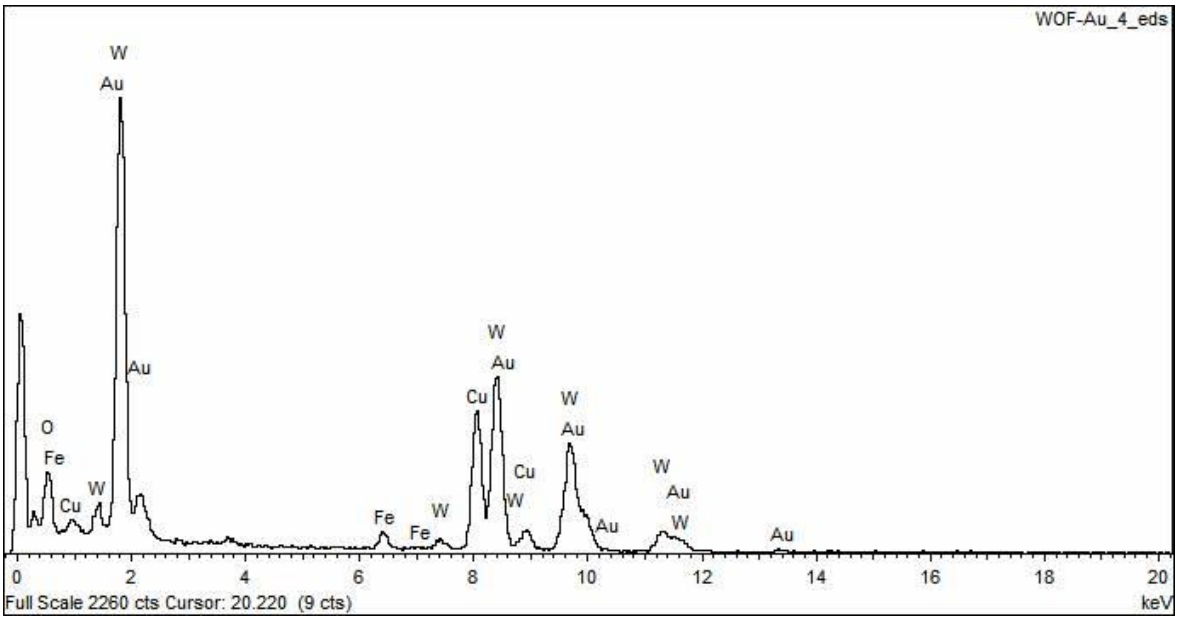

Figure S6.2: Representative EDX analysis collected on WOF-Au

EDX spectrum confirms that WOF-Au nanorods mainly compose of W, Fe, O, and Au. The Cu signals are from the substrate

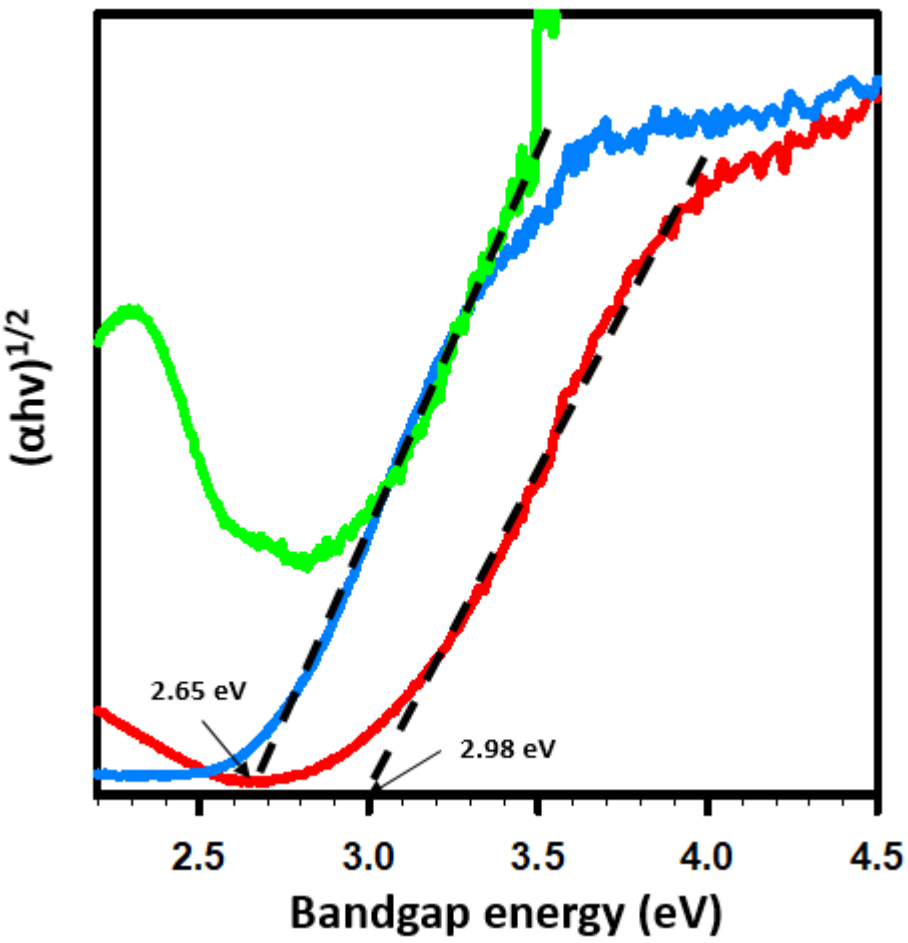

Figure S6.3: Tauc plot for bandgap determination of WO, WOF, and WOF-Au samples

The bandgap energy of the obtained samples was estimated using Tauc plot, which is found to be 2.98, 2.65, and 2.65 for WO, WOF, and WOF-Au, respectively.

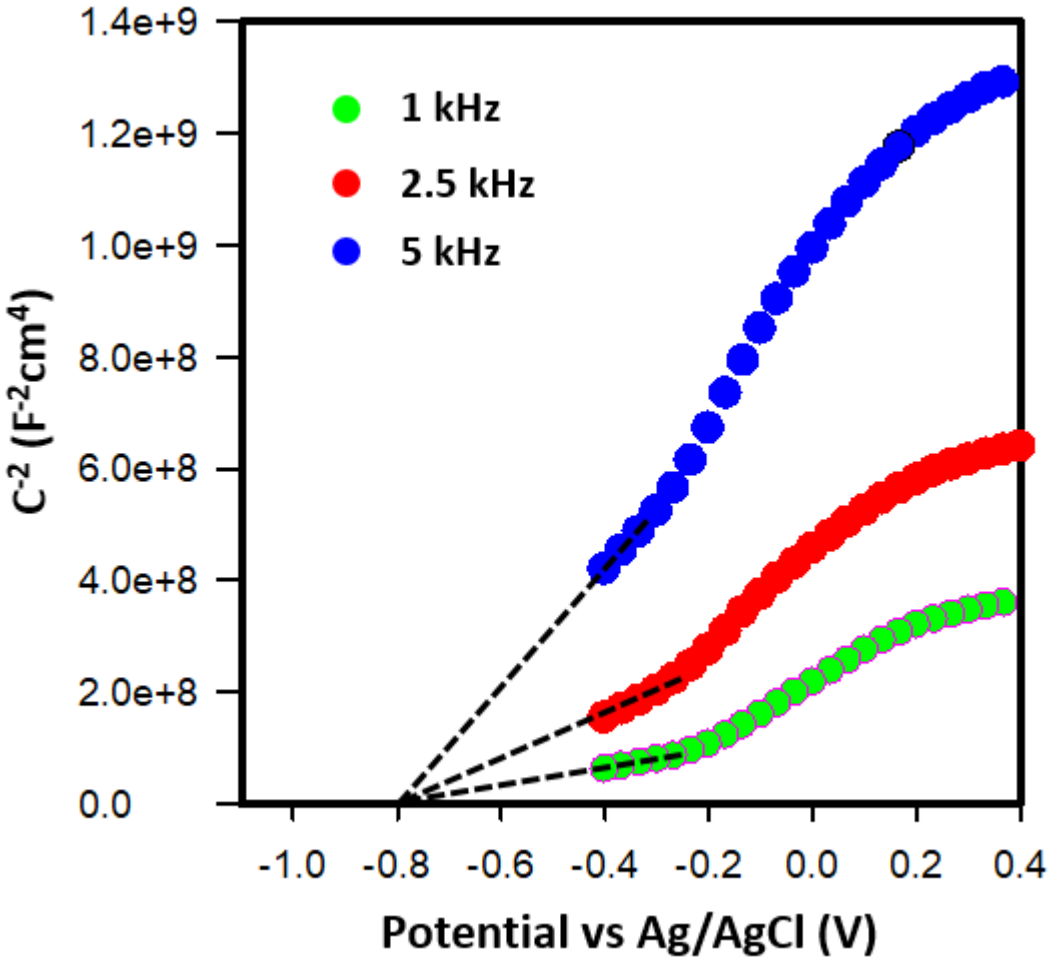

Figure S6.4: Mott-Schottky plots of the WOF-Au nanorods at different frequencies

The value of flat band potential of WOF-Au catalyst was estimated to be -0.8 V vs. Ag/AgCl by Mott-Schottky plots, which is approximately corresponded to -0.24 V vs. RHE

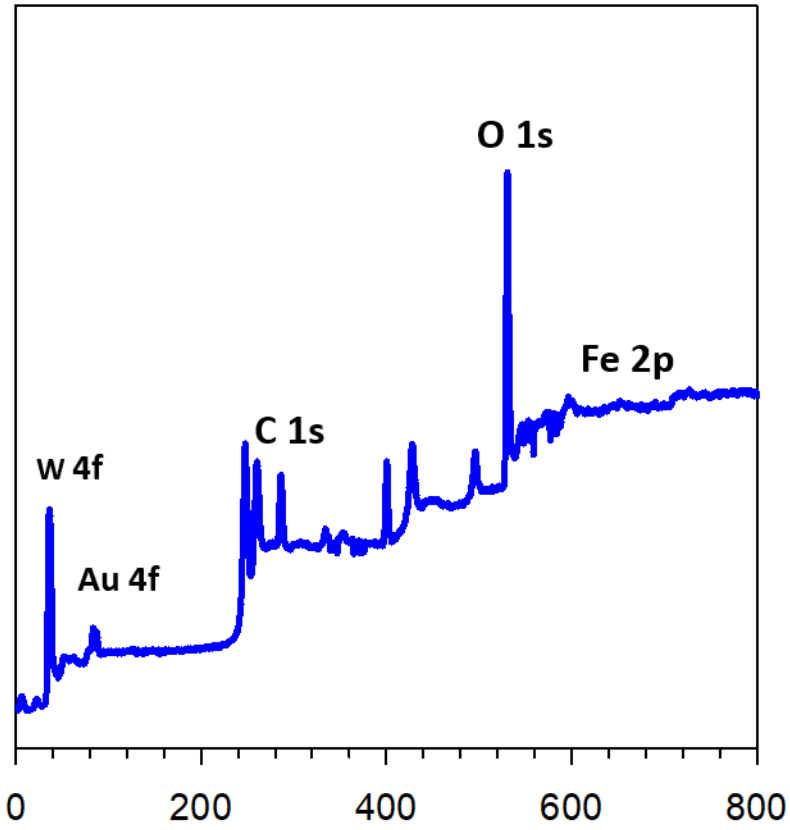

Figure S6.5: XPS survey spectra of WOF-Au sample

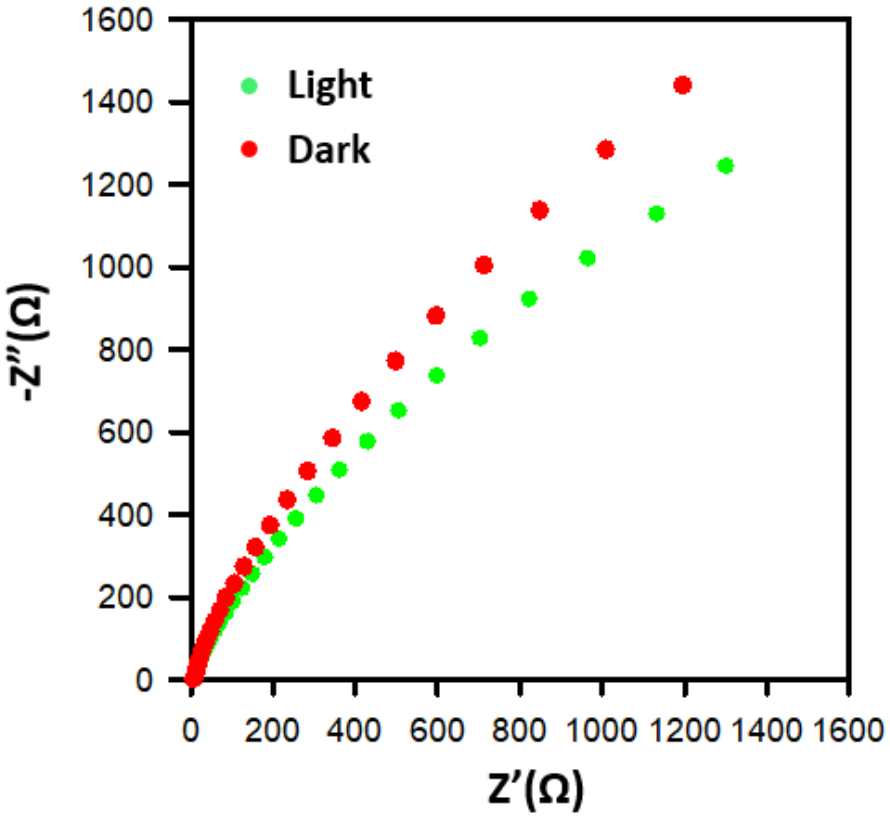

Figure S6.6: Electrochemical impedance Nyquist plots of the WOF-Au sample at an applied potential of -0.6V vs. Ag/AgCl in N_2-saturated 0.5M Na_2SO_4 Electrolyte

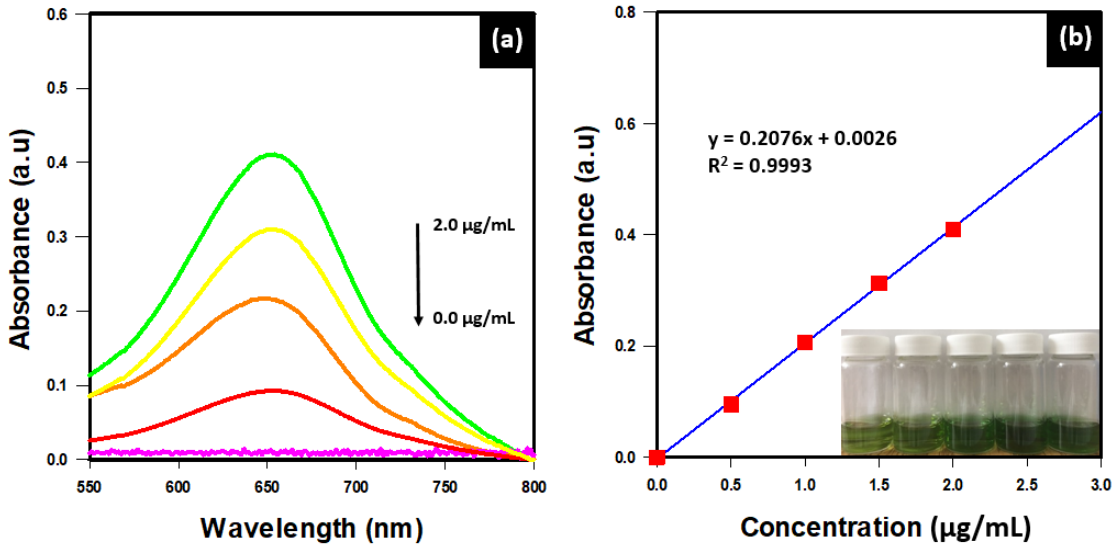

Figure S6.7: (a) UV-vis spectra for ammonium quantification using the indophenol-blue method with the concentration of 0.0, 0.5, 1.0, 1.5, 2.0 µg/L in 0.5M Na_2SO_4, respectively; (b) The calibration curve for ammonium quantification (NH_4^+ concentration versus absorbance at 655 nm).

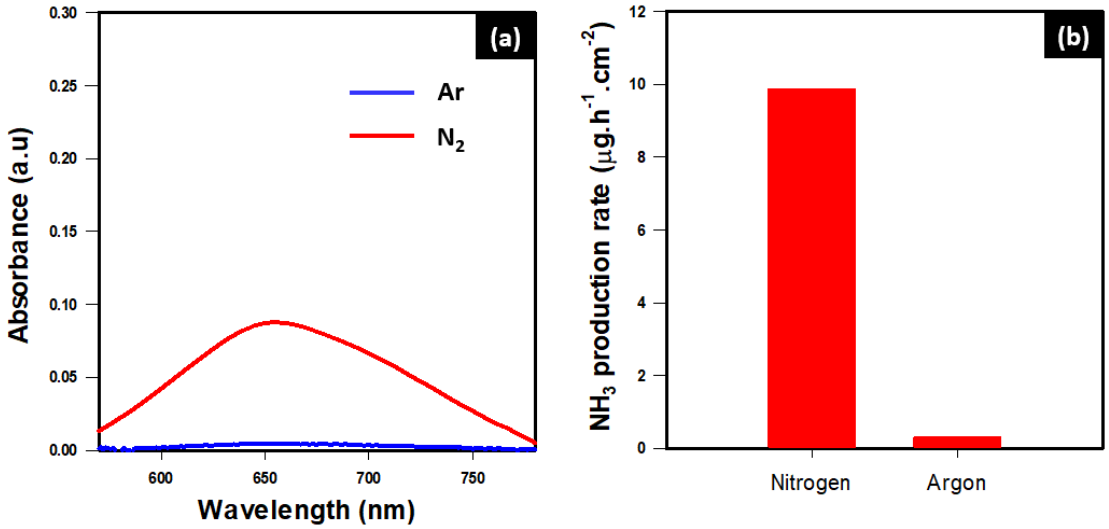

Figure S6.8: (a) UV-vis spectra of the electrolyte after 2 h of photocatalysis reaction with N_2 and Ar bubbling; (b) PEC NH_3 production rate of WOF-Au material with N_2 and Ar bubbling

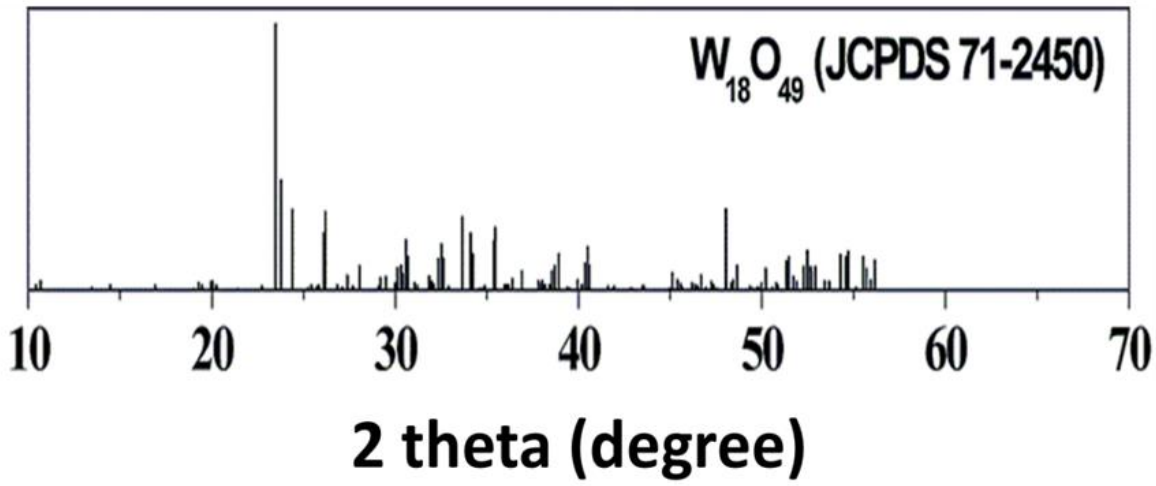

Figure S6.9: the JCPDS data of $W_{18}O_{49}$

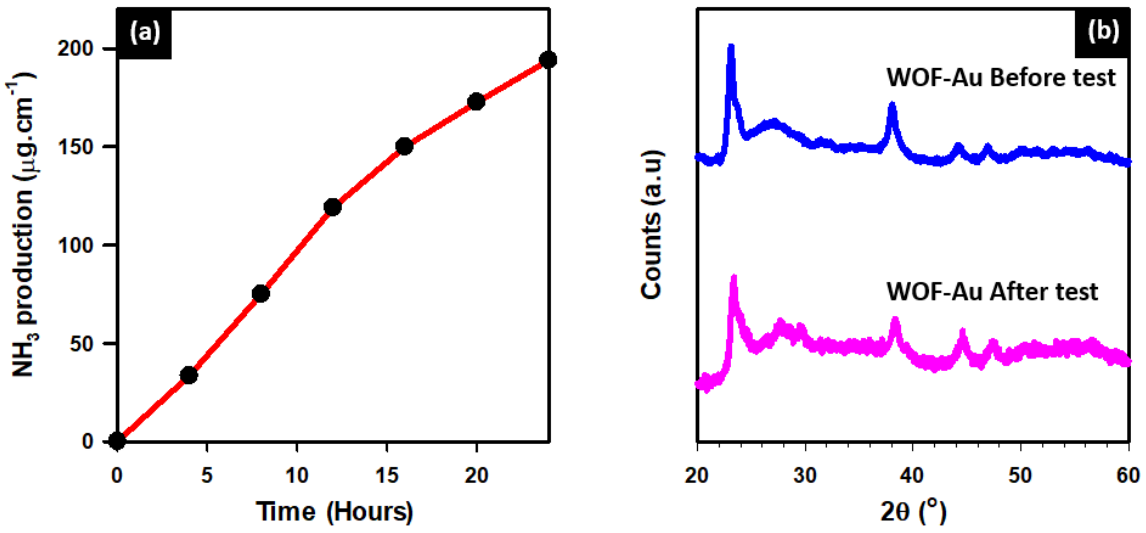

Figure S6.10: (a) Long-term stability test of WOF-Au sample for N_2 fixation; (b) the XRD spectra of WOF-Au before and after 24-hours-testing

Figure S6.10(a) shows that the catalytic activity of the sample is still maintained after 24-hours testing, suggested excellent stability of the sample.

The XRD results of WOF-Au before and after long-term testing (24 hours) were also provided in the revised supporting information. The results indicated that the crystalline structure of the sample was maintained after 24-hours-testing

Chapter 7: Construction of Ru doped In_2O_3 hollow peanut-like structure for enhanced photocatalytic nitrogen reduction under solar light irradiation

Manh-Hiep Vu, Toan Anh Quach, Trong-On Do*

Department of Chemical Engineering, Laval University, Québec (Québec), G1V 0A6, Canada

*E-mail: *trong-on.do@gch.ulaval.ca*

Submitted to ACS Applied Energy Materials 2020

Ru doped In_2O_3 hollow peanuts consisting of abundant surface oxygen vacancies exhibit enhanced photocatalytic NH_3 production under sunlight

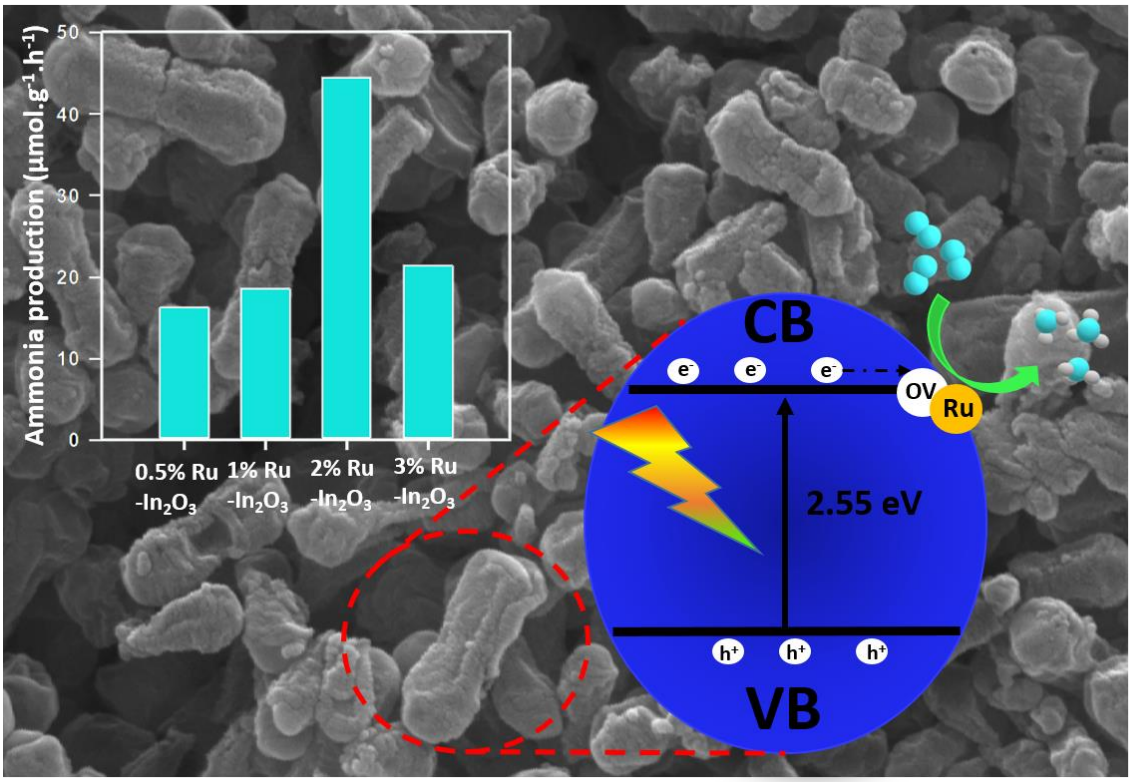

Résumé

La production de matériaux à structure organo-métallique (MOF) a été largement adoptée comme stratégie efficace pour la conception et la fabrication de divers photocatalyseurs nanostructurés fonctionnels à base de métaux. Ici, nous rapportons qu'une cacahuète creuse d'oxyde d'indium dopés au Ru (dénotées Ru-In_2O_3 HPN) peut être construite par la calcination du précurseur MIL-68-In(Ru). Le photocatalyseur nanostructuré préparé a été utilisé pour une photofixation de l'azote à température ambiante. Les images de TEM révèlent la formation uniforme de nanoparticules In_2O_3, qui sont assemblées in situ pour former une structure de cacahuète creuse. En conséquence, la nanostructure composée de cacahuète creuse facilite la séparation et le transport des électrons et les trous photoinduits ainsi qu'elle favorise l'absorbance de la lumière par multi-réflexion. De plus, des dopants de Ru sont introduits dans la nanoparticule In_2O_3, ce qui réduit l'énergie de la bande interdite et provoque la formation en abondance de lacunes d'oxygène, favorisant la réaction de réduction photocatalytique. Ainsi, cette structure unique d'In_2O_3 dopé au Ru a atteint l'activité photocatalytique la plus élevée de 44.5 µmol. $g^{-1}.h^{-1}$ pour la production d'ammoniac sous irradiation solaire, ce qui est 5.6 fois supérieure à celle du In_2O_3 pur et beaucoup plus élevée que l'In_2O_3 en vrac. En outre, les Ru-In_2O_3 HPNs ont présenté une très grande stabilité pour la fixation photocatalytique de l'azote en ne montrant aucune décroissance d'activité évidente après 6 cycles consécutifs (12 h). Ce travail ainsi ouvre des perspectives sur la conception ciblée de matériaux creux pour la fixation photocatalytique de l'azote.

Abstract

The synthesis of metal-organic framework (MOF) materials has been considered as an effective strategy for the design and fabrication of various nanostructured metal-based functional photocatalysts recently. Herein, Ru doped In_2O_3 hollow peanuts (denoted as Ru-In_2O_3 HPNs) were derived from MIL-68-In(Ru) precursors calcined in the air which is employed as an efficient photocatalytic system for the photoreduction of nitrogen. The TEM images revealed the uniform distribution of In_2O_3 nanoparticles, which are in situ-assembled to form a hollow peanut structure. Accordingly, this tailored nanostructure facilitates the separation and transportation of photoinduced electron-hole and favors light harvesting by multi-reflection/scattering. Moreover, Ru dopants are intentionally introduced into the In_2O_3 semiconductor as active sites, which not only narrows the bandgap energy but also causes the formation of abundant oxygen vacancies (OVs), promoting the photocatalytic reduction reaction. As a result, the unique structure of Ru-In_2O_3 exhibited the highest photocatalytic activity of 44.5 $\mu mol.g^{-1}.h^{-1}$ for ammonia production under solar-light irradiation, which is 5.6-time and much higher than that of pure In_2O_3 hollow peanuts and bulk In_2O_3, respectively. Further, the Ru-In_2O_3 HPNs exhibited excellent stability for photocatalytic nitrogen fixation by showing no obvious activity decay for the six consecutive two-hour tests (12h). This work might open up some insights into the target-directed design of hollow materials for photocatalytic nitrogen fixation.

7.1 Introduction

Ammonia (NH_3) is the one of most essential nitrogen-containing compounds of commerce, which can derive a wide range of organic compounds such as amines, amino acids, and amides, that are widely utilized for chemical synthesis and as agricultural fertilizers. Moreover, ammonia is also considered as a novel hydrogen storage material owing to high hydrogen density. Because N_2 contributes 78% to the total volume of the air, making it the most abundant gas in the atmosphere, hence, the study on the reduction of nitrogen to produce ammonia has attracted much attention. Currently, ammonia is industrially produced from N_2 and H_2 obtained from the steam reforming of methane, namely the Haber-Bosch (HB) process[363]. Although this process can achieve 80% of conversion yield, it requires harsh conditions with a high temperature of 450 ^oC and high pressure of 50 MPa[324], which cause the massive consumption of fossil fuel as well as emitting an enormous amount of greenhouse gases, consequently leading to a series of environmental issues. Therefore, finding a suitable alternative for the HB process has become a hot research topic in recent years. In this direction, the photocatalytic nitrogen fixation, driven by solar energy under mild conditions, has been exploited as a promising and sustainable approach toward ammonia production since it can generate ammonia from water and nitrogen[216]. At present, many different semiconductor materials, including TiO_2, C_3N_4, WO_3, BiOCl, CdS[157, 364-367], have been investigated for their photocatalytic activity toward nitrogen reduction. Unfortunately, the scalable applications of these materials are greatly limited by their insufficient efficiency to break the incredibly stable N≡N bond with dissociation energy of 945 $kJmol^{-1}$, poor light absorption, low charge separation, and lack of surface-active sites[316, 368]. In order to overcome these limitations and promote photocatalytic performances, various strategies have been employed to develop a wide range of potential photocatalysts such as active site doping[369], cocatalyst loading[370], morphology design[371], and construction of nanocomposites[317, 322, 372].

Indium (III) oxide, an n-type semiconductor, is considered as a promising candidate for photocatalytic nitrogen fixation applications, owing to its small bandgap energy (2.7 eV), low toxicity, high thermodynamic stability, and abundant oxygen vacancy defects[373-375]. For example, Xu and coworkers[376] reported In_2O_3/In_2S_3 nanocomposites with abundant oxygen vacancies that achieved a maximum nitrogen fixation rate of 40.04 $\mu mol.g^{-1}.h^{-1}$.

Additionally, Han *et al.* indicated that assembling In_2O_3 with plasmonic Au nanocrystals could promote the catalytic performance toward photofixation of nitrogen by more than 8-times as compared to bare In_2O_3[377]. Although the catalytic activity of these materials was improved, it is still far from achieving the desired yield. Thus, in this work, some efforts have been made to ameliorate the optical and electronic properties of indium oxide semiconductor by constructing hollow structure and doping with active metal dopants of ruthenium, thereby to enhance its photocatalytic efficiencies.

Most recently, hollow structure-based materials have attracted considerable interest in diverse areas of research. These hollow architectures demonstrate enormous advantages in the field of photocatalysis owing to their unique properties[136, 378]. Notably, assesmbling small nanoparticles into a structure with high porosity not only shortens the diffusion length but it also enhances the accessibility of reactants to reach the active sites rapidly as well as reducing the travel pathway of photogenerated electron-holes from the bulk to the surface, thereby facilitating the charge separation and redox reaction[379]. Moreover, the closely-packed hollow particles can effectively harvest photon energy by multi-light reflection within the interior walls[380-381]. On the other hand, it has been reported that ruthenium can serve as an active site to promote the catalytic performance of ZrO_2 and TiO_2 materials towards nitrogen fixation, which have a crucial role in suppressing the competition of hydrogen evolution reaction[382-383]

Herein, we designed and developed a new type of In-based hollow peanut-like photocatalyst through a simple self-template one-pot synthesis method for boosting the solar-light driven N_2 reduction efficiencies under room temperature. The formation of a hollow structure enhances light absorption capability and promotes the separation of electron-hole, whereas the incorporation of Ru dopant narrows down the bandgap energy and generates surface oxygen vacancies. As a result, the as-synthesized Ru doped In_2O_3 hollow peanuts showed a significant improvement for the photoreduction of nitrogen to ammonia. The combination of all the strategies, as mentioned above, as proposed in this study, may greatly contribute to the development of a new photocatalytic system with high efficiency for solar-driven nitrogen fixation applications.

7.2 Experimental

7.2.1 Materials

Indium (III) Chloride ($InCl_3$), Ruthenium (III) Chloride, Terephthalic acid (H_2BDC), n,n-dimethylformamide (DMF) purchased from Sigma Andric, and Alfa Aesar. Ethanol and distilled water were purchased from commercial sources. All chemical products used in this work were purchased in analytical grade and used without any purification.

7.2.2 Synthesis of MIL-68 peanut-like morphology

The MIL-68-In(Ru) sample was synthesized according to a previous report[384] with some modification. Briefly, a certain amount of $RuCl_3$, 50 mg of $InCl_3$, and 55 mg of terephthalic acid were dissolved in 20 mL of DMF and stirred for 10 min. Then the mixture of the dark-green solution was placed in a heat mantle at 100 ^oC for 30 min. After cooling down to temperature, the white-brown precipitated product was separated by centrifugation at 9000 rpm for 10 min and washed with anhydrous ethanol for three times. Finally, the MIL-68-In(Ru) sample was dried at 70 ^oC in a vacuum oven overnight for further utilization and characterization.

7.2.3 Synthesis of Ru doped In_2O_3 hollow peanuts

In order to obtain the Ru doped In_2O_3 hollow peanuts, the as-synthesized MIL-68 was then calcined at 450 °C in air for 1 h with a slow heating rate of 1 °C per min in a muffle furnace. The obtained samples are denoted as x wt% Ru-In_2O_3, where x is the weight percent of $RuCl_3$ precursor

7.2.4 Synthesis of In_2O_3 hollow peanuts

The bare In_2O_3 hollow peanuts were prepared in the same procedure of Ru doped In_2O_3 hollow peanuts, without adding ruthenium (III) chloride at the initial stage.

7.2.5 Synthesis of bulk In_2O_3

The bulk In_2O_3 was synthesized as following. Typically, 50 mg of $InCl_3$ were dissolved in ethanol. Then, a mixture of concentrated ammonia solution was added dropwise to the as-prepared solution and stirred for 1 h at room temperature, resulting in a precipitated gel was

formed. In the next step, the suspension was dried at 70°C overnight. Finally, the bulk sample of In_2O_3 was obtained by calcination in air at 400°C.

7.2.6 Photocatalyst characterization

Transmission electron microscopy (TEM) images of the samples were obtained on a JEOL JEM 1230 operated at 120 kV. Powder X-ray diffraction (XRD) patterns of the samples were collected on a Bruker SMART APEXII X-ray diffractometer equipped with a Cu Kα radiation source (λ = 1.5418 Å). The UV-Vis absorption spectra were recorded on a Cary 300 Bio UV-Vis spectrophotometer. Photoluminescence and Time-resolved spectra were measured with an Horiba QuantaMaster 8000. The photocurrent measurements were carried out in a conventional three electrodes station (Autolab PGSTAT204). EPR was performed with Bruker Elexsys E580 X-band EPR Spectrometer.

7.2.7 PEC Measurements

Commercial F-doped SnO_2-coated (FTO) glass was employed as a substrate for loading catalysts. In general, the working electrodes were prepared as follows: 5 mg of photocatalysts was dispersed in 2 mL anhydrous ethanol to make the slurry of the materials. Then, the slurry was coated onto an FTO glass electrode (1 cm x 1 cm) by the drop-casting method. Next, the as-prepared electrodes were dried naturally overnight under vacuum. Transient photocurrent response was performed by an electrochemical workstation (Autolab PGSTAT204) based on a standard three-electrode system using the as-prepared WOF-Au/FTO cell as the working electrodes. A Pt wire and Ag/AgCl cell were used as counter and reference electrodes, respectively. The photocurrent was measured under solar light irradiation (1 sun with AM 1.5G filter) with 10 seconds light-on-off cycles) with the applied potential of -0.5 V vs. Ag/AgCl. For the electrochemical impedance (Nyquist plots) measurements, the perturbation-signal was set to be 10 mV, and the frequency range was between 0.1 MHz to 0.1 Hz. The experiment was carried out under solar light illumination. EPR spectroscopy was conducted at room temperature.

7.2.8 Photocatalytic ammonia production

In a typical photocatalytic experiment, an optimized amount of 50 mg of the photocatalyst was dispersed in a solution containing 200 ml water and 20 ml of the sacrificial agent

(Methanol) and taken in the reactor cell. Then, the reactor cell was illuminated using a solar simulator (1 sun with AM 1.5G filter) 2 h. During the test, N_2 gas was continuously bubbled into the solution (the suspended solution was purged with N_2 for 30 mins prior to the test).

7.3 Result and discussion

Figure 7.1 schematically illustrates the formation mechanism of the Ru doped In_2O_3 hollow peanuts**.** As mentioned in experimental details, the initial bimetallic MOF was prepared via a one-pot synthesis, which is used as the carbon template to yield the Ru doped In_2O_3 photocatalyst. Terephthalic acid, $Ru^{3+,}$ and In^{3+} precursors were firstly dissolved in DMF solution to form a bimetallic InRu-terephthalate complex. By heating the mixture at 100^oC, the metal-linker complexes were coordinated and polymerized to form a 3D structural framework, which was assembled in a peanut-like morphology. Moreover, the morphological evolution of MIL-68-In(Ru) peanuts into rod-like shapes were observed upon increasing the reaction time and temperature (Supporting information, **Figure S7.2**). In the next step, the process of calcination under air removed the organic linkers, leading to the formation of Ru-doped In_2O_3 HPNs. It can be explained that the incorporation of Ru dopant was originated from the substitution of indium center by ruthenium on the framework, as demonstrated in the process (I).

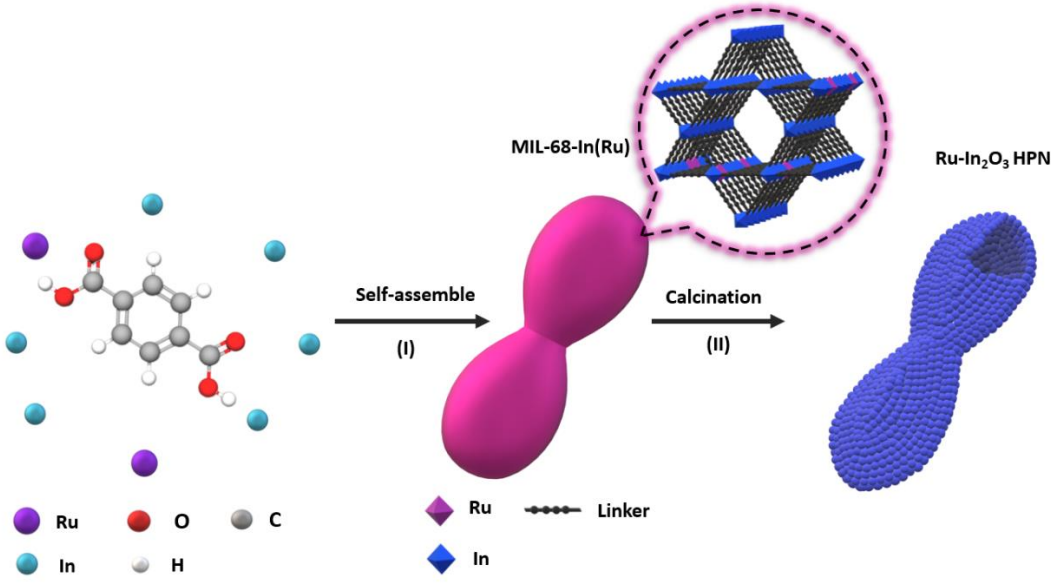

Figure 7.1: Schematic illustration of the synthetic process of the Ru doped In_2O_3 hollow peanuts.

The influence of the concentration of Ru dopants on the morphological structure and optical characteristics of Ru-In_2O_3 HPNs was investigated using scanning electron microscopy (SEM) and ultraviolet-visible microscopy (UV-vis). **Figure 7.2(a-d)** displays the SEM images of Ru-In_2O_3 HPNs with different Ru contents of 0.5, 1, 2, and 3 wt%, respectively. It can be seen that increasing the concentration of Ru^{3+} precursors does not affect the morphology of growing particles. Moreover, the inset image shows a closer view of the broken particles that essentially confirms the hollow structure of the Ru-In_2O_3 samples. The UV-Vis absorbance spectra of the as-prepared Ru-In_2O_3 HNPs are displayed in **Figure 7.2(d)**. It is observed that the Ru-In_2O_3 samples exhibit an intense absorption edge between 200 and 500 nm, suggesting that these In-based photocatalysts can perform catalytic activity under visible light irradiation. It is worth noting that the increasing concentration of Ru dopant leads to an improvement the visible light absorption of the materials.

The solar-driven photocatalytic test towards nitrogen reduction by the as-synthesized samples was conducted in N_2-saturated water and methanol as the solvent and sacrificial agent, respectively. The ammonia production yield was determined by UV-vis spectroscopy with an indophenol blue reagent. The photocatalytic performance of all samples was evaluated and showed in **Figure 7.2(e).** Among all samples, the 2wt% Ru-In_2O_2 exhibited the highest photocatalytic activity of 44.5 $\mu mol.g^{-1}.h^{-1}$. It can be observed that the increasing amount of Ru doping leads to the enhanced yield of ammonia generation. As shown in **Figure 7.2(e)**, the average production rate of produced NH_3 was determined to be 16.3 and 18.6 $\mu mol.g^{-1}.h^{-1}$ for 0.5% and 1% Ru-In_2O_3. Further, the photocatalytic activity tends to decrease with 3% of Ru doping. It is expected that when the ruthenium content is higher than 2%, it leads to the excessive formation of the impurity phases and structural defects. Thus, the presence of these undesired defects drastically inhibits the separation of photogenerated charge carriers, hence limits the photocatalytic performance.

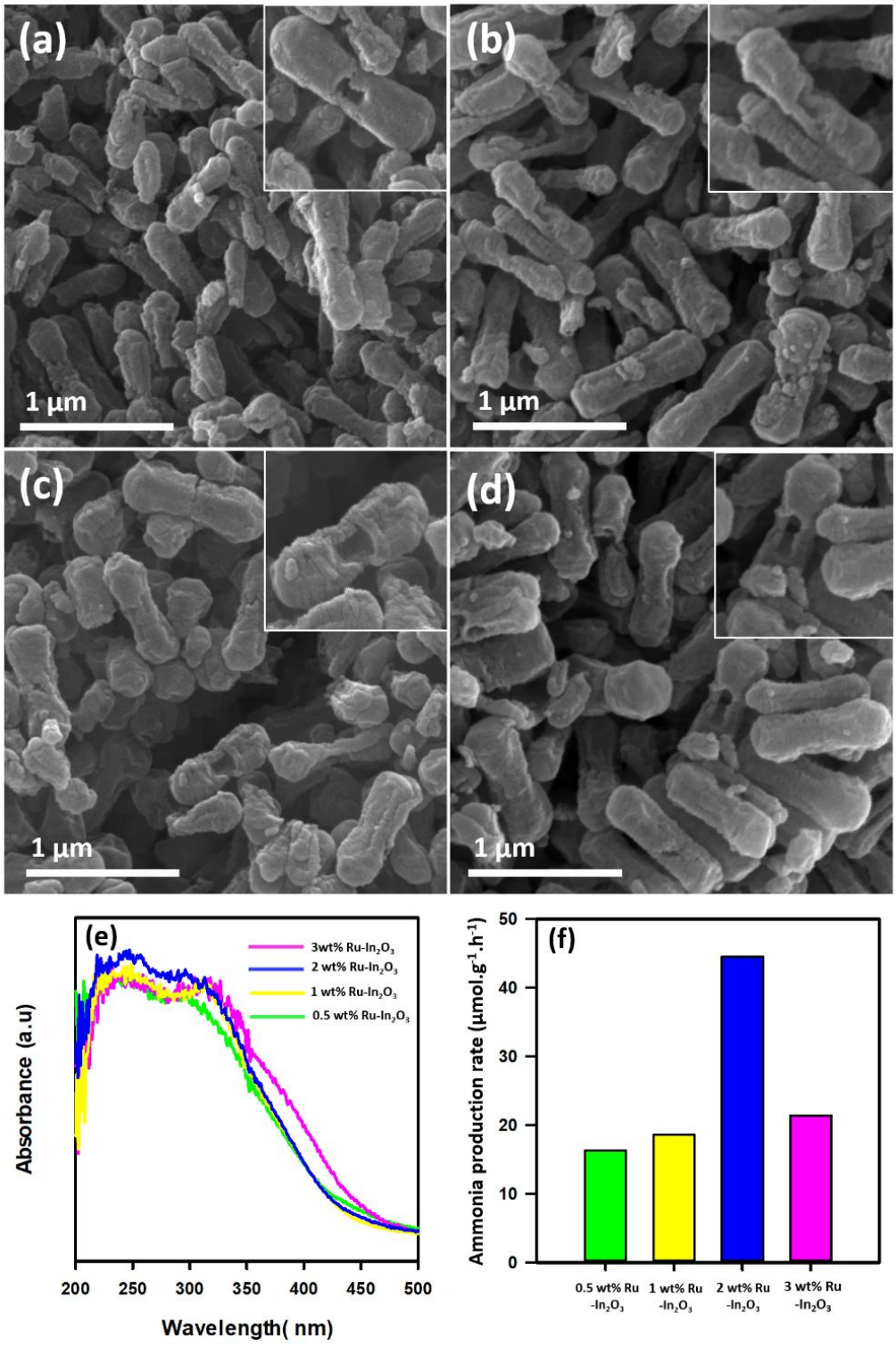

Figure 7.2: (a)-(d) SEM images of 0.5% 1, 2, and 3 wt% Ru-In_2O_3 HPNs, respectively; (e) UV-Vis spectra of Ru-In_2O_3 HPNs samples with different content of Ru precursors; (f) Photocatalytic ammonia production over different Ru-In_2O_3 HPNs samples

Based on the above results, it reveals that the 2% Ru-In_2O_3 HPNs sample showed a significant enhancement in photocatalytic activity among all the samples. Therefore, this sample was further examined to understand its photocatalytic mechanism. Besides, the photocatalytic performance and structural characteristics of the bare In_2O_3 HPNs samples were also studied for comparison with the 2% Ru-In_2O_3 HPNs sample. **Figure S7.3** displays the TEM image of the MIL-68-In(Ru) peanut-like templates, with the average length and diameter of 1 μm and 300 nm, respectively. The XRD analysis further confirmed the formation of In-based MIL-68, as depicted in **Figure S7.4**. After the calcination at 450 ^oC, the MIL-68-In(Ru) solid peanuts were directly transformed into In_2O_3 hollow peanuts because of the combustion of terephthalic linkers, releasing highly uniform nanoparticles. It was observed that the color of the sample changed from white brown to light yellow, suggesting the formation of indium oxide. **Figure 7.3** shows the TEM images of as-synthesized 2wt% Ru doped In_2O_3 sample with well-defined peanut-like morphology derived from their In-based MOF precursors. It is clearly seen that the surface of peanut-like particles become rough after the calcination under air. Moreover, the inset image of **Figure 7.3(c)** reveals that these hollow peanuts are composed of numerous randomly packed nanoparticles with an average size of 20 nm, which could be particularly advantageous for the photocatalytic process by shortening the travel path of electron-hole. Energy-dispersive X-ray spectroscopy (EDS) analysis was also employed to examine the surface composition of the 2 wt% Ru-In_2O_3 sample, where only the In, Ru, and O elements are detected (**Figure S7.4**), indicating the presence of Ru dopants on the In_2O_3 hollow peanut. In addition, the value of In:O ratio was determined to be 2:2.87 which suggests the presence of oxygen vacancies on the 2% wt Ru doped In_2O_3 samples. Similarly, the XRD spectrum of the 2 wt% Ru-In_2O_3 sample affirmed the complete transformation of the In-based MOF into the In_2O_3 without leading to the formation of any secondary phase **(Figure S7.5).** This suggested that the incorporation of Ru dopant does not affect the crystal structure of In_2O_3.

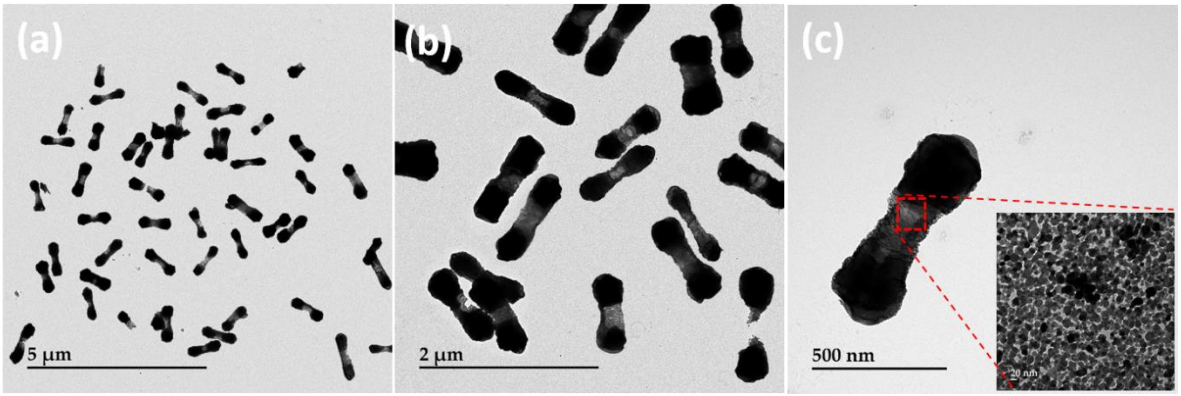

Figure 7.3: (a)-(c) TEM images of 2 wt% Ru doped In_2O_3 with different scales; (Insert image shows the closer view of the respective morphology)

The optical properties of photocatalysts is one of the crucial factors affecting the overall catalytic performance[385]. Hence, the absorption ability of the 2wt% Ru-In_2O_3 and pure In_2O_3 samples were further investigated by UV-Vis diffuse reflectance spectroscopy in the wavelength window of 200 to 700 nm. As shown in **Figure 7.4(a)**, a broad and robust absorption edge was observed up to 400 nm for In_2O_3 HNPs, indicating that the scope of absorption capability is mostly in the UV and near-visible region. Meanwhile, upon the incorporation of Ru dopants, the Ru-In_2O_3 HNPs exhibited a red-shifted absorption band that extending up to 500 nm. This observed improvement suggested that the Ru doping has modified the electronic and bandgap structure of Ru-In_2O_3 HNPs. Accordingly, the changes in bandgap energy were calculated by a Kubelka-Munk function[386], and **Figure 7.4(b)** shows the $(\alpha h\nu)^{1/2}$ versus photon energy plots for the estimation of the bandgap energy of the samples. From the plots, the optical bandgap (E_g) of In_2O_3 HPNs and 2 wt% Ru-In_2O_3 HPNs was determined to be 2.75 and 2.55 eV, respectively.

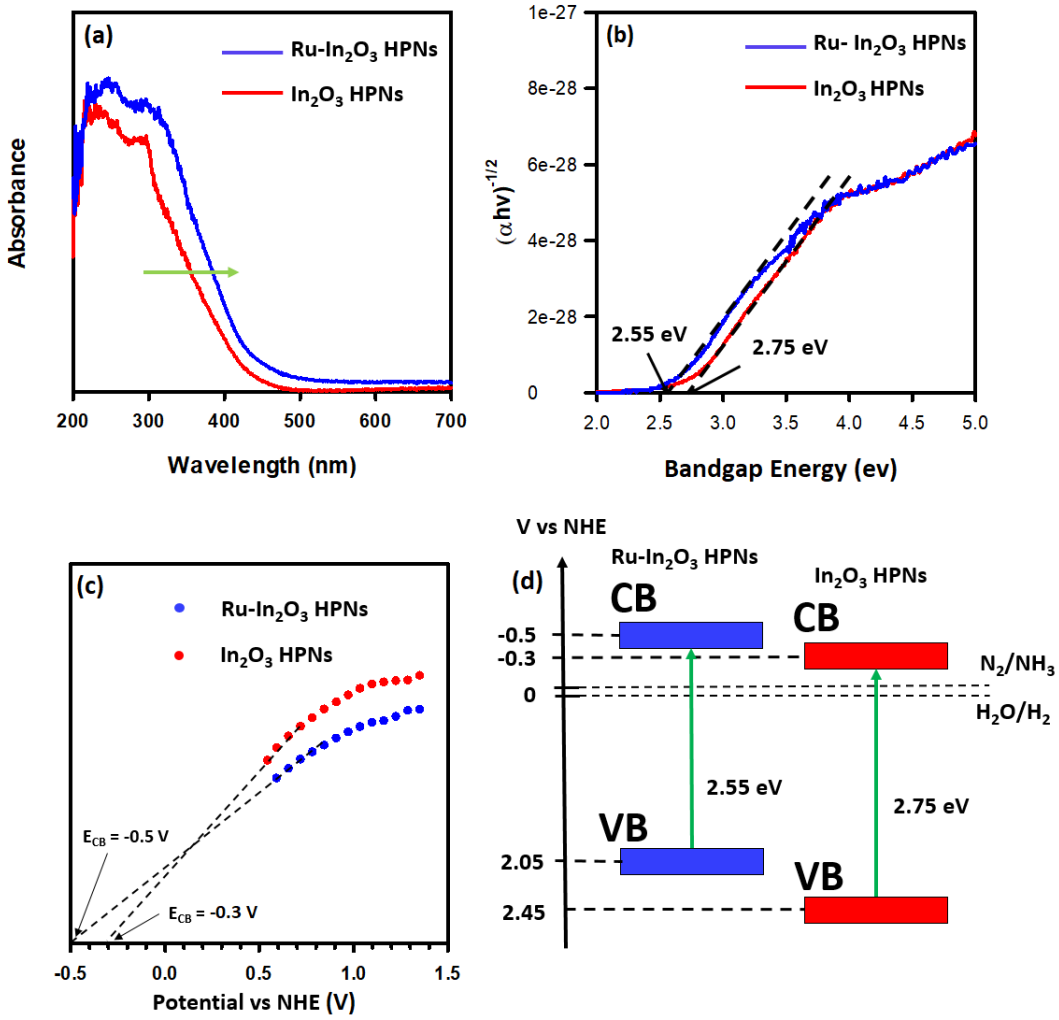

Figure 7.4: (a) UV-Visible absorption spectra, (b) estimated bandgap energies, and (c) Mott-Schottky plots, (d) the band structure alignments of In_2O_3 HPNs and 2 wt% Ru-In_2O_3 HPNs samples.

It is worth noting that the energy position of the band edge level of the valence band (VB) and conduction band (CB) is an essential parameter to validate the suitability of the materials for photocatalytic applications. For an efficient nitrogen reduction reaction, the band edge position of the CB should be more negative than the reduction potential of nitrogen to ammonia (E_{red} = -0.092 V vs. NHE)[387]. Therefore, the Mott-Schottky curves of In_2O_3 HPNs and 2 wt% Ru-In_2O_3 HPNs samples were plotted to figure out the bandgap structure of these samples[32]. As can be seen from **Figure 7.4(c)**, the values of CB potential (E_{CB}) of In_2O_3 and 2 wt% Ru-In_2O_3 photocatalysts are determined to be -0.50 and -0.30 V vs. NHE, respectively.

Interestingly, the CB potential of 2 wt% Ru doped In_2O_3 HPNs exposed an upshift by -0.2 V vs. NHE as compared to the pure In_2O_3 samples. This suggests the enhanced reduction ability of Ru-In_2O_3 HPNs towards nitrogen fixation (**Figure 7.4(d)**). Accordingly, the CB levels of pure In_2O_3 and 2 wt% Ru-In_2O_3 photocatalyst are found to be in a higher position than the N_2/NH_3 potential (-0.092 V vs NHE), indicating that both the bare In_2O_3 and Ru-In_2O_3 are suitable for the photoreduction of nitrogen to ammonia reaction.

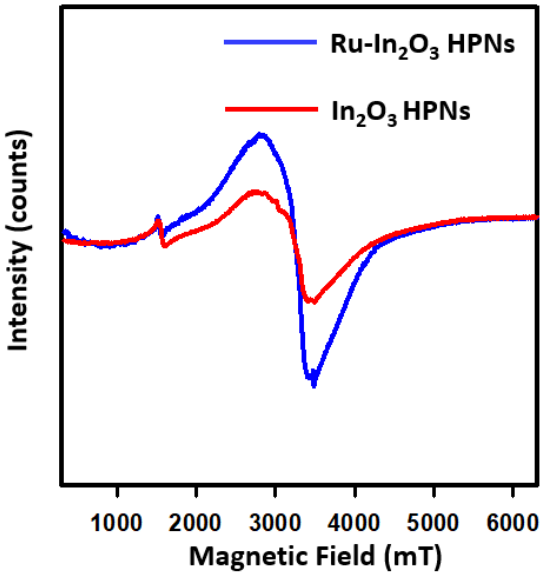

Figure 7.5: EPR spectra of In_2O_3 and 2 wt% Ru-In_2O_3HPNs sample at room temperature

It is known that the surface defects such as oxygen vacancies can serve as efficient active sites, which not only promote the separation of electron-hole but also facilitate the adsorption and activation of nitrogen molecules[123, 388]. Hence, to prove the existence of oxygen vacancies on In_2O_3 and 2wt% Ru-In_2O_3 HNPs samples, the electron magnetic resonance (EPR) analysis was performed. As depicted in **Figure 7.5**, the pure In_2O_3 sample exhibited two broad symmetrical EPR signals at g~2.003, which is assigned to a moderate concentration of oxygen vacancies. According to the previous report, nanosized particles have a tendency to eliminate more oxygen ions, which generate more oxygen vacancies than bulk material[389]. Besides, the EPR spectrum of 2wt% Ru-In_2O_3HPNs displayed a sharp and intense peak. The observed stronger signal implies a higher concentration of oxygen vacancies in the system[390] as compared to bare-In_2O_3. It has been reported that the substitution of host metal cation with a noble metal such as Ru could prolong the M-O and Ru-O bonds

as compared to those in MO_x and RuO_2[391], respectively, that activate the lattice oxygen, increasing mobility of oxygen atoms. Hence, these oxygen atoms easily generate oxygen vacancies. Hence, Ru doping could be an effective strategy to induce more oxygen vacancies on In_2O_3 and thereby produce more active centers for the effective adsorption and activation of N_2.

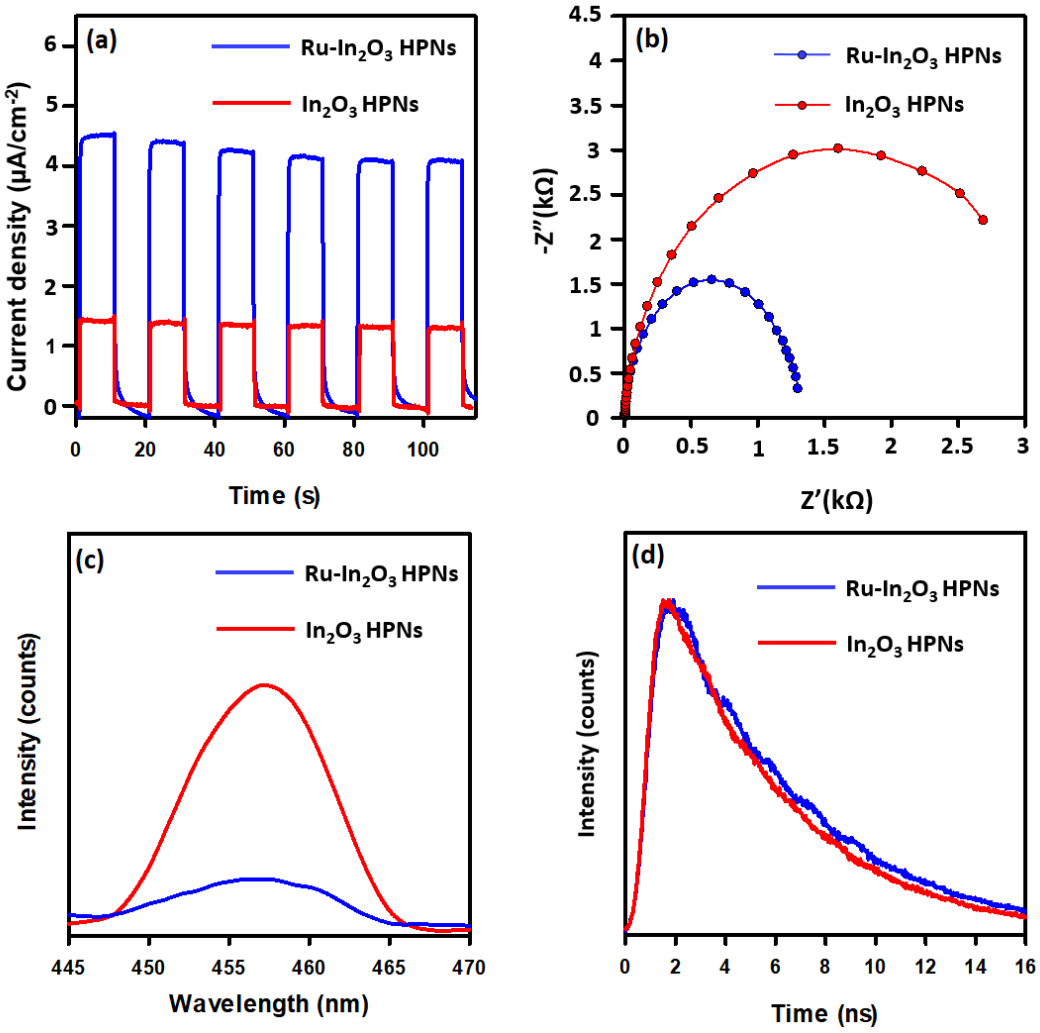

Figure 7.6: (a) Photocurrent responses and (b) Nyquist plots of In_2O_3 HPNs and 2 wt% Ru-In_2O_3 HPNs in 0.5M Na_2SO_4 under saturated N_2, (c) Steady-state and (d) Time-resolved photoluminescence decay of In_2O_3 HPNs and 2 wt% Ru-In_2O_3 HPNs at room temperature

The transient photocurrent response and photoelectrochemical impedance behavior of In_2O_3 HPNs and Ru-In_2O_3 HPNs are recorded and displayed in **Figure 7.6(a-b)**, respectively. The photocurrent measurements of these samples were carried out with the

repetition of six on-off cycles. It is observed that the current intensity of 2wt% Ru-In_2O_3 HPNs is found to be three times higher than that of In_2O_3 HPNs, which suggests a noticeable improvement in charge separation of photoinduced charge carriers. Further, as it is clearly visible in **Figure 7.6(b)**, the Nyquist plot of 2wt% Ru-In_2O_3 HPNs exhibits a smaller semicircle as compared to the In_2O_3 HPNs sample, which implies the decreased electron transfer resistance in Ru-In_2O_3 HPNs as compared to the pure In_2O_3 HPNs[392]. These observations are in good agreement with the obtained photocurrent response of the samples.

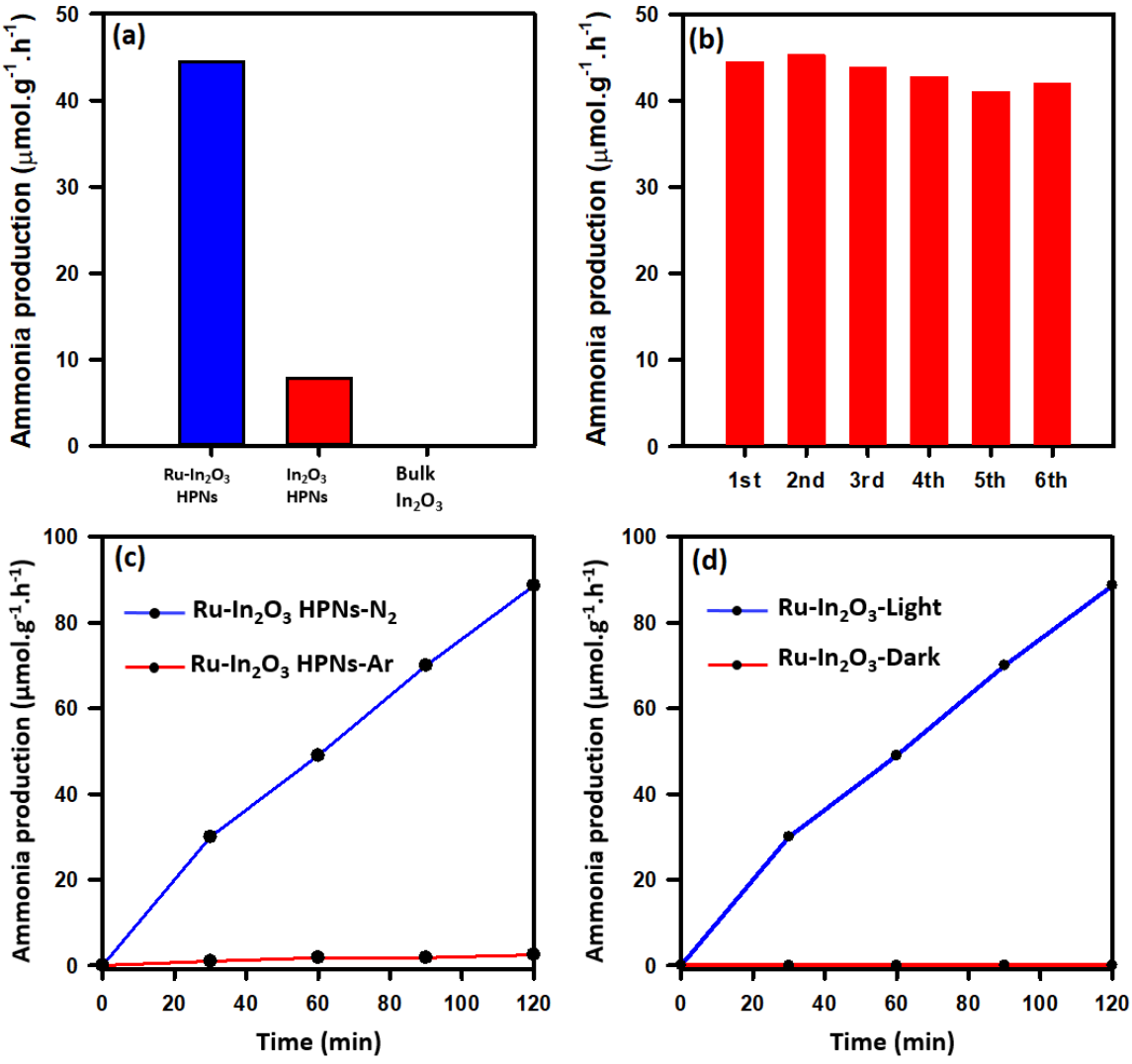

Figure 7.7: (a) Photocatalytic NH_3 production rate of bulk In_2O_3, In_2O_3 HPNs, and 2wt% Ru-In_2O_3 HPNs under solar light irradiation (b) catalytic recycling tests for 2wt% Ru-In_2O_3 HPNs under saturated N_2 in the water and methanol. (c) Photocatalytic nitrogen fixation tests

for 2wt% Ru-In_2O_3 HPNs under saturated N_2 and Ar in water and methanol. (d) Photocatalytic nitrogen fixation tests for Ru-In_2O_3 HPNs under saturated N_2 in dark and light

To further understand the improvement in the photoexcited charge transfer and to calculate the electron lifetime in the samples, the steady-state and time-resolved photoluminescence properties of the samples were investigated. **Figure 7.6(c)** displays the PL spectra of In_2O_3 HPNs and 2wt% Ru-In_2O_3 HPNs at ambient temperature under an excitation wavelength of 350 nm. It can be seen that the emission peak of the samples centered at 455 nm is originated during the recombination of electrons and holes in the system. As compared to pure In_2O_3, the steady-state PL spectrum of 2wt% Ru-In_2O_3 shows a significant decrement in PL intensity, indicating a lower recombination rate of photogenerated electron-hole pairs, which is mainly caused by the abundant number of oxygen vacancies in the 2wt% Ru-In_2O_3 system. These oxygen vacancies essentially act as trapping centers to capture the photogenerated electrons, thereby suppress their recombination. The decay curves of the excited electrons in Ru-In_2O_3 and pure In_2O_3 system are displayed in **Figure 7.6(d)**. The fluorescence lifetime of 2wt% Ru-In_2O_3 HPNs shows a longer decay time (5.47 ns) in comparison with pure In_2O_3 HPNs (4.82 ns), which can be corroborated with steady-state PL results, suggesting the efficient separation of electron-hole pairs in Ru-In_2O_3 HPNs, which could be more beneficial for photocatalytic process.

Figure 7.7(a) compares the photocatalytic activity of the 2wt% Ru-In_2O_3 HPNs with the In_2O_3 HPNs and bulk In_2O_3 sample. Under sunlight irradiation, the pure In_2O_3 HPNs only showed a moderate activity for the nitrogen fixation with the ammonia production rate of 7.8 $\mu mol.h^{-1}.g^{-1}$, whereas the bulk In_2O_3 is incapable of producing ammonia, suggesting that the morphology of In_2O_3 plays a crucial role in improving the photocatalytic activity of the material. It is worth noting that the hollow peanut structure is composed of abundant nanoparticles, which is beneficial for the charge separation due to the large surface area, lower travel path, and the high density of active sites[136]. Further, multiple light reflections inside the hollow walls can also effectively absorb photon energy. Thus, the photocatalytic activity can be enhanced. Accordingly, when the Ru-In_2O_3 hollow peanuts were employed, the photocatalytic performance towards ammonia synthesis reached up to 44.5 $\mu mol.h^{-1}.g^{-1}$, which is around 5.6 times higher than that of pure In_2O_3 HPNs. This significant enhancement

can be attributed to the introduction of Ru element into the lattices of In_2O_3 HPNs, which enhanced the overall photocatalytic efficiencies by narrow down the bandgap energy, enhancing the reduction capability, and providing numerous oxygen vacancies on the surface of In_2O_3 nanoparticles. In addition, different transition metal dopants (such as Fe, Cu, and Mo) were also systematically investigated. The amount of ammonia production rate of these systems was found to be in the order Ru-In_2O_3 > Fe-In_2O_3> Mo-In_2O_3 > Cu-In_2O_3 (**Figure S7.6,** supporting information). This observation suggests that Ru dopants might serve as active sites, which facilitate the reduction of nitrogen. Moreover, a previous report claimed that the introduction of the Ru element can suppress the generation of hydrogen, which highly competes against the reduction of nitrogen[383]. Hence, it is expected that Ru dopant is more advantageous to nitrogen reduction than the other dopant. In order to evaluate the photocatalytic recyclability of 2wt% Ru-In_2O_3 HPNs, the recycle tests were conducted, as shown in **Figure 7.7(b)**. The obtained results showed excellent stability without any evident decrements during six consecutive cycles under the solar simulator. It suggests that 2wt% Ru-In_2O_3 HPNs could be a promising catalyst for the photoreduction of nitrogen to ammonia. Moreover, the control experiments were also performed to affirm the nitrogen source for ammonia production. As seen in **Figure 7.7(c)**, a negligible amount of ammonia generation was detected in the Ar-saturated environment, and no trace of NH_3 was found without light irradiation (**Figure 7.7(d)**). These observations indicated that NH_3 was primarily evolved from N_2 gas rather than from the other sources.

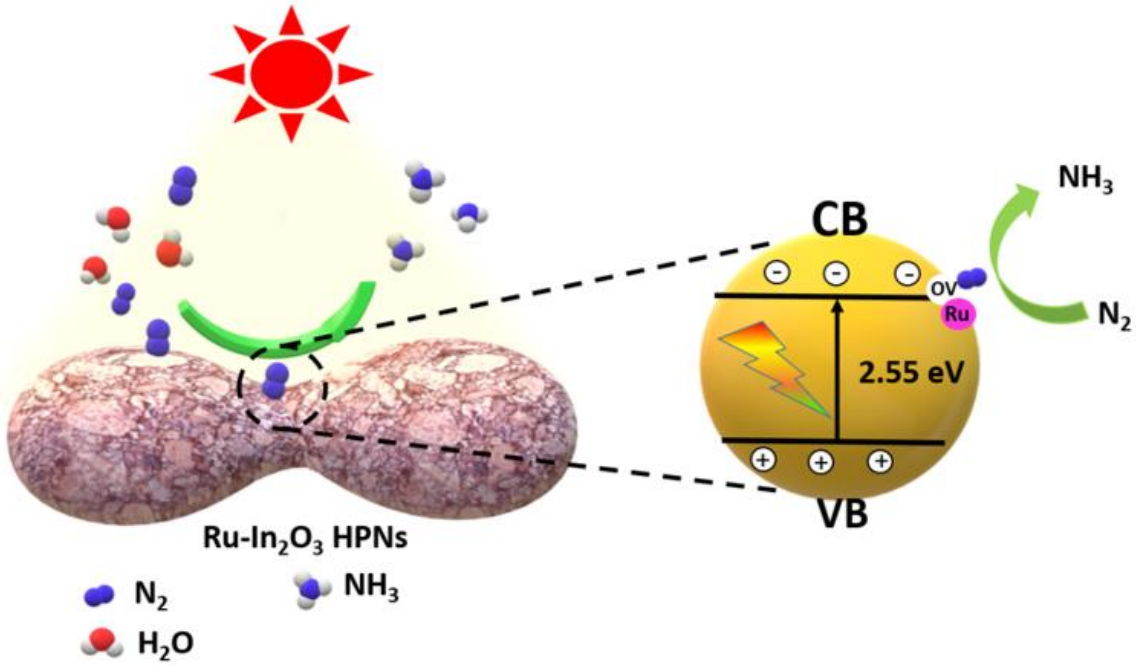

Figure 7.8: Schematic demonstration of the proposed mechanism for the photocatalytic nitrogen fixation over the Ru-In_3O_3 HPNs

Based on the discussed results, we propose a possible mechanism of photocatalytic nitrogen fixation by Ru-In_3O_3 hollow peanut, as illustrated in **Figure 7.8**. Upon the solar light illumination, electrons are excited from the valence band to the conduction band of Ru-In_2O_3, and due to the small particle size and abundant surface defects, these photoexcited electrons were easily migrated to the surface of In_2O_3 nanoparticles and then these electrons were further trapped by Ru active centers and oxygen vacancies where nitrogen molecules were preferably adsorbed. Consequently, these trapped electrons activated the N-N triple bond and reduced N_2 to produce NH_3[375, 385]. Meanwhile, the highly oxidized holes on the VB are consumed by the electron donors (methanol) in the reaction mixture.

7.4 Conclusion

In summary, Ru-In_2O_3 hollow peanuts were successfully prepared by a simple self-template method as an efficient photocatalyst for the photoreduction of nitrogen to ammonia under solar light irradiation. The hollow peanut is composed of plentiful nanoparticles, which essentially minimizes the travel pathway of electrons and effectively utilizes the photon

energy of the solar spectrum. In contrast, the homogeneous distribution of Ru element in In_2O_3 improved the visible light absorption and provided the abundant oxygen vacancies as active sites in the material and promoted the rapid separation of the photogenerated charge carriers in the system. As a result, the Ru-In_2O_3 catalyst showed significant enhancements in the photocatalytic activity towards nitrogen fixation by achieving the highest ammonia production rate of 44.5 $\mu mol.g^{-1}.h^{-1}$ under the ambient condition, which is approximately 5.6-fold higher than that of the bare In_2O_3 HPNs and much higher than that of bulk In_2O_3. This observed enhanced catalytic efficiency could be attributed to the synergic effects of the hollow structure and the incorporation of Ru dopant. From the obtained results, Ru doped In_2O_3 hollow peanuts that derived from MOF-based material could be suggested as a promising photocatalyst for nitrogen fixation under solar light irradiation. This work may open up new guidelines for the design and construction of semiconductor materials with a hollow structure for a wide range of applications in the field of photocatalysis.

Acknowledgments

This work was supported by the Natural Science and Engineering Research Council of Canada (NSERC) through the Collaborative Research and Development (CRD), Strategic Project (SP), and Discovery Grants.

7.5 Supporting Information

Determination of ammonia

The ammonia concentration was spectrophotometrically measured by the indophenol blue method. Briefly, 1 mL of reacted solution was removed from the photoreactor. Next, 2 mL of 1M NaOH containing 5 wt% salicylic acid and 5 wt% sodium citrate, 1 mL of 0.05 M NaClO, and 0.2 mL of 1 wt% $C_5FeN_6Na_2O$ (sodium nitroferricyanide) were sequentially added to the solution. After 2 h at ambient temperature, 2 mL of as-prepared solution was drawn out for UV-Vis measurement at a wavelength of 655 nm to determine the formation on indophenol blue. For the calibration of the concentration-absorbance curve, standard ammonia chloride solution with a concentration of 10, 20, 30, 40, 50, 100 µM in 10 vol% MeOH was used (Figure S.1), which contained the same concentration of MeOH as in the testing solution.

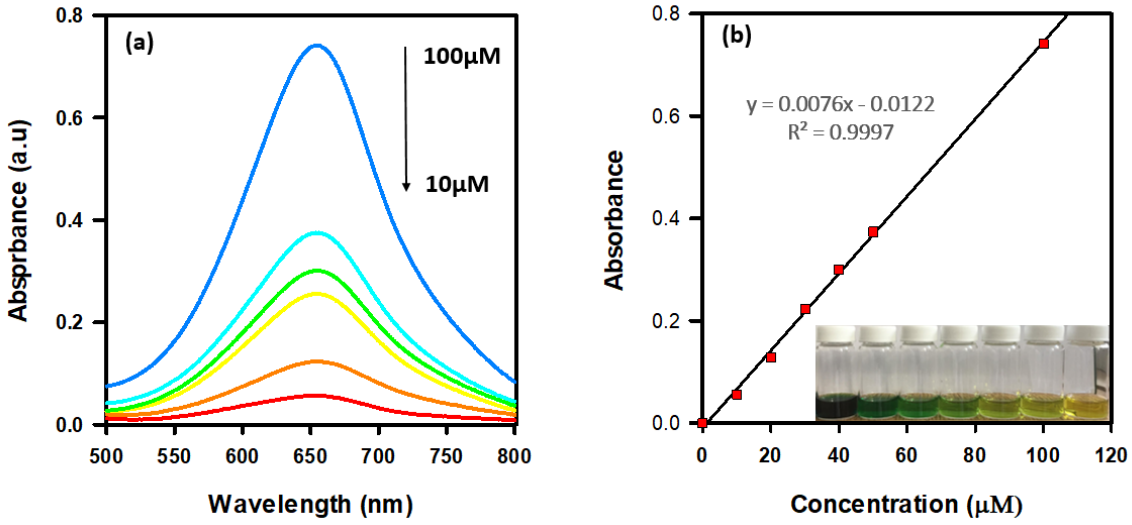

Figure S7.1: (a) UV-vis spectra for ammonium quantification using the indophenol-blue method with the concentration of 10, 20, 30, 40, 50, 100 µM in 10 vol% MeOH, respectively; (b) The calibration curve for ammonium quantification (NH_4^+ concentration versus absorbance at 655 nm).

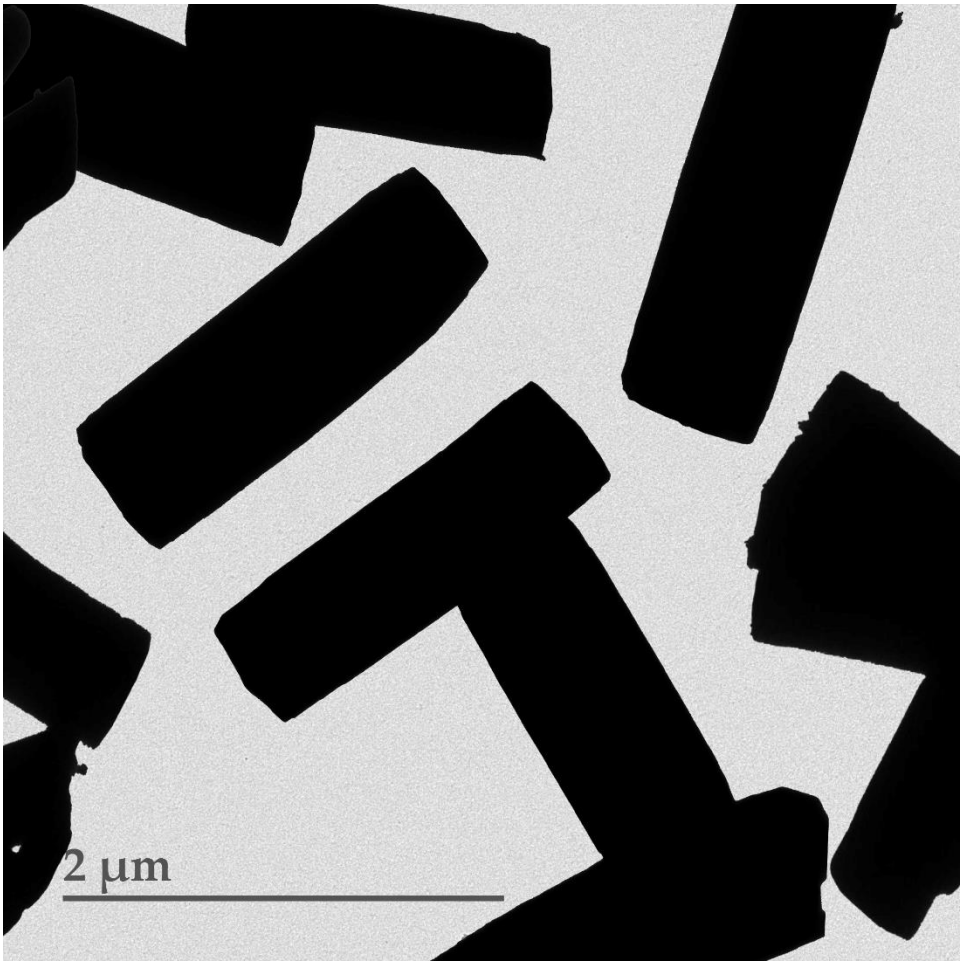

Figure S7.2 The TEM images of MIL-68-In(Ru) precursors for 1h reaction.

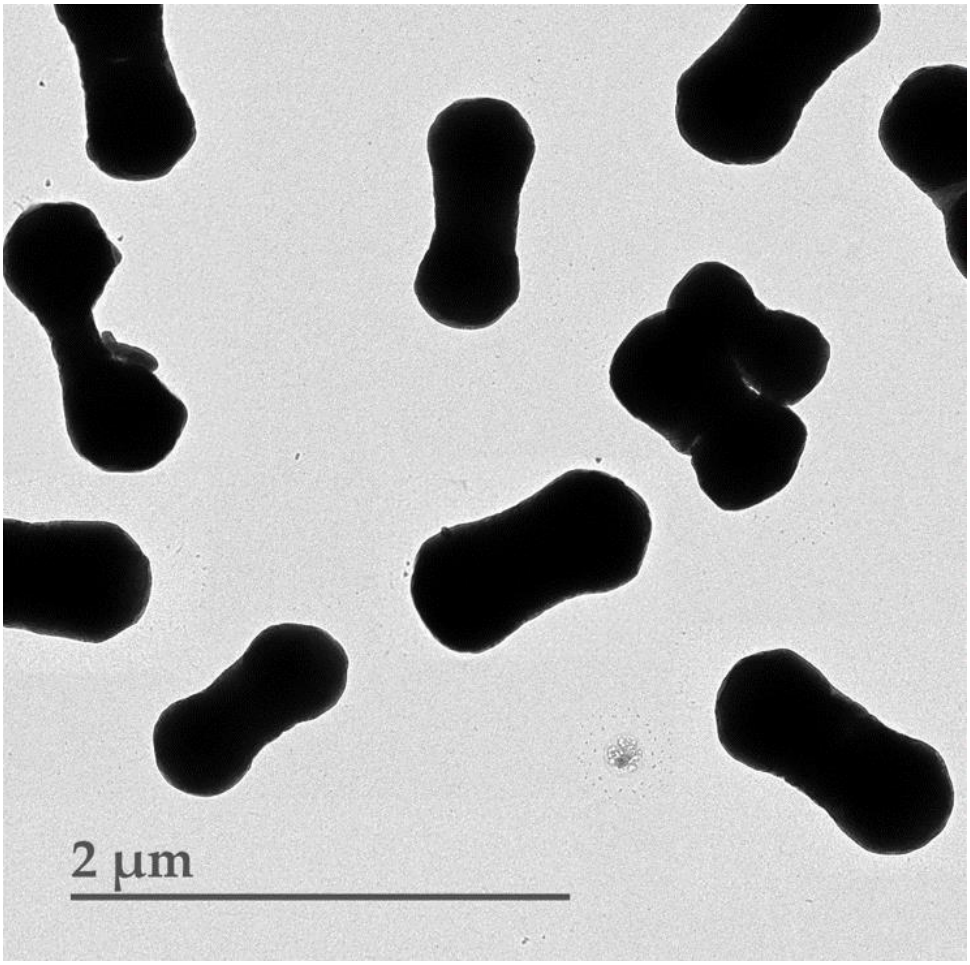

Figure S7.3 The TEM images of MIL-68-In(Ru) precursors with 2% Ru doping.

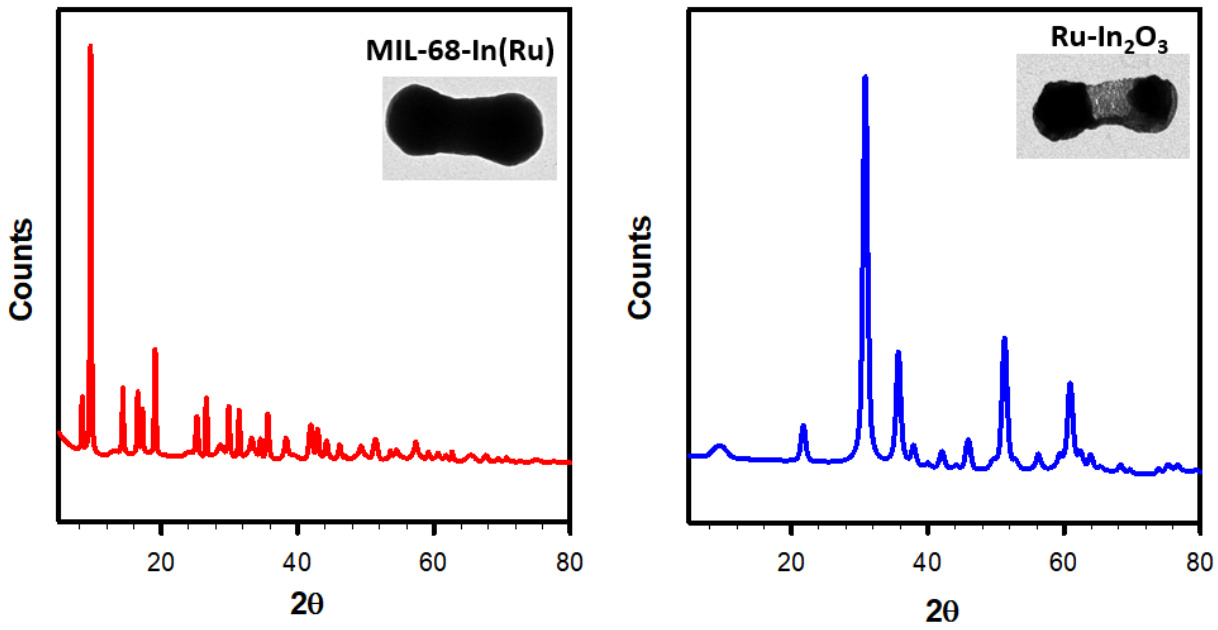

Figure S7.4: X-ray diffraction spectra of MIL-68-In(Ru) and 2 wt% Ru-In_2O_3 hollow peanut samples

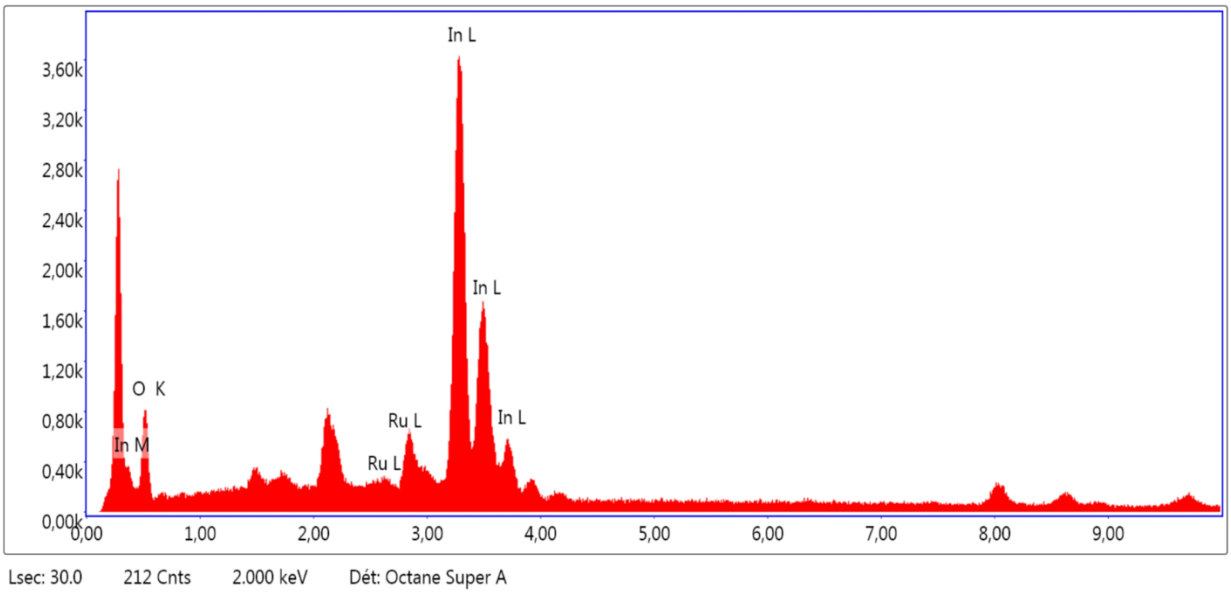

Figure S7.5: Representative EDX analysis collected on 2 wt% Ru-In_2O_3 HPNs samples

EDX spectrum confirms that Ru-In_2O_3 HPNs mainly compose of Ru, In and O. The Cu signals are from the substrate

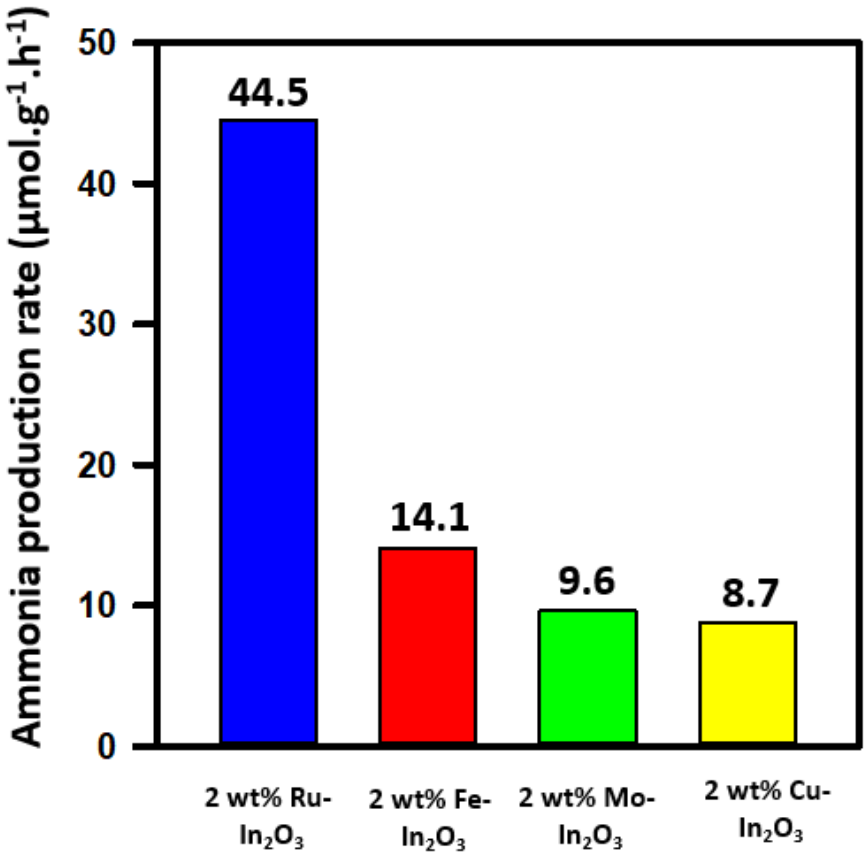

Figure S7.6: Photocatalytic NH_3 production rate of different transition metal dopants

Conclusion and Future outlook

This chapter summarizes the main conclusions of all the works performed in the thesis followed by an outlook for future research orientation.

8.1 General conclusion

The overarching goal of this thesis was to develop novel strategies for the preparation of efficient photocatalysts towards hydrogen evolution and reduction of nitrogen to ammonia. We have revealed several approaches to improve the photocatalytic activity of different materials, which can overcome the limitations such as low charge carrier separation, poor visible-light absorption, and insufficient active sites in the existing semiconductor-based photocatalysts. Our strategies include the construction of nanostructure, incorporation of foreign elements, coupling of the photocatalyst with a cocatalyst, and plasmonic materials. As a result, we have successfully demonstrated significant enhancements in the photocatalytic performance of $CdIn_2S_4$, g-C_3N_4, $W_{18}O_{49}$, and In_2O_3.

First, we started with the synthesis of Ni loaded $CdIn_2S_4$ sponge-like spheres for photocatalytic hydrogen generation. A novel combination of glycerate-template combustion and sulfidation by H_2S gas was introduced to fabricate single-phase $CdIn_2S_4$ spheres. The sponge-like sphere of $CdIn_2S_4$ is composed of numerous closely packed nanoparticles of an average size of 25 nm, which is beneficial for the separation and migration of electron from bulk to the surface by reducing the travel pathway of electrons. On the other hand, the replacement of oxygen by sulfur transformed the mixed oxide into single-phase sulfide, which drastically improved the visible light absorption of the as-obtained $CdIn_2S_4$. These advantageous features synergistically contributed to the improvement of the photocatalytic activity and yielded the apparent quantum efficiency of 3.35% at 420 nm, which was evolved as one of the best $CdIn_2S_4$-based photocatalysts working under sunlight illumination to date.

Based on the first project, we have realized that nickel coupled with sulfide-based photocatalyst can be active for the photocatalytic hydrogen evolution. Therefore, we continued to employ the H_2S treatment method to create Ni-S-C-N bonds on Ni supported g-C_3N_4. The resulted material exhibited a high separation rate of electron-hole and extended the light absorption towards visible light. Moreover, Ni cocatalyst can act as an active site to promote the generation of hydrogen. This work illustrated that the formation of chemical bonding between cocatalyst and host photocatalyst can be a relatively effective strategy, which is generally unable to obtain by conventional deposition. As a result, the as-synthesized sample was able to produce H_2 at a considerable rate under with high quantum

yield of 17.2% at 440 nm, which is relatively one of the highest values reported in the literature.

In chapter 5, we have synergistically utilized the localized surface plasmon resonance (LSPR) effect and doping strategy to design an efficient $W_{18}O_{49}$-based catalyst that can reduce the nitrogen to ammonia under visible-light irradiation. Although $W_{18}O_{49}$-based semiconductor possesses an abundant number of bulk oxygen vacancies, these oxygen vacancies act as bulk defects and prevent the separation of photogenerated charge carriers. Then, we introduced an appropriate amount of Fe dopant into the crystal structure of $W_{18}O_{49}$. The incorporation of Fe element not only removed the bulk defect but also enhanced the visible-light harvesting capability and electron-hole separation. To this system, Au nanoparticle was also coupled to induce the LSPR effect and thus the prepared Au decorated Fe-doped $W_{18}O_{49}$-system performed an excellent photo-electrocatalytic activity for the nitrogen fixation.

Finally, we constructed a hollow peanut structure of Ru doped In_2O_3 via a one-pot synthesis of MOF precursors followed by calcination in the air. The as-achieved Ru doped In_2O_3 photocatalyst exhibited outstanding photocatalytic performance for ammonia synthesis via nitrogen reduction. The utilization of a hollow structure effectively improved the separation and transportation of photoinduced charge carriers and efficiently harvested the photon energy by multiple reflection/scattering processes. The introduction of Ru dopants has not only extended the intrinsic absorption towards the visible light region but also generated the surface oxygen vacancies, which was beneficial for the reduction of nitrogen. This approach suggested a new avenue to prepare the highly efficient hollow-structured photocatalyst with unique features.

8.2 Future outlook

Since the first breakthrough proposed by Fujishima *et al.* in 1972, the scientific and engineering communities are continuously moving forward to develop sustainable and efficient photocatalysts for converting the incident solar energy into chemical energy that can be used as alternatives for fossil fuels. Recently, photocatalytic researches have opened up a new possibility of designing effective catalysts using single-atom active sites owing to their compelling advantages in promoting light-absorption, charger carrier separation, and surface reaction of a photocatalytic process. Single-atom photocatalysts (SAPC), identified as

isolated metal atoms anchored on appropriate support, can obtain the maximum efficiency of atomic utilization, reducing the amount of loaded catalyst. With the unique properties of unsaturated coordination sites, single-atom metal can serve as an active site for diverse photocatalytic reactions such as CO_2 and CO reduction. Additionally, the well-defined single-atom active sites facilitate a thorough understanding of the catalytic mechanism, which is beneficial for the design and construction of an efficient photocatalytic system. Based on these features, the fabrication of single-atom photocatalyst will be a promising strategy for the high-efficiency photochemical energy conversion process, particularly for hydrogen evolution and nitrogen fixation.

Individual active atoms with extreme-high surface energy always tend to agglomerate to form nanoparticles. Hence, isolating single metal atoms into the inner structure of its support is the most critical challenge for the preparation of a single-atom catalyst. There are several approaches for developing the single-atom photocatalyst, involving bonding with surface oxo ligands, anchoring with heteroatoms, and coordinating with surface defects. The durability and catalytic performance of the SAPCs highly depend on the stabilization of individual active sites by coordination bonds with neighboring atoms and confined space.

Bonding with surface oxo ligands: In this method, metal oxides such as TiO_2, Fe_2O_3, ZnO, and SiO_2 can be effectively used as supports for single-metal-atom sites. It should be noted that the abundant oxygen atoms presented on these metal oxide can coordinate with single metal atoms to prevent their movement and aggregation, resulting in stabilizing metal active-sites and enhancing catalytic performance.

Anchoring with heteroatoms: In addition to surface oxo ligands, the incorporation of extrinsic dopants could also isolate single metal atoms, forming chemical bonds among single metal atoms-dopant-support which effectively promote the photogenerated charge separation and eventually improve the light-harvesting capability. As a result, the photocatalytic activity can be significantly boosted.

Coordinating surface defects: On the surface of nanostructured material, the vacancies and monoatomic step edges are the two common intrinsic defects with high surface energy, where these types of defects can act as the surrounded coordinating environment to capture and stabilize the single metal atoms. Hence, the amount of defect decides the number of single

atomic sites. The advantage of this approach is the tunable concentration of defects, which can be adjusted by controlling the size of nanoparticles and the synthesis conditions, facilitate the preparation of SAPCs.

To summarize, various approaches such as the coordination with dopant sites, surface oxo ligands, and defects have been suggested towards improving the efficiency of photo(electro)catalytic materials under solar light irradiation. The significant roles of these methods are to essentially augment the ability of visible light absorption, enhance the charge-separation as well as decrease the charge-recombination processes and increase the number of active-sites in the photocatalytic systems towards achieving the enhanced photocatalytic activities.

References

1. Linsebigler, A. L.; Lu, G.; Yates, J. T., Photocatalysis on TiO_2 Surfaces: Principles, Mechanisms, and Selected Results. *Chem. Rev.* **1995,** *95* (3), 735-758, DOI 10.1021/cr00035a013.

2. Furube, A.; Asahi, T.; Masuhara, H.; Yamashita, H.; Anpo, M., Charge Carrier Dynamics of Standard TiO_2 Catalysts Revealed by Femtosecond Diffuse Reflectance Spectroscopy. *The Journal of Physical Chemistry B* **1999,** *103* (16), 3120-3127, DOI 10.1021/jp984162h.

3. Habisreutinger Severin, N.; Schmidt-Mende, L.; Stolarczyk Jacek, K., Photocatalytic Reduction of CO_2 on TiO_2 and Other Semiconductors. *Angew. Chem. Int. Ed.* **2013,** *52* (29), 7372-7408, DOI 10.1002/anie.201207199.

4. Li, X.; Yu, J.; Low, J.; Fang, Y.; Xiao, J.; Chen, X., Engineering heterogeneous semiconductors for solar water splitting. *Journal of Materials Chemistry A* **2015,** *3* (6), 2485-2534, DOI 10.1039/C4TA04461D.

5. Schiavello, M.; Augugliaro, V.; Palmisano, L., An experimental method for the determination of the photon flow reflected and absorbed by aqueous dispersions containing polycrystalline solids in heterogeneous photocatalysis. *J. Catal.* **1991,** *127* (1), 332-341, DOI https://doi.org/10.1016/0021-9517(91)90229-W.

6. Kisch, H.; Bahnemann, D., Best Practice in Photocatalysis: Comparing Rates or Apparent Quantum Yields? *The Journal of Physical Chemistry Letters* **2015,** *6* (10), 1907-1910, DOI 10.1021/acs.jpclett.5b00521.

7. Buriak, J. M.; Kamat, P. V.; Schanze, K. S., Best Practices for Reporting on Heterogeneous Photocatalysis. *ACS Applied Materials & Interfaces* **2014,** *6* (15), 11815-11816, DOI 10.1021/am504389z.

8. Khan, S. U. M.; Al-Shahry, M.; Ingler, W. B., Efficient Photochemical Water Splitting by a Chemically Modified n-TiO_2. *Science* **2002,** *297* (5590), 2243-2245, DOI 10.1126/science.1075035.

9. Jing, D.; Guo, L., A Novel Method for the Preparation of a Highly Stable and Active CdS Photocatalyst with a Special Surface Nanostructure. *The Journal of Physical Chemistry B* **2006,** *110* (23), 11139-11145, DOI 10.1021/jp060905k.

10. Cao, J.; Sun, J. Z.; Hong, J.; Li, H. Y.; Chen, H. Z.; Wang, M., Carbon Nanotube/CdS Core–Shell Nanowires Prepared by a Simple Room-Temperature Chemical Reduction Method. *Adv. Mater.* **2004,** *16* (1), 84-87, DOI 10.1002/adma.200306100.

11. Wang, X.; Liu, G.; Lu, G. Q.; Cheng, H.-M., Stable photocatalytic hydrogen evolution from water over ZnO–CdS core–shell nanorods. *Int. J. Hydrogen Energy* **2010,** *35* (15), 8199-8205, DOI https://doi.org/10.1016/j.ijhydene.2009.12.091.

12. Wang, X.; Liu, G.; Chen, Z.-G.; Li, F.; Wang, L.; Lu, G. Q.; Cheng, H.-M., Enhanced photocatalytic hydrogen evolution by prolonging the lifetime of carriers in ZnO/CdS heterostructures. *Chem. Commun.* **2009,** (23), 3452-3454, DOI 10.1039/B904668B.

13. Hou, J.; Wang, Z.; Kan, W.; Jiao, S.; Zhu, H.; Kumar, R. V., Efficient visible-light-driven photocatalytic hydrogen production using CdS@TaON core-shell composites coupled with graphene oxide nanosheets. *J. Mater. Chem.* **2012,** *22* (15), 7291-7299, DOI 10.1039/C2JM15791H.

14. Gur, I.; Fromer, N. A.; Geier, M. L.; Alivisatos, A. P., Air-Stable All-Inorganic Nanocrystal Solar Cells Processed from Solution. *Science* **2005,** *310* (5747), 462.

15. Steckel, J. S.; Zimmer, J. P.; Coe-Sullivan, S.; Stott, N. E.; Bulović, V.; Bawendi, M. G., Blue Luminescence from (CdS)ZnS Core–Shell Nanocrystals. *Angew. Chem. Int. Ed.* **2004,** *43* (16), 2154-2158, DOI 10.1002/anie.200453728.

16. Ohko, Y.; Tatsuma, T.; Fujii, T.; Naoi, K.; Niwa, C.; Kubota, Y.; Fujishima, A., Multicolour photochromism of TiO_2 films loaded with silver nanoparticles. *Nature Materials* **2002,** *2*, 29, DOI 10.1038/nmat796.

17. Zhao, H.; Pan, F.; Li, Y., A review on the effects of TiO_2 surface point defects on CO2 photoreduction with H_2O. *Journal of Materiomics* **2017,** *3* (1), 17-32, DOI https://doi.org/10.1016/j.jmat.2016.12.001.

18. Xin, Y.; Lu, Y.; Han, C.; Ge, L.; Qiu, P.; Li, Y.; Fang, S., Novel NiS cocatalyst decorating ultrathin 2D TiO_2 nanosheets with enhanced photocatalytic hydrogen evolution activity. *Mater. Res. Bull.* **2017,** *87*, 123-129, DOI https://doi.org/10.1016/j.materresbull.2016.11.027.

19. Li, C.; Wang, T.; Zhao, Z. J.; Yang, W.; Li, J. F.; Li, A.; Yang, Z.; Ozin Geoffrey, A.; Gong, J., Promoted Fixation of Molecular Nitrogen with Surface Oxygen Vacancies on

Plasmon-Enhanced TiO_2 Photoelectrodes. *Angew. Chem. Int. Ed.* **2018,** *57* (19), 5278-5282, DOI 10.1002/anie.201713229.

20. Reli, M.; Huo, P.; Šihor, M.; Ambrožová, N.; Troppová, I.; Matějová, L.; Lang, J.; Svoboda, L.; Kuśtrowski, P.; Ritz, M.; Praus, P.; Kočí, K., Novel TiO_2/C_3N_4 Photocatalysts for Photocatalytic Reduction of CO2 and for Photocatalytic Decomposition of N2O. *The Journal of Physical Chemistry A* **2016,** *120* (43), 8564-8573, DOI 10.1021/acs.jpca.6b07236.

21. Xu, C.; Rangaiah, G. P.; Zhao, X. S., Photocatalytic Degradation of Methylene Blue by Titanium Dioxide: Experimental and Modeling Study. *Industrial & Engineering Chemistry Research* **2014,** *53* (38), 14641-14649, DOI 10.1021/ie502367x.

22. Dariani, R. S.; Esmaeili, A.; Mortezaali, A.; Dehghanpour, S., Photocatalytic reaction and degradation of methylene blue on TiO_2 nano-sized particles. *Optik* **2016,** *127* (18), 7143-7154, DOI https://doi.org/10.1016/j.ijleo.2016.04.026.

23. Chen, L.; Zhao, C.; Dionysiou, D. D.; O'Shea, K. E., TiO_2 photocatalytic degradation and detoxification of cylindrospermopsin. *Journal of Photochemistry and Photobiology A: Chemistry* **2015,** *307-308*, 115-122, DOI https://doi.org/10.1016/j.jphotochem.2015.03.013.

24. Comer, B. M.; Medford, A. J., Analysis of Photocatalytic Nitrogen Fixation on Rutile TiO2(110). *ACS Sustainable Chemistry & Engineering* **2018,** *6* (4), 4648-4660, DOI 10.1021/acssuschemeng.7b03652.

25. Zhao, W.; Zhang, J.; Zhu, X.; Zhang, M.; Tang, J.; Tan, M.; Wang, Y., Enhanced nitrogen photofixation on Fe-doped TiO_2 with highly exposed (101) facets in the presence of ethanol as scavenger. *Applied Catalysis B: Environmental* **2014,** *144*, 468-477, DOI https://doi.org/10.1016/j.apcatb.2013.07.047.

26. Liu, Q.; Ai, L.; Jiang, J., MXene-derived TiO_2@C/g-C_3N_4 heterojunctions for highly efficient nitrogen photofixation. *Journal of Materials Chemistry A* **2018,** *6* (9), 4102-4110, DOI 10.1039/C7TA09350K.

27. Zhang, X.; Zhang, G.; Zou, J., Nitrogen reduction utilizing solvated electrons produced by thermal excitation of trapped electrons in reduced titanium oxide. *New J. Chem.* **2018,** *42* (8), 6084-6090, DOI 10.1039/C8NJ00560E.

28. Li, C.; Wang, T.; Zhao, Z.-J.; Yang, W.; Li, J.-F.; Li, A.; Yang, Z.; Ozin, G. A.; Gong, J., Promoted Fixation of Molecular Nitrogen with Surface Oxygen Vacancies on Plasmon-

Enhanced TiO_2 Photoelectrodes. *Angew. Chem. Int. Ed.* **2018,** *57* (19), 5278-5282, DOI 10.1002/anie.201713229.

29. Pan, J.; Jiang, S. P., Synthesis of nitrogen doped faceted titanium dioxide in pure brookite phase with enhanced visible light photoactivity. *J. Colloid Interface Sci.* **2016,** *469*, 25-30, DOI https://doi.org/10.1016/j.jcis.2016.02.013.

30. Perovskite-based photocatalysts for organic contaminants removal: Current status and future perspectives. *Catalysis Today* **2018**.

31. Gurylev, V.; Mishra, M.; Su, C.-Y.; Perng, T.-P., Enabling higher photoelectrochemical efficiency of TiO_2 via controlled formation of a disordered shell: an alternative to the hydrogenation process. *Chemical Communications* **2016,** *52* (48), 7604-7607, DOI 10.1039/C5CC10610A.

32. Vu, M.-H.; Sakar, M.; Nguyen, C.-C.; Do, T.-O., Chemically Bonded Ni Cocatalyst onto the S Doped g-C_3N_4 Nanosheets and Their Synergistic Enhancement in H_2 Production under Sunlight Irradiation. *ACS Sustainable Chemistry & Engineering* **2018,** *6* (3), 4194-4203, DOI 10.1021/acssuschemeng.7b04598.

33. Xiong, J.; Di, J.; Xia, J.; Zhu, W.; Li, H., Surface Defect Engineering in 2D Nanomaterials for Photocatalysis. *Adv. Funct. Mater.* **2018,** *28* (39), 1801983, DOI doi:10.1002/adfm.201801983.

34. Liu, M.; Chen, Y.; Su, J.; Shi, J.; Wang, X.; Guo, L., Photocatalytic hydrogen production using twinned nanocrystals and an unanchored NiS_x co-catalyst. *Nature Energy* **2016,** *1*, 16151, DOI 10.1038/nenergy.2016.151

35. Xie, Y.; Wang, T.-T.; Liu, X.-H.; Zou, K.; Deng, W.-Q., Capture and conversion of CO_2 at ambient conditions by a conjugated microporous polymer. *Nature Communications* **2013,** *4*, 1960, DOI 10.1038/ncomms2960

36. Ran, J.; Zhang, J.; Yu, J.; Jaroniec, M.; Qiao, S. Z., Earth-abundant cocatalysts for semiconductor-based photocatalytic water splitting. *Chem. Soc. Rev.* **2014,** *43* (22), 7787-7812, DOI 10.1039/C3CS60425J.

37. Khan, S. U. M.; Majumder, S. A., Optimization of p-silicon surface by etching and electrodeposition of Pt and Ni for photosplitting of water. *Int. J. Hydrogen Energy* **1989,** *14* (9), 653-660, DOI https://doi.org/10.1016/0360-3199(89)90041-4.

38. Akikusa, J.; Khan, S. U. M., Photoelectrolysis of water to hydrogen in p-SiC/Pt and p-SiC/ n-TiO_2 cells. *Int. J. Hydrogen Energy* **2002,** *27* (9), 863-870, DOI https://doi.org/10.1016/S0360-3199(01)00191-4.

39. Gurunathan, K., Photocatalytic hydrogen production using transition metal ions-doped γ-Bi_2O_3 semiconductor particles. *Int. J. Hydrogen Energy* **2004,** *29* (9), 933-940, DOI https://doi.org/10.1016/j.ijhydene.2003.04.001.

40. Jang, J. S.; Yoon, K. Y.; Xiao, X.; Fan, F.-R. F.; Bard, A. J., Development of a Potential Fe_2O_3-Based Photocatalyst Thin Film for Water Oxidation by Scanning Electrochemical Microscopy: Effects of Ag−Fe_2O_3 Nanocomposite and Sn Doping. *Chem. Mater*. **2009,** *21* (20), 4803-4810, DOI 10.1021/cm901056c.

41. Jang, J. S.; Choi, S. H.; Kim, H. G.; Lee, J. S., Location and State of Pt in Platinized CdS/TiO_2 Photocatalysts for Hydrogen Production from Water under Visible Light. *The Journal of Physical Chemistry C* **2008,** *112* (44), 17200-17205, DOI 10.1021/jp804699c.

42. Maeda, K.; Xiong, A.; Yoshinaga, T.; Ikeda, T.; Sakamoto, N.; Hisatomi, T.; Takashima, M.; Lu, D.; Kanehara, M.; Setoyama, T.; Teranishi, T.; Domen, K., Photocatalytic Overall Water Splitting Promoted by Two Different Cocatalysts for Hydrogen and Oxygen Evolution under Visible Light. *Angew. Chem. Int. Ed.* **2010,** *49* (24), 4096-4099, DOI 10.1002/anie.201001259.

43. Zeng, H.; Terazono, S.; Tanuma, T., A novel catalyst for ammonia synthesis at ambient temperature and pressure: Visible light responsive photocatalyst using localized surface plasmon resonance. *Catal. Commun.* **2015,** *59*, 40-44, DOI https://doi.org/10.1016/j.catcom.2014.09.034.

44. Oshikiri, T.; Ueno, K.; Misawa, H., Plasmon-Induced Ammonia Synthesis through Nitrogen Photofixation with Visible Light Irradiation. *Angew. Chem. Int. Ed.* **2014,** *53* (37), 9802-9805, DOI 10.1002/anie.201404748.

45. Yang, J.; Guo, Y.; Jiang, R.; Qin, F.; Zhang, H.; Lu, W.; Wang, J.; Yu, J. C., High-Efficiency "Working-in-Tandem" Nitrogen Photofixation Achieved by Assembling Plasmonic Gold Nanocrystals on Ultrathin Titania Nanosheets. *J. Am. Chem. Soc.* **2018,** *140* (27), 8497-8508, DOI 10.1021/jacs.8b03537.

46. Xiao, C.; Hu, H.; Zhang, X.; MacFarlane, D. R., Nanostructured Gold/Bismutite Hybrid Heterocatalysts for Plasmon-Enhanced Photosynthesis of Ammonia. *ACS*

Sustainable Chemistry & Engineering **2017,** *5* (11), 10858-10863, DOI 10.1021/acssuschemeng.7b02788.

47. Ali, M.; Zhou, F.; Chen, K.; Kotzur, C.; Xiao, C.; Bourgeois, L.; Zhang, X.; MacFarlane, D. R., Nanostructured photoelectrochemical solar cell for nitrogen reduction using plasmon-enhanced black silicon. *Nature Communications* **2016,** *7*, 11335, DOI 10.1038/ncomms11335

48. Oshikiri, T.; Ueno, K.; Misawa, H., Selective Dinitrogen Conversion to Ammonia Using Water and Visible Light through Plasmon-induced Charge Separation. *Angew. Chem.* **2016,** *128* (12), 4010-4014, DOI 10.1002/ange.201511189.

49. Naldoni, A.; Guler, U.; Wang, Z.; Marelli, M.; Malara, F.; Meng, X.; Besteiro, L. V.; Govorov, A. O.; Kildishev, A. V.; Boltasseva, A.; Shalaev, V. M., Broadband Hot-Electron Collection for Solar Water Splitting with Plasmonic Titanium Nitride. *Advanced Optical Materials* **2017,** *5* (15), 1601031, DOI doi:10.1002/adom.201601031.

50. Fujishima, A.; Honda, K., Electrochemical Photolysis of Water at a Semiconductor Electrode. *Nature* **1972,** *238* (5358), 37-38, DOI 10.1038/238037a0.

51. Bard, A. J., Photoelectrochemistry and heterogeneous photo-catalysis at semiconductors. *Journal of Photochemistry* **1979,** *10* (1), 59-75, DOI https://doi.org/10.1016/0047-2670(79)80037-4.

52. Zhang, J. Z., Metal oxide nanomaterials for solar hydrogen generation from photoelectrochemical water splitting. *MRS Bull.* **2011,** *36* (1), 48-55, DOI 10.1557/mrs.2010.9.

53. Bak, T.; Nowotny, J.; Rekas, M.; Sorrell, C. C., Photo-electrochemical hydrogen generation from water using solar energy. Materials-related aspects. *Int. J. Hydrogen Energy* **2002,** *27* (10), 991-1022, DOI https://doi.org/10.1016/S0360-3199(02)00022-8.

54. Subramanian, V.; Wolf, E.; Kamat, P., Semiconductor−Metal Composite Nanostructures. To What Extent Do Metal Nanoparticles Improve the Photocatalytic Activity of TiO_2 Films? *The Journal of Physical Chemistry B* **2001,** *105*, DOI 10.1021/jp011118k.

55. Anpo, M.; Takeuchi, M., The Design and Development of Highly Reactive Titanium Oxide Photocatalysts Operating Under Visible Light Irradiation. *J. Catal.* **2003,** *216*, 505-516, DOI 10.1016/S0021-9517(02)00104-5.

56. Iwase, A.; Kato, H.; Kudo, A., Nanosized Au Particles as an Efficient Cocatalyst for Photocatalytic Overall Water Splitting. *Catal. Lett.* **2006,** *108* (1), 7-10, DOI 10.1007/s10562-006-0030-1.

57. Domen, K.; Naito, S.; TMma, M.; Onishi, T.; Tamaru, K. In *Photocatalytic decomposition of water vapour on an Nio $SrTiO_3$ catalyst*, 1980.

58. Inoue, Y.; Hayashi, O.; Sato, K., Photocatalytic activities of potassium-doped lead niobates and the effect of poling. *J. Chem. Soc., Faraday Trans.* **1990,** *86* (12), 2277-2282, DOI 10.1039/FT9908602277.

59. Shen, S.; Shi, J.; Guo, P.; Guo, L., Visible-Light-driven Photocatalytic Water Splitting on Nanostructured Semiconducting materials. *International Journal of Nanotechnology* **2011,** *8*, 523-591, DOI 10.1504/IJNT.2011.040192.

60. Nowotny, J.; Sorrell, C. C.; Bak, T.; Sheppard, L. R., Solar-hydrogen: Unresolved problems in solid-state science. *Solar Energy* **2005,** *78* (5), 593-602, DOI https://doi.org/10.1016/j.solener.2005.01.008.

61. Zou, Z.; Ye, J.; Sayama, K.; Arakawa, H., Direct splitting of water under visible light irradiation with an oxide semiconductor photocatalyst. *Nature* **2001,** *414* (6864), 625-627, DOI 10.1038/414625a.

62. Chen, X.; Shen, S.; Guo, L.; Mao, S. S., Semiconductor-based Photocatalytic Hydrogen Generation. *Chem. Rev.* **2010,** *110* (11), 6503-6570, DOI 10.1021/cr1001645.

63. Maeda, K.; Teramura, K.; Domen, K., Effect of post-calcination on photocatalytic activity of $(Ga_{1-x}Zn_x)(N_{1-x}O_x)$ solid solution for overall water splitting under visible light. *J. Catal.* **2008,** *254* (2), 198-204, DOI https://doi.org/10.1016/j.jcat.2007.12.009.

64. Li, Z.; Zhang, P.; Li, J.; Shao, T.; Wang, J.; Jin, L., Synthesis of In_2O_3 porous nanoplates for photocatalytic decomposition of perfluorooctanoic acid (PFOA). *Catal. Commun.* **2014,** *43*, 42-46, DOI https://doi.org/10.1016/j.catcom.2013.09.004.

65. Zhao, H.; Dong, H.; Zhang, L.; Wang, X.; Yang, H., Controlled synthesis and photocatalytic properties of porous hollow In_2O_3 microcubes with different sizes. *Mater. Chem. Phys.* **2011,** *130* (3), 921-931, DOI https://doi.org/10.1016/j.matchemphys.2011.08.013.

66. Nguyen, P.; Ng, H. T.; Yamada, T.; Smith, M. K.; Li, J.; Han, J.; Meyyappan, M., Direct Integration of Metal Oxide Nanowire in Vertical Field-Effect Transistor. *Nano Lett.* **2004,** *4* (4), 651-657, DOI 10.1021/nl0498536.

67. Fang, Y.; Wen, X.; Yang, S., Hollow and Tin-Filled Nanotubes of Single-Crystalline $In(OH)_3$ Grown by a Solution–Liquid–Solid–Solid Route. *Angew. Chem. Int. Ed.* **2006,** *45* (28), 4655-4658, DOI 10.1002/anie.200601024.

68. Pan, Z. W.; Dai, Z. R.; Wang, Z. L., Nanobelts of Semiconducting Oxides. *Science* **2001,** *291* (5510), 1947-1949, DOI 10.1126/science.1058120.

69. Yang, H.; Zhang, R.; Dong, H.; Yu, J.; Yang, W.; Chen, D., In Situ Growth of Self-Assembled and Single In2O3 Nanosheets on the Surface of Indium Grains. *Crystal Growth & Design* **2008,** *8* (9), 3154-3159, DOI 10.1021/cg070019e.

70. Avivi, S.; Mastai, Y.; Gedanken, A., Sonohydrolysis of In^{3+} Ions: Formation of Needlelike Particles of Indium Hydroxide. *Chem. Mater.* **2000,** *12* (5), 1229-1233, DOI 10.1021/cm9903677.

71. Seo, W. S.; Jo, H. H.; Lee, K.; Park, J. T., Preparation and Optical Properties of Highly Crystalline, Colloidal, and Size-Controlled Indium Oxide Nanoparticles. *Adv. Mater.* **2003,** *15* (10), 795-797, DOI 10.1002/adma.200304568.

72. Tang, Q.; Zhou, W.; Zhang, W.; Ou, S.; Jiang, K.; Yu, W.; Qian, Y., Size-Controllable Growth of Single Crystal In(OH)3 and In2O3 Nanocubes. *Crystal Growth & Design* **2005,** *5* (1), 147-150, DOI 10.1021/cg049914d.

73. Chu, D.; Masuda, Y.; Ohji, T.; Kato, K., Shape-Controlled Growth of $In(OH)_3/In_2O_3$ Nanostructures by Electrodeposition. *Langmuir* **2010,** *26* (18), 14814-14820, DOI 10.1021/la102255k.

74. Li, B.; Xie, Y.; Jing, M.; Rong, G.; Tang, Y.; Zhang, G., In_2O_3 Hollow Microspheres: Synthesis from Designed In(OH)3 Precursors and Applications in Gas Sensors and Photocatalysis. *Langmuir* **2006,** *22* (22), 9380-9385, DOI 10.1021/la061844k.

75. Lalitha, K.; Kumari, V.; Subrahmanyam, M., In_2O_3/TiO_2 nano photocatalysts for solar hydrogen production from methanol: Water mixtures. *Indian Journal of Chemistry - Section A Inorganic, Physical, Theoretical and Analytical Chemistry* **2014,** *53*, 472-477.

76. Vinothkumar, N.; De, M., Hydrogen production from water–methanol solution over visible light active indium–titanium oxide photocatalysts modified with copper oxide. *Int. J.*

Hydrogen Energy **2014,** *39* (22), 11494-11500, DOI https://doi.org/10.1016/j.ijhydene.2014.05.095.

77. Gupta, U.; Rao, B. G.; Maitra, U.; Prasad, B. E.; Rao, C. N. R., Visible-Light-Induced Generation of H2 by Nanocomposites of Few-Layer TiS_2 and TaS_2 with CdS Nanoparticles. *Chemistry – An Asian Journal* **2014,** *9* (5), 1311-1315, DOI 10.1002/asia.201301537.

78. Hu, S.; Chi, B.; Pu, J.; Jian, L., Novel heterojunction photocatalysts based on lanthanum titanate nanosheets and indium oxide nanoparticles with enhanced photocatalytic hydrogen production activity. *Journal of Materials Chemistry A* **2014,** *2* (45), 19260-19267, DOI 10.1039/C4TA04177A.

79. Martha, S.; Reddy, K. H.; Parida, K. M., Fabrication of In_2O_3 modified ZnO for enhancing stability, optical behaviour, electronic properties and photocatalytic activity for hydrogen production under visible light. *Journal of Materials Chemistry A* **2014,** *2* (10), 3621-3631, DOI 10.1039/C3TA14285J.

80. Lv, J.; Kako, T.; Li, Z.; Zou, Z.; Ye, J., Synthesis and Photocatalytic Activities of NaNbO3 Rods Modified by In_2O_3 Nanoparticles. *The Journal of Physical Chemistry C* **2010,** *114* (13), 6157-6162, DOI 10.1021/jp906550t.

81. Nashim, A.; Martha, S.; Parida, K., $Gd_2Ti_2O_7/In_2O_3$: Efficient Visible-Light-Driven Heterojunction-Based Composite Photocatalysts for Hydrogen Production. *ChemCatChem* **2013,** *5*, 2352-2359, DOI 10.1002/cctc.201300037.

82. Xu, L.; Ni, L.; Shi, W.; Guan, J., Photocatalytic Activity for Hydrogen Evolution over Well-Dispersed Heterostructured In_2O_3/Ta_2O_5 Composites. *Chinese Journal of Catalysis* **2012,** *33* (7), 1101-1108, DOI https://doi.org/10.1016/S1872-2067(11)60382-3.

83. Diehl, R.; Nitsche, R., Vapour growth of three In_2S_3 modifications by iodine transport. *J. Cryst. Growth* **1975,** *28* (3), 306-310, DOI https://doi.org/10.1016/0022-0248(75)90067-6.

84. Chen, L.-Y.; Zhang, Z.-D.; Wang, W.-Z., Self-Assembled Porous 3D Flowerlike β-In2S3 Structures: Synthesis, Characterization, and Optical Properties. *The Journal of Physical Chemistry C* **2008,** *112* (11), 4117-4123, DOI 10.1021/jp710074h.

85. Fu, X.; Wang, X.; Chen, Z.; Zhang, Z.; Li, Z.; Leung, D. Y. C.; Wu, L.; Fu, X., Photocatalytic performance of tetragonal and cubic β-In_2S_3 for the water splitting under

visible light irradiation. *Applied Catalysis B: Environmental* **2010,** *95* (3), 393-399, DOI https://doi.org/10.1016/j.apcatb.2010.01.018.

86. Chai, B.; Peng, T.; Zeng, P.; Mao, J., Synthesis of floriated In_2S_3 decorated with TiO_2 nanoparticles for efficient photocatalytic hydrogen production under visible light. *J. Mater. Chem.* **2011,** *21* (38), 14587-14593, DOI 10.1039/C1JM11566A.

87. Shen, Z.; Chen, G.; Wang, Q.; Yu, Y.; Zhou, C.; Wang, Y., Sonochemistry synthesis and enhanced photocatalytic H2-production activity of nanocrystals embedded in CdS/ZnS/In_2S_3 microspheres. *Nanoscale* **2012,** *4* (6), 2010-2017, DOI 10.1039/C2NR12045C.

88. Shen, F.; Que, W.; Liao, Y.; Yin, X., Photocatalytic Activity of TiO2 Nanoparticles Sensitized by $CuInS_2$ Quantum Dots. *Industrial & Engineering Chemistry Research* **2011,** *50* (15), 9131-9137, DOI 10.1021/ie2007467.

89. Chen, B.; Chang, S.; Li, D.; Chen, L.; Wang, Y.; Chen, T.; Zou, B.; Zhong, H.; Rogach, A. L., Template Synthesis of $CuInS_2$ Nanocrystals from In_2S_3 Nanoplates and Their Application as Counter Electrodes in Dye-Sensitized Solar Cells. *Chem. Mater.* **2015,** *27* (17), 5949-5956, DOI 10.1021/acs.chemmater.5b01971.

90. Luo, J.; Tilley, S. D.; Steier, L.; Schreier, M.; Mayer, M. T.; Fan, H. J.; Grätzel, M., Solution Transformation of Cu_2O into $CuInS_2$ for Solar Water Splitting. *Nano Lett.* **2015,** *15* (2), 1395-1402, DOI 10.1021/nl504746b.

91. Zhao, J.; Minegishi, T.; Zhang, L.; Zhong, M.; Gunawan, G.; Nakabayashi, M.; Ma, G.; Hisatomi, T.; Katayama, M.; Ikeda, S.; Shibata, N.; Yamada, T.; Domen, K., Enhancement of Solar Hydrogen Evolution from Water by Surface Modification with CdS and TiO_2 on Porous $CuInS_2$ Photocathodes Prepared by an Electrodeposition–Sulfurization Method. *Angew. Chem. Int. Ed.* **2014,** *53*, DOI 10.1002/anie.201406483.

92. Knowles, K. E.; Kilburn, T. B.; Alzate, D. G.; McDowall, S.; Gamelin, D. R., Bright CuInS2/CdS nanocrystal phosphors for high-gain full-spectrum luminescent solar concentrators. *Chem. Commun.* **2015,** *51* (44), 9129-9132, DOI 10.1039/C5CC02007G.

93. Shen, S.; Chen, X.; Ren, F.; Kronawitter, C. X.; Mao, S. S.; Guo, L., Solar light-driven photocatalytic hydrogen evolution over ZnIn2S4 loaded with transition-metal sulfides. *Nanoscale Res Lett* **2011,** *6* (1), 290, DOI 10.1186/1556-276X-6-290.

94. Li, K.; Chai, B.; Peng, T.; Mao, J.; Zan, L., Preparation of $AgIn_5S_8/TiO_2$ Heterojunction Nanocomposite and Its Enhanced Photocatalytic H2 Production Property under Visible Light. *ACS Catalysis* **2013,** *3* (2), 170-177, DOI 10.1021/cs300724r.

95. Cui, W.; Guo, D.; Liu, l.; Hu, J.; Rana, D.; Liang, Y., Preparation of $ZnIn_2S_4/K_2La_2Ti_3O_{10}$ composites and their photocatalytic H2 evolution from aqueous Na_2S/Na_2SO_3 under visible light irradiation. *Catal. Commun.* **2014,** *48*, 55–59, DOI 10.1016/j.catcom.2014.01.026.

96. Hu, P.; Ngaw, C. K.; Tay, Y. Y.; Cao, S.; Barber, J.; Tan, T. T. Y.; Loo, S. C. J., A "uniform" heterogeneous photocatalyst: integrated p–n type $CuInS_2/NaInS_2$ nanosheets by partial ion exchange reaction for efficient H_2 evolution. *Chem. Commun.* **2015,** *51* (45), 9381-9384, DOI 10.1039/C5CC02237A.

97. Ye , C.; Regulacio , M. D.; Lim, S. H.; Li, S.; Xu, Q.-H.; Han, M.-Y., Alloyed ZnS–$CuInS_2$ Semiconductor Nanorods and Their Nanoscale Heterostructures for Visible-Light-Driven Photocatalytic Hydrogen Generation. *Chemistry – A European Journal* **2015,** *21* (26), 9514-9519, DOI 10.1002/chem.201500781.

98. Shi, F.; Chen, L.; Chen, M.; Jiang, D., A g-C_3N_4/nanocarbon/$ZnIn_2S_4$ nanocomposite: an artificial Z-scheme visible-light photocatalytic system using nanocarbon as the electron mediator. *Chem. Commun.* **2015,** *51* (96), 17144-17147, DOI 10.1039/C5CC05323D.

99. Chen, D.; Ye, J., Photocatalytic H_2 evolution under visible light irradiation on $AgIn_5S_8$ photocatalyst. *J. Phys. Chem. Solids* **2007,** *68* (12), 2317-2320, DOI https://doi.org/10.1016/j.jpcs.2007.07.059.

100. Hou, J.; Yang, C.; Cheng, H.; Wang, Z.; Jiao, S.; Zhu, H., Ternary 3D architectures of CdS QDs/graphene/$ZnIn_2S_4$ heterostructures for efficient photocatalytic H_2 production. *PCCP* **2013,** *15* (37), 15660-15668, DOI 10.1039/C3CP51857D.

101. Singh, A.; Coughlan, C.; Milliron, D. J.; Ryan, K. M., Solution Synthesis and Assembly of Wurtzite-Derived Cu–In–Zn–S Nanorods with Tunable Composition and Bandgap. *Chem. Mater.* **2015,** *27* (5), 1517-1523, DOI 10.1021/cm5035613.

102. Tang, X.; Tay, Q.; Chen, Z.; Chen, Y.; Goh, G. K. L.; Xue, J., CuInZnS-decorated graphene nanosheets for highly efficient visible-light-driven photocatalytic hydrogen production. *Journal of Materials Chemistry A* **2013,** *1* (21), 6359-6365, DOI 10.1039/C3TA01602A.

103. Li, Y.; Chen, G.; Zhou, C.; Sun, J., A simple template-free synthesis of nanoporous ZnS–In2S_3–Ag_2S solid solutions for highly efficient photocatalytic H_2 evolution under visible light. *Chem. Commun.* **2009,** (15), 2020-2022, DOI 10.1039/B819300B.

104. Li, Y.; Chen, G.; Wang, Q.; Wang, X.; Zhou, A.; Shen, Z., Hierarchical ZnS-In_2S_3-CuS Nanospheres with Nanoporous Structure: Facile Synthesis, Growth Mechanism, and Excellent Photocatalytic Activity. *Adv. Funct. Mater.* **2010,** *20* (19), 3390-3398, DOI 10.1002/adfm.201000604.

105. Kaga, H.; Saito, K.; Kudo, A., Solar hydrogen production over novel metal sulfide photocatalysts of $AGa_2In_3S_8$ (A = Cu or Ag) with layered structures. *Chem. Commun.* **2010,** *46* (21), 3779-3781, DOI 10.1039/B927362J.

106. Tsuji, I.; Kato, H.; Kudo, A., Photocatalytic Hydrogen Evolution on ZnS−CuInS2−AgInS2 Solid Solution Photocatalysts with Wide Visible Light Absorption Bands. *Chem. Mater.* **2006,** *18* (7), 1969-1975, DOI 10.1021/cm0527017.

107. Tsuji, I.; Kato, H.; Kudo, A., Visible-Light-Induced H_2 Evolution from an Aqueous Solution Containing Sulfide and Sulfite over a ZnS–$CuInS_2$–$AgInS_2$ Solid-Solution Photocatalyst. *Angew. Chem. Int. Ed.* **2005,** *44* (23), 3565-3568, DOI 10.1002/anie.200500314.

108. Tsuji, I.; Kato, H.; Kobayashi, H.; Kudo, A., Photocatalytic H_2 Evolution Reaction from Aqueous Solutions over Band Structure-Controlled $(AgIn)_xZn_{2(1-x)}S_2$ Solid Solution Photocatalysts with Visible-Light Response and Their Surface Nanostructures. *J. Am. Chem. Soc.* **2004,** *126* (41), 13406-13413, DOI 10.1021/ja048296m.

109. Kandiel, T. A.; Anjum, D. H.; Takanabe, K., Nano-Sized Quaternary $CuGa_2In_3S_8$ as an Efficient Photocatalyst for Solar Hydrogen Production. *ChemSusChem* **2014,** *7* (11), 3112-3121, DOI 10.1002/cssc.201402525.

110. Tsuji, I.; Kato, H.; Kobayashi, H.; Kudo, A., Photocatalytic H_2 Evolution under Visible-Light Irradiation over Band-Structure-Controlled $(CuIn)_xZn_{2(1-x)}S_2$ Solid Solutions. *The Journal of Physical Chemistry B* **2005,** *109* (15), 7323-7329, DOI 10.1021/jp044722e.

111. Pai, M. R.; Singhal, A. M.; Banerjee, A. M.; Tewari, R.; Dey, G. K.; Tyagi, A. K.; Bharadwaj, S. R., Synthesis, characterization and photocatalytic H_2 generation over ternary indium titanate nanoparticles. *Journal of nanoscience and nanotechnology* **2012,** *12* (3), 1957-66, DOI 10.1166/jnn.2012.5187.

112. Ren, L.; Yang, F.; Deng, Y.-R.; Yan, N.-N.; Huang, S.; Lei, D.; Sun, Q.; Yu, Y., Synthesis of $(CuIn)_xCd_{2(1-x)}S_2$ photocatalysts for H_2 evolution under visible light by using a low-temperature hydrothermal method. *Int. J. Hydrogen Energy* **2010,** *35* (8), 3297-3305, DOI https://doi.org/10.1016/j.ijhydene.2010.01.074.

113. Yan, W.; Zhang, Y.; Xie, W.; Sun, S.; Ding, J.; Bao, J.; Gao, C., $CaIn_2O_4$/Fe-TiO_2 Composite Photocatalysts with Enhanced Visible Light Performance for Hydrogen Production. *The Journal of Physical Chemistry C* **2014,** *118* (12), 6077-6083, DOI 10.1021/jp412810n.

114. Zou, Z.; Ye, J.; Arakawa, H., Structural properties of $InNbO_4$ and $InTaO_4$: Correlation with photocatalytic and photophysical properties. *Chem. Phys. Lett.* **2000,** *332*, 271–277, DOI 10.1016/S0009-2614(00)01265-3.

115. Ding, J.; Yan, W.; Sun, S.; Bao, J.; Gao, C., Fabrication of graphene/$CaIn_2O_4$ composites with enhanced photocatalytic activity from water under visible light irradiation. *Int. J. Hydrogen Energy* **2014,** *39* (1), 119-126, DOI https://doi.org/10.1016/j.ijhydene.2013.10.077.

116. Liu, M.; Xia, P.; Zhang, L.; Cheng, B.; Yu, J., Enhanced Photocatalytic H_2-Production Activity of g-C3N4 Nanosheets via Optimal Photodeposition of Pt as Cocatalyst. *ACS Sustainable Chemistry & Engineering* **2018,** *6* (8), 10472-10480, DOI 10.1021/acssuschemeng.8b01835.

117. Shiraishi, Y.; Kanazawa, S.; Sugano, Y.; Tsukamoto, D.; Sakamoto, H.; Ichikawa, S.; Hirai, T., Highly Selective Production of Hydrogen Peroxide on Graphitic Carbon Nitride (g-C_3N_4) Photocatalyst Activated by Visible Light. *ACS Catalysis* **2014,** *4* (3), 774-780, DOI 10.1021/cs401208c.

118. Fu, J.; Yu, J.; Jiang, C.; Cheng, B., g-C_3N_4-Based Heterostructured Photocatalysts. *Advanced Energy Materials* **2018,** *8* (3), 1701503, DOI 10.1002/aenm.201701503.

119. Alcudia-Ramos, M. A.; Fuentez-Torres, M. O.; Ortiz-Chi, F.; Espinosa-González, C. G.; Hernández-Como, N.; García-Zaleta, D. S.; Kesarla, M. K.; Torres-Torres, J. G.; Collins-Martínez, V.; Godavarthi, S., Fabrication of g-C_3N_4/TiO_2 heterojunction composite for enhanced photocatalytic hydrogen production. *Ceram. Int.* **2020,** *46* (1), 38-45, DOI https://doi.org/10.1016/j.ceramint.2019.08.228.

120. Zhang, J.; Wang, Y.; Jin, J.; Zhang, J.; Lin, Z.; Huang, F.; Yu, J., Efficient Visible-Light Photocatalytic Hydrogen Evolution and Enhanced Photostability of Core/Shell CdS/g-C_3N_4 Nanowires. *ACS Applied Materials & Interfaces* **2013,** *5* (20), 10317-10324, DOI 10.1021/am403327g.

121. Ding, X.; Li, Y.; Zhao, J.; Zhu, Y.; Li, Y.; Deng, W.; Wang, C., Enhanced photocatalytic H_2 evolution over CdS/Au/g-C_3N_4 composite photocatalyst under visible-light irradiation. *APL Materials* **2015,** *3* (10), 104410, DOI 10.1063/1.4926935.

122. Zhao, W.; Xie, L.; Zhang, M.; Ai, Z.; Xi, H.; Li, Y.; Shi, Q.; Chen, J., Enhanced photocatalytic activity of all-solid-state g-C_3N_4/Au/P25 Z-scheme system for visible-light-driven H2 evolution. *Int. J. Hydrogen Energy* **2016,** *41* (15), 6277-6287, DOI https://doi.org/10.1016/j.ijhydene.2016.02.148.

123. Li, H.; Shang, J.; Ai, Z.; Zhang, L., Efficient Visible Light Nitrogen Fixation with BiOBr Nanosheets of Oxygen Vacancies on the Exposed {001} Facets. *J. Am. Chem. Soc.* **2015,** *137* (19), 6393-6399, DOI 10.1021/jacs.5b03105.

124. Yuan, S.-J.; Chen, J.-J.; Lin, Z.-Q.; Li, W.-W.; Sheng, G.-P.; Yu, H.-Q., Nitrate formation from atmospheric nitrogen and oxygen photocatalysed by nano-sized titanium dioxide. *Nature Communications* **2013,** *4*, 2249, DOI 10.1038/ncomms3249 https://www.nature.com/articles/ncomms3249#supplementary-information.

125. Wang, S.; Ichihara, F.; Pang, H.; Chen, H.; Ye, J., Nitrogen Fixation Reaction Derived from Nanostructured Catalytic Materials. *Advanced Functional Materials* **2018,** *0* (0), 1803309, DOI 10.1002/adfm.201803309.

126. Kim, J.; Rees, D. C., Nitrogenase and biological nitrogen fixation. *Biochemistry* **1994,** *33* (2), 389-397, DOI 10.1021/bi00168a001.

127. Anderson, J. S.; Rittle, J.; Peters, J. C., Catalytic conversion of nitrogen to ammonia by a molecular Fe model complex. *Nature* **2013,** *501* (7465), 84-87, DOI 10.1038/nature12435.

128. Wang, K.; Smith, D.; Zheng, Y., Electron-driven heterogeneous catalytic synthesis of ammonia: Current states and perspective. *Carbon Resources Conversion* **2018,** *1* (1), 2-31, DOI https://doi.org/10.1016/j.crcon.2018.06.004.

129. Ghosh, S.; Kouamé, N. A.; Ramos, L.; Remita, S.; Dazzi, A.; Deniset-Besseau, A.; Beaunier, P.; Goubard, F.; Aubert, P.-H.; Remita, H., Conducting polymer nanostructures for photocatalysis under visible light. *Nature Materials* **2015,** *14*, 505, DOI 10.1038/nmat4220

130. Khan, S. B.; Hou, M.; Shuang, S.; Zhang, Z., Morphological influence of TiO2 nanostructures (nanozigzag, nanohelics and nanorod) on photocatalytic degradation of organic dyes. *Appl. Surf. Sci.* **2017,** *400*, 184-193, DOI https://doi.org/10.1016/j.apsusc.2016.12.172.

131. Yang, J.; Wang, D.; Han, H.; Li, C., Roles of Cocatalysts in Photocatalysis and Photoelectrocatalysis. *Acc. Chem. Res.* **2013,** *46* (8), 1900-1909, DOI 10.1021/ar300227e.

132. Bi, W.; Li, X.; Zhang, L.; Jin, T.; Zhang, L.; Zhang, Q.; Luo, Y.; Wu, C.; Xie, Y., Molecular co-catalyst accelerating hole transfer for enhanced photocatalytic H_2 evolution. *Nature Communications* **2015,** *6*, 8647, DOI 10.1038/ncomms9647.

133. Xiong, K.; Wang, P.; Yang, G.; Liu, Z.; Zhang, H.; Jin, S.; Xu, X., Functional Group Effects on the Photoelectronic Properties of MXene (Sc(2)CT(2), T = O, F, OH) and Their Possible Photocatalytic Activities. *Scientific reports* **2017,** *7* (1), 15095-15095, DOI 10.1038/s41598-017-15233-8.

134. Liu, S.; Li, D.; Sun, H.; Ang, H. M.; Tadé, M. O.; Wang, S., Oxygen functional groups in graphitic carbon nitride for enhanced photocatalysis. *J. Colloid Interface Sci.* **2016,** *468*, 176-182, DOI https://doi.org/10.1016/j.jcis.2016.01.051.

135. Feng, J.; Liu, G.; Yuan, S.; Ma, Y., Influence of functional groups on water splitting in carbon nanodot and graphitic carbon nitride composites: a theoretical mechanism study. *PCCP* **2017,** *19* (7), 4997-5003, DOI 10.1039/C6CP08622E.

136. Nguyen, C. C.; Vu, N. N.; Do, T.-O., Recent advances in the development of sunlight-driven hollow structure photocatalysts and their applications. *Journal of Materials Chemistry A* **2015,** *3* (36), 18345-18359, DOI 10.1039/C5TA04326C.

137. Reza Gholipour, M.; Dinh, C.-T.; Béland, F.; Do, T.-O., Nanocomposite heterojunctions as sunlight-driven photocatalysts for hydrogen production from water splitting. *Nanoscale* **2015,** *7* (18), 8187-8208, DOI 10.1039/C4NR07224C.

138. Alexander, B. D.; Kulesza, P. J.; Rutkowska, I.; Solarska, R.; Augustynski, J., Metal oxide photoanodes for solar hydrogen production. *J. Mater. Chem.* **2008,** *18* (20), 2298-2303, DOI 10.1039/B718644D.

139. Xie, W.; Li, R.; Xu, Q., Enhanced photocatalytic activity of Se-doped TiO_2 under visible light irradiation. *Scientific Reports* **2018,** *8* (1), 8752, DOI 10.1038/s41598-018-27135-4.

140. Thomann, I.; Pinaud, B. A.; Chen, Z.; Clemens, B. M.; Jaramillo, T. F.; Brongersma, M. L., Plasmon Enhanced Solar-to-Fuel Energy Conversion. *Nano Lett.* **2011,** *11* (8), 3440-3446, DOI 10.1021/nl201908s.

141. Zhao, Y.; Zhao, Y.; Waterhouse, G. I. N.; Zheng, L.; Cao, X.; Teng, F.; Wu, L.-Z.; Tung, C.-H.; O'Hare, D.; Zhang, T., Layered-Double-Hydroxide Nanosheets as Efficient Visible-Light-Driven Photocatalysts for Dinitrogen Fixation. *Adv. Mater.* **2017,** *29* (42), 1703828, DOI 10.1002/adma.201703828.

142. Zhao, Y.; Zhao, Y.; Shi, R.; Wang, B.; Waterhouse, G. I. N.; Wu, L.-Z.; Tung, C.-H.; Zhang, T., Tuning Oxygen Vacancies in Ultrathin TiO2 Nanosheets to Boost Photocatalytic Nitrogen Fixation up to 700 nm. *Adv. Mater.* **2019,** *0* (0), 1806482, DOI 10.1002/adma.201806482.

143. Hirakawa, H.; Hashimoto, M.; Shiraishi, Y.; Hirai, T., Photocatalytic Conversion of Nitrogen to Ammonia with Water on Surface Oxygen Vacancies of Titanium Dioxide. *Journal of the American Chemical Society* **2017,** *139* (31), 10929-10936, DOI 10.1021/jacs.7b06634.

144. Shiraishi, Y.; Shiota, S.; Kofuji, Y.; Hashimoto, M.; Chishiro, K.; Hirakawa, H.; Tanaka, S.; Ichikawa, S.; Hirai, T., Nitrogen Fixation with Water on Carbon-Nitride-Based Metal-Free Photocatalysts with 0.1% Solar-to-Ammonia Energy Conversion Efficiency. *ACS Applied Energy Materials* **2018,** *1* (8), 4169-4177, DOI 10.1021/acsaem.8b00829.

145. Li, H.; Shang, J.; Shi, J.; Zhao, K.; Zhang, L., Facet-dependent solar ammonia synthesis of BiOCl nanosheets via a proton-assisted electron transfer pathway. *Nanoscale* **2016,** *8* (4), 1986-1993, DOI 10.1039/C5NR07380D.

146. Wang, S.; Hai, X.; Ding, X.; Chang, K.; Xiang, Y.; Meng, X.; Yang, Z.; Chen, H.; Ye, J., Light-Switchable Oxygen Vacancies in Ultrafine Bi_5O_7Br Nanotubes for Boosting Solar-Driven Nitrogen Fixation in Pure Water. *Adv. Mater.* **2017,** *29* (31), 1701774, DOI 10.1002/adma.201701774.

147. Ye, L.; Han, C.; Ma, Z.; Leng, Y.; Li, J.; Ji, X.; Bi, D.; Xie, H.; Huang, Z., Ni_2P loading on Cd0.5Zn0.5S solid solution for exceptional photocatalytic nitrogen fixation under

visible light. *Chem. Eng. J.* **2017,** *307*, 311-318, DOI https://doi.org/10.1016/j.cej.2016.08.102.

148. Oshikiri, T.; Ueno, K.; Misawa, H., Selective Dinitrogen Conversion to Ammonia Using Water and Visible Light through Plasmon-induced Charge Separation. *Angew. Chem.* **2016,** *128* (12), 4010-4014, DOI 10.1002/ange.201511189.

149. Oshikiri, T.; Ueno, K.; Misawa, H., Plasmon-Induced Ammonia Synthesis through Nitrogen Photofixation with Visible Light Irradiation. *Angew. Chem. Int. Ed.* **2014,** *53* (37), 9802-9805, DOI 10.1002/anie.201404748.

150. Özkar, S., Enhancement of catalytic activity by increasing surface area in heterogeneous catalysis. *Applied Surface Science* **2009,** *256* (5), 1272-1277, DOI https://doi.org/10.1016/j.apsusc.2009.10.036.

151. Bai, X. P.; Zhao, X.; Fan, W. L., Preparation and enhanced photocatalytic hydrogen-evolution activity of $ZnGa_2O_4$/N-rGO heterostructures. *RSC Advances* **2017,** *7* (84), 53145-53156, DOI 10.1039/C7RA09981A.

152. Yang, H.; Zhou, Y.; Wang, Y.; Hu, S.; Wang, B.; Liao, Q.; Li, H.; Bao, J.; Ge, G.; Jia, S., Three-dimensional flower-like phosphorus-doped g-C_3N_4 with a high surface area for visible-light photocatalytic hydrogen evolution. *Journal of Materials Chemistry A* **2018,** *6* (34), 16485-16494, DOI 10.1039/C8TA05723K.

153. Montoya, A. T.; Gillan, E. G., Enhanced Photocatalytic Hydrogen Evolution from Transition-Metal Surface-Modified TiO2. *ACS Omega* **2018,** *3* (3), 2947-2955, DOI 10.1021/acsomega.7b02021.

154. Nahar, S.; Zain, F. M.; Kadhum, A. A.; Hasan, A. H.; Hasan, R. M., Advances in Photocatalytic CO_2 Reduction with Water: A Review. *Materials* **2017,** *10* (6), DOI 10.3390/ma10060629.

155. Yang, M.-Q.; Xu, Y.-J., Photocatalytic conversion of CO_2 over graphene-based composites: current status and future perspective. *Nanoscale Horizons* **2016,** *1* (3), 185-200, DOI 10.1039/C5NH00113G.

156. Xie, S.; Zhang, Q.; Liu, G.; Wang, Y., Photocatalytic and photoelectrocatalytic reduction of CO_2 using heterogeneous catalysts with controlled nanostructures. *Chem. Commun.* **2016,** *52* (1), 35-59, DOI 10.1039/C5CC07613G.

157. Dong, G.; Ho, W.; Wang, C., Selective photocatalytic N_2 fixation dependent on g-C3N4 induced by nitrogen vacancies. *Journal of Materials Chemistry A* **2015,** *3* (46), 23435-23441, DOI 10.1039/C5TA06540B.

158. Feng, X.; Chen, H.; Jiang, F.; Wang, X., Enhanced visible-light photocatalytic nitrogen fixation over semicrystalline graphitic carbon nitride: Oxygen and sulfur co-doping for crystal and electronic structure modulation. *J. Colloid Interface Sci.* **2018,** *509*, 298-306, DOI https://doi.org/10.1016/j.jcis.2017.09.026.

159. Hu, S.; Chen, X.; Li, Q.; Li, F.; Fan, Z.; Wang, H.; Wang, Y.; Zheng, B.; Wu, G., Fe3+ doping promoted N2 photofixation ability of honeycombed graphitic carbon nitride: The experimental and density functional theory simulation analysis. *Applied Catalysis B: Environmental* **2017,** *201*, 58-69, DOI https://doi.org/10.1016/j.apcatb.2016.08.002.

160. Li, S.; Chen, X.; Hu, S.; Li, Q.; Bai, J.; Wang, F., Infrared ray assisted microwave synthesis: a convenient method for large-scale production of graphitic carbon nitride with outstanding nitrogen photofixation ability. *RSC Advances* **2016,** *6* (51), 45931-45937, DOI 10.1039/C6RA08817A.

161. Saadatjou, N.; Jafari, A.; Sahebdelfar, S., Ruthenium Nanocatalysts for Ammonia Synthesis: A Review. *Chemical Engineering Communications* **2015,** *202* (4), 420-448, DOI 10.1080/00986445.2014.923995.

162. Aika, K.-i.; Hori, H.; Ozaki, A., Activation of nitrogen by alkali metal promoted transition metal I. Ammonia synthesis over ruthenium promoted by alkali metal. *Journal of Catalysis* **1972,** *27* (3), 424-431, DOI https://doi.org/10.1016/0021-9517(72)90179-0.

163. Légaré, M.-A.; Bélanger-Chabot, G.; Dewhurst, R. D.; Welz, E.; Krummenacher, I.; Engels, B.; Braunschweig, H., Nitrogen fixation and reduction at boron. *Science* **2018,** *359* (6378), 896.

164. Simpson, F. B.; Burris, R. H., A nitrogen pressure of 50 atmospheres does not prevent evolution of hydrogen by nitrogenase. *Science* **1984,** *224* (4653), 1095.

165. Schubert, K. R.; Evans, H. J., Hydrogen evolution: A major factor affecting the efficiency of nitrogen fixation in nodulated symbionts. *Proceedings of the National Academy of Sciences of the United States of America* **1976,** *73* (4), 1207-1211.

166. Indra, A.; Menezes, P. W.; Kailasam, K.; Hollmann, D.; Schröder, M.; Thomas, A.; Brückner, A.; Driess, M., Nickel as a co-catalyst for photocatalytic hydrogen evolution on

graphitic-carbon nitride (sg-CN): what is the nature of the active species? *Chem. Commun.* **2016,** *52* (1), 104-107, DOI 10.1039/C5CC07936E.

167. Wang, D.; Liu, Z.-P.; Yang, W.-M., Revealing the Size Effect of Platinum Cocatalyst for Photocatalytic Hydrogen Evolution on TiO2 Support: A DFT Study. *ACS Catalysis* **2018,** *8* (8), 7270-7278, DOI 10.1021/acscatal.8b01886.

168. Kong, C.; Li, Z.; Lu, G., The dual functional roles of Ru as co-catalyst and stabilizer of dye for photocatalytic hydrogen evolution. *Int. J. Hydrogen Energy* **2015,** *40* (17), 5824-5830, DOI https://doi.org/10.1016/j.ijhydene.2015.03.014.

169. Ranjit, K. T.; Varadarajan, T. K.; Viswanathan, B., Photocatalytic reduction of dinitrogen to ammonia over noble-metal-loaded TiO_2. *Journal of Photochemistry and Photobiology A: Chemistry* **1996,** *96* (1), 181-185, DOI https://doi.org/10.1016/1010-6030(95)04290-3.

170. Abghoui, Y.; Garden, A. L.; Howalt, J. G.; Vegge, T.; Skúlason, E., Electroreduction of N_2 to Ammonia at Ambient Conditions on Mononitrides of Zr, Nb, Cr, and V: A DFT Guide for Experiments. *ACS Catalysis* **2016,** *6* (2), 635-646, DOI 10.1021/acscatal.5b01918.

171. Choi, C.; Back, S.; Kim, N.-Y.; Lim, J.; Kim, Y.-H.; Jung, Y., Suppression of Hydrogen Evolution Reaction in Electrochemical N_2 Reduction Using Single-Atom Catalysts: A Computational Guideline. *ACS Catalysis* **2018,** *8* (8), 7517-7525, DOI 10.1021/acscatal.8b00905.

172. Zhao, J.; Chen, Z., Single Mo Atom Supported on Defective Boron Nitride Monolayer as an Efficient Electrocatalyst for Nitrogen Fixation: A Computational Study. *J. Am. Chem. Soc.* **2017,** *139* (36), 12480-12487, DOI 10.1021/jacs.7b05213.

173. Skúlason, E.; Bligaard, T.; Gudmundsdóttir, S.; Studt, F.; Rossmeisl, J.; Abild-Pedersen, F.; Vegge, T.; Jónsson, H.; Nørskov, J. K., A theoretical evaluation of possible transition metal electro-catalysts for N_2 reduction. *PCCP* **2012,** *14* (3), 1235-1245, DOI 10.1039/C1CP22271F.

174. Shi, A.; Li, H.; Yin, S.; Hou, Z.; Rong, J.; Zhang, J.; Wang, Y., Photocatalytic NH3versus H2 evolution over g-C_3N_4/Cs_xWO_3: O_2 and methanol tipping the scale. *Applied Catalysis B: Environmental* **2018,** *235*, 197-206, DOI https://doi.org/10.1016/j.apcatb.2018.04.081.

175. Lee, J.; Park, H.; Choi, W., Selective Photocatalytic Oxidation of NH_3 to N_2 on Platinized TiO2 in Water. *Environmental Science & Technology* **2002,** *36* (24), 5462-5468, DOI 10.1021/es025930s.

176. Madia, G.; Koebel, M.; Elsener, M.; Wokaun, A., Side Reactions in the Selective Catalytic Reduction of NOx with Various NO_2 Fractions. *Industrial & Engineering Chemistry Research* **2002,** *41* (16), 4008-4015, DOI 10.1021/ie020054c.

177. Kominami, H.; Nishimune, H.; Ohta, Y.; Arakawa, Y.; Inaba, T., Photocatalytic hydrogen formation from ammonia and methyl amine in an aqueous suspension of metal-loaded titanium(IV) oxide particles. *Applied Catalysis B: Environmental* **2012,** *111-112*, 297-302, DOI https://doi.org/10.1016/j.apcatb.2011.10.011.

178. Li, R., Photocatalytic nitrogen fixation: An attractive approach for artificial photocatalysis. *Chinese Journal of Catalysis* **2018,** *39* (7), 1180-1188, DOI https://doi.org/10.1016/S1872-2067(18)63104-3.

179. Bozso, F.; Ertl, G.; Grunze, M.; Weiss, M., Interaction of nitrogen with iron surfaces: I. Fe(100) and Fe(111). *J. Catal.* **1977,** *49* (1), 18-41, DOI https://doi.org/10.1016/0021-9517(77)90237-8.

180. Tennakone, K.; Wickramanayake, S.; Fernando, C. A. N.; Ileperuma, O. A.; Punchihewa, S., Photocatalytic nitrogen reduction using visible light. *J. Chem. Soc., Chem. Commun.* **1987,** (14), 1078-1080, DOI 10.1039/C39870001078.

181. Khader, M. M.; Lichtin, N. N.; Vurens, G. H.; Salmeron, M.; Somorjai, G. A., Photoassisted catalytic dissociation of water and reduction of nitrogen to ammonia on partially reduced ferric oxide. *Langmuir* **1987,** *3* (2), 303-304, DOI 10.1021/la00074a028.

182. Soria, J.; Conesa, J. C.; Augugliaro, V.; Palmisano, L.; Schiavello, M.; Sclafani, A., Dinitrogen photoreduction to ammonia over titanium dioxide powders doped with ferric ions. *The Journal of Physical Chemistry* **1991,** *95* (1), 274-282, DOI 10.1021/j100154a052.

183. Rusina, O.; Linnik, O.; Eremenko, A.; Kisch, H., Nitrogen Photofixation on Nanostructured Iron Titanate Films. *Chemistry – A European Journal* **2003,** *9* (2), 561-565, DOI 10.1002/chem.200390059.

184. Linnik, O.; Kisch, H., On the mechanism of nitrogen photofixation at nanostructured iron titanate films. *Photochemical & Photobiological Sciences* **2006,** *5* (10), 938-942, DOI 10.1039/B608396J.

185. Lashgari, M.; Zeinalkhani, P., Photocatalytic N_2 conversion to ammonia using efficient nanostructured solar-energy-materials in aqueous media: A novel hydrogenation strategy and basic understanding of the phenomenon. *Applied Catalysis A: General* **2017,** *529*, 91-97, DOI https://doi.org/10.1016/j.apcata.2016.10.017.

186. Schrauzer, G. N.; Guth, T. D., Photocatalytic reactions. 1. Photolysis of water and photoreduction of nitrogen on titanium dioxide. *J. Am. Chem. Soc.* **1977,** *99* (22), 7189-7193, DOI 10.1021/ja00464a015.

187. Tennakone, K.; Bandara, J. M. S.; Thaminimulla, C. T. K.; Jayatilake, W. D. W.; Ketipearachchi, U. S.; Ileperuma, O. A.; Priyadarshana, M. K. A., Photoreduction of dinitrogen to ammonia by ultrafine particles of iron hydroxide oxide (Fe(O)OH) formed by photohydrolysis of Iron(II) bicarbonate. *Langmuir* **1991,** *7* (10), 2166-2168, DOI 10.1021/la00058a032.

188. Lu, Y.; Yang, Y.; Zhang, T.; Ge, Z.; Chang, H.; Xiao, P.; Xie, Y.; Hua, L.; Li, Q.; Li, H.; Ma, B.; Guan, N.; Ma, Y.; Chen, Y., Photoprompted Hot Electrons from Bulk Cross-Linked Graphene Materials and Their Efficient Catalysis for Atmospheric Ammonia Synthesis. *ACS Nano* **2016,** *10* (11), 10507-10515, DOI 10.1021/acsnano.6b06472.

189. Tennakone, K.; Fernando, C. A. N.; Wickramanayake, S.; Damayanthi, M. W. P.; Silva, L. H. K.; Wijeratne, W.; Illeperuma, O. A.; Punchihewa, S., Photocatalytic reduction of nitrogen to ammonia with coprecipitated Fe(III) and Ti(IV) hydrous oxides. *Solar Energy Materials* **1988,** *17* (1), 47-53, DOI https://doi.org/10.1016/0165-1633(88)90036-6.

190. Ileperuma, O. A.; Kiridena, W. C. B.; Dissanayake, W. D. D., Photoreduction of nitrogen and water on montmorillonite clays loaded with hydrous ferric oxide. *Journal of Photochemistry and Photobiology A: Chemistry* **1991,** *59* (2), 191-197, DOI https://doi.org/10.1016/1010-6030(91)87007-I.

191. Baumann, R.; Stumpf, R.; Davis, W. M.; Liang, L.-C.; Schrock, R. R., Titanium and Zirconium Complexes That Contain the Tridentate Diamido Ligands $[(i\text{-}PrN\text{-}o\text{-}C6H4)2O]^{2-}$ ($[i\text{-}PrNON]^{2-}$) and $[(C6H11N\text{-}o\text{-}C6H4)2O]^{2-}$ ($[CyNON]^{2-}$). *J. Am. Chem. Soc.* **1999,** *121* (34), 7822-7836, DOI 10.1021/ja983549v.

192. Van Tamelen, E. E.; Fechter, R. B.; Schneller, S. W., Conversion of molecular nitrogen to hydrazine. *J. Am. Chem. Soc.* **1969,** *91* (25), 7196-7196, DOI 10.1021/ja01053a054.

193. Sun, S.; Li, X.; Wang, W.; Zhang, L.; Sun, X., Photocatalytic robust solar energy reduction of dinitrogen to ammonia on ultrathin MoS_2. *Applied Catalysis B: Environmental* **2017,** *200*, 323-329, DOI https://doi.org/10.1016/j.apcatb.2016.07.025.

194. Banerjee, A.; Yuhas, B. D.; Margulies, E. A.; Zhang, Y.; Shim, Y.; Wasielewski, M. R.; Kanatzidis, M. G., Photochemical Nitrogen Conversion to Ammonia in Ambient Conditions with FeMoS-Chalcogels. *J. Am. Chem. Soc.* **2015,** *137* (5), 2030-2034, DOI 10.1021/ja512491v.

195. Liu, J.; Kelley, M. S.; Wu, W.; Banerjee, A.; Douvalis, A. P.; Wu, J.; Zhang, Y.; Schatz, G. C.; Kanatzidis, M. G., Nitrogenase-mimic iron-containing chalcogels for photochemical reduction of dinitrogen to ammonia. *Proceedings of the National Academy of Sciences* **2016,** *113* (20), 5530-5535, DOI 10.1073/pnas.1605512113.

196. Hoffman, B. M.; Lukoyanov, D.; Yang, Z.-Y.; Dean, D. R.; Seefeldt, L. C., Mechanism of nitrogen fixation by nitrogenase: the next stage. *Chem. Rev.* **2014,** *114* (8), 4041-4062, DOI 10.1021/cr400641x.

197. Pan, X.; Yang, M.-Q.; Fu, X.; Zhang, N.; Xu, Y.-J., Defective TiO_2 with oxygen vacancies: synthesis, properties and photocatalytic applications. *Nanoscale* **2013,** *5* (9), 3601-3614, DOI 10.1039/C3NR00476G.

198. Li, H.; Li, J.; Ai, Z.; Jia, F.; Zhang, L., Oxygen Vacancy-Mediated Photocatalysis of BiOCl: Reactivity, Selectivity, and Perspectives. *Angew. Chem. Int. Ed.* **2017,** *57* (1), 122-138, DOI 10.1002/anie.201705628.

199. Hu, S.; Li, Y.; Li, F.; Fan, Z.; Ma, H.; Li, W.; Kang, X., Construction of g-C3N4/Zn0.11Sn0.12Cd0.88S1.12 Hybrid Heterojunction Catalyst with Outstanding Nitrogen Photofixation Performance Induced by Sulfur Vacancies. *ACS Sustainable Chemistry & Engineering* **2016,** *4* (4), 2269-2278, DOI 10.1021/acssuschemeng.5b01742.

200. Hu, S.; Chen, X.; Li, Q.; Zhao, Y.; Mao, W., Effect of sulfur vacancies on the nitrogen photofixation performance of ternary metal sulfide photocatalysts. *Catalysis Science & Technology* **2016,** *6* (15), 5884-5890, DOI 10.1039/C6CY00622A.

201. Zhang, Q.; Hu, S.; Fan, Z.; Liu, D.; Zhao, Y.; Ma, H.; Li, F., Preparation of g-C3N4/ZnMoCdS hybrid heterojunction catalyst with outstanding nitrogen photofixation performance under visible light via hydrothermal post-treatment. *Dalton Transactions* **2016,** *45* (8), 3497-3505, DOI 10.1039/C5DT04901F.

202. Niu, P.; Liu, G.; Cheng, H.-M., Nitrogen Vacancy-Promoted Photocatalytic Activity of Graphitic Carbon Nitride. *The Journal of Physical Chemistry C* **2012,** *116* (20), 11013-11018, DOI 10.1021/jp301026y.

203. Wang, S.; Hai, X.; Ding, X.; Chang, K.; Xiang, Y.; Meng, X.; Yang, Z.; Chen, H.; Ye, J., Light-Switchable Oxygen Vacancies in Ultrafine Bi5O7Br Nanotubes for Boosting Solar-Driven Nitrogen Fixation in Pure Water. *Adv. Mater.* **2017,** *29* (31), 1701774, DOI 10.1002/adma.201701774.

204. Sun, S.; An, Q.; Wang, W.; Zhang, L.; Liu, J.; Goddard Iii, W. A., Efficient photocatalytic reduction of dinitrogen to ammonia on bismuth monoxide quantum dots. *Journal of Materials Chemistry A* **2017,** *5* (1), 201-209, DOI 10.1039/C6TA09275F.

205. Bai, Y.; Ye, L.; Chen, T.; Wang, L.; Shi, X.; Zhang, X.; Chen, D., Facet-Dependent Photocatalytic N2 Fixation of Bismuth-Rich Bi5O7I Nanosheets. *ACS Applied Materials & Interfaces* **2016,** *8* (41), 27661-27668, DOI 10.1021/acsami.6b08129.

206. Hao, Y.; Dong, X.; Zhai, S.; Ma, H.; Wang, X.; Zhang, X., Hydrogenated Bismuth Molybdate Nanoframe for Efficient Sunlight-Driven Nitrogen Fixation from Air. *Chemistry – A European Journal* **2016,** *22* (52), 18722-18728, DOI 10.1002/chem.201604510.

207. Li, J.; Li, H.; Zhan, G.; Zhang, L., Solar Water Splitting and Nitrogen Fixation with Layered Bismuth Oxyhalides. *Acc. Chem. Res.* **2017,** *50* (1), 112-121, DOI 10.1021/acs.accounts.6b00523.

208. Ma, H.; Shi, Z.; Li, Q.; Li, S., Preparation of graphitic carbon nitride with large specific surface area and outstanding N2 photofixation ability via a dissolve-regrowth process. *J. Phys. Chem. Solids* **2016,** *99*, 51-58, DOI https://doi.org/10.1016/j.jpcs.2016.08.008.

209. Zhou, N.; Qiu, P.; Chen, H.; Jiang, F., KOH etching graphitic carbon nitride for simulated sunlight photocatalytic nitrogen fixation with cyano groups as defects. *Journal of the Taiwan Institute of Chemical Engineers* **2018,** *83*, 99-106, DOI https://doi.org/10.1016/j.jtice.2017.11.028.

210. Cao, Y.; Hu, S.; Li, F.; Fan, Z.; Bai, J.; Lu, G.; Wang, Q., Photofixation of atmospheric nitrogen to ammonia with a novel ternary metal sulfide catalyst under visible light. *RSC Advances* **2016,** *6* (55), 49862-49867, DOI 10.1039/C6RA08247E.

211. Cao, S.; Fan, B.; Feng, Y.; Chen, H.; Jiang, F.; Wang, X., Sulfur-doped g-C_3N_4 nanosheets with carbon vacancies: General synthesis and improved activity for simulated solar-light photocatalytic nitrogen fixation. *Chem. Eng. J.* **2018,** *353*, 147-156, DOI https://doi.org/10.1016/j.cej.2018.07.116.

212. Matanovic, I.; Garzon, F. H., Nitrogen electroreduction and hydrogen evolution on cubic molybdenum carbide: a density functional study. *PCCP* **2018,** *20* (21), 14679-14687, DOI 10.1039/C8CP01643G.

213. Khan Mirza, M. T.; Bhardwaj Ramesh, C.; Bhardwaj, C., Catalytic Fixation of Nitrogen by the Photocatalytic CdS/Pt/RuO2 Particulate System in the Presence of Aqueous $[Ru(Hedta)N_2]^{\ominus}$ Complex. *Angewandte Chemie International Edition in English* **1988,** *27* (7), 923-925, DOI 10.1002/anie.198809231.

214. Miyama, H.; Fujii, N.; Nagae, Y., Heterogeneous photocatalytic synthesis of ammonia from water and nitrogen. *Chem. Phys. Lett.* **1980,** *74* (3), 523-524, DOI https://doi.org/10.1016/0009-2614(80)85266-3.

215. Rao, N. N.; Dube, S.; Manjubala; Natarajan, P., Photocatalytic reduction of nitrogen over (Fe, Ru or Os) /TiO_2 catalysts. *Applied Catalysis B: Environmental* **1994,** *5* (1), 33-42, DOI https://doi.org/10.1016/0926-3373(94)00042-5.

216. Medford, A. J.; Hatzell, M. C., Photon-Driven Nitrogen Fixation: Current Progress, Thermodynamic Considerations, and Future Outlook. *ACS Catalysis* **2017,** *7* (4), 2624-2643, DOI 10.1021/acscatal.7b00439.

217. Qiu, P.; Xu, C.; Zhou, N.; Chen, H.; Jiang, F., Metal-free black phosphorus nanosheets-decorated graphitic carbon nitride nanosheets with CP bonds for excellent photocatalytic nitrogen fixation. *Applied Catalysis B: Environmental* **2018,** *221*, 27-35, DOI https://doi.org/10.1016/j.apcatb.2017.09.010.

218. Wang, R.; Lu, K.-Q.; Tang, Z.-R.; Xu, Y.-J., Recent progress in carbon quantum dots: synthesis, properties and applications in photocatalysis. *Journal of Materials Chemistry A* **2017,** *5* (8), 3717-3734, DOI 10.1039/C6TA08660H.

219. Wang, H.; Li, H.; Zhang, M.; Song, Y.; Huang, J.; Huang, H.; Shao, M.; Liu, Y.; Kang, Z., Carbon Dots Enhance the Nitrogen Fixation Activity of Azotobacter Chroococcum. *ACS Applied Materials & Interfaces* **2018,** *10* (19), 16308-16314, DOI 10.1021/acsami.8b03758.

220. Li, X.; Wang, W.; Jiang, D.; Sun, S.; Zhang, L.; Sun, X., Efficient Solar-Driven Nitrogen Fixation over Carbon–Tungstic-Acid Hybrids. *Chemistry – A European Journal* **2016,** *22* (39), 13819-13822, DOI 10.1002/chem.201603277.

221. Shao, M.; Shao, Y.; Chen, W.; Ao, K. L.; Tong, R.; Zhu, Q.; Chan, I. N.; Ip, W. F.; Shi, X.; Pan, H., Efficient nitrogen fixation to ammonia on MXenes. *PCCP* **2018,** *20* (21), 14504-14512, DOI 10.1039/C8CP01396A.

222. Comer, B. M.; Liu, Y.-H.; Dixit, M. B.; Hatzell, K.; Ye, Y.; Crumlin, E. J.; Hatzell, M. C.; Medford, A. J., The Role of Adventitious Carbon on Photocatalytic Nitrogen Fixation by Titania. *J. Am. Chem. Soc.* **2018**, DOI 10.1021/jacs.8b08464.

223. Ueno, K.; Oshikiri, T.; Shi, X.; Zhong, Y.; Misawa, H., Plasmon-induced artificial photosynthesis. *Interface Focus* **2015,** *5* (3), DOI 10.1098/rsfs.2014.0082.

224. Mao, C.; Yu, L.; Li, J.; Zhao, J.; Zhang, L., Energy-confined solar thermal ammonia synthesis with K/Ru/$TiO_{2-x}H_x$. *Applied Catalysis B: Environmental* **2018,** *224*, 612-620, DOI https://doi.org/10.1016/j.apcatb.2017.11.010.

225. Hu, S.; Zhang, W.; Bai, J.; Lu, G.; Zhang, L.; Wu, G., Construction of a 2D/2D g-C3N4/rGO hybrid heterojunction catalyst with outstanding charge separation ability and nitrogen photofixation performance via a surface protonation process. *RSC Advances* **2016,** *6* (31), 25695-25702, DOI 10.1039/C5RA28123G.

226. Cao, S.; Zhou, N.; Gao, F.; Chen, H.; Jiang, F., All-solid-state Z-scheme 3,4-dihydroxybenzaldehyde-functionalized Ga_2O_3/graphitic carbon nitride photocatalyst with aromatic rings as electron mediators for visible-light photocatalytic nitrogen fixation. *Applied Catalysis B: Environmental* **2017,** *218*, 600-610, DOI https://doi.org/10.1016/j.apcatb.2017.07.013.

227. Vega-Manzano, O. Structural Dimensional Limits on Materials Properties: Anisotropic Conduction in Organic Semiconductors and Low Dimensional Ferroelectricity in Organic Ferroelectrics. 2018.

228. Zhang, K.; Guo, L., Metal sulphide semiconductors for photocatalytic hydrogen production. *Catalysis Science & Technology* **2013,** *3* (7), 1672-1690, DOI 10.1039/C3CY00018D.

229. Yue, Z.; Liu, A.; Zhang, C.; Huang, J.; Zhu, M.; Du, Y.; Yang, P., Noble-metal-free hetero-structural CdS/Nb_2O_5/N-doped-graphene ternary photocatalytic system as visible-

light-driven photocatalyst for hydrogen evolution. *Applied Catalysis B: Environmental* **2017,** *201*, 202-210, DOI http://dx.doi.org/10.1016/j.apcatb.2016.08.028.

230. Wu, Y.; Yue, Z.; Liu, A.; Yang, P.; Zhu, M., P-Type Cu-Doped $Zn_{0.3}Cd_{0.7}S$/Graphene Photocathode for Efficient Water Splitting in a Photoelectrochemical Tandem Cell. *ACS Sustainable Chemistry & Engineering* **2016,** *4* (5), 2569-2577, DOI 10.1021/acssuschemeng.5b01795.

231. Shiga, Y.; Umezawa, N.; Srinivasan, N.; Koyasu, S.; Sakai, E.; Miyauchi, M., A metal sulfide photocatalyst composed of ubiquitous elements for solar hydrogen production. *Chem. Commun.* **2016,** *52* (47), 7470-7473, DOI 10.1039/C6CC03199D.

232. Bhirud, A.; Chaudhari, N.; Nikam, L.; Sonawane, R.; Patil, K.; Baeg, J.-O.; Kale, B., Surfactant tunable hierarchical nanostructures of $CdIn_2S_4$ and their photohydrogen production under solar light. *Int. J. Hydrogen Energy* **2011,** *36* (18), 11628-11639, DOI http://dx.doi.org/10.1016/j.ijhydene.2011.06.061.

233. Song, J.-P.; Yin, P.-F.; Mao, J.; Qiao, S.-Z.; Du, X.-W., Catalytically active and chemically inert $CdIn_2S_4$ coating on a CdS photoanode for efficient and stable water splitting. *Nanoscale* **2017,** *9* (19), 6296-6301, DOI 10.1039/C7NR01170A.

234. Zhu, M.; Cai, X.; Fujitsuka, M.; Zhang, J.; Majima, T., Au/$La_2Ti_2O_7$ Nanostructures Sensitized with Black Phosphorus for Plasmon-Enhanced Photocatalytic Hydrogen Production in Visible and Near-Infrared Light. *Angew. Chem. Int. Ed.* **2017,** *56* (8), 2064-2068, DOI 10.1002/anie.201612315.

235. Yue, X.; Yi, S.; Wang, R.; Zhang, Z.; Qiu, S., Cadmium Sulfide and Nickel Synergetic Co-catalysts Supported on Graphitic Carbon Nitride for Visible-Light-Driven Photocatalytic Hydrogen Evolution. *Scientific Reports* **2016,** *6*, 22268, DOI 10.1038/srep22268.

236. Wang, Y.; Wu, J.; Zheng, J.; Jiang, R.; Xu, R., Ni^{2+}-doped ZnxCd1-xS photocatalysts from single-source precursors for efficient solar hydrogen production under visible light irradiation. *Catalysis Science & Technology* **2012,** *2* (3), 581-588, DOI 10.1039/C2CY00310D.

237. Joo, J. B.; Zhang, Q.; Lee, I.; Dahl, M.; Zaera, F.; Yin, Y., Mesoporous Anatase Titania Hollow Nanostructures though Silica-Protected Calcination. *Adv. Funct. Mater.* **2012,** *22* (1), 166-174, DOI 10.1002/adfm.201101927.

238. Wang, Z.; Hou, J.; Yang, C.; Jiao, S.; Huang, K.; Zhu, H., Hierarchical metastable [gamma]-TaON hollow structures for efficient visible-light water splitting. *Energy & Environmental Science* **2013,** *6* (7), 2134-2144, DOI 10.1039/C3EE24370B.

239. Li, H.; Bian, Z.; Zhu, J.; Zhang, D.; Li, G.; Huo, Y.; Li, H.; Lu, Y., Mesoporous Titania Spheres with Tunable Chamber Stucture and Enhanced Photocatalytic Activity. *J. Am. Chem. Soc.* **2007,** *129* (27), 8406-8407, DOI 10.1021/ja072191c.

240. Nguyen, C.-C.; Vu, N.-N.; Do, T.-O., Efficient hollow double-shell photocatalysts for the degradation of organic pollutants under visible light and in darkness. *Journal of Materials Chemistry A* **2016,** *4* (12), 4413-4419, DOI 10.1039/C5TA09016D.

241. Shen, L.; Yu, L.; Wu, H. B.; Yu, X.-Y.; Zhang, X.; Lou, X. W., Formation of nickel cobalt sulfide ball-in-ball hollow spheres with enhanced electrochemical pseudocapacitive properties. **2015,** *6*, 6694, DOI 10.1038/ncomms7694

242. Vioux, A., Nonhydrolytic Sol−Gel Routes to Oxides. *Chem. Mater.* **1997,** *9* (11), 2292-2299, DOI 10.1021/cm970322a.

243. Yang, F. F.; Fang, L.; Zhang, S. F.; Sun, J. S.; Xu, Q. T.; Wu, S. Y.; Dong, J. X.; Kong, C. Y., Structure and electrical properties of $CdIn_2O_4$ thin films prepared by DC reactive magnetron sputtering. *Appl. Surf. Sci.* **2008,** *254* (17), 5481-5486, DOI http://dx.doi.org/10.1016/j.apsusc.2008.02.090.

244. Carevic, M. V.; Comor, M. I.; Mitric, M. N.; Barudzija, T. S.; Ahrenkiel, S. P.; Abazovic, N. D., The influence of reaction media on $CdIn_2S_4$ and $ZnIn_2S_4$ nanocrystallite formation and growth of mesocrystal structures. *CrystEngComm* **2015,** *17* (44), 8492-8499, DOI 10.1039/C5CE01432H.

245. Chen, X.; Li, L.; Zhang, W.; Li, Y.; Song, Q.; Dong, L., Fabricate Globular Flower-like CuS/$CdIn_2S_4$/$ZnIn_2S_4$ with High Visible Light Response via Microwave-assisted One–step Method and Its Multipathway Photoelectron Migration Properties for Hydrogen Evolution and Pollutant Degradation. *ACS Sustainable Chemistry & Engineering* **2016,** *4* (12), 6680-6688, DOI 10.1021/acssuschemeng.6b01543.

246. Li, D.; Shi, F.; Jiang, D.; Chen, M.; Shi, W., $CdIn_2S_4$/g-C_3N_4 heterojunction photocatalysts: enhanced photocatalytic performance and charge transfer mechanism. *RSC Advances* **2017,** *7* (1), 231-237, DOI 10.1039/C6RA24809H.

247. Li, S.; Lin, Y.-H.; Zhang, B.-P.; Li, J.-F.; Nan, C.-W., $BiFeO_3/TiO_2$ core-shell structured nanocomposites as visible-active photocatalysts and their optical response mechanism. *J. Appl. Phys.* **2009,** *105* (5), 054310, DOI 10.1063/1.3091286.

248. Habibi-Yangjeh, A.; Shekofteh-Gohari, M., Novel magnetic $Fe_3O_4/ZnO/NiWO_4$ nanocomposites: Enhanced visible-light photocatalytic performance through p-n heterojunctions. *Sep. Purif. Technol.* **2017,** *184*, 334-346, DOI http://dx.doi.org/10.1016/j.seppur.2017.05.007.

249. Yu, Y.; Chen, G.; Wang, G.; Lv, Z., Visible-light-driven $ZnIn_2S_4/CdIn_2S_4$ composite photocatalyst with enhanced performance for photocatalytic H_2 evolution. *Int. J. Hydrogen Energy* **2013,** *38* (3), 1278-1285, DOI https://doi.org/10.1016/j.ijhydene.2012.11.020.

250. Yeom, H. I.; Ko, J. B.; Mun, G.; Park, S. H. K., High mobility polycrystalline indium oxide thin-film transistors by means of plasma-enhanced atomic layer deposition. *Journal of Materials Chemistry C* **2016,** *4* (28), 6873-6880, DOI 10.1039/C6TC00580B.

251. Deokate, R. J., Temperature dependant physical properties of $CdIn_2O_4$ thin films grown by spray pyrolysis. *Superlattices Microstruct.* **2014,** *76*, 16-25, DOI https://doi.org/10.1016/j.spmi.2014.08.026.

252. Ghazzal, M. N.; Wojcieszak, R.; Raj, G.; Gaigneaux, E. M., Study of mesoporous CdS-quantum-dot-sensitized TiO2 films by using X-ray photoelectron spectroscopy and AFM. *Beilstein J Nanotechnol* **2014,** *5*, 68-76, DOI 10.3762/bjnano.5.6.

253. Dinh, C.-T.; Pham, M.-H.; Kleitz, F.; Do, T.-O., Design of water-soluble CdS-titanate-nickel nanocomposites for photocatalytic hydrogen production under sunlight. *Journal of Materials Chemistry A* **2013,** *1* (42), 13308-13313, DOI 10.1039/C3TA12914D.

254. Zou, X.; Su, J.; Silva, R.; Goswami, A.; Sathe, B. R.; Asefa, T., Efficient oxygen evolution reaction catalyzed by low-density Ni-doped Co_3O_4 nanomaterials derived from metal-embedded graphitic C_3N_4. *Chem. Commun.* **2013,** *49* (68), 7522-7524, DOI 10.1039/C3CC42891E.

255. Agegnehu, A. K.; Pan, C.-J.; Rick, J.; Lee, J.-F.; Su, W.-N.; Hwang, B.-J., Enhanced hydrogen generation by cocatalytic Ni and NiO nanoparticles loaded on graphene oxide sheets. *J. Mater. Chem.* **2012,** *22* (27), 13849-13854, DOI 10.1039/C2JM30474K.

256. Pauling, L., The Nature of Chemical bond. **1960**.

257. Kudo, A.; Miseki, Y., Heterogeneous photocatalyst materials for water splitting. *Chem. Soc. Rev.* **2009,** *38* (1), 253-278, DOI 10.1039/B800489G.

258. Onsuratoom, S.; Puangpetch, T.; Chavadej, S., Comparative investigation of hydrogen production over Ag-, Ni-, and Cu-loaded mesoporous-assembled TiO_2–ZrO_2 mixed oxide nanocrystal photocatalysts. *Chem. Eng. J.* **2011,** *173* (2), 667-675, DOI http://dx.doi.org/10.1016/j.cej.2011.08.016.

259. Tran, P. D.; Xi, L.; Batabyal, S. K.; Wong, L. H.; Barber, J.; Chye Loo, J. S., Enhancing the photocatalytic efficiency of TiO_2 nanopowders for H2 production by using non-noble transition metal co-catalysts. *PCCP* **2012,** *14* (33), 11596-11599, DOI 10.1039/C2CP41450C.

260. Mousavi, M.; Habibi-Yangjeh, A.; Abitorabi, M., Fabrication of novel magnetically separable nanocomposites using graphitic carbon nitride, silver phosphate and silver chloride and their applications in photocatalytic removal of different pollutants using visible-light irradiation. *J. Colloid Interface Sci.* **2016,** *480*, 218-231, DOI http://dx.doi.org/10.1016/j.jcis.2016.07.021.

261. Dresselhaus, M. S.; Thomas, I. L., Alternative energy technologies. *Nature* **2001,** *414*, 332, DOI 10.1038/35104599.

262. Su, C.-Y.; Cheng, H.; Li, W.; Liu, Z.-Q.; Li, N.; Hou, Z.; Bai, F.-Q.; Zhang, H.-X.; Ma, T.-Y., Zinc-Air Batteries: Atomic Modulation of FeCo–Nitrogen–Carbon Bifunctional Oxygen Electrodes for Rechargeable and Flexible All-Solid-State Zinc–Air Battery (Adv. Energy Mater. 13/2017). *Advanced Energy Materials* **2017,** *7* (13), n/a-n/a, DOI 10.1002/aenm.201770067.

263. Liu, Z.-Q.; Cheng, H.; Li, N.; Ma, T. Y.; Su, Y.-Z., $ZnCo_2O_4$ Quantum Dots Anchored on Nitrogen-Doped Carbon Nanotubes as Reversible Oxygen Reduction/Evolution Electrocatalysts. *Adv. Mater.* **2016,** *28* (19), 3777-3784, DOI 10.1002/adma.201506197.

264. Cao, S.; Low, J.; Yu, J.; Jaroniec, M., Polymeric Photocatalysts Based on Graphitic Carbon Nitride. *Adv. Mater.* **2015,** *27* (13), 2150-2176, DOI 10.1002/adma.201500033.

265. Wei, R.-B.; Kuang, P.-Y.; Cheng, H.; Chen, Y.-B.; Long, J.-Y.; Zhang, M.-Y.; Liu, Z.-Q., Plasmon-Enhanced Photoelectrochemical Water Splitting on Gold Nanoparticle

Decorated ZnO/CdS Nanotube Arrays. *ACS Sustainable Chemistry & Engineering* **2017,** *5* (5), 4249-4257, DOI 10.1021/acssuschemeng.7b00242.

266. Zhu, M.; Zhai, C.; Sun, M.; Hu, Y.; Yan, B.; Du, Y., Ultrathin graphitic C_3N_4 nanosheet as a promising visible-light-activated support for boosting photoelectrocatalytic methanol oxidation. *Applied Catalysis B: Environmental* **2017,** *203*, 108-115, DOI https://doi.org/10.1016/j.apcatb.2016.10.012.

267. Bi, L.; Meng, D.; Bu, Q.; Lin, Y.; Wang, D.; Xie, T., Electron acceptor of Ni decorated porous carbon nitride applied in photocatalytic hydrogen production. *PCCP* **2016,** *18* (46), 31534-31541, DOI 10.1039/C6CP05618K.

268. Wang, X.; Maeda, K.; Thomas, A.; Takanabe, K.; Xin, G.; Carlsson, J. M.; Domen, K.; Antonietti, M., A metal-free polymeric photocatalyst for hydrogen production from water under visible light. *Nat Mater* **2009,** *8* (1), 76-80, DOI http://www.nature.com/nmat/journal/v8/n1/suppinfo/nmat2317_S1.html.

269. Zheng, D.; Pang, C.; Liu, Y.; Wang, X., Shell-engineering of hollow g-C_3N_4 nanospheres via copolymerization for photocatalytic hydrogen evolution. *Chem. Commun.* **2015,** *51* (47), 9706-9709, DOI 10.1039/C5CC03143E.

270. Liang, Q.; Li, Z.; Yu, X.; Huang, Z.-H.; Kang, F.; Yang, Q.-H., Macroscopic 3D Porous Graphitic Carbon Nitride Monolith for Enhanced Photocatalytic Hydrogen Evolution. *Adv. Mater.* **2015,** *27* (31), 4634-4639, DOI 10.1002/adma.201502057.

271. Kailasam, K.; Epping, J. D.; Thomas, A.; Losse, S.; Junge, H., Mesoporous carbon nitride-silica composites by a combined sol-gel/thermal condensation approach and their application as photocatalysts. *Energy & Environmental Science* **2011,** *4* (11), 4668-4674, DOI 10.1039/C1EE02165F.

272. Schwinghammer, K.; Tuffy, B.; Mesch, M. B.; Wirnhier, E.; Martineau, C.; Taulelle, F.; Schnick, W.; Senker, J.; Lotsch, B. V., Triazine-based Carbon Nitrides for Visible-Light-Driven Hydrogen Evolution. *Angew. Chem. Int. Ed.* **2013,** *52* (9), 2435-2439, DOI 10.1002/anie.201206817.

273. Xiong, T.; Cen, W.; Zhang, Y.; Dong, F., Bridging the g-C_3N_4 Interlayers for Enhanced Photocatalysis. *ACS Catalysis* **2016,** *6* (4), 2462-2472, DOI 10.1021/acscatal.5b02922.

274. Gao, D.; Liu, Y.; Liu, P.; Si, M.; Xue, D., Atomically Thin B doped g-C3N4 Nanosheets: High-Temperature Ferromagnetism and calculated Half-Metallicity. **2016,** *6*, 35768, DOI 10.1038/srep35768

275. Wang, K.; Li, Q.; Liu, B.; Cheng, B.; Ho, W.; Yu, J., Sulfur-doped g-C_3N_4 with enhanced photocatalytic CO_2-reduction performance. *Applied Catalysis B: Environmental* **2015,** *176*, 44-52, DOI http://dx.doi.org/10.1016/j.apcatb.2015.03.045.

276. Zhou, Y.; Zhang, L.; Liu, J.; Fan, X.; Wang, B.; Wang, M.; Ren, W.; Wang, J.; Li, M.; Shi, J., Brand new P-doped g-C3N4: enhanced photocatalytic activity for H_2 evolution and Rhodamine B degradation under visible light. *Journal of Materials Chemistry A* **2015,** *3* (7), 3862-3867, DOI 10.1039/C4TA05292G.

277. Xu, Y.; Fu, Z.-C.; Cao, S.; Chen, Y.; Fu, W.-F., Highly selective oxidation of sulfides on a CdS/C3N4 catalyst with dioxygen under visible-light irradiation. *Catalysis Science & Technology* **2017,** *7* (3), 587-595, DOI 10.1039/C6CY01568A.

278. Naseri, A.; Samadi, M.; Pourjavadi, A.; Moshfegh, A. Z.; Ramakrishna, S., Graphitic carbon nitride (g-C_3N_4)-based photocatalysts for solar hydrogen generation: recent advances and future development directions. *Journal of Materials Chemistry A* **2017,** *5* (45), 23406-23433, DOI 10.1039/C7TA05131J.

279. Niu, P.; Zhang, L.; Liu, G.; Cheng, H.-M., Graphene-Like Carbon Nitride Nanosheets for Improved Photocatalytic Activities. *Adv. Funct. Mater.* **2012,** *22* (22), 4763-4770, DOI 10.1002/adfm.201200922.

280. Wang, N.; Fan, H.; Sun, J.; Han, Z.; Dong, J.; Ai, S., Fluorine-doped carbon nitride quantum dots: Ethylene glycol-assisted synthesis, fluorescent properties, and their application for bacterial imaging. *Carbon* **2016,** *109*, 141-148, DOI http://dx.doi.org/10.1016/j.carbon.2016.08.004.

281. Shao, X.; Xu, J.; Huang, Y.; Su, X.; Duan, H.; Wang, X.; Zhang, T., Pd@C_3N_4 nanocatalyst for highly efficient hydrogen storage system based on potassium bicarbonate/formate. *AlChE J.* **2016,** *62* (7), 2410-2418, DOI 10.1002/aic.15218.

282. Liang, S.; Xia, Y.; Zhu, S.; Zheng, S.; He, Y.; Bi, J.; Liu, M.; Wu, L., Au and Pt co-loaded g-C_3N_4 nanosheets for enhanced photocatalytic hydrogen production under visible light irradiation. *Appl. Surf. Sci.* **2015,** *358*, 304-312, DOI http://dx.doi.org/10.1016/j.apsusc.2015.08.035.

283. Liu, G.; Niu, P.; Sun, C.; Smith, S. C.; Chen, Z.; Lu, G. Q.; Cheng, H.-M., Unique Electronic Structure Induced High Photoreactivity of Sulfur-Doped Graphitic C_3N_4. *J. Am. Chem. Soc.* **2010,** *132* (33), 11642-11648, DOI 10.1021/ja103798k.

284. Samadi, M.; Zirak, M.; Naseri, A.; Khorashadizade, E.; Moshfegh, A. Z., Recent progress on doped ZnO nanostructures for visible-light photocatalysis. *Thin Solid Films* **2016,** *605*, 2-19, DOI https://doi.org/10.1016/j.tsf.2015.12.064.

285. Liu, G.; Wang, L.; Yang, H. G.; Cheng, H.-M.; Lu, G. Q., Titania-based photocatalysts-crystal growth, doping and heterostructuring. *J. Mater. Chem.* **2010,** *20* (5), 831-843, DOI 10.1039/B909930A.

286. Ma, X.; Lv, Y.; Xu, J.; Liu, Y.; Zhang, R.; Zhu, Y., A Strategy of Enhancing the Photoactivity of g-C_3N_4 via Doping of Nonmetal Elements: A First-Principles Study. *The Journal of Physical Chemistry C* **2012,** *116* (44), 23485-23493, DOI 10.1021/jp308334x.

287. Lu, Y.; Chu, D.; Zhu, M.; Du, Y.; Yang, P., Exfoliated carbon nitride nanosheets decorated with NiS as an efficient noble-metal-free visible-light-driven photocatalyst for hydrogen evolution. *PCCP* **2015,** *17* (26), 17355-17361, DOI 10.1039/C5CP01657F.

288. Chen, G.-F.; Ma, T. Y.; Liu, Z.-Q.; Li, N.; Su, Y.-Z.; Davey, K.; Qiao, S.-Z., Efficient and Stable Bifunctional Electrocatalysts Ni/NixMy (M = P, S) for Overall Water Splitting. *Adv. Funct. Mater.* **2016,** *26* (19), 3314-3323, DOI 10.1002/adfm.201505626.

289. Liu, M.; Chen, Y.; Su, J.; Shi, J.; Wang, X.; Guo, L., Photocatalytic hydrogen production using twinned nanocrystals and an unanchored NiS_x co-catalyst. **2016,** *1*, 16151, DOI 10.1038/nenergy.2016.151

290. Simon, T.; Bouchonville, N.; Berr, M. J.; Vaneski, A.; Adrović, A.; Volbers, D.; Wyrwich, R.; Döblinger, M.; Susha, A. S.; Rogach, A. L.; Jäckel, F.; Stolarczyk, J. K.; Feldmann, J., Redox shuttle mechanism enhances photocatalytic H_2 generation on Ni-decorated CdS nanorods. *Nat Mater* **2014,** *13* (11), 1013-1018, DOI 10.1038/nmat4049

291. Li, S.; Dai, D.; Ge, L.; Gao, Y.; Han, C.; Xiao, N., Synthesis of layer-like $Ni(OH)_2$ decorated $ZnIn_2S_4$ sub-microspheres with enhanced visible-light photocatalytic hydrogen production activity. *Dalton Transactions* **2017**, DOI 10.1039/C7DT00819H.

292. Indra, A.; Menezes, P. W.; Kailasam, K.; Hollmann, D.; Schroder, M.; Thomas, A.; Bruckner, A.; Driess, M., Nickel as a co-catalyst for photocatalytic hydrogen evolution on

graphitic-carbon nitride (sg-CN): what is the nature of the active species? *Chem. Commun.* **2016,** *52* (1), 104-107, DOI 10.1039/C5CC07936E.

293. Chen, Z.; Sun, P.; Fan, B.; Zhang, Z.; Fang, X., In Situ Template-Free Ion-Exchange Process to Prepare Visible-Light-Active g-C3N4/NiS Hybrid Photocatalysts with Enhanced Hydrogen Evolution Activity. *The Journal of Physical Chemistry C* **2014,** *118* (15), 7801-7807, DOI 10.1021/jp5000232.

294. Zhang, G.; Lan, Z.-A.; Lin, L.; Lin, S.; Wang, X., Overall water splitting by Pt/g-C_3N_4 photocatalysts without using sacrificial agents. *Chemical Science* **2016,** *7* (5), 3062-3066, DOI 10.1039/C5SC04572J.

295. Liang, Q.; Li, Z.; Huang, Z.-H.; Kang, F.; Yang, Q.-H., Holey Graphitic Carbon Nitride Nanosheets with Carbon Vacancies for Highly Improved Photocatalytic Hydrogen Production. *Adv. Funct. Mater.* **2015,** *25* (44), 6885-6892, DOI 10.1002/adfm.201503221.

296. Xu, C.; Han, Q.; Zhao, Y.; Wang, L.; Li, Y.; Qu, L., Sulfur-doped graphitic carbon nitride decorated with graphene quantum dots for an efficient metal-free electrocatalyst. *Journal of Materials Chemistry A* **2015,** *3* (5), 1841-1846, DOI 10.1039/C4TA06149G.

297. Sergey, S.; Sebastian, Z., Sulfur doping effects on the electronic and geometric structures of graphitic carbon nitride photocatalyst: insights from first principles. *J. Phys.: Condens. Matter* **2013,** *25* (8), 085507.

298. Sun, L.; Yang, M.; Huang, J.; Yu, D.; Hong, W.; Chen, X., Freestanding Graphitic Carbon Nitride Photonic Crystals for Enhanced Photocatalysis. *Adv. Funct. Mater.* **2016,** *26* (27), 4943-4950, DOI 10.1002/adfm.201600894.

299. Zhang, X.; Gong, Y.; Dong, X.; Zhang, X.; Ma, C.; Shi, F., Fabrication and efficient visible light-induced photocatalytic activity of Bi_2WO_6/$BiVO_4$ heterojunction. *Mater. Chem. Phys.* **2012,** *136* (2), 472-476, DOI https://doi.org/10.1016/j.matchemphys.2012.07.013.

300. Zhang, X.; Du, L.; Wang, H.; Dong, X.; Zhang, X.; Ma, C.; Ma, H., Highly ordered mesoporous BiVO4: Controllable ordering degree and super photocatalytic ability under visible light. *Microporous Mesoporous Mater.* **2013,** *173*, 175-180, DOI https://doi.org/10.1016/j.micromeso.2013.02.029.

301. Yu, J.; Wang, K.; Xiao, W.; Cheng, B., Photocatalytic reduction of CO_2 into hydrocarbon solar fuels over g-C_3N_4-Pt nanocomposite photocatalysts. *PCCP* **2014,** *16* (23), 11492-11501, DOI 10.1039/C4CP00133H.

302. Liao, G.; Chen, S.; Quan, X.; Yu, H.; Zhao, H., Graphene oxide modified g-C_3N_4 hybrid with enhanced photocatalytic capability under visible light irradiation. *J. Mater. Chem.* **2012,** *22* (6), 2721-2726, DOI 10.1039/C1JM13490F.

303. Yu, J.; Wang, S.; Cheng, B.; Lin, Z.; Huang, F., Noble metal-free $Ni(OH)_2$-g-C_3N_4 composite photocatalyst with enhanced visible-light photocatalytic H_2-production activity. *Catalysis Science & Technology* **2013,** *3* (7), 1782-1789, DOI 10.1039/C3CY20878H.

304. Yang, Y.; Guo, Y.; Liu, F.; Yuan, X.; Guo, Y.; Zhang, S.; Guo, W.; Huo, M., Preparation and enhanced visible-light photocatalytic activity of silver deposited graphitic carbon nitride plasmonic photocatalyst. *Applied Catalysis B: Environmental* **2013,** *142* (Supplement C), 828-837, DOI https://doi.org/10.1016/j.apcatb.2013.06.026.

305. Bai, X.; Wang, L.; Zong, R.; Zhu, Y., Photocatalytic Activity Enhanced via g-C_3N_4 Nanoplates to Nanorods. *The Journal of Physical Chemistry C* **2013,** *117* (19), 9952-9961, DOI 10.1021/jp402062d.

306. Zhang, W.; Wang, Y.; Wang, Z.; Zhong, Z.; Xu, R., Highly efficient and noble metal-free NiS/CdS photocatalysts for H2 evolution from lactic acid sacrificial solution under visible light. *Chem. Commun.* **2010,** *46* (40), 7631-7633, DOI 10.1039/C0CC01562H.

307. Li, Y.; Lin, S.; Peng, S.; Lu, G.; Li, S., Modification of $ZnS_{1-x-0.5y}Ox(OH)_y$–ZnO photocatalyst with NiS for enhanced visible-light-driven hydrogen generation from seawater. *Int. J. Hydrogen Energy* **2013,** *38* (36), 15976-15984, DOI https://doi.org/10.1016/j.ijhydene.2013.09.149.

308. Zhang, L.; Tian, B.; Chen, F.; Zhang, J., Nickel sulfide as co-catalyst on nanostructured TiO_2 for photocatalytic hydrogen evolution. *Int. J. Hydrogen Energy* **2012,** *37* (22), 17060-17067, DOI https://doi.org/10.1016/j.ijhydene.2012.08.120.

309. Breysse, M.; Furimsky, E.; Kasztelan, S.; Lacroix, M.; Perot, G., HYDROGEN ACTIVATION BY TRANSITION METAL SULFIDES. *Catalysis Reviews* **2002,** *44* (4), 651-735, DOI 10.1081/CR-120015483.

310. Kong, L.; Dong, Y.; Jiang, P.; Wang, G.; Zhang, H.; Zhao, N., Light-assisted rapid preparation of a Ni/g-C_3N_4 magnetic composite for robust photocatalytic H_2 evolution from water. *Journal of Materials Chemistry A* **2016,** *4* (25), 9998-10007, DOI 10.1039/C6TA03178A.

311. Bi, L.; Xu, D.; Zhang, L.; Lin, Y.; Wang, D.; Xie, T., Metal Ni-loaded g-C_3N_4 for enhanced photocatalytic H_2 evolution activity: the change in surface band bending. *PCCP* **2015,** *17* (44), 29899-29905, DOI 10.1039/C5CP05158D.

312. Hong, J.; Wang, Y.; Wang, Y.; Zhang, W.; Xu, R., Noble-Metal-Free NiS/C_3N_4 for Efficient Photocatalytic Hydrogen Evolution from Water. *ChemSusChem* **2013,** *6* (12), 2263-2268, DOI 10.1002/cssc.201300647.

313. Mendoza, M. L. Z.; Resendis-Antonio, O., Metabolism Nitrogen Fixation. In *Encyclopedia of Systems Biology*, Dubitzky, W.; Wolkenhauer, O.; Cho, K.-H.; Yokota, H., Eds. Springer New York: New York, NY, 2013; pp 1275-1279.

314. Lan, R.; Tao, S., Ammonia as a Suitable Fuel for Fuel Cells. *Frontiers in Energy Research* **2014,** *2* (35), DOI 10.3389/fenrg.2014.00035.

315. Klerke, A.; Christensen, C. H.; Nørskov, J. K.; Vegge, T., Ammonia for hydrogen storage: challenges and opportunities. *J. Mater. Chem.* **2008,** *18* (20), 2304-2310, DOI 10.1039/B720020J.

316. Vu, M.-H.; Sakar, M.; Do, T.-O., Insights into the Recent Progress and Advanced Materials for Photocatalytic Nitrogen Fixation for Ammonia (NH_3) Production. *Catalysts* **2018,** *8* (12), 621.

317. Vu, M.-H.; Sakar, M.; Hassanzadeh-Tabrizi, S. A.; Do, T.-O., Photo(electro)catalytic Nitrogen Fixation: Problems and Possibilities. *Advanced Materials Interfaces* **2019,** *6* (12), 1900091, DOI 10.1002/admi.201900091.

318. Milton, R. D.; Cai, R.; Abdellaoui, S.; Leech, D.; De Lacey, A. L.; Pita, M.; Minteer, S. D., Bioelectrochemical Haber–Bosch Process: An Ammonia-Producing H_2/N_2 Fuel Cell. *Angew. Chem. Int. Ed.* **2017,** *56* (10), 2680-2683, DOI 10.1002/anie.201612500.

319. Ye, W.; Arif, M.; Fang, X.; Mushtaq, M. A.; Chen, X.; Yan, D., Efficient Photoelectrochemical Route for the Ambient Reduction of N_2 to NH_3 Based on Nanojunctions Assembled from MoS_2 Nanosheets and TiO_2. *ACS Applied Materials & Interfaces* **2019,** *11* (32), 28809-28817, DOI 10.1021/acsami.9b06596.

320. Ali, M.; Zhou, F.; Chen, K.; Kotzur, C.; Xiao, C.; Bourgeois, L.; Zhang, X.; MacFarlane, D. R., Nanostructured photoelectrochemical solar cell for nitrogen reduction using plasmon-enhanced black silicon. *Nature Communications* **2016,** *7* (1), 11335, DOI 10.1038/ncomms11335.

321. Zheng, J.; Lyu, Y.; Qiao, M.; Wang, R.; Zhou, Y.; Li, H.; Chen, C.; Li, Y.; Zhou, H.; Jiang, S. P.; Wang, S., Photoelectrochemical Synthesis of Ammonia on the Aerophilic-Hydrophilic Heterostructure with 37.8% Efficiency. *Chem* **2019,** *5* (3), 617-633, DOI https://doi.org/10.1016/j.chempr.2018.12.003.

322. Cheng, M.; Xiao, C.; Xie, Y., Photocatalytic nitrogen fixation: the role of defects in photocatalysts. *Journal of Materials Chemistry A* **2019,** *7* (34), 19616-19633, DOI 10.1039/C9TA06435D.

323. Feng, X.; Chen, H.; Jiang, F.; Wang, X., Enhanced visible-light photocatalytic nitrogen fixation over semicrystalline graphitic carbon nitride: Oxygen and sulfur co-doping for crystal and electronic structure modulation. *Journal of Colloid and Interface Science $V 509* **2018**, 298-306.

324. Xue, X.; Chen, R.; Yan, C.; Zhao, P.; Hu, Y.; Zhang, W.; Yang, S.; Jin, Z., Review on photocatalytic and electrocatalytic artificial nitrogen fixation for ammonia synthesis at mild conditions: Advances, challenges and perspectives. *Nano Research* **2019,** *12* (6), 1229-1249, DOI 10.1007/s12274-018-2268-5.

325. Xue, X.; Chen, R.; Chen, H.; Hu, Y.; Ding, Q.; Liu, Z.; Ma, L.; Zhu, G.; Zhang, W.; Yu, Q.; Liu, J.; Ma, J.; Jin, Z., Oxygen Vacancy Engineering Promoted Photocatalytic Ammonia Synthesis on Ultrathin Two-Dimensional Bismuth Oxybromide Nanosheets. *Nano Lett.* **2018,** *18* (11), 7372-7377, DOI 10.1021/acs.nanolett.8b03655.

326. Xue, X.; Chen, R.; Yan, C.; Hu, Y.; Zhang, W.; Yang, S.; Ma, L.; Zhu, G.; Jin, Z., Efficient photocatalytic nitrogen fixation under ambient conditions enabled by the heterojunctions of n-type Bi_2MoO_6 and oxygen-vacancy-rich p-type BiOBr. *Nanoscale* **2019,** *11* (21), 10439-10445, DOI 10.1039/C9NR02279A.

327. Zhang, N.; Jalil, A.; Wu, D.; Chen, S.; Liu, Y.; Gao, C.; Ye, W.; Qi, Z.; Ju, H.; Wang, C.; Wu, X.; Song, L.; Zhu, J.; Xiong, Y., Refining Defect States in $W_{18}O_{49}$ by Mo Doping: A Strategy for Tuning N_2 Activation towards Solar-Driven Nitrogen Fixation. *J. Am. Chem. Soc.* **2018,** *140* (30), 9434-9443, DOI 10.1021/jacs.8b02076.

328. Sun, Z.; Huo, R.; Choi, C.; Hong, S.; Wu, T.-S.; Qiu, J.; Yan, C.; Han, Z.; Liu, Y.; Soo, Y.-L.; Jung, Y., Oxygen vacancy enables electrochemical N_2 fixation over WO_3 with tailored structure. *Nano Energy* **2019,** *62*, 869-875, DOI https://doi.org/10.1016/j.nanoen.2019.06.019.

329. Tian, H.; Cui, X.; Zeng, L.; Su, L.; Song, Y.; Shi, J., Oxygen vacancy-assisted hydrogen evolution reaction of the Pt/WO_3 electrocatalyst. *Journal of Materials Chemistry A* **2019,** *7* (11), 6285-6293, DOI 10.1039/C8TA12219A.

330. Han, N.; Yang, K. R.; Lu, Z.; Li, Y.; Xu, W.; Gao, T.; Cai, Z.; Zhang, Y.; Batista, V. S.; Liu, W.; Sun, X., Nitrogen-doped tungsten carbide nanoarray as an efficient bifunctional electrocatalyst for water splitting in acid. *Nature Communications* **2018,** *9* (1), 924, DOI 10.1038/s41467-018-03429-z.

331. Liu, Q.; Wang, F.; Lin, H.; Xie, Y.; Tong, N.; Lin, J.; Zhang, X.; Zhang, Z.; Wang, X., Surface oxygen vacancy and defect engineering of WO_3 for improved visible light photocatalytic performance. *Catalysis Science & Technology* **2018,** *8* (17), 4399-4406, DOI 10.1039/C8CY00994E.

332. Li, Y.; Tang, Z.; Zhang, J.; Zhang, Z., Defect Engineering of Air-Treated WO3 and Its Enhanced Visible-Light-Driven Photocatalytic and Electrochemical Performance. *The Journal of Physical Chemistry C* **2016,** *120* (18), 9750-9763, DOI 10.1021/acs.jpcc.6b00457.

333. Wei, Z.; Zhang, Y.; Wang, S.; Wang, C.; Ma, J., Fe-doped phosphorene for the nitrogen reduction reaction. *Journal of Materials Chemistry A* **2018,** *6* (28), 13790-13796, DOI 10.1039/C8TA03989E.

334. Luo, J.; Bai, X.; Li, Q.; Yu, X.; Li, C.; Wang, Z.; Wu, W.; Liang, Y.; Zhao, Z.; Liu, H., Band structure engineering of bioinspired Fe doped $SrMoO_4$ for enhanced photocatalytic nitrogen reduction performance. *Nano Energy* **2019**, 104187, DOI https://doi.org/10.1016/j.nanoen.2019.104187.

335. Yan, C.; Xue, X.; Zhang, W.; Li, X.; Liu, J.; Yang, S.; Hu, Y.; Chen, R.; Yan, Y.; Zhu, G.; Kang, Z.; Kang, D. J.; Liu, J.; Jin, Z., Well-designed Te/SnS2/Ag artificial nanoleaves for enabling and enhancing visible-light driven overall splitting of pure water. *Nano Energy* **2017,** *39*, 539-545, DOI https://doi.org/10.1016/j.nanoen.2017.07.039.

336. Zhang, W.; Hu, Y.; Yan, C.; Hong, D.; Chen, R.; Xue, X.; Yang, S.; Tian, Y.; Tie, Z.; Jin, Z., Surface plasmon resonance enhanced direct Z-scheme TiO_2/ZnTe/Au nanocorncob heterojunctions for efficient photocatalytic overall water splitting. *Nanoscale* **2019,** *11* (18), 9053-9060, DOI 10.1039/C9NR01732A.

337. Leong, K. H.; Aziz, A. A.; Sim, L. C.; Saravanan, P.; Jang, M.; Bahnemann, D., Mechanistic insights into plasmonic photocatalysts in utilizing visible light. *Beilstein J Nanotechnol* **2018,** *9*, 628-648, DOI 10.3762/bjnano.9.59.

338. Chen, D.; Ge, L.; Yin, L.; Shi, H.; Yang, D.; Yang, J.; Zhang, R.; Shao, G., Solvent-regulated solvothermal synthesis and morphology-dependent gas-sensing performance of low-dimensional tungsten oxide nanocrystals. *Sensors and Actuators B: Chemical* **2014,** *205*, 391-400, DOI https://doi.org/10.1016/j.snb.2014.09.007.

339. Sun, S.; Chang, X.; Dong, L.; Zhang, Y.; Li, Z.; Qiu, Y., $W_{18}O_4{}_9$ nanorods decorated with Ag/AgCl nanoparticles as highly-sensitive gas-sensing material and visible-light-driven photocatalyst. *J. Solid State Chem.* **2011,** *184* (8), 2190-2195, DOI https://doi.org/10.1016/j.jssc.2011.06.024.

340. Zhong, X.; Sun, Y.; Chen, X.; Zhuang, G.; Li, X.; Wang, J.-G., Mo Doping Induced More Active Sites in Urchin-Like W18O49 Nanostructure with Remarkably Enhanced Performance for Hydrogen Evolution Reaction. *Adv. Funct. Mater.* **2016,** *26* (32), 5778-5786, DOI 10.1002/adfm.201601732.

341. Fang, Z.; Jiao, S.; Kang, Y.; Pang, G.; Feng, S., Photothermal Conversion of $W_{18}O_{49}$ with a Tunable Oxidation State. *ChemistryOpen* **2017,** *6* (2), 261-265, DOI 10.1002/open.201600149.

342. Khalil, M. M. H.; Ismail, E. H.; El-Magdoub, F., Biosynthesis of Au nanoparticles using olive leaf extract: 1st Nano Updates. *Arabian Journal of Chemistry* **2012,** *5* (4), 431-437, DOI https://doi.org/10.1016/j.arabjc.2010.11.011.

343. Cong, S.; Yuan, Y.; Chen, Z.; Hou, J.; Yang, M.; Su, Y.; Zhang, Y.; Li, L.; Li, Q.; Geng, F.; Zhao, Z., Noble metal-comparable SERS enhancement from semiconducting metal oxides by making oxygen vacancies. *Nature Communications* **2015,** *6* (1), 7800, DOI 10.1038/ncomms8800.

344. Lv, Y.; Zhu, Y.; Zhu, Y., Enhanced Photocatalytic Performance for the $BiPO_{4-x}$ Nanorod Induced by Surface Oxygen Vacancy. *The Journal of Physical Chemistry C* **2013,** *117* (36), 18520-18528, DOI 10.1021/jp405596e.

345. Sadakane, M.; Sasaki, K.; Kunioku, H.; Ohtani, B.; Abe, R.; Ueda, W., Preparation of 3-D ordered macroporous tungsten oxides and nano-crystalline particulate tungsten oxides using a colloidal crystal template method, and their structural characterization and

application as photocatalysts under visible light irradiation. *J. Mater. Chem.* **2010,** *20* (9), 1811-1818, DOI 10.1039/B922416E.

346. Shi, L.; Li, Z.; Marcus, K.; Wang, G.; Liang, K.; Niu, W.; Yang, Y., Integration of Au nanoparticles with a g-C_3N_4 based heterostructure: switching charge transfer from type-II to Z-scheme for enhanced visible light photocatalysis. *Chem. Commun.* **2018,** *54* (30), 3747-3750, DOI 10.1039/C8CC01370E.

347. Hai, G.; Huang, J.; Cao, L.; Jie, Y.; Li, J.; Wang, X., Shape Evolution of Hierarchical $W_{18}O_{49}$ Nanostructures: A Systematic Investigation of the Growth Mechanism, Properties and Morphology-Dependent Photocatalytic Activities. *Nanomaterials* **2016,** *6* (12), 240.

348. Steiner, S.; Seo, I.-T.; Ren, P.; Li, M.; Keeble, D. J.; Frömling, T., The effect of Fe-acceptor doping on the electrical properties of $Na_{1/2}Bi_{1/2}TiO_3$ and 0.94 $(Na_{1/2}Bi_{1/2})TiO_3$–0.06 $BaTiO_3$. *J. Am. Ceram. Soc.* **2019,** *102* (9), 5295-5304, DOI 10.1111/jace.16401.

349. Minh Vuong, N.; Kim, D.; Kim, H., Porous Au-embedded WO_3 Nanowire Structure for Efficient Detection of CH_4 and H_2S. *Scientific Reports* **2015,** *5*, 11040, DOI 10.1038/srep11040

350. You, L.; Liu, B.; Liu, T.; Fan, B.; Cai, Y.; Guo, L.; Sun, Y., Organic Solar Cells Based on $WO_{2.72}$ Nanowire Anode Buffer Layer with Enhanced Power Conversion Efficiency and Ambient Stability. *ACS Applied Materials & Interfaces* **2017,** *9* (14), 12629-12636, DOI 10.1021/acsami.6b15762.

351. Wang, J.; Zhang, N.; Su, J.; Guo, L., α-Fe_2O_3 quantum dots: low-cost synthesis and photocatalytic oxygen evolution capabilities. *RSC Advances* **2016,** *6* (47), 41060-41066, DOI 10.1039/C6RA04464F.

352. Martínez, L.; Benito, M.; Mata, I.; Soler, L.; Molins, E.; Llorca, J., Preparation and photocatalytic activity of Au/TiO_2 lyogels for hydrogen production. *Sustainable Energy & Fuels* **2018,** *2* (10), 2284-2295, DOI 10.1039/C8SE00293B.

353. Tang, X.; Huang, J.; Liao, H.; Chen, G.; Mo, Z.; Ma, D.; Zhan, R.; Li, Y.; Luo, J., Growth of $W_{18}O_{49}$/WOx/W dendritic nanostructures by one-step thermal evaporation and their high-performance photocatalytic activities in methyl orange degradation. *CrystEngComm* **2019,** *21* (39), 5905-5914, DOI 10.1039/C9CE01047E.

354. McIntyre, N. S.; Zetaruk, D. G., X-ray photoelectron spectroscopic studies of iron oxides. *Anal. Chem.* **1977,** *49* (11), 1521-1529, DOI 10.1021/ac50019a016.

355. Gong, H.; Cao, Y.; Zhang, Y.; Zhang, Y.; Liu, K.; Cao, H.; Yan, H., The synergetic effect of dual co-catalysts on the photocatalytic activity of square-like WO_3 with different exposed facets. *RSC Advances* **2017,** *7* (31), 19019-19025, DOI 10.1039/C7RA01149K.

356. Li, J.; Liu, Y.; Zhu, Z.; Zhang, G.; Zou, T.; Zou, Z.; Zhang, S.; Zeng, D.; Xie, C., A full-sunlight-driven photocatalyst with super long-persistent energy storage ability. *Scientific Reports* **2013,** *3* (1), 2409, DOI 10.1038/srep02409.

357. Catchpole, K. R.; Polman, A., Design principles for particle plasmon enhanced solar cells. *Appl. Phys. Lett.* **2008,** *93* (19), 191113, DOI 10.1063/1.3021072.

358. Clavero, C., Plasmon-induced hot-electron generation at nanoparticle/metal-oxide interfaces for photovoltaic and photocatalytic devices. *Nature Photonics* **2014,** *8*, 95, DOI 10.1038/nphoton.2013.238.

359. Hou, Y.; Zuo, F.; Dagg, A.; Feng, P., A Three-Dimensional Branched Cobalt-Doped α-Fe_2O_3 Nanorod/$MgFe_2O_4$ Heterojunction Array as a Flexible Photoanode for Efficient Photoelectrochemical Water Oxidation. *Angew. Chem.* **2013,** *125* (4), 1286-1290, DOI 10.1002/ange.201207578.

360. Nootchanat, S.; Ninsonti, H.; Baba, A.; Ekgasit, S.; Thammacharoen, C.; Shinbo, K.; Kato, K.; Kaneko, F., Investigation of localized surface plasmon/grating-coupled surface plasmon enhanced photocurrent in TiO_2 thin films. *PCCP* **2014,** *16* (44), 24484-24492, DOI 10.1039/C4CP03885A.

361. Nazemi, M.; El-Sayed, M. A., Plasmon-enhanced photo(electro)chemical nitrogen fixation under ambient conditions using visible light responsive hybrid hollow Au-Ag_2O nanocages. *Nano Energy* **2019,** *63*, 103886, DOI https://doi.org/10.1016/j.nanoen.2019.103886.

362. Shi, M.-M.; Bao, D.; Wulan, B.-R.; Li, Y.-H.; Zhang, Y.-F.; Yan, J.-M.; Jiang, Q., Au Sub-Nanoclusters on TiO_2 toward Highly Efficient and Selective Electrocatalyst for N_2 Conversion to NH_3 at Ambient Conditions. *Adv. Mater.* **2017,** *29* (17), 1606550, DOI 10.1002/adma.201606550.

363. Modak, J., Haber process for ammonia synthesis. *Resonance* **2002,** *7*, 69-77, DOI 10.1007/BF02836187.

364. Zhang, G.; Yang, X.; He, C.; Zhang, P.; Mi, H., Constructing a tunable defect structure in TiO_2 for photocatalytic nitrogen fixation. *Journal of Materials Chemistry A* **2020,** *8* (1), 334-341, DOI 10.1039/C9TA10471B.

365. Kong, W.; Zhang, R.; Zhang, X.; Ji, L.; Yu, G.; Wang, T.; Luo, Y.; Shi, X.; Xu, Y.; Sun, X., WO3 nanosheets rich in oxygen vacancies for enhanced electrocatalytic N2 reduction to NH3. *Nanoscale* **2019,** *11* (41), 19274-19277, DOI 10.1039/C9NR03678D.

366. Xiao, C.; Wang, H.; Zhang, L.; Sun, S.; Wang, W., Enhanced Photocatalytic Nitrogen Fixation on MoO_2/BiOCl Composite. *ChemCatChem* **2019,** *11* (24), 6467-6472, DOI 10.1002/cctc.201901635.

367. Vu, M.-H.; Nguyen, C.-C.; Do, T.-O., Synergistic Effect of Fe Doping and Plasmonic Au Nanoparticles on W18O49 Nanorods for Enhancing Photoelectrochemical Nitrogen Reduction. *ACS Sustainable Chemistry & Engineering* **2020**, DOI 10.1021/acssuschemeng.0c04662.

368. Zhang, S.; Zhao, Y.; Shi, R.; Waterhouse, G. I. N.; Zhang, T., Photocatalytic ammonia synthesis: Recent progress and future. *EnergyChem* **2019,** *1* (2), 100013, DOI https://doi.org/10.1016/j.enchem.2019.100013.

369. Yao, X.; Zhang, W.; Huang, J.; Du, Z.; Hong, X.; Chen, X.; Hu, X.; Wang, X., Enhanced photocatalytic nitrogen fixation of Ag/B-doped g-C_3N_4 nanosheets by one-step in-situ decomposition-thermal polymerization method. *Applied Catalysis A: General* **2020,** *601*, 117647, DOI https://doi.org/10.1016/j.apcata.2020.117647.

370. Gao, X.; An, L.; Qu, D.; Jiang, W.; Chai, Y.; Sun, S.; Liu, X.; Sun, Z., Enhanced photocatalytic N_2 fixation by promoting N_2 adsorption with a co-catalyst. *Science Bulletin* **2019,** *64* (13), 918-925, DOI https://doi.org/10.1016/j.scib.2019.05.009.

371. Huang, T.; Pan, S.; Shi, L.; Yu, A.; Wang, X.; Fu, Y., Hollow porous prismatic graphitic carbon nitride with nitrogen vacancies and oxygen doping: a high-performance visible light-driven catalyst for nitrogen fixation. *Nanoscale* **2020,** *12* (3), 1833-1841, DOI 10.1039/C9NR08705B.

372. Chen, Y.; Zhao, C.; Ma, S.; Xing, P.; Hu, X.; Wu, Y.; He, Y., Fabrication of a Z-scheme AgBr/$Bi4O_5Br_2$ nanocomposite and its high efficiency in photocatalytic N_2 fixation and dye degradation. *Inorganic Chemistry Frontiers* **2019,** *6* (11), 3083-3092, DOI 10.1039/C9QI00782B.

373. Pan, Y.-X.; You, Y.; Xin, S.; Li, Y.; Fu, G.; Cui, Z.; Men, Y.-L.; Cao, F.-F.; Yu, S.-H.; Goodenough, J. B., Photocatalytic CO_2 Reduction by Carbon-Coated Indium-Oxide Nanobelts. *J. Am. Chem. Soc.* **2017,** *139* (11), 4123-4129, DOI 10.1021/jacs.7b00266.

374. Gan, X.; Zheng, R.; Liu, T.; Meng, J.; Chen, R.; Sun, X.; Sun, X., N-Doped Mesoporous In_2O_3 for Photocatalytic Oxygen Evolution from the In-based Metal–Organic Frameworks. *Chemistry – A European Journal* **2017,** *23* (30), 7264-7271, DOI 10.1002/chem.201605576.

375. Wang, Z.; Hou, C.; De, Q.; Gu, F.; Han, D., One-Step Synthesis of Co-Doped In_2O_3 Nanorods for High Response of Formaldehyde Sensor at Low Temperature. *ACS Sensors* **2018,** *3* (2), 468-475, DOI 10.1021/acssensors.7b00896.

376. Xu, H.; Wang, Y.; Dong, X.; Zheng, N.; Ma, H.; Zhang, X., Fabrication of In_2O_3/In_2S_3 microsphere heterostructures for efficient and stable photocatalytic nitrogen fixation. *Applied Catalysis B: Environmental* **2019,** *257*, 117932, DOI https://doi.org/10.1016/j.apcatb.2019.117932.

377. Han, R.; Chang, S.; Xu, X., Gold nanocrystal anchored In_2O_3 hollow nanospheres for N_2 photofixation to ammonia. *Inorganic Chemistry Frontiers* **2020,** *7* (15), 2778-2782, DOI 10.1039/D0QI00311E.

378. Nguyen, C.-C.; Vu, N.-N.; Chabot, S.; Kaliaguine, S.; Do, T.-O., Role of CxNy-Triazine in Photocatalysis for Efficient Hydrogen Generation and Organic Pollutant Degradation Under Solar Light Irradiation. *Solar RRL* **2017,** *1* (5), 1700012, DOI 10.1002/solr.201700012.

379. Zhang, P.; Lou, X. W., Design of Heterostructured Hollow Photocatalysts for Solar-to-Chemical Energy Conversion. *Adv. Mater.* **2019,** *31* (29), 1900281, DOI 10.1002/adma.201900281.

380. Xiao, M.; Wang, Z.; Lyu, M.; Luo, B.; Wang, S.; Liu, G.; Cheng, H.-M.; Wang, L., Hollow Nanostructures for Photocatalysis: Advantages and Challenges. *Adv. Mater.* **2019,** *31* (38), 1801369, DOI 10.1002/adma.201801369.

381. Liu, S.; Yu, J.; Jaroniec, M., Tunable Photocatalytic Selectivity of Hollow TiO_2 Microspheres Composed of Anatase Polyhedra with Exposed {001} Facets. *J. Am. Chem. Soc.* **2010,** *132* (34), 11914-11916, DOI 10.1021/ja105283s.

382. Tao, H.; Choi, C.; Ding, L.-X.; Jiang, Z.; Han, Z.; Jia, M.; Fan, Q.; Gao, Y.; Wang, H.; Robertson, A. W.; Hong, S.; Jung, Y.; Liu, S.; Sun, Z., Nitrogen Fixation by Ru Single-Atom Electrocatalytic Reduction. *Chem* **2019,** *5* (1), 204-214, DOI https://doi.org/10.1016/j.chempr.2018.10.007.

383. Liu, S.; Wang, Y.; Wang, S.; You, M.; Hong, S.; Wu, T.-S.; Soo, Y.-L.; Zhao, Z.; Jiang, G.; Jieshan, Q.; Wang, B.; Sun, Z., Photocatalytic Fixation of Nitrogen to Ammonia by Single Ru Atom Decorated TiO2 Nanosheets. *ACS Sustainable Chemistry & Engineering* **2019,** *7* (7), 6813-6820, DOI 10.1021/acssuschemeng.8b06134.

384. Wang, S.; Guan, B. Y.; Lu, Y.; Lou, X. W. D., Formation of Hierarchical In_2S_3–$CdIn_2S_4$ Heterostructured Nanotubes for Efficient and Stable Visible Light CO_2 Reduction. *J. Am. Chem. Soc.* **2017,** *139* (48), 17305-17308, DOI 10.1021/jacs.7b10733.

385. Khalifa, Z. S.; Mahmoud, S. A., Photocatalytic and optical properties of titanium dioxide thin films prepared by metalorganic chemical vapor deposition. *Physica E: Low-dimensional Systems and Nanostructures* **2017,** *91*, 60-64, DOI https://doi.org/10.1016/j.physe.2017.03.010.

386. Tu, D.; Liao, H.; Deng, Q.; Liu, X.; Shang, R.; Zhang, X., Renewable biomass derived porous BCN nanosheets and their adsorption and photocatalytic activities for the decontamination of organic pollutants. *RSC Advances* **2018,** *8*, 21905-21914, DOI 10.1039/C8RA03689F.

387. Qing, G.; Ghazfar, R.; Jackowski, S. T.; Habibzadeh, F.; Ashtiani, M. M.; Chen, C.-P.; Smith, M. R.; Hamann, T. W., Recent Advances and Challenges of Electrocatalytic N_2 Reduction to Ammonia. *Chem. Rev.* **2020,** *120* (12), 5437-5516, DOI 10.1021/acs.chemrev.9b00659.

388. Liu, Y.; Li, C.; Guan, L.; Li, K.; Lin, Y., Oxygen Vacancy Regulation Strategy Promotes Electrocatalytic Nitrogen Fixation by Doping Bi into Ce-MOF-Derived CeO_2 Nanorods. *The Journal of Physical Chemistry C* **2020**, DOI 10.1021/acs.jpcc.0c05949.

389. Soni, S.; Kumar, S.; Dalela, B.; Kumar, S.; Alvi, P. A.; Dalela, S., Defects and oxygen vacancies tailored structural and optical properties in CeO_2 nanoparticles doped with Sm^{3+} cation. *J. Alloys Compd.* **2018,** *752*, 520-531, DOI https://doi.org/10.1016/j.jallcom.2018.04.157.

390. Wu, S.; Xiong, J.; Sun, J.; Hood, Z.; Zeng, W.; Yang, Z.; Gu, L.; Zhang, X.; Yang, S.-Z., Hydroxyl-Dependent Evolution of Oxygen Vacancies Enables the Regeneration of BiOCl Photocatalyst. *ACS Applied Materials & Interfaces* **2017,** *9,* DOI 10.1021/acsami.7b01701.

391. Paier, J.; Penschke, C.; Sauer, J., Oxygen Defects and Surface Chemistry of Ceria: Quantum Chemical Studies Compared to Experiment. *Chem. Rev.* **2013,** *113* (6), 3949-3985, DOI 10.1021/cr3004949.

392. Zhang, B.; Wang, L.; Zhang, Y.; Ding, Y.; Bi, Y., Ultrathin FeOOH Nanolayers with Abundant Oxygen Vacancies on BiVO4 Photoanodes for Efficient Water Oxidation. *Angew. Chem. Int. Ed.* **2018,** *57* (8), 2248-2252, DOI 10.1002/anie.201712499.

List of publications and presentations

List of publications

1) **Manh-Hiep Vu**, Chinh-Chien Nguyen, Mohan Sakar, Trong-On Do. "*Ni supported $CdIn_2S_4$ sponge-like spheres: a noble metal free high-performance sunlight driven photocatalyst for hydrogen production*", Phys. Chem. Chem. Phys., **2017**, 19, 29429-29437.

2) **Manh-Hiep Vu**, Mohan Sakar, Chinh-Chien Nguyen, Trong-On Do. "*Chemically Bonded Ni Cocatalyst onto the S Doped g-C_3N_4 Nanosheets and Their Synergistic Enhancement in H_2 Production under Sunlight Irradiation*", ACS Sustainable Chemistry & Engineering, **2018**, 6 (3), 4194-4203.

3) **Manh-Hiep Vu,** Chinh-Chien Nguyen, Trong-On Do, "*Synergistic Effect of Fe doping and plasmonic Au nanoparticles on $W_{18}O_{49}$ nanorods for enhancing photoelectrochemical nitrogen reduction"*, ACS Sustainable Chemistry & Engineering, **2020**.

4) **Manh-Hiep Vu**, Mohan Sakar, Trong-ON Do, "*Insights into the Recent Progress and Advanced Materials for Photocatalytic Nitrogen Fixation for Ammonia (NH_3) Production", Catalysts*, **2018**, 8 (12), 621.

5) **Manh-Hiep Vu**, Mohan Sakar, Sayed Ali Hassanzadeh-Tabrizi, Trong-On Do, "*Photo(electro)catalytic Nitrogen Fixation: Problems and Possibilities", Advanced Materials Interfaces*, **2019**, 6 (12), 1900091.

6) **Manh-Hiep Vu**, Toan Anh Quach, Trong On Do, "*Construction of Ru doped In_2O_3 hollow peanut as efficient photocatalyst for solar light-driven nitrogen reduction*" Submitted

7) **Manh-Hiep Vu**, Mohan Sakar, Chinh-Chien Nguyen, Trong-ON Do, "*Enhanced hydrogen production by the protonated, sulfur doped and Pt-loaded g-C_3N_4 nanolayers*". Material Letter, **2018**, 218, 169-177.

8) Yu-Hsuan Liu, **Manh Hiep Vu**, JeongHoon Lim, Trong-On Do, Marta C. Hatzell. "*Influence of carbonaceous species on aqueous photo-catalytic nitrogen fixation by titania*" Faraday Discussion, **2019**, 215 (0), 379-392

9) Driss Mrabet**, Manh-Hiep Vu**, Serge Kaliaguine, Trong-On Do, "*A new route to the shape-controlled synthesis of nano-sized γ-alumina and Ag/γ-alumina for selective catalytic reduction of NO in the presence of propene*", Journal of Colloid Interface Science, **2017**, 485, 144-151

10) Chinh-Chien Nguyen, Mohan Sakar, **Manh-Hiep Vu**, Trong-On Do, "*Nitrogen Vacancies-Assisted Enhanced Plasmonic Photoactivities of Au/g-C_3N_4 Crumpled Nanolayers: A Novel Pathway toward Efficient Solar Light-Driven Photocatalysts*", *Industrial & Engineering Chemistry Research,* **2019,** 58 (9), 3698-3706.

11) Mohan Sakar, Chinh-Chien Nguyen, **Manh-Hiep Vu**, Trong-On Do, "*Materials and Mechanisms of Photo-Assisted Chemical Reactions under Light and Dark Conditions: Can Day–Night Photocatalysis Be Achieved?*", *ChemSusChem* **2018,** 11 (5), 809-820.

Conference presentations

1) Yu-Hsuan Liu, **Manh Hiep Vu**, JeongHoon Lim, Trong-On Do, Marta C. Hatzell. "*Influence of carbonaceous species on aqueous photo-catalytic nitrogen fixation by titania*" Poster presentation, 10th CGCC Annual Meeting, October 10, 2019, Université de Montréal, Montreal city, Canada.

2) **Manh-Hiep Vu**, Mohan Sakar, Chinh-Chien Nguyen, Trong-On Do. "*Chemically Bonded Ni Cocatalyst onto the S Doped g-C_3N_4 Nanosheets and Their Synergistic Enhancement in H_2 Production under Sunlight Irradiation*" McGill-Polytechnique-Laval Journée de la recherche en génie chimique 2019